UNIVERSITY OF SOUTHAMPTON

FACULTY OF ENGINEERING AND THE ENVIRONMENT

National Centre for Advanced Tribology at Southampton (nCATS)

A Study on Microstructural Alterations in White Etching Cracks, Dark Etching Region, and White Etching Bands in Rolling Contacts

By

Viktorija Rumpf

(née Šmeļova)

Supervisors:

Prof. Ling Wang[a], Prof. Dr. Walter Holweger[a, b]

[a] National Centre for Advanced Tribology at Southampton (nCATS), University of Southampton, UK

[b] Basic Tribology, Competence centre of Surface Technology, Schaeffler Technologies AG & Co. KG, Herzogenaurach, Germany

Thesis for the degree of Doctor of Philosophy

May 2018

UNIVERSITY OF SOUTHAMPTON

ABSTRACT

FACULTY OF ENGINEERING AND THE ENVIRONMENT

National Centre for Advanced Tribology at Southampton (nCATS)

Thesis for the degree of Doctor of Philosophy

A STUDY ON THE MICROSTRUCTURAL ALTERATIONS IN WHITE ETCHING CRACKS, DARK ETCHING REGION, AND WHITE ETCHING BANDS IN ROLLING CONTACTS

Viktorija Rumpf

The formation of subsurface White Etching Cracks (WECs) is found to cause catastrophic bearing failures by spalling in their early service life. WECs cause failures in a wide range of engineering applications with a large amount being reported in wind turbines in recent years. One of the characteristics that makes WECs a unique and complex failure mode is that the cracks are accompanied by White Etching Area (WEA). Many mechanisms, including adiabatic shear bands, electromagnetic field impact, severe localised deformation, carbide dissolution, accumulation of plastic deformation, low temperature recrystallisation, and others, have been suggested as possible WECs formation mechanisms. However, due to lack of supporting evidence for altered microstructure evolvement, the WECs initiation and development mechanisms are still under debate. Other microstructure alterations forming in rolling bearings, namely Dark Etching Region (DER) and White Etching Bands (WEBs) known to be caused by Rolling Contact Fatigue (RCF) were frequently reported in literature between 1940s and 1990s, however their formation mechanisms and especially their links to WECs are also not fully understood.

This study aims to investigate the initiation and propagation mechanisms of WECs as well as DER and WEBs through detailed microstructural characterisation of these features in typical AISI 52100 through-hardened martensitic bearing steels. A combination of hardness and microscopy characterisation techniques, including Scanning Electron Microscopy (SEM), Electron Backscatter Diffraction (EBSD)

combined with Energy Dispersive X-ray spectroscopy (EDX) have been used throughout this study.

Initially, the analyses have been conducted on WECs, DER and WEBs in failed bearings from service or laboratory rigs, where all features were at their fully developed stage. The results have revealed that the microstructural alterations in WECs have many similarities to the RCF features including the manifestation of equiaxed and elongated grains in all these features. The fact that DER still contains unaltered primary spheroidised carbides $(Fe, Cr)_3C$ suggests that formation of such equiaxed and elongated grains could be the initial stage of all the microstructure alterations. It has also been observed that primary spheroidised carbides have disintegrated in the WECs and WEBs, accompanying the observation of carbon and chromium redistribution in these areas. This has led to believe that primary spheoridised carbide disintegration may play a key role in the formation and development of white etching microstructure in both WECs and WEBs.

The study was then moved on to investigating the initiation and development stages of WECs and RCF features by analysing bearings tested under controlled laboratory conditions over a sequence of rolling cycles. This enabled the chronological examination of the microstructure alterations. The results have revealed that the formation of microcracks (approx. 2-4 μm in length) in the very early stage of rolling contact may be the initiation stage of WECs developed in the bearing steel in the later stages under electrical current influence. The initial microcracking is found to be followed by crack branching and microstructural change adjacent to the cracks or formation of WEA. However, in the bearings subjected to prolonged RCF testing, it has been found that initially equiaxed grains form, followed by formation of carbon-rich area adjacent to the newly formed grains and then growth of both under continuous cyclic loading. Electrochemical processes involving the 'bad lubricant' and electrical current may be responsible for the initial microcracks formation, however further investigation of WECs formation under other operating conditions should be conducted to explore whether same mechanisms are involved. The detailed findings from this study provide a significant breakthrough in the understanding of WECs as well as its relation to DER and WEBs in RCF.

Table of Contents

List of Tables

List of Figures

Declaration of Authorship

I, Viktorija Rumpf, declare that the thesis entitled '*A study of microstructural alterations in White Etching Cracks, Dark Etching Region, and White Etching Bands in rolling contacts*' and the work presented in the thesis are my own, and has been generated by me as the result of my own original research. I confirm that:

- this work was done wholly or mainly while in candidature for a research degree at this University;
- where any part of this thesis has previously been submitted for a degree or any other qualification at this University or any other institution, this has been clearly stated;
- where I have consulted the published work of others, this is always clearly attributed;
- where I have quoted from the work of others, the source is always given. With the exception of such quotations, this thesis is entirely my own work;
- I have acknowledged all main sources of help;
- where the thesis is based on work done by myself jointly with others, I have made clear exactly what was done by others and what I have contributed myself. See acknowledgements;
- Parts of this work have been published as:
    - V. Šmeļova, A. Schwedt, L. Wang, W. Holweger, and J. Mayer, "Electron Microscopy Investigations of Microstructural Alterations Due to Classical Rolling Contact Fatigue (RCF) in Martensitic AISI 52100 Bearing Steel," *International Journal of Fatigue,* vol. 98, pp. 142-154, 2017.
    - V. Šmeļova, A. Schwedt, L. Wang, W. Holweger, and J. Mayer, "Microstructural Changes in White Etching Cracks (WECs) and Their Relationship with Those in Dark Etching Region (DER) and White Etching Bands (WEBs) Due to Rolling Contact Fatigue (RCF)," *International Journal of Fatigue*, vol. 100, Part 1, pp. 148-158, 2017.

Signed: Viktorija Rumpf .....

Date: 22/May/2018

Acknowledgements

This thesis is the culmination of a defining journey that lasted three and a half years. I have grown a lot both personally and professionally during the journey, and I will always value each joyous and tough moment of it – there were plenty of both. However, this journey would not have taken place if it was not for my fellow travellers and pathfinders. Even though I will not mention every person that has supported me along the way, I am for ever grateful for their help in pushing me forward.

The first acknowledgement goes to *Ling* and *Walter* who acted as supervisors of this project, not only for their guidance and the continuous support during the course of this PhD study, but also for giving me so many wonderful opportunities. Not many PhDs involve a yearlong position abroad or the chance to attend several international conferences! I thank Ling wholeheartedly for help through the good and the bad times of the research - I truly appreciate her willingness to meet me at short notice and the effort it took to go through several drafts of my thesis.

My doctoral studies were made possible by Schaeffler and EPSRC who funded this project as well as the Armourers & Brasiers' company, RMS, and IMechE who provided travel grants to attend several conferences. I would like to thank employees of Schaeffler for conducting tests, supplying all the specimens in addition to the information on it and kindly collaboration with us.

A very special thank you goes out to *Prof. Joachim Mayer*, who has kindly provided me with an opportunity to join the GFE team at RWTH Aachen University (Germany) as a yearlong visiting researcher. I am indebted to you for giving me access to the laboratory and research facilities as well as for your support, invaluable insights and suggestions. My sincere gratitude also goes to *Alexander*, who was always there to help with microscopy and analyses. I am extremely grateful for his patience, motivation, vast knowledge, and all the productive discussions and brainstorming sessions. I am also grateful to the following GFE, RWTH Aachen university colleagues: *Melonie, Nelly, Fabian, Prof. Thomas Weirich, Kevin, Sebastian, Michael,* along with others, for their unfailing support and

assistance. A big thanks also to all for organising great events and celebrations which gave me an opportunity to experience German culture and traditions. I had a wonderful time in Aachen and I could not have imagined having a better working environment for my PhD study.

Thank you to my fellow past and present colleagues who have made my time at Southampton immensely enjoyable. Many thanks to *Alex* for introducing me to metallographic preparation methods, *Pawee* for helping and assisting me at the start of my SEM journey, *John* for FIB training, and *Vanesa* for providing training and helping with hardness measurements. I would also like to take this opportunity to thank *Prof. Brian Mellor* and *Dr. John Walker* - my internal examiners, for their insightful comments, suggestions, encouragement, and for the hard questions which pushed me to think about my research from various perspectives.

I also must acknowledge all *my friends around the globe*, old and new, although not directly involved in the work, nevertheless contributed by encouraging, believing and supporting me during these years as a PhD student, you know who you are! Thank you all for your friendship and support in one way or another, it means the world to me.

Words cannot express the feelings I have for *my parents, my sister and my in-laws* for supporting me through the years of studying and my life in general. Their love, understanding and support was essential to make it through. Special thanks to my mum, whose encouragement knows no limits: you are my life-coach!

Слова не могут выразить чувства, которые я испытываю к своим родителям, сестре и родственникам, которые меня поддерживали на всех этапах работы над диссертацией и моей жизни в целом. Их любовь, понимание и поддержка были необходимы для преодоления всех трудностей. Отдельная благодарность моей маме: ты мой учитель жизни!

Finally, last but by no means least, I want to thank my husband *Clemens*. He has been an unwavering source of strength and inspiration. There were times during the past four years when everything seemed hopeless and I was ready to give up. It was his determination and constant encouragement that ultimately made it possible for me to see this project through to the end. Thank you for all the help, advice, crazy trips and travels, for little surprises and for the days full of happiness.

Contribution to the work:

- All bearing specimens investigated in this study have been provided by Schaeffler group. Test conditions for bearings investigated in Chapters 5 & 6 were partly designed by myself, but tests were operated and executed by Mr. Michael Warmuth (Schaeffler).

- The calculations of the stresses, depths of maximum shear stresses and load cycles presented in Chapter 4 & 5 were calculated by Mr. Martin Correns (Schaeffler).

- Preparation of samples were guided and partly done by myself but also Ms. Melanie Keil, Mr. Fabian Mariano, and Mr. Kevin Kistermann (GFE, RWTH Aachen).

- The SEM and EBSD/EDX work presented in Chapter 4 was guided and partly operated by myself but also Dr. Alexander Schwedt (GFE, RWTH Aachen).

- Berkovich hardness measurements were designed and performed by myself with guidance from Dr. Vanesa Martinez (nCATS). Vickers nanohardness measurements were designed by myself and Dr. Alexander Schwedt (GFE, RWTH Aachen), but performed by Ms. Melanie Keil and Ms. Ruth Harscheidt (GFE, RWTH Aachen).

- The Transmission Electron Microscopy (TEM) work presented in Chapter 4 was guided by myself but operated by Mr. Sebastian Zischke (GFE, RWTH Aachen). SAED patterns indexing has been performed by myself with guidance from Prof. Thomas E. Weirich.

- The heat treatments in large chamber SEM (Mira VP) presented in Chapter 5 were guided and partly operated by myself but also Mr. Michael Spähn (GFE, RWTH Aachen).

Definitions and Abbreviations

AISI	American Iron and Steel Institute
APT	Atom Probe Tomography
BCC	Body Centred Cubic
BCT	Body Centred Tetragonal
BF	Bright Field
BSE	Backscattered Electrons
CI	Confidence Index
CT	Computed Tomography
DER	Dark Etching Region
DF	Dark Field
DGBB	Deep Grove Ball Bearing
EBSD	Electron Backscattered Diffraction
EDX	Energy-dispersive X-ray Spectroscopy
EPMA	Electron Probe Microanalysis
FCC	Face Centred Cubic
FIB	Focused Ion Beam
HAB	High Angle Bands
HAGB	High Angle Grain Boundary
HV0.001	Vickers hardness; number indicates the load used in kgf
IPA	Isopropyl Alcohol
IPF	Inverse Pole Figure
IQ	Image Quality
IR	Inner Ring

ISE	Indentation Size Effect
KAM	Kernel Average Misorientation
LAB	Low Angle Bands
LOM	Light Optical Microscopy
ND	Normal Direction
OP-S	Colloidal Silica Suspension
OR	Outer Ring
PAO	Poly-alpha-olefins
RCF	Rolling Contact Fatigue
SAE	Society of Automotive Engineers
SAED	Selected-Area Electron Diffraction
SE	Secondary Electrons
SEM	Scanning Electron Microscopy
SRR	Slide to Roll Ratio
TEM	Transmission Electron Microscopy
WD	Working Distance
WEA	White Etching Area
WEB	White Etching Band
WEC	White Etching Crack
WSF	White Structure Flaking
XRD	X-ray Diffraction
ZDDP	Zinc Dialkyl-dithiophosphates

Units

°	degrees
°C	degree Celsius
µm	micrometre
A	ampere
at.%	atomic percentage
kgf	kilogram force
kV	kilovolts
min	minutes
mm	millimetre
mN/s	milinewtons per second
N	newton
nm	nanometre
Pa	pascal
rpm	revolutions per minute
s	seconds
wt.%	weight percentage

Chapter 1
Introduction

1.1 Statement of the Problem

Rolling element bearings are one of the most widely used components in a range of applications, starting from very simple (e.g. bicycle, home appliances) to very complex machinery (e.g. transmissions, gearboxes). Rolling element bearings are used to transmit loads and facilitate smooth rotation instead of sliding motion required in rotating machinery. Extreme operating conditions, such as heavy loading, high speeds, and high or low operation temperatures, that exceed design limits, may lead to severe bearing breakdowns and, therefore, limit the useful life of whole systems. Bearings can also fail due to improper handling or mounting, overloading, inadequate lubrication or deficient sealing, passage of electricity or other tribological issues [1, 2]. Even under ideal operating conditions when bearings are properly designed, handled, installed, lubricated without overloading, bearings fail eventually due to material deterioration, which is commonly known as Rolling Contact Fatigue (RCF) [3-5]. High cycle fatigue conditions in combination with pure mechanical loading are often observed to result in local irreversible forms of microstructural changes in the subsurface of the bearing, for example, Dark Etching Region (DER) and White Etching Bands (WEBs) in the forms of Low Angle Bands (LABs) and High Angle Bands (HABs) [6, 7]. The terminologies of DER and WEBs came from the features observed in bearing steels that appear to be 'dark' and 'white' under Light Optical Microscopy (LOM) after being etched with nital.

However, another phenomenon related to surface spalling or axial cracking, named White Structure Flacking (WSF) has been increasingly reported in recent literature, as a bearing failure mode that occurs in the early life of bearings in a wide range of bearing applications [8-19]. WSF of wind turbine gearbox bearings has been the most prominent example amongst the applications over the last decade due to the

significant financial losses it has caused to the renewable energy industry [20-23], estimated at about £ 0.1-0.3 million per gearbox replacement [14, 24, 25]. This has thus become an urgent research topic for many researchers.

WSF is associated with a specific type of cracks, known as White Etching Cracks (WECs) that are bordered by a microstructure alteration called White Etching Area (WEA). DER, WEBs and WECs are three different but all irreversible microstructural changes occurring in the subsurface of bearing steels at different stages of rolling element bearing life. DER and WEBs form typically after prolonged cyclic loading that do not affect the useful life of the bearings in general, while the occurrence of WECs leading to WSF and early failures of bearings. For example, it has been reported that replacement of bearings in wind turbine gearboxes due to WSF could take place as early as within the first few years of service, despite their designed life of 20+ years [14, 26-28].

Since the discovery of WECs in the 1960s [29] a significant amount of investigation has been undertaken to find the root cause of WECs and, although many hypotheses have been proposed [14, 30], the initiation, propagation and root causes of WECs are still not clearly defined. Typically, failed bearings from service or laboratory rigs, where all features are at their fully developed stage are presented and analysed in literature, which makes it difficult to understand the initiation and development stages of the WECs. Complex microstructure of the WECs containing various shape and size grains have been only reported in the recent studies, however there is still little understanding on such material microstructural changes and it influence on WECs formation. Development of various shape and size grains, relation between crack and WEA, influence of primary spheroidised carbides have to be studied in more details. Moreover, despite the similarities found in WEA and WEBs through the literature review, no detailed studies on RCF and it relation with WECs failure had been performed in the recent years. The behaviour of the typical bearing steel under prolonged cyclic loading should be investigated in details to understand the microstructure alterations in RCF and whether it has any connections to the formation of the unpredictable WECs failure.

This study focuses on the investigation of evolution of WECs, DER and WEBs in typical AISI 52100 martensitic through-hardened bearing steel by analysing the features using a combination of advanced material microstructure

characterisation techniques. The study will investigate both, early and late stages of WECs to find out how WECs initiate in the original steel matrix and eventually lead to the final WSF. The study will also investigate the relation between WECs and DER/WEBs to understand the microstructure changes leading to the formation of WECs.

The aim of this study is to investigate the initiation and formation stages of WECs and their relationship with the RCF failure modes - DER and WEBs.

The key objectives of the study are:

- To learn the state-of-the-art research and development in relevant topics through a comprehensive and continuous literature review, including DER, WEBs, WECs and especially the influence of material on their formation.
- To learn and develop skills in the advanced microstructural characterisation techniques, such as SEM, EDX, EBSD, focused ion beam (FIB), TEM, as well as nanoindentation hardness measurement.
- To perform initial investigations of WECs, DER and WEBs failed components retrieved from different testing rigs and field bearing, where all features were at their fully developed stage, by use of learnt microscopy techniques and instruments.
- To design RCF experiments in collaboration with Schaeffler Group on Schaeffler laboratory test rigs under controlled conditions in order to observe chronological microstructure change in DER, WEBs and WECs for further in-depth systematic study of altered microstructure in typical AISI 52100 through-hardened martensitic bearing steel.
- To perform comprehensive systematic microstructural analyses of the DER, WEBs and WECs focusing on the initiation and development stages.
- To suggest the mechanism of failure and the controlling factors of WECs formation through the learnt aspects of the microstructure changes.

Chapter 2

State-of-the-Art of Rolling Bearing Failure Research

This chapter firstly introduces rolling element bearing types and bearing steels followed by a brief review of typical bearing failures discussed in the literature. A more detailed review on white and dark etching phenomena observed in rolling element bearings is then given, especially the current understanding of the WSF, its initiators and formation drivers. The review focuses on the influences of materials such as material microstructural changes and WEA morphology, which is the main focus of this study.

2.1 Rolling Element Bearings

Rolling element bearings are simple components that provide rotational freedom under loading and typically consist of an outer race, a cage, a number of rolling elements and an inner race, illustrated in Figure 2.1. They are used to connect two rotating parts in a machine for independent rotation, which is done by connecting one part to inner and the other to outer rings. Rolling element bearings perhaps are the most widely used component in diverse mechanisms and assemblies. Nowadays rolling element bearings can be found in everything from miniature household appliances to motors, gearboxes and more complex industrial machinery.

There are a number of types of rolling bearings depending on the shape of the rolling elements, e.g. ball, cylindrical roller, spherical roller and tapered roller bearings, in either single row or double row arrangement, illustrated in Figure 2.1. Different types of bearings can be used in different applications depending on their load and lubrication requirements.

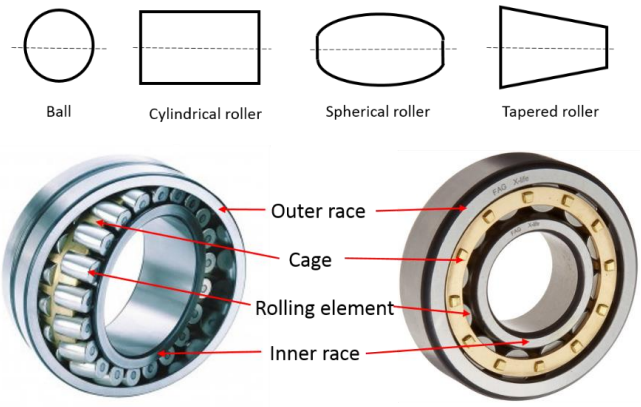

Figure 2.1: Illustrations of the structure and various types of rolling elements in bearings: ball, cylindrical roller, spherical roller and tapered roller.

2.1.1 Bearing Steels

Materials used for rolling element bearings should have high resistance to wear, corrosion, creep, and RCF. Particular care has to be taken to ensure bearings have sufficient hardness and limited inclusions which act as stress raisers and could possibly reduce fatigue life. For economic reasons minimising the cost of bearings is one of the key parameters in steel selection.

Two categories of steel, such as through-hardened (martensite or bainite) or case-hardened steels, are typically used for roller element bearings [6]. There are numerous alloy variations suitable for bearing production (list of steels for bearings can be found in [6]), however case-hardened AISI 4320 and AISI 9310 and through-hardened AISI 52100 are the oldest (introduced over 100 years) and still the most widely used bearing steel grades [6, 31]. This thesis will focus on AISI 52100 as it was the primary material investigated throughout this study.

AISI 52100 is low alloy, high carbon and chromium steel, which is equivalent to 100Cr6, SUJ2, EN 31 [3]. Typical chemical composition of the AISI 52100 bearing steel in accordance with the official ISO 683-17 is outlined in Table 2.1. Bearings made of AISI 52100 are typically through-hardened resulting in uniform hardness and toughness throughout the cross-section of bearings.

Table 2.1: Compositions in wt.% of the AISI 52100 bearing steels in accordance with the official ISO 683-17 [32].

	C	Cr	Mn	Si	P, max	S, max	Mo
AISI 52100	0.93-1.05	1.35-1.60	0.25-0.45	0.15-0.35	0.025	0.015	0.10

Initially AISI 52100 steel, a pearlitic structure with proeutectoid cementite at the prior-austenite grain boundaries, undergoes an annealing (i.e. spheroidisation) heat treatment to minimise the cementite networks and spheroidise the cementite that have shown to reduce bearing's RCF life [6]. The amount of spheroidised carbides and carbon content can be controlled by varying the annealing temperature and holding time. This heat treatment, however, results in material with low hardness and toughness, hence hardening heat treatments such as austenitisation and tempering are required subsequently to meet the requirements for bearings.

Standard austenitisation of AISI 52100 is at approx. 820-900°C that results in about 3-4 wt.% of undissolved cementite (often called spheroidised, primary or residual carbides), however the exact content of cementite depends on the austenitisation time and the initial steel microstructure. Cementite can be fully dissolved or refined at higher temperatures and over an extended austenitisation duration, although some cementite content is desirable as it acts to increase the strength and wear resistance of the steel. The cementite can also absorb some of the chromium in the steel resulting in iron-chromium carbides. Chromium content in these carbides varies as a function of time and temperature during austenitisation. [6, 33, 34] Primary spheroidised carbides are typically spherical of about 0.4-1 μm in diameter [6, 35]. However, elongated and irregular spheroidised carbides are not uncommon and frequently observed in AISI 52100 though-hardened steel.

After the austenitisation process, steel is either rapidly quenched in water or oil bath to room temperature or is held at approximately 500°C (isothermally in a salt bath) for a short period of time following by slow cooling to room temperature resulting in martensitic or bainitic microstructure, respectively. Martensitic microstructure forms by a diffusionless shear transformation during the rapid cooling in carbon steels. Martensite has highly strained body centred tetragonal (bct) form of ferrite that is supersaturated with carbon since during the quenching there is no time for carbon atoms to diffuse out of the crystal structure to form cementite (Fe_3C). Bainitic microstructure typically consists of dislocation-rich ferrite (body centred cubic (bcc) crystal structure) and high total fraction of carbides in comparison to martensitic steel since the slow cooling rate results in the formation of inter-lath cementite (i.e. secondary carbides or tempered carbides)

[36]. Ferrite and cementite in bainitic microstructure are arranged in a non-lamellar fashion as opposed to pearlite where the arrangement is lamellar.

Both microstructures usually also contain retained austenite, but, the amount of retained austenite varies depending on the heat treatment and chemical composition of the steel. For example, martensitic through-hardened steels typically contain approx. 3-15% of retained austenite, whereas bainitic through-hardened steels have only 1-5%.

Lastly, the steel is tempered at approx. 150-230°C to enhance toughness whilst maintaining high hardness. Tempering results in the precipitation of a variety of transition iron carbides, such as ε ($Fe_{2.4}C$), η (Fe_2C) and θ (i.e. cementite Fe_3C) [2, 6, 37], which often referred as tempered carbides. Tempered carbides appear as disk-shaped of 0.1-0.5 μm in size at grain boundaries, or inside martensite or bainite structures [36, 38]. The balance between the two types of carbides (primary and tempered) provides an ideal steel strength and toughness for roller element bearings.

Recent studies by Song et al. [36] on carbides in AISI 52100 through-hardened bainitic and martensitic steels using TEM and Atom Probe Tomography (APT) have shown that primary spheroidised carbides are of $(Fe, Cr)_3C$ structure with about 12 wt.% chromium, which is in line with about 11 wt.% chromium reported by Diederichs [39, 40]. Maximum concentration of chromium was reported at the surface of the primary spheroidised carbides and it gradually decreases towards the core, whereas carbon is homogeneously distributed throughout the primary spheroidised carbides [36]. Addition of chromium to a steel improves its strength, hardness and wear resistance of the material.

Inclusions are an unavoidable part of the bearing steel microstructure. Typical inclusions in bearing steels are: manganese sulphide (MnS) with or without oxide encapsulations, alumina (Al_2O_3), silicate, globular oxide (pure or in combination with Al, Ca, Mg, etc.), and titanium carbonitride [19]. The inclusions are typically harmful to RCF life as they can act as stress raisers and crack initiators [19]. Manufacturers continue to make the efforts to decrease the amount of inclusions in bearing steels. One of the ways is vacuum processing that reduces or eliminates non-metallic inclusions and entrapped gases resulting in much cleaner material, but a disadvantage of this process is much higher costs. It is suggested that

bearing steel life is increased after such treatment mainly due to the elimination of hard oxides that act as stress raisers [3].

2.2 Rolling Contact Fundamentals

Cyclic loading takes place under rolling contact resulting in different stresses in each portion of the material during each load cycle. Understanding the stress state during rolling contact is important to elucidate the mechanisms of subsurface microstructure alteration processes.

In 1882, Heinrich Rudolf Hertz [41] published his contact mechanics theory, explaining local stresses and elastic deformation of solids. Hertz's model is still used for stress state analysis during rolling bearing contact even though the model is limited to static conditions, where the load is normal to the contact surface and no traction force is present. According to his theory, under elastic loading conditions, the contact between a ball and an inner race in a radial loaded bearing has an elliptical contact area, see Figure 2.2(a). The load applied on the two contact bodies generates a semi-spherical contact pressure distribution with a contact zone width of *2b*, see Figure 2.2(b). The dimensions of the elliptical contact area are dependent on the radial load applied on the bearing, rigidity of the housing, number of balls in the bearing, ball diameter, radius of the groove in the inner ring, diameter of this ring, Young's moduli and Poisson ratio's of the ball and ring materials [42, 43]. In an ideal Hertzian contact (e.g. two identical spheres roll against each other or a sphere rolls on a flat surface under a normal load), a plane contact area will be formed. In the case of a ball and an inner race the contact area is not planar resulting in complicated calculations of contact parameters and maximum Hertzian contract pressure [42]. The detailed mathematical formulae for the calculations of the contact parameters and maximum Hertzian contact pressure in the ideal Hertzian case can be found in [41, 44].

Normal (σ) and shear (τ) stresses exist below the contact surface due to contact pressure, see Figure 2.3. The magnitude of normal and shear stresses varies with the depth below the contact surface, which also depends on the load and contact area. Stress components σ_x, σ_y and σ_z (where x represents the over-rolling direction, y the width and z the depth) show their maximum at the surface, whereas the maximum shear stress is located below the surface. [2, 45-47] In lubricated rolling element bearings, the contact stresses are affected by the

lubricant film and surface interaction type (e.g. pure rolling or pure sliding or partial sliding and rolling). As the level of sliding increases so does the friction force, resulting in the maximum shear stresses relocation towards the surface. [46]

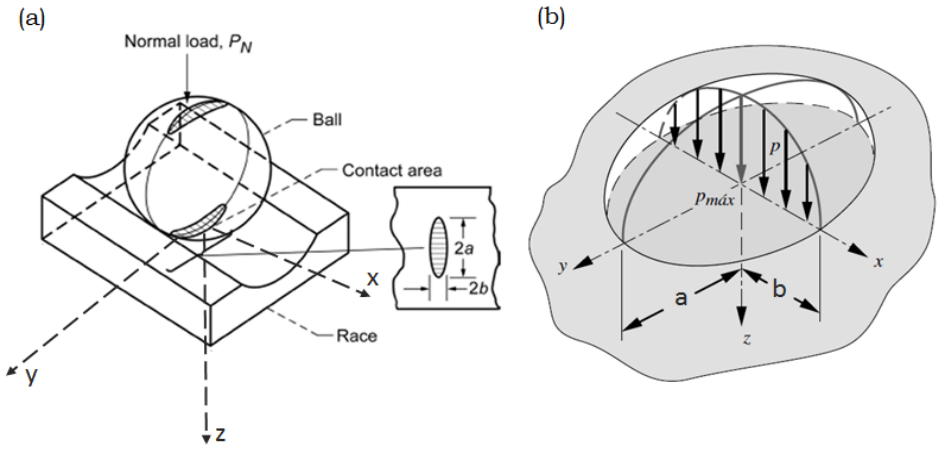

Figure 2.2: Illustrations of: (a) a ball on a race model for an elliptical contact; (b) contact pressure distributions in a spherical contact, where a semi-major axis *'a'* defines the stress generated during the contact. Adapted from [47, 48].

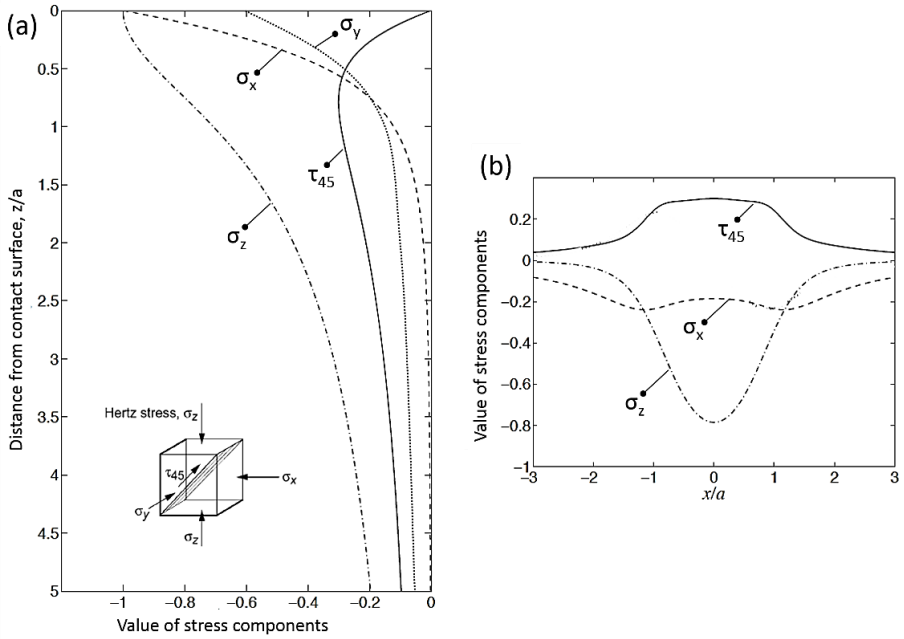

Figure 2.3: Distribution of normal and shear stresses as a function of: (a) depth (z) below the surface at x = 0; (b) x at the location (z) of maximum shear stress. Adapted from [2, 47].

2.3 Bearing Failures

Unfavourable operating conditions faced by bearings lead to severe breakdowns and, therefore, limit the useful life of the whole system. Bearings can fail by various failure modes due to improper handling or mounting, inadequate lubrication or deficient sealing, overloading, passage of electricity or other tribological issues [1, 2]. Common bearing failures include brinelling, scuffing, smearing, fretting, fracture, corrosion and creep. Their causes and countermeasures are well documented and described in [5, 49].

Even under ideal operating conditions when bearings are properly designed, handled, installed, lubricated without overloading, bearings fail eventually due to material deterioration, which is commonly known as RCF [3-5]. It often is observed that the original microstructure in the subsurface of the roller element bearings undergoes local microstructural changes when subjected to RCF [6, 7]. The irreversible forms of microstructural changes are manifested during high rolling contact stresses over a prolonged period of time, for example, DER and WEBs were reported frequently in the scientific literature between 1940s and 1990s.

However, at the early life of bearings, surface spalling, named WSF has been reported frequently, especially in recent literature, as a predominant bearing failure mode. It has been observed in a range of different applications, such as wind turbine gearbox bearings [11, 16-19], aircraft engine gears and bearings [13], paper mills [9, 10], train rail tracks and wheels [11, 12], marine propulsion systems [9], automotive alternators [8-10], water pumps [14], washing machines and others [15] and was found to be independent of bearing type of steel [27, 50]. WSF in wind turbine bearings has pushed research over the last decade to find its root causes due to the most significant financial losses caused by the early failures in the renewable energy industry. WSF has been associated with butterflies and WECs, which are features observed in bearing subsurface that are cracks bordered by WEA. Similar to the above mentioned DER and WEBs, WEA is also a microstructure transformation in bearing steels appearing to be white under LOM after nital etching. More details about these microstructure features will be discussed next in subchapters 2.4-2.6.

2.4 Dark Etching Region

The microstructure of DER was first observed beneath a ball track of bearing inner raceways and described as 'mechanical troostite' by Jones in 1946 [51]. Later DER microstructure was also reported to consists of tempered martensite [52, 53], low temperature bainite [54], and finally confirmed to be ferrite [52, 54-58]. DER was also reported by others with different names such as dark tint or needle [59] or dark etching constitution [60, 61]. DER has been reported commonly to form typically under moderate to high contact stresses in the area of maximum shear stress after a high number of rolling cycles (5-100 million revolutions or later) [29, 52, 54, 58, 61-68]. DER typically spans between 0.1-2 mm in the depth direction, however, grows with running time and contact pressure [34, 51, 52, 61, 63, 69]. The boundary between DER and the unaltered steel matrix is typically sharp at the upper boundary and gradual with lighter etching on the lower side of DER. DER has a symmetric sickle-like shape in the axial cross-section (perpendicular to rolling direction) or appears parallel to the contact surface in the circumferential cross-section (parallel to rolling direction), as shown in Figure 2.4.

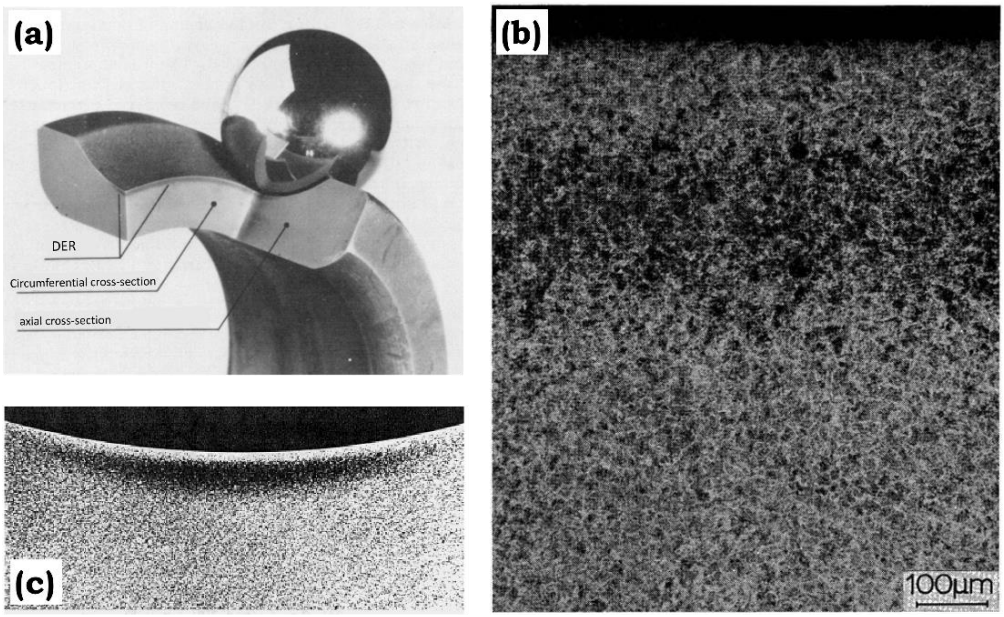

Figure 2.4: (a) an example of an inner ring with marked cross-sections and DER; (b) DER viewed with LOM in circumferential cross-section (Nital etched); (c) DER viewed with LOM in axial cross-section (Nital etched). Adapted from [35, 52, 68].

The dark contrast observed in DER under LOM was subsequently found to be due to randomly scattered deformed elongated patches under high magnification

imaging due to a stronger etch attack [2, 52, 54, 63], shown in Figure 2.5(a&b). TEM investigations have shown the dark etched patches to consist of a group of parallel ferritic discs of 0.05-0.1 μm thickness and 1 μm width intermixed with residual martensite, an example is shown in Figure 2.5(c) [52, 54, 57, 58]. Ferrite is etched stronger by Nital resulting in deep groove appearance of the discs under SEM. The direction of the elongated patches was suggested to be related to the orientation of original martensite plates [63], although varied orientations of elongated patches were also reported [52, 70]. A formation of polygonal cell structures has also been observed in DER during the TEM investigations [63]. The hardness of the DER was reported to be same [71], or lower [29, 51, 52, 59, 63, 72] than the surrounding matrix. Variation in reported hardness is likely due to the uncertainty about exact features that were indented in DER.

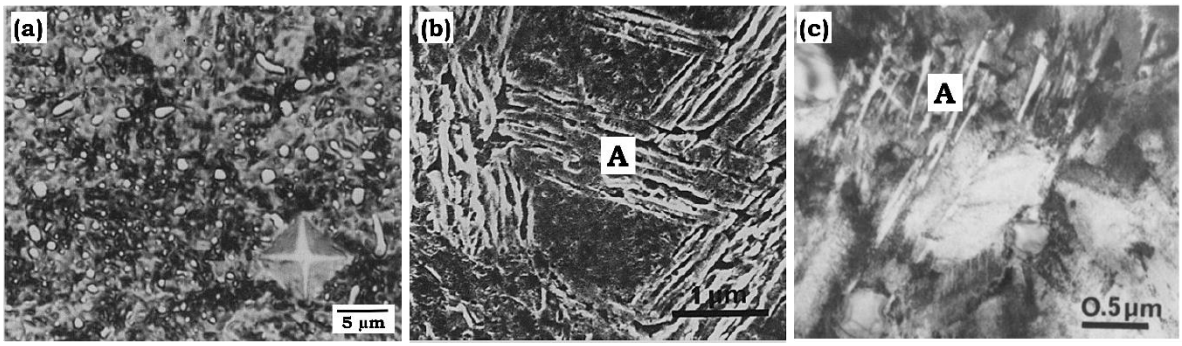

Figure 2.5: DER under (a) LOM (Nital etched); (b) SEM (Nital etched); (c) TEM. A - parallel ferritic discs or elongated patches of DER [54].

Sugino et al. [63] reported that spheroidised carbides were not affected by the formation of DER, whereas others [52, 57, 68] observed instances where spheroidised carbides had been cut by ferritic discs, as shown in Figure 2.6. In general the energy required to dissolve spheroidised carbides is considerable, and typically will be provided thermally, during austenisation or long duration annealing [57]. However, it has been suggested that a large amount of plastic deformation due to millions of stress cycles may result in high dislocation densities movement, making spheroidised carbides break-up and carbon diffusion possible. Carbon migrates from decaying carbides and follows the growing ferritic discs by pinning to dislocations or other defects. [57] Recent investigations of DER by APT have shown carbon depletion in newly formed ferritic components of DER that are surrounded by transition carbides [72]. It has been suggested that these transition carbides act as carbon 'absorbers' during martensite decay, although no direct evidence has been provided.

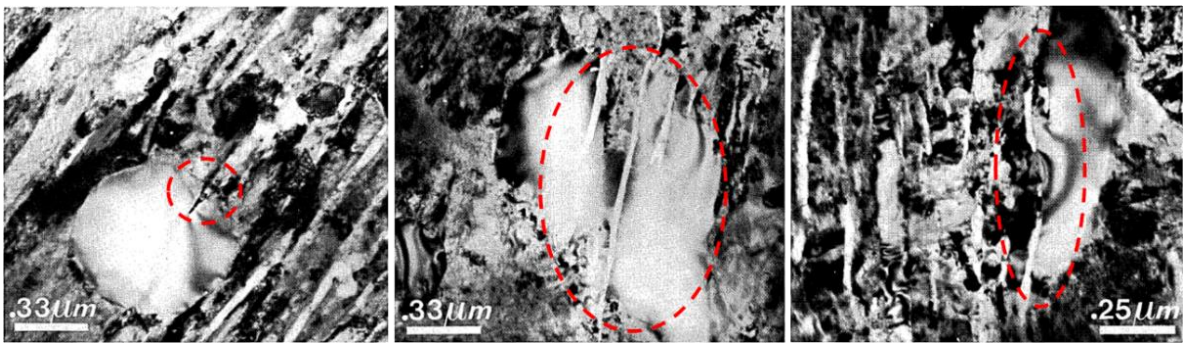

Figure 2.6: TEM micrographs of primary carbides in different stages of decay [57].

2.5 White Etching Bands

After about 100 million revolutions, WEBs, also named as grey lines [51], white etching areas [55, 73, 74], non-etching bands or dark lines [59], start to form typically within DER [34, 52, 54, 58, 67, 68, 74, 75], but have also been observed without DER formation [34, 55, 76]. The density of WEBs has been found to increase with the rolling cycles [52, 55, 68, 73, 77]. WEBs are three-dimensional plate-like structures that appear parallel to the contact surface in the axial cross-section (perpendicular to rolling direction), inclined to the surface in the circumferential cross-section (parallel to rolling direction), and broadened in their own plane [54, 55, 65, 67, 68, 78]. WEBs are typically shown as LABs and HABs as a result of RCF.

LABs, 5 to 30 μm long, 0.1 to 0.5 μm thick bands rising towards the surface in the rolling direction typically at an angle of 30° [52, 54, 55, 58, 67, 68, 79], have been found to form prior to HABs. Thicker bands (up to 2 μm thickness) [67, 69, 76] and different inclination angles LABs (in the range from 20 to 30°) [55, 64, 67, 75, 80] have also been reported. For example, angles between 22 and 24° have been observed in deep groove ball bearings (DGBBs), whereas 30° angle bands in cylindrical roller bearings [55, 74, 77].

There are three main microstructural components present in these bands, i.e. cell ferrite, carbide discs, and needle-like structures, which had been reported with different names by various authors in literature prior to 1975 that had caused some confusion. Fine cell ferrite is the predominant microstructure in LABs that are completely free of resolvable carbides [37, 54, 55, 58] with the sizes of the cells in the range of 100-200 nm [37]. Bands of fine cell ferrite are typically bordered on either or both sides by carbide discs that appear as unusual narrow elongated

features and are not affected by the etchant [37, 54] and not broken during tempering [55, 56]. In TEM investigations carbide discs appear as a dark ribbons often displayed a 'rung-like' internal contrast, hence often referred to as 'rung-like carbides' [52], 'disc-shaped carbides' [54, 58], or 'lenticular carbides' [37, 55, 56, 69, 73, 74]. Carbide discs have been reported to be approx. 1 µm thick and approx. 15 µm wide [54, 58]. However, recent investigations showed thickening of the carbide discs from 0.12 to 0.49 µm with increasing number of cycles [37]. Higher operation temperature and contact pressure was shown to accelerate the growth of the carbide discs, however increasing rotational speed appeared to have a negative effect due to carbon flux decrease [37]. Microprobe and energy-dispersive analysis have shown that carbide discs consist of approx. 15-30 at% carbon and 3 at% chromium [58]. Carbide discs have been proposed to be formed by deformation/flattering of the primary spheroidised carbides [69]. However, TEM investigations have shown that carbide discs are sets of regular rectangular blocks (also called carbide crystallites) of different widths [37, 58], example shown in Figure 2.7. Most of the blocks contain parallel and narrow fringes (similar contrast shift as of twin structures) where the direction of the fringes changes from block to block. Carbide discs have often been seen to be bordered by strongly etched needle-like structure [34, 37, 54, 63, 73], suspected to be ferritic [54, 58] that appears as featureless white ribbon in TEM bright field (BF) imaging but sometimes also containing dislocations [52].

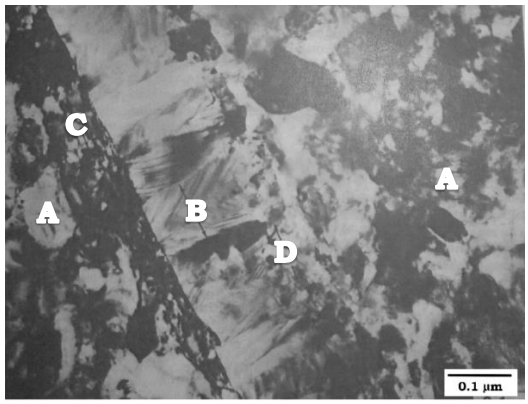

Figure 2.7: BF TEM image, showing transformed phases with cell ferrite (at A), a carbide disc (at B), ferrite layer (at C), and irregular interface (at D). Reprinted from [58] with permission from Elsevier.

HABs form during the final stage of the microstructure transformation sequence as the bands rising towards the surface in the rolling direction at an angle of 80° in the circumferential cross-section (parallel to rolling direction) [34, 52, 55, 67,

68]. The angles have, however, been found to vary between 65° and 85° depending on the bearing types (e.g. ball or cylindrical roller bearings) [55, 64, 67, 75, 80]. HABs have mostly been reported to form in addition to the formation of LABs over more than 500 million rolling cycles and locate closer to the rolling surface [52, 68, 80]. HABs appear to cut through the entire previously formed LABs microstructure [52]. However, Mitamura et al. [61] observed mostly HABs with only very few LABs in the later stages of over-rolling in thrust bearings tested under high contact pressures of 4.6 GPa or 5.5 GPa. More research is thus required to fully understand these processes.

HABs are also longer and thicker bands, compared to LABs and are typically about 100 μm long and 8-10 μm thick [52, 76], examples shown in Figure 2.8. It has been observed that the thickness of HABs increases with the increase of test temperature [61]. HABs have been reported to consist of almost dislocation free cell ferrite [52]. Needle-like grains have often been observed at the edge of the bands [52, 68], but also extended from LABs and growing through HABs [52], as shown at A in Figure 2.8.

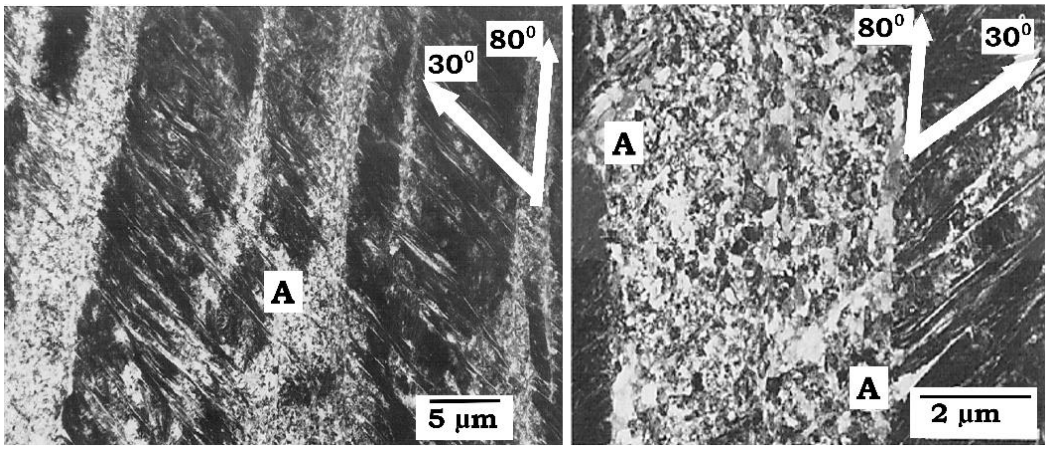

Figure 2.8: TEM micrographs of HABs [52].

It has been reported that no primary spheroidised and/or tempered carbides have been observed within developed LABs and/or HABs [52, 54, 55, 57, 61, 74]. Muroga et al. [81] found the concentration of carbon in LABs and HABs being 0.2 wt% and 0 wt% respectively. Others also reported very low carbon concentration in HABs [34, 52, 82], e.g. 0.06 wt% and zero.

LABs and HABs have been reported to have a lower hardness than the matrix due to its lower carbon content [75, 76]. However, similar to DER, hardness measurements presented in early literature had in general lack of details and

conflicting conclusions have been reported. Therefore, further systematic hardness analysis is required to clarify the hardness of these features.

2.5.1 Formation of the altered microstructures

It is considered that the formation of altered microstructure is related to the stress state of the Hertzian contact, however which stress components are responsible for such alterations is still under debate. Some authors [52, 55, 67, 73, 83] reported maximum DER/LABs density to correspond with the depth of maximum unidirectional shear stress, whereas others [68, 72] observed the start of the microstructure alterations in the region of maximum orthogonal shear stress. It should, however, be mentioned that the depths of maximum shear stresses are typically calculated for non-lubricated and Hertzian loading conditions, which is not completely valid for typical RCF conditions. Therefore, correlations between the calculated stresses and microstructure alterations may not be meaningful [55].

It was suggested that DER formation was a consequence of a tempering effect caused by heat generated by elastic hysteresis due to cyclic stressing [29]. However, if this was the case, i.e. DER was a tempering effect, then one could assume that the microstructure should be uniformly transformed rather than being transformed into patches with randomly varied orientations. The fact that DER transformation has only been observed over certain stress levels suggests it is stress-induced transformation [63, 64, 68], which also agrees with the formation of WEBs since the bands have been seen to change their inclination when the rolling direction was reversed [67, 80, 84].

Other causes for DER formation have also been suggested, including over-tempering of martensite, since some authors [55, 85] reported that DER was not observed in steels initially tempered to a hardness of about 700 HV or higher, however, others [52, 54, 68] presented DER in sample with initial hardness above 850 HV. Presence of non-metallic inclusions was also assumed to be responsible for the DER appearance due to the stress concentration around it that causes change in etching characteristics [86], however, DER have also manifested in steels with low amount of non-metallic inclusions [65]. Furthermore, the amount of retained austenite in the initial microstructure was also suggested to be responsible for DER formation, as DER was not observed in the material with low retained austenite amount [55, 71].

It has been suggested that stress-induced carbon diffusion, though negligible during each cycle, is of importance over millions of rolling contact cycles. Therefore, after a large number of over-rolling cycles under medium to high loads martensite starts to decay and very fine tempered carbides start to dissolve into the matrix. Considerable dislocation motion takes place to transform martensite plate structure into a cell dislocation structures and break the coherence of spheroidised carbides with martensite and even cut carbides themselves [77]. This consequently results in excess carbon that migrates from the martensite and small tempered carbides to the dislocation-rich region (walls of the cell structures). [57, 63, 67, 77] Excess carbon pinned at the dislocations serves as sinks for additional carbon atoms during further cycles [58, 82].

Martin et al. [55] were one of the first who discovered cells of low dislocation density surrounded by walls consisting of tangled dislocations. The dislocation density inside a cell was found to be considerably lower than dislocation density at the cell walls. The cells were identified with Selected-Area Electron Diffraction (SAED) as ferrite [54, 55]. Martin et al. further suggested that, with higher numbers of over-rolling cycles the dislocation clusters would become more tangled until they gradually start to align themselves along certain favourable crystallographic planes [55], suggesting the nucleation of LABs. Formation of the LABs has also been suggested to be due to recrystallisation [58] or dynamic recrystallisation in a preferred crystallographic direction [61, 67]. Many suggested that supersaturated localised carbon areas may precipitate in the form of carbide discs at the edge of the LABs [56, 57, 63, 67, 73, 77]. However, no discussion on the formation and growth of needle-like structures, which typically appear next to carbide discs or HABs, has been found in literature. Additionally, why and how a new sets of 80° bands form after a certain number of over-rolling cycles remains unclear.

Many studies have been conducted to model the formation processes and orientation of the WEBs analytically and numerically [37, 67, 72, 78, 80]. Most studies prior to 1990s only considered maximum shear and principal stresses, or maximum plastic principal strain in their models for WEBs formation based on the fact that WEBs have typically been seen around areas of the maximum shear stress. Moreover, 2.5 GPa has been reported as the lowest contact pressure threshold for the microstructural alterations, suggesting its relationship with plastic deformation [64]. Polonsky and Keer [79] also attempted to correlate microstructural alteration with carbon diffusion, however due to limitations in

their models, the WEBs formation mechanism question remains unanswered. Recently, authors [37, 72] proposed a model based on a dislocation-assisted carbon migration mechanism to predict the formation of DER and carbide discs in LABs depending on loading and amount of cycles. However, the formation of parallel ferrite discs in DER and the mechanisms why LABs and HABs form at particular angles have not been satisfactory explained.

2.6 White Etching Cracks

WECs were firstly reported by Scott et al. [29] and subsequently have been named as 'white bands' [59], 'white etching constituent' [87, 88], 'white phase' [13], 'light etching areas', 'brittle flaking' [89], 'branching cracks with non-etching borders' [90], 'White Etching Matter' [91, 92], and 'irregular White Etching Area' [93, 94]. WECs have been commonly accepted by the community and is used widely in recent publications hence will be used throughout this thesis.

WECs have been found to be long, parallel or branching microcrack networks formed in bearing subsurface, depending on the cross-section plane WECs are viewed, at varied depth [11, 14]. In the circumferential plane (parallel to rolling direction) cracks appear more vertically orientated branching down to the core, whereas in the axial plane (perpendicular to rolling direction) cracks are more parallel with the surface with less vertical branching being observed [95-99]. WECs have been found to propagate through grains (i.e. transgranular) [17, 100], suggesting that the grain boundaries have little influence on WECs propagation directions. WECs have been found in a wide range of steels, such as AISI 52100 bearing steels [11, 16, 18, 97, 101-103], tool steels [13, 29], M50 high speed steels [104], high carbon chromium steels [105, 106], graphite steels [106], 18CrNiMo14-6 [11], 100CrMo7 [107], bainite 100CrMo7-3 [17], carburised 20Cr4 (equivalent to SAE 5120) [108], 17CrNiMo6 [109], and others, thus are not limited to any particular types of steels.

Another subsurface microstructural alteration in steels often mentioned in the context of WECs formation is butterflies. A butterfly is a form of crack that initiates at stress raisers in steels, such as non-metallic inclusions [63, 74, 88, 90, 110-114], voids [106, 115] or carbides [13, 101, 104, 112] and typically propagates at 30°-50° and 130°-150° to the over-rolling direction [74, 88, 104, 106, 113-115]. Butterflies usually have two wings, although four-wing butterflies have also been

observed as a result of changing the direction of bearing rotation [74]. This suggests that loading parameters play an important role in butterfly formation and that the butterflies are stress induced rather than thermally activated [104]. One side of the butterfly crack is typically decorated with WEA, morphology of which was suggested to be the same as in WECs [90, 100]. Typical length of butterfly is 10-250 μm (wing's tip to tip) [14, 104, 106, 115], which are usually much smaller than WEC networks. It has been suggested that, over time, the initially formed small butterflies could grow extensively by linking-up with other inclusions/butterflies and create WEC networks that eventually reach the surface and result in surface spalling [88]. However, there is a lack of evidence in confirming whether WECs are the extension of butterflies or whether WECs that initiated elsewhere propagate through the inclusions [14, 16, 98, 102, 109, 110, 116]. The relationship between butterflies and WECs is unfortunately still unclear.

2.6.1 White Etching Area

As mentioned above, WEA appears in both WECs and butterfly wings. However, the interface between WEA and base material in a butterfly appears feathery and the change from one to the other is gradual [112, 113], whereas in WECs the change appears to be clear and distinct [17, 38]. WEA has been reported to be mainly around cracks parallel or inclined to the raceway rather than around cracks perpendicular to the surface in WECs, see Figure 2.9 [16, 18]. This has been explained based on the fact that only cracks orientated normal (or close to normal) to the compression axis of the contact stress can result in rubbing between the crack faces, leading to the formation of WEA at the crack face [92]. More details about the face rubbing hypothesis are given in subchapter 2.6.2 of this chapter.

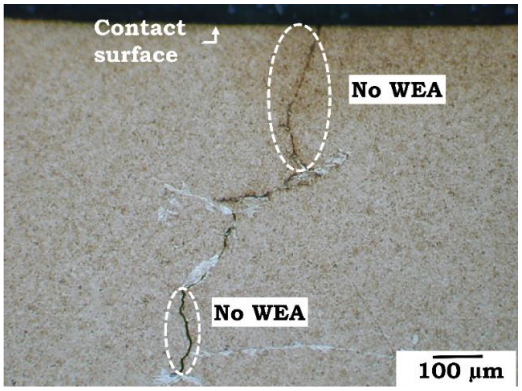

Figure 2.9: LOM image of WEC network where perpendicular to the surface crack appear without WEA [16].

WEA is known to have an irregular microstructure that appears white under LOM after being etched, typically with Nital or Picral. WEA has been identified by SAED patterns as nanocrystalline ferrite that is supersaturated with carbon [29, 40, 55, 65, 114]. However, recent APT investigations have shown that carbon is segregated at the grain boundaries rather than in the ferrite grains [117, 118]. An average carbon concentrations in APT sample containing WEA was reported to be higher than the concentration of carbon in the unaltered part of the sample [117]. Further X-ray microanalysis is required to examine the carbon distribution to reveal the mechanism of carbon redistribution at a bigger scale than that of APT.

Grain sizes within WEA have been reported to be up to 20-30 nm [88, 105], whereas some reported grains between 10-300 nm [16, 65, 107, 115]. Coarser grains have often been found at the boundary between WEA and unaffected steel matrix [100], but also irregular zones of coarser grains intermixed with nanocrystalline areas in WEA were reported in butterfly wing studies [104, 114], as well as in WECs [100]. Recent APT analysis has revealed grains to be equiaxed 10 nm ferrite grains within WEA [117, 118]. Amorphous like structures in WEA have also been reported [105, 113-115, 119, 120]. Localised plastic deformation and recrystallisation have been proposed as possible cause of the nanocrystalline grains formation [14, 114, 117, 118]. The hardness of the nanocrystalline WEA has been found to be 30-50% higher than the surrounding matrix, which is suggested to be related to the ultrafine structure and carbon supersaturation in WEA [11, 29, 88, 90, 104, 114].

Typical WEA has smooth appearance under LOM, however fine structural features and markings [11, 17, 29, 91, 102, 107, 109] as well as voids and cavities within WEA have been observed [91, 101, 103, 113, 114, 118]. In WEAs of Nital-etched specimens, microcracks have been shown under SEM imaging with secondary electrons (SE) [11, 88, 101, 105, 113, 114, 121]. However, a recent study by Diederichs et al. [100] revealed that some of the 'microcracks' shown in WEA were in fact elongated grain structures (also called needle-shape grains) and suggested that they were a product of annealing processes in WEA. The elongated grain structures were confirmed by backscattered electrons (BSE) imaging in SEM and EBSD in colloidal silica (OP-S) polished specimens (not etched with Nital). It was thus suggested that elongated grains within WEA may have the tendency to be etched more with Nital due to its chemical composition, for example different carbon content, and hence had been interpreted as microcracks. The elongated

grains were also found to grow mostly from the cracks into the WEA and have lower misorientation [100]. FIB and TEM investigations have shown that elongated grains in WEA have a three-dimensional plate-like structures with a clear boundary without gradual transition between the elongated grain structures and the nanocrystalline WEA [91, 100]. The elongated grain structures have appeared relatively dislocation free with the same ferritic crystal structure as nanocrystalline WEA. Earlier, Grabulov et al. [114] presented similar EBSD images of WEA from a butterfly, however called them elongated 'lamellar' structures and suggested that they had originated from fragmented martensite lamellas. They did, however, also show low misorientation in the elongated 'lamellar' structures and proposed that incomplete recrystallisation processes had occurred leading to the dislocation free elongated 'lamellar' structures. Recently, Ooi et al. [91] also found elongated grains that were confirmed by diffraction to be ferritic, however named them 'engineering bands' that likely to be adiabatic shear bands. Adiabatic shearing has been assumed to take place during rolling contact that resulted in a local temperature increase consequently softening of WEA followed by the growth of 'engineering bands' in WEA [91]. By use of advance microstructure characterisation techniques, it become clear that WEA is complex altered microstructure that consists of not only nanocrystalline ferrite, but also elongated ferritic disc-shaped features. The formation processes and drivers, especially whether increase of a temperature has an influence on a growth of these elongated features [91, 100], have still to be confirmed.

Some researchers have also reported that WEA appears as an area predominantly free from carbides while the adjacent material matrix contains unchanged primary spheroidised carbides [11, 17, 63, 73, 100, 103, 106, 115, 118], whereas others reported that deformed carbides were observed in WEA [17, 29, 63, 106, 107, 113, 115, 122]. Cut off carbides with remaining carbide structure being unaffected have also been reported in WEC failed specimens [40]. The disappearing and/or deformation of the primary spheroidised carbides in WEA has been suggested to be a result of carbide dissolution or breaking-up due to severe plastic deformation, increased dislocation interaction and grain refinement; following which, carbon diffuses from carbides into WEA [17, 29, 63, 73, 97, 106, 110, 117, 118, 123, 124] and segregates at the grain boundaries [117, 118, 124]. Elimination of the primary spheroidised carbides in steel microstructure has been suggested in order to stop the formation of hard WEA [92], although other study has shown the formation of

WEA without primary spheroidised carbides suggesting that primary and tempered carbides have to be eliminated to stop the hard WEA formation [119]. It has been proposed that without any carbides ferrite will deform into nanocrystalline structure, but without being enriched by carbon, no hard WEA will be formed [119]. As for example, no hard WEA formation was observed during RCF testing of carbide-free nanostructured bainitic steel [125, 126].

2.6.2 Initiation, Formation and Drivers

A large amount of research and investigations have been conducted on WECs over decades proposing multiple hypotheses on the initiation and formation mechanisms, as well as drivers for WECs formation. This section outlines several most prominent hypotheses proposed in WSF literature.

- **Initiation and Formation**

Different WECs initiation mechanisms have been proposed based on specific findings, such as initiating at the surface or in subsurface. The surface initiation hypothesis suggests that WECs initiate from damage or microcracks on the surface, which are caused by the ruptures of lubricant film due to high surface stress concentration, and subsequently propagate into the subsurface [88, 98, 127-129]. It has been shown that WEA will only form on the crack's face of the surface initiated crack, if traction force is in the same direction as raceway movement [129].

The subsurface initiation hypothesis suggests that WECs initiate from material defects or stress raisers (e.g. inclusions, voids, large carbides etc.) in the maximum shear stress region under the bearing contacting surface then network and propagate towards the bearing surface leading to WSF failures [13, 63, 96, 101, 118, 130]. Small size inclusions (1-20 μm), especially sulfides, aluminum oxide and globular sulfide-oxide inclusions, were found to interact with the WEC networks the most [13, 96, 97, 101, 103, 110, 131]. Oxide type inclusions were found to be the most frequent due to its hardness mismatch with the material matrix, tensile residual stresses (due to different coefficient of thermal expansion compared to matrix) and poor coherence between the oxides and the matrix [90, 114]. Despite the fact, that inclusions have been predominantly agreed to play a

role in WECs formation [110], there is little detailed chronological analysis to show initiation and development stages of this WECs formation mechanism.

Due to the complicated three dimensional WEC networks, it is extremely difficult to confirm whether a particular WEC network was initiated in subsurface then propagated to the surface or initiated at the surface and propagated to the subsurface. Recent research results provide more and more evidence for the subsurface initiation theory through detailed WEC networks analysis using serial sectioning methods and x-ray tomography [97, 102, 103, 110, 132]. It was also shown that subsurface pre-cracked samples fail much quicker that surface pre-cracked samples during RCF testing [119], which leads to the suggestion that WECs are more likely to be subsurface initiated as they were always reported to occur much earlier than the bearing's design life. However, one should understand that the differences in the initiation of WECs is possible, as for example author believes that surface initiation is possible when final WECs are associated with axial cracking (i.e. line-crack) at the surface, whereas surface spalling is most likely manifested due to the subsurface WECs formation and its propagation to the surface.

Whether microcracks or WEA form first or is it a cooperative growth of the two is still unclear. All investigations in laboratory have been conducted under certain accelerated conditions and analyses on already failed specimens from service make it difficult to capture the initiation of WECs (WEA or microcrack). However, from the literature, there is more micrograph evidence of cracks without WEA than WEA without cracks [110], hence led to believe that microcracks may form first followed by WEA formation [13, 17, 30, 92]. This has been explained as that, after cracks formed, the crack faces rub against each other under RCF leading to the formation of WEA [9, 13, 59, 88, 92, 95, 98, 119, 122]. However, evidence of large WEA with small microcrack on the side or the fact that most of the WEA is located on one of the crack faces makes the 'crack faces rubbing' hypothesis questionable. And even with those that WEA formed on both crack faces [17, 100, 129], the WEA on one side of the crack is typically much larger than that on the other. This has been a major challenge towards the face rubbing hypothesis in the WECs formation discussions.

- **Drivers**

A number of possible drivers for WECs formation have been suggested in research based on the particular methods used in experiments, for example hydrogen diffusion into bearing steel [60, 87, 89, 95, 98, 127, 133-141], transient load and/or speed [18, 26, 30, 93, 131], electrothermal effects [116, 142], and other drivers [30, 122, 143].

Hydrogen generation and diffusion into the steel matrix has been frequently assumed to occur due to a lubricant and a nascent metal surface interaction [14, 30]. However, extensive WECs were found in specimens from screw vacuum pumps that used fully fluorinated oil for lubrication to avoid the release of hydrogen [100] that suggests that hydrogen is not the only possible driver for WECs initiation. Nevertheless, surface crack tip and bulk hydrogen diffusion mechanisms have been frequently proposed depending on surface or subsurface WECs formation hypotheses, respectively.

Lubricant trapped in the surface crack decomposes due to the cyclic stresses and subsequently release hydrogen, which enters the material through the nascent surface of the crack tip resulting in further crack formation and microstructure alteration explained by the hydrogen enhanced embrittlement mechanisms [9, 88]. However, no WEA has been found to form during the experiment where surface crack mouth was opened by the tractive force (due to positive slide to roll ratio (SRR)) that allow high exposure of the crack tip to the lubricant [122, 129]. Whereas, at a surface crack (i.e. nascent steel surface), which appear to be bordered by WEA, no remnants of oil or its additive elements were observed [129]. Further suggesting that lubricant decomposition and hydrogen diffusion is not the only possible mechanism for WEA formation at a surface crack tip.

During bulk hydrogen diffusion mechanism, the tribofilm is assumed to be damaged resulting in a nascent metal surface that is exposed to the lubricant. Lubricant then decomposes leading to a hydrogen release and diffusion into a steel where it is trapped at material defects [87, 89, 136, 137]. This assumed to result in a similar effect as hydrogen embrittlement, which is known to reduce the energy required for crack initiation and increase the dislocation density leading to local plastic deformation and further crack development [137]. However, no severe wear, which proposes that tribofilm stayed intact, has been seen on raceways of the

WECs failed bearings from service [9, 16], suggesting that hydrogen bulk diffusion due to the tribofilm damage or hydrogen penetration itself is not the only possible mechanism for extensive WECs formation.

Lubricants containing anti-corrosion overbased calcium sulphonate (CaS) and antiwear additives based on short chain zinc dialkyl-dithiophosphates (ZDDPs) were also suggested to be responsible for WECs failures and have been frequently referred as a 'bad lubricant' or 'WEC critical oil' [111, 116, 127, 129]. 'Bad lubricant' has been shown to produce an inhomogeneous tribofilm that causes high surface shear forces and sliding resulting in axial cracking (i.e. line-crack) at the surface. These axial cracks propagate into the subsurface where WEA was observed to form on the crack sides due to the crack faces rubbing, if traction force was in the same direction as raceway movement [129]. Large amounts of metallic elements and sulphur, as well as much higher water content than in a mineral oil has been assumed to be responsible for inhomogeneous tribofilm formation [129]. Others have also believed that the 'bad lubricant' has high influence on the formation of the WECs due to the hydrogen diffusion. This recently has been supported by study [144] where number of WECs was found to correlate with diffusible hydrogen detected in post-test bearing rollers tested with 'bad lubricant' and without hydrogen pre-charging.

Even though, hydrogen might not be the dominant cause of WECs formation, but it has been widely accepted to be an accelerator for crack growth [30, 92]. This resulted in many studies that have ran tests in hydrogen atmosphere or have used hydrogen pre-charged specimens. Laboratory studies on hydrogen pre-charged specimens have shown that hydrogen dramatically decreases RCF life and leads to the formation of WECs compared to specimens without a hydrogen pre-charge [138]. However, there is little detailed analysis to show whether the hydrogen pre-charging has affected the steel's microstructure prior to RCF testing. Microstructure changes, such as micro-pores, flaws and decrease in number of spheroidised carbides with shape change, were observed in the specimens that were tested in the hydrogen atmosphere, whereas no such microstructure changes were observed in analysis of the specimens tested in air [60]. Moreover, formation of 'slip bands', 'engineering bands' and circular voids has been observed in hydrogen pre-charged samples, which have not been detected in samples tested without hydrogen pre-charge [91]. This suggests that hydrogen charging (pre-

charging or atmosphere) has an effect on microstructure and results in modified WECs formation, which could be different to the real case scenario.

Impact loading has also been proposed to form WECs that have been described as networks of adiabatic shear bands [18, 26]. However, no material evidence has been provided to confirm this process. Impact loading has also been proposed to result in cracking at MnS inclusions, which assumed to serve as initiation and further propagation of WECs [131]. However, others [63, 74, 90] have observed crack formation at MnS inclusions only in case when oxide part is present.

Overloading of the bearings has also been proposed as one of the drivers for WECs formation [11]. However, Luyckx [18] contested the overloading hypothesis based on the fact that overloads were not observed during bearing operation through their load measurement campaigns. Furthermore, no damage was observed on other mechanical components near WEC failed bearings, hence suggesting that WECs are unlikely to be caused by overloading [18].

Sliding was proposed as another driver, where magnitude and direction of sliding plays a dominant role for WECs generation [99, 118, 120, 122, 127, 143]. For example, using negative 30% SRR has resulted in WECs generation, whereas positive 30% and positive or negative 5% SRR have not. Another study on FE8 cylindrical bearings showed the formation of cracks in raceway of the washer on the side of positive and negative slide tested with mineral oil and 'bad lubricant'. However, only combination of 'bad lubricant' and negative slide zone has resulted in formation of WEA on the crack sides [129]. This, therefore, suggests that combination of drivers could be essential for WECs initiation and further propagation.

Based on modelling, electromagnetic effect caused by electrical current occurring in wind turbine gearbox bearings due to self-charging and discharging of lubricant has been proposed as yet another driver for subsurface WECs initiation [142]. Models have been developed to predict the effects of EM on different microstructural components within a steel structure, however exact origins, distribution, magnitude and other characteristics of current in bearings were not specified in publication. The model showed that localised resistivity heat could cause thermal expansion and localized stresses at the interface between carbides and the steel matrix since carbides have the lowest conductivity properties compared to bainitic and martensitic structures in steels [145]. Overheated

carbides suffer plastic deformation resulting in dissolution and carbon diffusion, which has been considered to initiate the WEA formation. The EM theory, thus, have suggested that cracks form after formation of WEA. Static electricity was also suggested to play a significant role in WECs formation, as when the metal balls in the bearings were replaced by ceramic ones, WECs were not observed anymore [135].

2.7 Summary and Research Strategy

A large amount of studies have been reported in earlier literature to understand microstructural alterations in form of DER, LABs and HABs that form after prolonged RCF testing under moderate to high loading conditions in bearing steels. In recent years, however, the focus has shifted primarily on to investigations of the WECs as a bearing failure mode that occurs unpredictably in the early life of bearings in a wide range of applications. Mostly, WECs research has been focusing on the creation of the WECs under accelerated conditions in order to identify the formation mechanisms especially the influences of operating conditions, such as load, impact, slip, electricity, lubrication and additives.

DER, WEBs and WECs are three different irreversible though in some ways similar microstructural alterations that appear in the subsurface of rolling element bearings but at the different stages of bearing life. The main findings on these features are briefly summarised below:

- DER consists of parallel ferrite discs that were seen to interact with primary spheroidised carbides. Carbon movement from ferritic grains via dislocation-assisted carbon migration has been proposed. However, the location of an excess carbon has not been defined.
- LABs start to form typically within DER, but have also been observed without DER formation. LABs consist of three main microstructural components: cell ferrite, carbide discs, and needle-like structures, whereas HABs consist predominantly of bigger size cell ferrite. Similar carbon movement mechanism as in DER has been proposed, where carbon supersaturates at locations that later appear as carbide discs. LABs and HABs have been reported to have a lower hardness than the matrix. Only fully grown altered microstructure has been characterised in literature,

hence, causing difficulties in understanding the formation of an each individual feature and the sequence of their appearance.

- WECs are typical bordered by nanocrystalline WEA that has smooth appearance under LOM, although fine structural features and markings, voids and cavities as well as microcracks within WEA of the Nital etched specimens have been observed. Microcracks in Nital etched specimens may have been wrongly interpreted and in fact are elongated grain structures. Elongated grain structures were only revealed after OP-S polishing and BSE imaging in SEM or EBSD.
- Nanocrystalline WEA has been confirmed to consist of ferritic grains with carbon pinned at grain boundaries. Carbon comes from dissolution of carbides during WEA formation and it has been suggested that eliminating both primary and tempered carbides in steel microstructure will stop the formation of hard WEA. It was proposed that without any carbides ferrite will deform into nanocrystalline structure, but without being enriched by carbon, no hard WEA will be formed.
- The debate on whether WEC is surface or subsurface initiated is still on going. WECs initiated at non-metallic inclusions in subsurface has been proposed as at least one of the WECs formation mechanisms. Techniques, including serial sectioning and CT have been used to reveal the structure and interactions of WECs in the subsurface. The author, however, believes that both surface and subsurface initiations are possible, where axial cracking (i.e. line-cracks) contribute to a surface WECs initiation and WSF is a result of subsurface WECs initiation.
- Whether microcracks or WEA forms first or is it a cooperative growth of the two is still unclear. Formation of the WEA by the rubbing of crack faces against each other under RCF is predominantly accepted in scientific literature. However, the appearance of WEA only on one of the crack sides has not been satisfactory explained.
- Many researchers attributed WEC formation to the influence of hydrogen even though it has been difficult to confirm the role of hydrogen especially the mechanisms involving hydrogen generation, diffusion, trapping and etc. It is believed that hydrogen is at least an accelerator for cracks growth.
- 'Bad lubricants' contain anti-corrosion and anti-wear additives have been found to accelerate failures due to the WEC in laboratory testing. However,

why exactly 'bad lubricants' lead to the microstructure change has not been fully investigated.

- Negative SRR have been found to promote the formation of WEC, although in some studies an addition of 'bad lubricant' is necessary for WEC formation.
- Modelling have shown that electromagnetic effects could possibly result in localised microstructure transformation starting with carbides dissolution and nucleation of WEA following by formation of the crack.

As discussed above, many different hypotheses on initiation and propagation, as well as drivers of the WECs have been proposed in scientific literature during the past few decades. Despite the significance of the problem and the amount of efforts being made over decades, the initiation, formation and root causes of the WECs are still not clear. Additionally, little has been found in scientific literature comparing the microstructural alterations observed in WECs to these formed in prolonged RCF bearings. Understanding the behaviour of the typical AISI 52100 through-hardened steel under prolonged cyclic loading can possibly provide the link to understanding the microstructure transformation leading to the unpredictable WECs failure.

To fully understand the initiation and formation mechanisms of the microstructural alterations observed in WECs, as well as DER and WEBs, initiation stages of the phenomena have to be captured and examined in details using a combination of advanced microstructural characterisation techniques. In the past, microstructural characterisations of the WECs were performed mainly in Nital etched condition, which is known to change greatly the appearance of the material resulting in doubtful etching effects. Microstructural alterations formed in prolonged RCF loading were mainly characterised by TEM, which limits the observations to a specific locations, or LOM, which cannot provide the required resolution for detailed microstructure observations. It has been shown that the combination of BSE imaging with EBSD and EDX can provide important information for the comprehensive characterisation of an altered microstructure without being Nital etched. A larger area of examination in SEM compared to TEM or APT is a big advantage that allows to carry out analysis on a much bigger scale under higher resolution compared to LOM.

At the beginning of this study, therefore, detailed investigations and comparison were conducted on the microstructure morphology of WECs, DER and WEBs in already failed bearings, where all features were at their fully developed stage. This is done in order to understand whether DER and WEBs are related to WSF that triggers failures well below the designed bearing life in the through-hardened martensitic AISI 52100 bearing steel. Further, the analyses of the microstructural changes at different formation stages through series of time controlled testing have been performed in order to capture the initiation stage of material transformation, to help understand WEA formation mechanisms. Lastly, additional experiments varying test conditions have been performed to distinguish root cause (i.e. driver) of the microstructure alterations observed in this study. Advanced microstructure characterisation techniques, such as SEM with BSE and SE imaging, combined EBSD/EDX, and TEM have been employed throughout this study and are described in the next chapter.

Chapter 3

Characterisation Procedure and Methods

3.1 Introduction

This chapter describes the methods and techniques used for microstructure characterisation in this study to examine microstructure alterations in field failed bearings and test specimens obtained under various test conditions (details are given in next chapters). A number of microscopic techniques, including LOM, SE and BSE imaging in SEM, EDX, EBSD, and TEM have been used in this study. All material characterisation steps follow a well-defined procedure, shown in Figure 3.1, where a flow of the key steps undertaken during microstructural characterisation is presented. Details of the techniques and settings are described in the following sections.

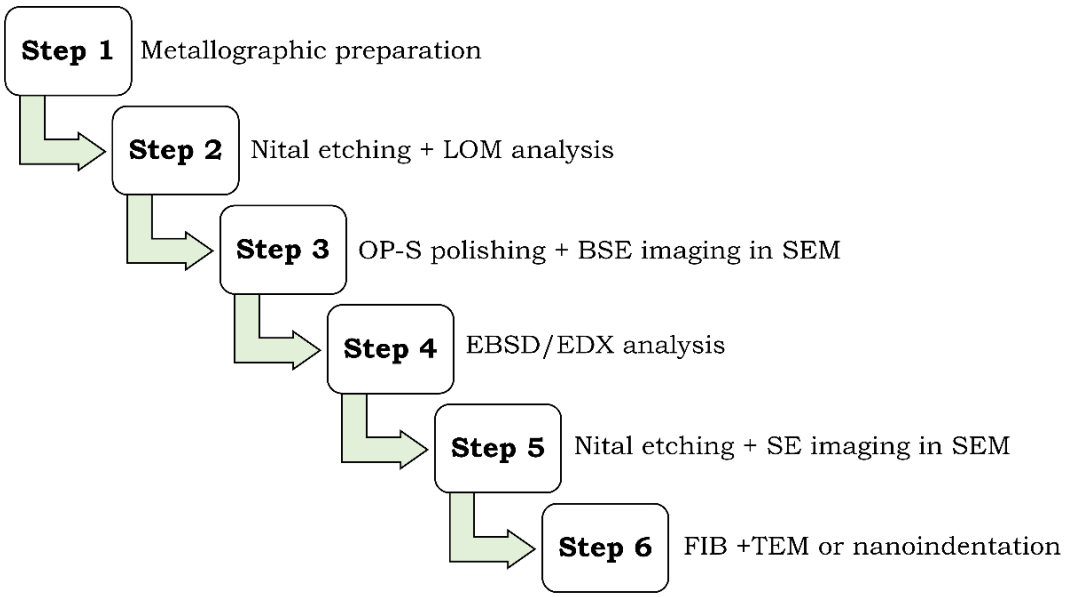

Figure 3.1: A flow chart describing the microstructural characterisation procedural steps.

3.2 Metallographic Specimen Preparation

All experimental samples were carefully prepared in order to reveal the structural features and image them at the desired magnification and resolution. Due to the short depth of field of LOM, samples have to be sufficiently flat to achieve focused images of a relatively large area. Hence, metallographic preparation, such as cutting, grinding and polishing, is essential for LOM analysis. In this study, circumferential and axial cross-sections were cut, as example the ball bearing indicating both cross-sections are shown on Figure 3.2.

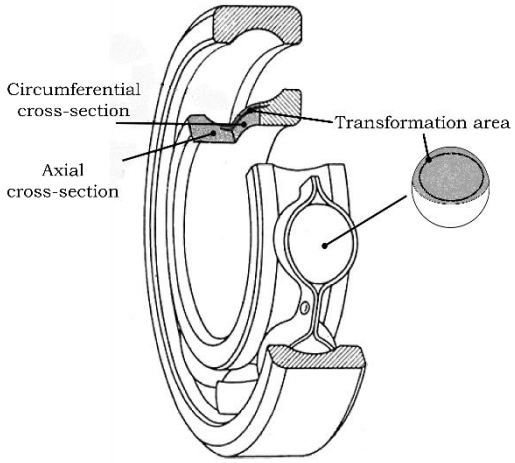

Figure 3.2: Ball bearing example indicating circumferential and axial cross-sections and transformation area in inner ring and ball element. Adapted from [54].

The first step of the metallographic preparation of the specimens was to choose and cut a sample using a precision saw (Presi, Mecatome T210 or Buehler IsoMet 5000) with a diamond disk. A mix of water and Struers cooling fluid was used as a lubricant and coolant to avoid material transformation during the cutting. The specimens were then hot mounted in a Bakelite resin for grinding and polishing. During the hot mounting, an automatic hot mounting press (ATM, OPAL 410) is used for short period of time (~ 15 min) under ~180°C temperature and ~200 bar pressure. The Bakelite resin contains conductive carbon fillers for SEM examination of specimens in the mounts. Most of the samples investigated in the Chapter 5 & 6 were not mounted in Bakelite resin, since initially APT was planned to be used, where APT resolution could have detected any possible changes in microstructure due to an elevated temperature and pressure during mounting.

Wet grinding with silicon carbide (SiC) paper grit of 120 grade was firstly used as a starting step to remove damage and/or scratches from cutting, as well as to attain desired zone and flat surface. SiC papers grit of 320, 600, 800, 1200 and 4000 were subsequently used followed by polishing with 3 μm, 1 μm and 0.25 μm diamond suspensions on special cloths (Schmitz MoITEC Poliertuch for 3 μm and Schmitz FoxTEC II for 1 and 0.25 μm). Initially, the polished surface was etched to reveal the bearing steel microstructure features and to identify the exact areas of interest. For the etching, a 1-3% Nital solution (1-3 ml HNO_3, 99-97 ml Ethanol) was applied for 1-3 seconds before the surface is imaged under LOM (Olympus BX51).

After initial analysis by LOM specimens were slightly re-polished to remove the etched topography and colloidal silica suspension (OP-S) was used as the final preparation step to achieve the necessary deformation-free surface and to avoid influences from the topography for obtaining orientation contrasts in the BSE imaging in SEM and EBSD/EDX analyses. After BSE and EBSD/EDX analyses the specimens were slightly re-polished to remove the contamination layer of the prior analyses, which was done so that imaged layer stayed as close as possible for corresponding imaging with SE in the SEM after etching it with Nital.

Specimens were cleaned in an ultrasonic bath with Isopropyl Alcohol (IPA) solution between each polishing step to avoid any particle residuals that could result in scratches in the following steps. Cleaning was also performed prior to every microscopy analysis.

3.3 Scanning Electron Microscopy

After LOM analysis, investigations with SEM were performed. In the present study, a JEOL JSM 7000F field emission SEM equipped with a combined EDAX Pegasus EDX/EBSD system was used. The BSE and SE imaging in the SEM were used extensively throughout all investigations. SEM analyses were performed at an accelerating voltage of 10 kV with working distance (WD) of approximately 5 mm for BSE imaging and 10 mm for SE imaging. The smallest available aperture and a medium probe current of approx. 2.5 nA were used for both SE and BSE imaging. BSE and SE imaging were always done on the same region that enabled direct comparison of the observed microstructure through both imaging methods.

BSE imaging detects primary electrons that penetrate into the specimen and after a series of scattering events finally are able to emerge from the specimen again. They typically have energies of the order of the beam energy (some kV) and have penetrated up to several hundred nm into the material on their path through the specimen. BSE imaging reveals features due to material composition and grain orientation. Material composition influences the brightness of the image, where lighter elements (with a lower atomic number, Z) result in darker appearance and heaver elements result in brighter appearance. The stronger composition contrast is achieved by using higher voltage, hence to reduce the influence of the composition on the overall contrast, comparatively low voltages of 10 kV were used throughout this study. Brightness in the orientation contrast imaging is influenced by grain orientation with respect to the incoming electron beam, see Figure 3.3(a). For example, if single grains in the sample are orientated in a way that single lattice planes and the incoming electron beam are coplanar, the primary electrons can penetrate deeper into the material, thus resulting in the darker contrast. Whereas, arbitrary angle between electron beam and lattice plane result in lower penetration, thus brighter contrast.

SE imaging detects electrons are released in the course of the inelastic scattering events from the specimen material. SE usually have lower energies (by definition < 50 eV, typically about 2-5 eV) compared to BSE and are therefore able to leave the specimen only from the topmost regions of the interaction volume. Imaging with SE provides clear surface topographical images, see Figure 3.3 (b). For example, if the electron beam hits a depression on the sample, a larger part of the generated signal penetrates deeper into the material, whereas the detectable fraction of the generated signal gets smaller, thus the corresponding point in the image becomes darker. On the contrary, if the electron beam hits a local elevation or an edge on the specimen, the number of directions, into which a generated signal finally can leave the specimen, increases, resulting in a more intense signal at these positions consequently the image gets brighter.

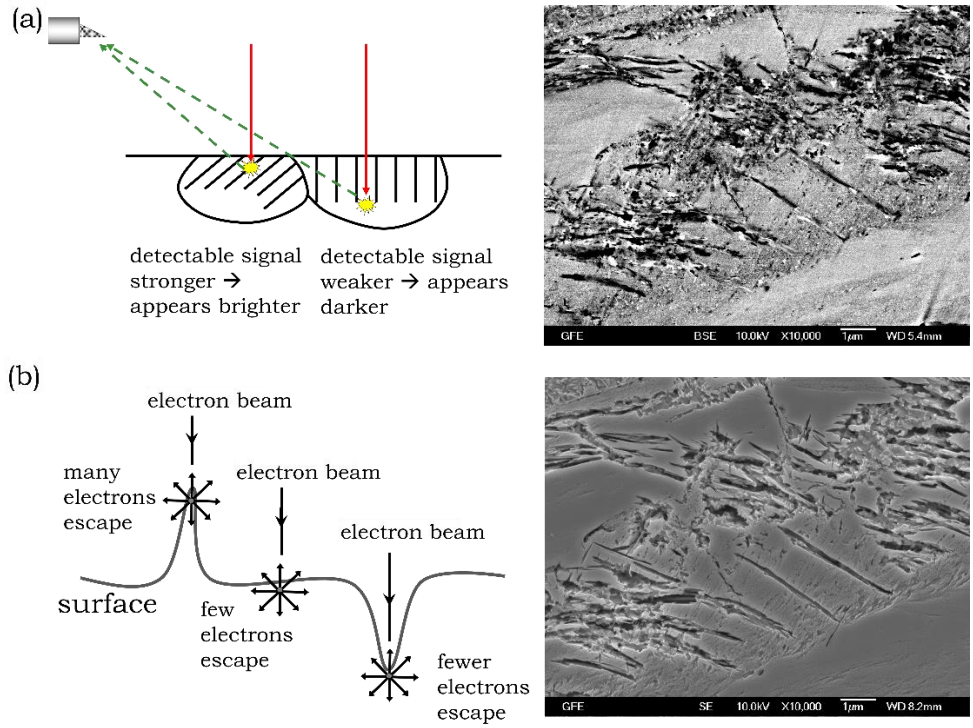

Figure 3.3: Schematic diagrams and SEM images of microstructure alterations in AISI 52100 bearing steel imaged at the same location: (a) BSE imaging (OP-S polished); (b) SE imaging (Nital etched).

3.3.1 Energy-dispersive X-ray Spectroscopy and Electron Backscatter Diffraction

EDX and EBSD are common analytical methods used in an SEM, where EDX provides chemical analysis and EBSD provides crystallographic information of the specimens. In the present study, EDX and EBSD data have been collected simultaneously to ensure complementary information from the same area is obtained. An accelerating voltage of 15 kV and probe current of 30-35 nA under a WD of 15-17 mm with varied step size, such as **25 nm** and **50 nm** have been set for the EBSD/EDX investigations in this study. The EBSD data have been evaluated using EDAX OIM 7.3 and various maps, including phase, Image Quality (IQ), Kernel Average Misorientation (KAM), Inverse Pole Figure (IPF) maps, have been produced based on the information need to be gathered. For indexing purposes the phases of α-Fe, γ-Fe and Fe_3C and Confidence Index (CI) (the accuracy of measured data in the scale from 0 to 1, with 1 being the best) more than 0.1 has always been chosen. With exception of the non martensite-martensite High Angle Grain Boundary (HAGB) maps (will be discussed below), no clean-up

of the data has been carried out. For a better visibility in the print, brightness and contrast corrections have been applied on the EDX maps.

EDX was equipped with an 'octane plus' silicon drift detector (SDD) with 30mm^2 detector area. A 'super-ultra thin window' (i.e 300nm thin polyurethane foil) or thin silicon nitride window were used during course of investigations, which are known to be the most sensitive detectors with windows for low-energy x-ray detection. In EDX analysis map mode has been used to measure the distribution of elements. The results typically are presented as maps where the image intensity is taken to be relative to the local concentration of the elements present. Several elements, such as carbon, chromium, iron, manganese, sulphur, aluminium, silicon, and others, have been analysed at the same time.

During EBSD analysis an electron beam scans a preselected region on a tilted conductive crystalline sample and the backscattered electrons form a pattern on a fluorescent screen due to diffraction when exiting the sample. The resulting diffraction patterns, also known as backscatter Kikuchi patterns, are characteristic of the crystal structure and orientation of the analysed region on the specimen. The patterns can be further analysed to provide information including the preferred crystal orientations (texture), grain boundaries, point-to-point orientation correlations, and for phase identification. EBSD offers a good method for gathering both, basic and advanced information about microstructure and crystallography of a specimen. The ability of EBSD to collect data from large areas of a specimen makes it a powerful tool for in-depth microstructural analysis.

However, the EBSD technique in SEM is limited to materials with grain size larger than several tens of nanometres in diameter due to the step size limitations in EBSD. That is the reason that some areas in the EBSD maps presented in the results chapters appear black due to very small unindexed grains (below the spatial resolution). In EBSD a grain is defined by a collection of adjacent pixels that have a misorientation less than a predefined angle (typically 15°). Factors such as specimen condition and microscope operating conditions can affect the quality of the EBSD pattern, and thus the identification rate. Since the measurable diffraction typically occurs in a few nm depth, the specimen surface preparation plays an important role in getting high quality EBSD results, for the example specimen surface has to be very smooth and deformation free to avoid influences of topography on the generated patterns. In the present study OP-S polishing has

been used as the final preparation step prior to EBSD imaging to ensure a sufficient specimen surface finishing for the analysis.

EBSD data are typically presented in a form of map, including the following five types:

- **Phase map**

Phase mapping is used to identify crystallographic phases in a material by comparing observed symmetries in the measured pattern with symmetries of known phases stored in the EBSD library of the SEM. Retained austenite phase (i.e. γ-Fe, fcc) can be easily distinguished from ferrite (i.e. α-Fe, bcc), whereas it is more difficult to distinguish martensite (i.e. bct) from ferrite. This typically results in martensite being indexed as ferrite, hence the application of IQ and KAM mapping is typically used to further distinguish them [146-148].

- **Image Quality map**

IQ maps provide a useful visualization of microstructures. It is a measure for the intensity of Kikuchi bands in an EBSD pattern, and is strongly affected by local perfection or imperfection of a crystal lattice within the interaction volume of the electrons. The contrast in an IQ map can be affected by local strain, grain boundaries, phases, topography, grain orientation, contamination and sample preparation [149]. IQ maps are thus often used to identify microstructural features, such as grain boundaries, grains, internal grains structures and surface damage (e.g. scratches). Grain boundaries, internal grains structures, cracks, defects, scratches, areas of higher strain or dislocation density will typically have poorer pattern quality and hence appear as darker points on the map, whereas brighter points correspond to higher pattern quality and therefore grains with low internal strain. For example, ferrite and bainite phases typically have lower internal strains compared to martensite, hence will have higher IQ values in comparison with those in martensite [146-148]. Moreover, IQ mapping is the only EBSD-based parameter that is independent of the indexing, hence structures can still be seen within the areas where patterns cannot be indexed anymore (e.g. areas such as WEA).

- **Kernel Average Misorientation map**

KAM analysis calculates the average degree of misorientation (i.e. orientation change) for every pixel within a kernel. A kernel is a set of pixels of described size surrounding the scan pixel of interest. Figure 3.4(a&b) show examples of a 1st and a 2nd nearest-neighbour kernel. The average grain internal orientation change of the crystal lattice calculated for the kernel is assigned to the scan point at the centre of the kernel. Going to a larger radius usually gives larger (i.e. less noisy) orientation changes, but the spatial resolution in the resulting map decreases. Large misorientation could be detected, if the kernel contains grain boundaries, hence a threshold should be specified in order to exclude pixels on the other side of the grain boundary from the calculation of the KAM, see Figure 3.4(c). KAM maps can be shown to have each separate or all phases in one map. For example, KAM(100nm, 5°) abbreviation describes the map that depicts the average grain internal orientation change (up to 5°) of the crystal lattice over a distance of 100 nm (e.g. 100 nm stands for 2nd nearest neighbour kernels in an EBSD measurement with 50 nm step size).

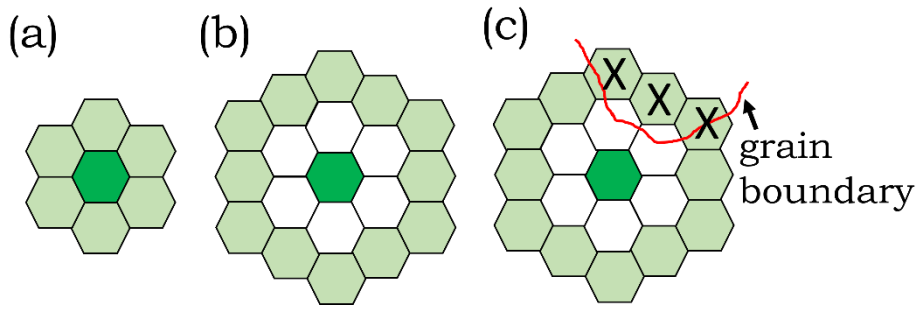

Figure 3.4: Schematic illustration of: (a) 1st nearest-neighbour kernel; (b) 2nd nearest-neighbour kernel; (c) kernel with excluded pixels due to grain boundary.

KAM maps are used to depict the build-up or relaxation of internal strains and dislocation densities in the analysed material. The rotations in crystals as a result of geometrically necessary dislocations or high internal strains (i.e. deformations) will be manifested by a high KAM value. For example, bainite and martensite phases have higher internal strains compared to ferrite, hence will result in higher KAM values [146-148].

- **Non martensite-martensite High Angle Grain Boundaries map**

The non martensite-martensite HAGBs map is a useful tool to observe phase transformation and recrystallisation in the material. It presents grain boundaries with misorientations exceeding 15° that are not typical ones between martensite plates, see an example shown in Figure 3.5. Initially γ-Fe and Fe_3C are identified in the area of interest and marked in red and purple, respectively. Then, all the pixels identified as HAGBs are painted in blue. Afterwards, the retained austenite-martensite and martensite-martensite boundaries predicted by orientation relation models of the martensitic transformation, developed by Kurdyumov-Sachs [150], Nishiyama-Wassermann [151], Greninger-Troiano [152] and Pitsch [153], are painted in yellow and white, respectively. A few examples of such axes of rotation with their corresponding rotation angles are shown in the legend and a full list of directions and angles for each model are given in Appendix A. The remaining HAGBs observed on the maps are the ones that are not expected as boundaries between martensite plates growing from the same austenite grain (e.g. prior-austenite grain boundaries), or the HAGBs which are formed by processes other than martensitic transformation (e.g. newly formed grains).

In order to reduce the optical disturbance by grain boundaries around erroneously indexed individual pixels, prior to the calculation of this map, a moderate clean-up using the 'neighbour CI correlation' algorithm implemented in the software has been applied.

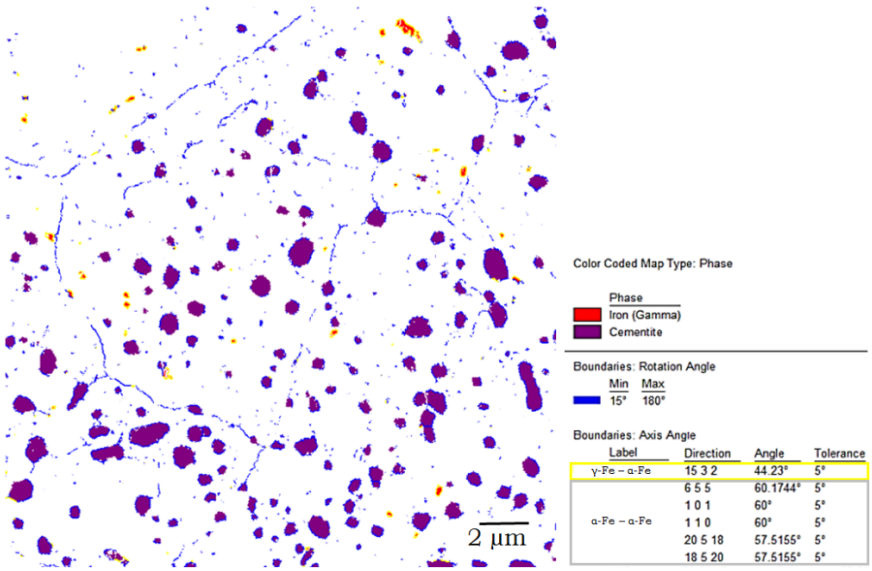

Figure 3.5: An example of non martensite-martensite HAGBs map collected from a virgin matrix of AISI 52100.

- **Inverse Pole Figure map**

The IPF map is a crystal orientation map that is coloured by a mixture of different colours depending on the crystal planes and it can provide diversity of information about the specimen microtexture. Maps can be produced based on a predetermined reference axis, for example x, y, and z directions in this study. The crystallographic direction is measured at a single point that corresponds to the particular specimen direction. [154] A single IPF map does not explicitly indicate the complete orientations of the crystals in a polycrystalline sample, but only the orientations of selected crystalline planes or directions. IPF maps are best used to detect preferential grain growth orientation (i.e. texture).

3.4 Focused Ion Beam and Transmission Electron Microscopy

TEM analysis has been conducted on some specimens prepared using a FIB work station FEI Strata 205 in this study. A tungsten layer has been deposited for surface protection and Ga^+ ion milling has been performed at an acceleration voltage of 30 kV with different currents starting with 20.2 nA and finishing off with 3.49 pA. The cut lamella was placed onto a copper grid for imaging. TEM Bright Field (BF) and Dark Field (DF) images, as well as SAED patterns have been obtained using an FEI Tecnai F20, operating at 200 kV.

Just like in SEM, some parts of electrons scatter elastically and others inelastically. Inelastic scattering is possible when the specimen is thick enough that results in deviation angle <0.5º and contributes to the generation of X-ray photons for EDX. Elastic scattering can be coherent or incoherent depending on interactions between electrons and nuclei, respectively, which result in different deviation angles. Coherent electrons are strongly affected by the arrangement of atoms within the specimen, thus scattered through a small angle (0.5°-1.5º) and are the most significant scattering in TEM. Coherent elastic scattering results in the formation of diffraction patterns, BF and DF imaging.

In crystalline specimens many electrons undergo elastic scattering from various planes producing many diffracted beams. A combination of all beams will produce poor contrast image, therefore some of the beams should be cancelled out, see Figure 3.6. For example, to form BF image only the transmitted beam should pass,

whereas all the electrons that have been deflected are cancelled out. In contrast, for formation of a DF image only one diffracted beam passes to contribute to the image. In BF and DF images weak diffractions in specimen result in bright and dark intensities respectively.

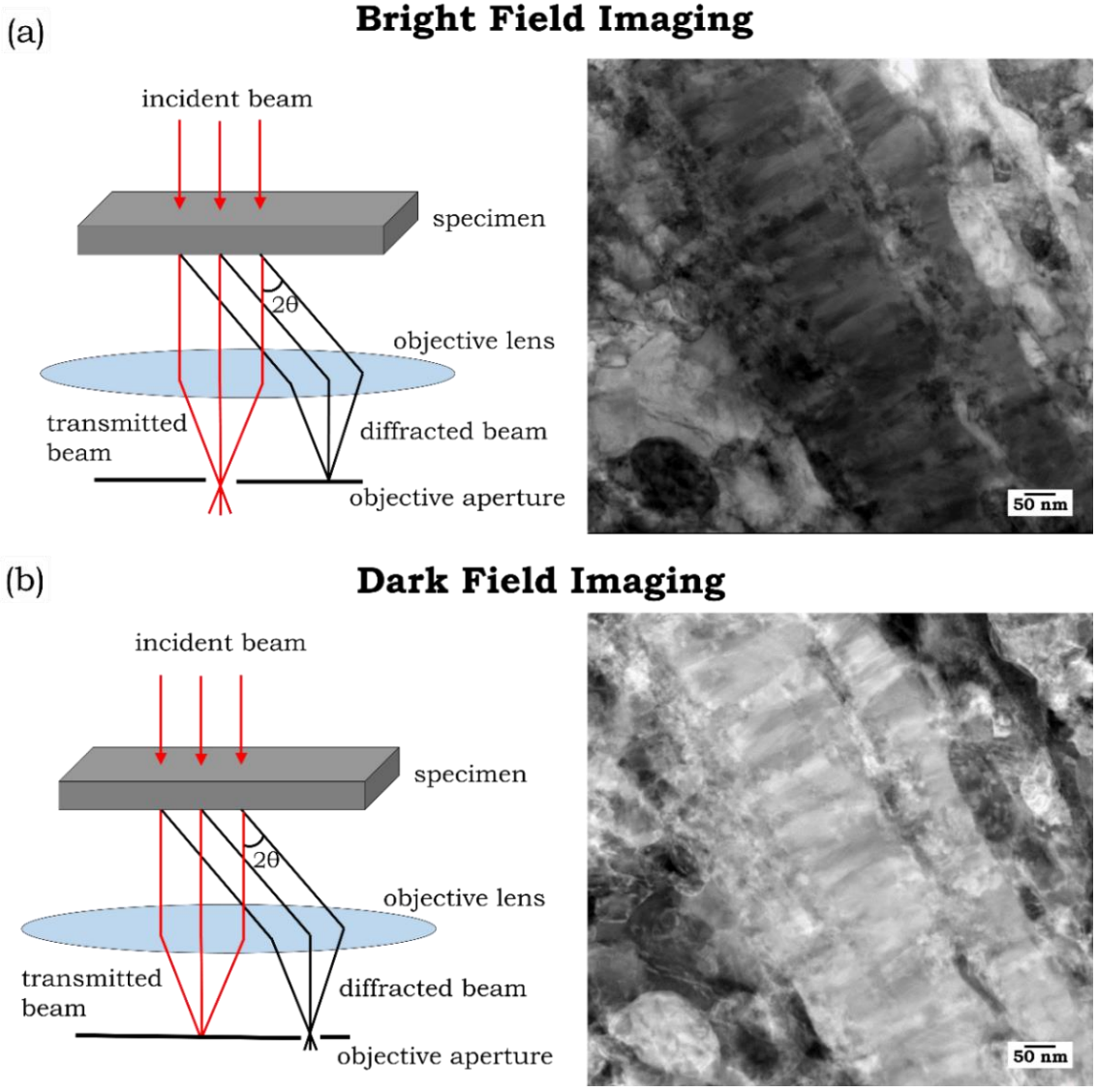

Figure 3.6: Diagrams and images showing formation of: (a) BF TEM; (b) DF TEM.

SAED is another technique in TEM that produces information on structure and orientation of crystals. SAED patterns are used to measure distance between crystallographic lattice planes and to find orientation of single crystal and crystal structure of unknown material (identification of phases). Single crystals produce a spot pattern, whereas polycrystalline and amorphous specimens produce ring patterns, see Figure 3.7. Ring patterns are essentially the sum of individual patterns obtained from single crystals. Each ring comes from one set of planes. Larger crystals result in more 'spotty' ring patterns, whereas amorphous regions

produce diffused rings. If a diffracted area has a preferential orientation (i.e. texture) arcs of greater intensity are seen in the diffraction rings.

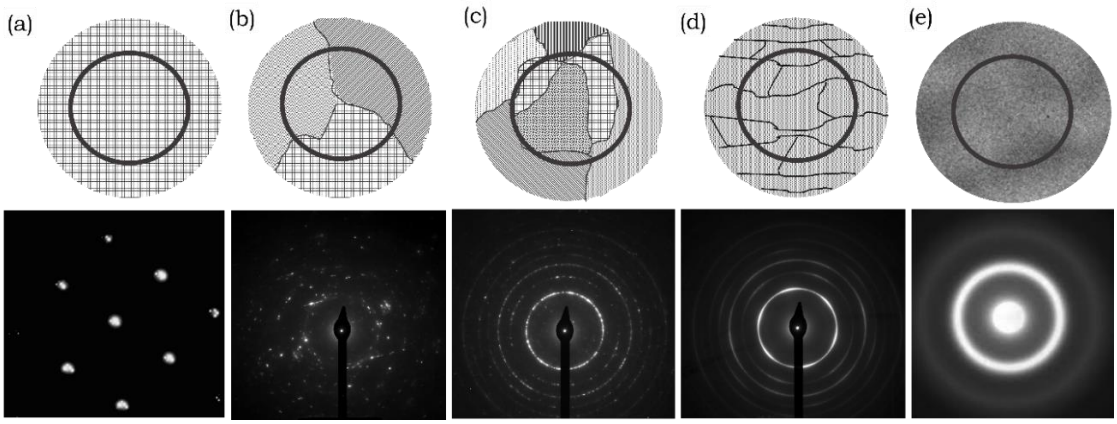

Figure 3.7: Examples of SAED patterns from: (a) a single crystal; (b) polycrystalline matrix with large crystals; (c) typical nano-crystalline matrix; (d) matrix with slight texturing; (e) amorphous matrix.

3.5 Nanoindentation

Indentation is a technique that measures mechanical material properties, such as hardness and elastic modulus, by bringing material of interest to contact with a known material. Different indenter shapes are available for hardness measurements. This study used Berkovich and Vickers indenters that are three and four-side pyramids, respectively, shown in Figure 3.8.

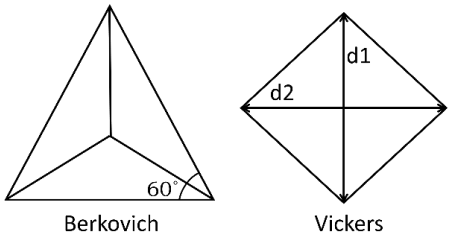

Figure 3.8: Diagrams of Berkovich and Vickers indentations.

Nanohardness measurements have been performed on microstructural alterations presented in Chapter 4.2 using a NanoTest Vantage (Micro Materials) nanoindentation system with Berkovich tip at University of Southampton. Nanoindentation mapping tests have been carried out on selected test specimens in depth control mode by applying a maximum depth of 300 nm. In accordance with BS EN ISO 14577-1:2015 standards, the arithmetic mean deviation of the surface roughness should be no more than 5% of the minimum penetration depth

to ensure that the surface roughness has no effect on the hardness mapping. The specimens surfaces have been slightly etched prior to the hardness test after satisfying the surface roughness measurements using a Talylor-Hobson Talysurf 120L profilometer where the arithmetic mean deviation surface roughness of less than 10 nm requirement has been met. Etching has been used for easier identification of the areas of interest using SE SEM. A fixed 2 mN/s loading/unloading rate and 20 s dwell time at the maximum load have been used for all nanohardness measurements. Thermal drift correction data have been collected for 30 s before and after the indentation test. Hardness of the features of interest has then been extracted from the load-displacement curve. After nanohardness analysis all the indents have been checked with SE SEM (JEOL, JSM-6500F) to confirm the areas of indentation. An average of at least 3 indent measurements was used as the hardness value for each feature.

Nanohardness tests have also been performed on microstructural alterations presented in Chapter 4.3 using a Fischerscope H100C (Helmut Fischer GmbH, Sindelfingen) system with Vickers tip at RWTH Aachen university. Indentations have been made in force control mode by applying a force of 10 mN. A fixed loading/unloading rate of 0.5 mN/s and a dwell time at maximum load of 5 s have been used for all hardness measurements in this study. After the indentation all the indents have been imaged by SEM to examine the indents and analyse the results. Hardness of the features has been extracted from the projected contact area and calculated using equation [155]:

$$HV = 1.854\ \frac{F}{d^2},$$

where F is load in kgf (1 kgf = 9.80665 N) and d is arithmetic mean of the two diagonals, *d1* and *d2* in mm (shown in Figure 3.8).

Conversion between Vickers hardness, *HV*, and Berkovich hardness, H_{IT}, can be achieved using equation [156]:

$$HV = 94.5 \times H_{IT}\ (\text{in GPa})$$

However, it should be noted that indentation size effect (ISE), which results in higher hardness values obtained with lower applied loads, should be considered for tests performed at different loads during their hardness values conversion [157].

Chapter 4

Results: Characterisation of Failed Bearings

Despite the amount of efforts given to the topics of DER, LABs, HABs, and WECs over the past few decades, little effort had been made to compare these microstructural alterations and to investigate the correlations and differences in the transformed microstructures, their hardness and formation mechanisms.

At the beginning of this study, detailed analyses were conducted on fully developed DER, LABs, HABs and WECs in AISI 52100 bearing steel to understand these features and their correlations. A combination of microstructure characterisation techniques, such as SEM, EBSD, EDX, TEM, and nanoindentation, described in Chapter 3 have been used to analyse the microstructure, chemistry and hardness of these phenomena. The experimental details of the bearing samples, the analysis results and the comparison results are presented in this chapter, which have also been published in two papers in the International Journal of Fatigue [158, 159].

Additionally, this chapter presents details of the heat treatment, chemical composition and microstructural analysis of a virgin through-hardened martensitic AISI 52100 steel. The characterisation of a virgin specimen will serve as base line for comparison with laboratory tested or field retrieved specimens.

4.1 Virgin Material

Throughout this study all bearings analysed have used the standard through-hardened martensitic AISI 52100 bearing steel, subjected to a standard heat treatment process including austenitisation at 845°C for 20 minutes and quenching in oil to 60°C followed by cooling in air to room temperature and finally tempering at 180°C for 2 hours. The oxide layer created by this procedure is then removed with sandblasting and finally the bearings are honed to achieve the desire

surface roughness. A typical microstructure would consist of tempered martensite with homogeneously distributed primary spheroidised carbides $(Fe, Cr)_3C$, tempered carbides and approximately 10-12% retained austenite.

The chemical composition of the virgin specimen cut from unused deep groove ball bearing (DGBB) 6206 type, measured by the Sheffield Assay Office using an inductively coupled plasma optical emission spectrometry, is given in Table 4.1. The elements carbon and sulphur were determined using combustion analysis.

Table 4.1: Chemical composition of the virgin specimen, wt%.

C	Cr	Mn	Si	Ni	Cu	Al	Mo	S	Co	P	Sn	Zn
1.01	1.57	0.44	0.25	0.06	0.04	0.02	0.03	0.005		<0.01		

Figure 4.1 and Figure 4.2 show a BSE and an SE SEM images of same large area on a virgin bearing cut, which were produced by stitching a number of SEM images taken at 5000 magnification using Adobe Photoshop CS6. Typically between 9 and up to 60 images are acquired to produce large-size panoramic SEM maps, which are ideal to observe inhomogeneity, defect, inclusions, distribution of the phases, or texture in the material, as well as for comparison with EBSD/EDX maps. For specific details higher magnification imagining is also necessary.

As can be seen in these images, the microstructure of the virgin steel consists of martensite plates and randomly distributed primary spheroidised carbides. Martensitic plates are randomly orientated, resulting in contrast variations in BSE imaging, see Figure 4.1. Defects, such as microcracks, which potentially could have been induced by quench stresses, pores or voids due to inadequate material production, have not been observed in the virgin microstructure, neither many non-metallic inclusions have been detected across analysis of a virgin bearing examination. Small holes due to the metallographic preparation have been observed in the material occasionally, see examples marked with red arrows in Figure 4.1.

Figure 4.3 shows two typical orientation imaging maps of the virgin through-hardened martensitic AISI 52100 obtained by the SEM/EBSD method. The IQ map, shown in Figure 4.3(a), shows a homogeneous distribution of grains and strain, as well as demonstrating that a good surface preparation was achieved. Figure 4.3(b) shows an IPF map, showing that martensitic plates are randomly

orientated with no texture observed in virgin material as expected. IPF maps have been plotted with respect to axis that is parallel to normal direction of the bearing raceway (i.e. rolling normal direction) for all sample presented in this thesis.

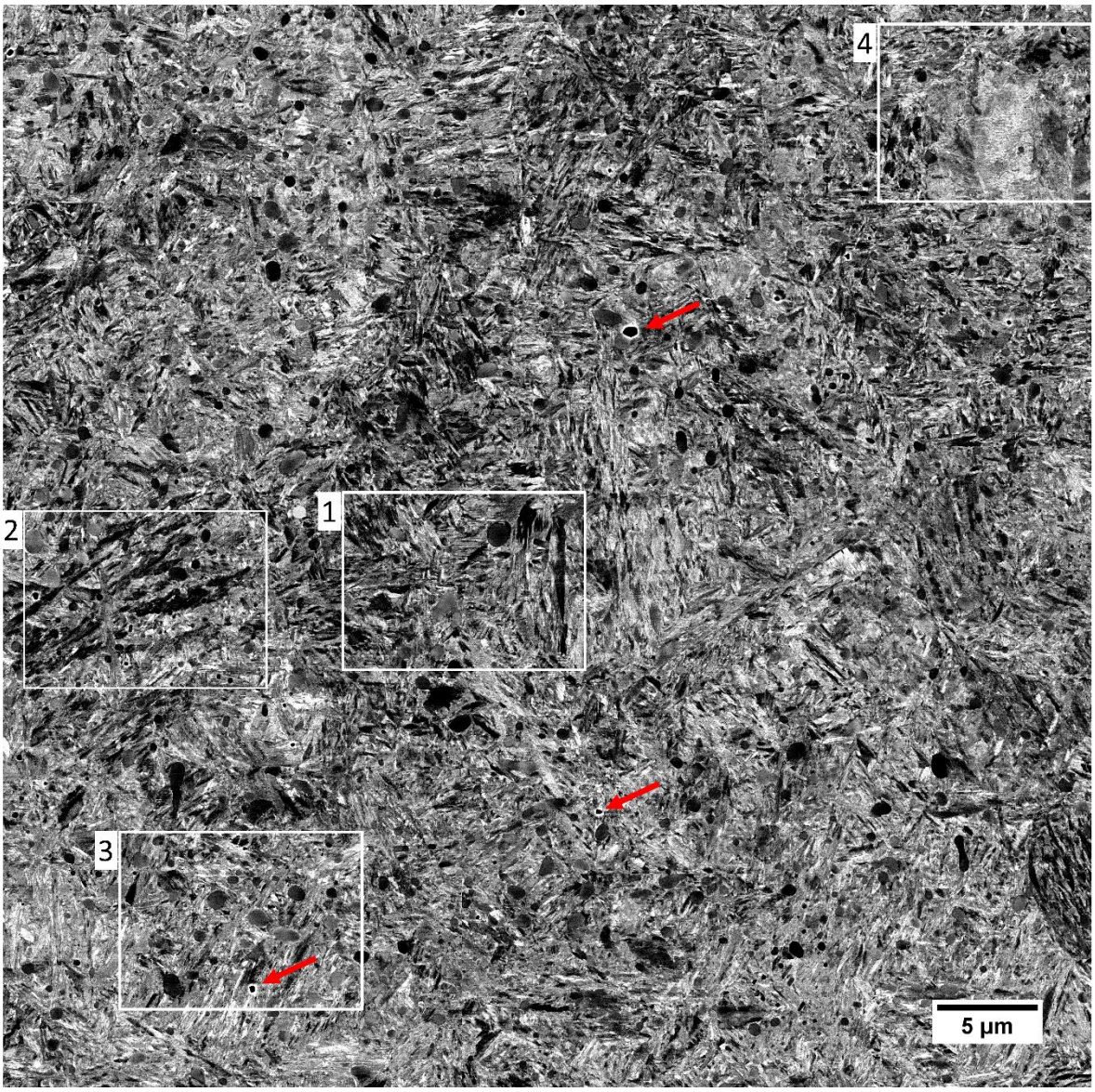

Figure 4.1: BSE SEM of virgin material (OP-S polished). Four areas are marked for the zoom-in locations shown in Figure 4.6 and Figure 4.7. Defects due to the metallographic preparation are marked with red arrows.

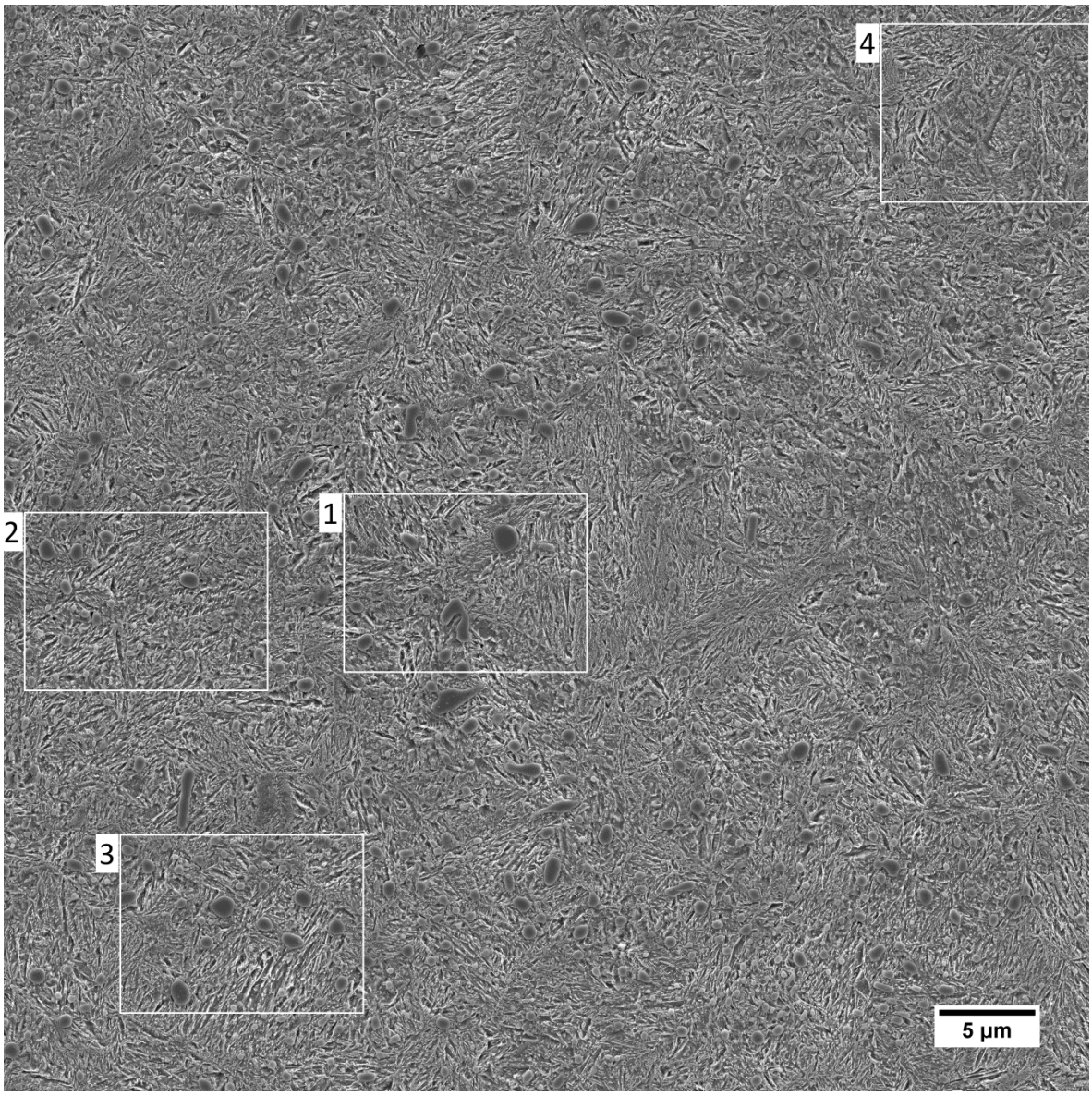

Figure 4.2: SE SEM of virgin material (Nital etched). Four areas are marked for the zoom-in locations shown in Figure 4.6 and Figure 4.7.

Another two maps obtained by the SEM/EBSD method, a KAM map and a non martensite-martensite HAGBs map, are shown in Figure 4.4. Figure 4.4(a) shows a homogeneous distribution of KAM values with slightly higher values observed closer to the grain boundaries. This clearly shows that virgin martensitic material has homogenised strain distribution without any localised strain points. Higher misorientation values have not been observed around primary spheroidised carbides suggesting they are well integrated into the material and do not act as stress raisers. Figure 4.4(b) shows non martensite-martensite HAGBs, such as grain boundaries of the prior-austenite grains that are indubitably non martensite-martensite grain boundaries, throughout the virgin martensitic microstructure.

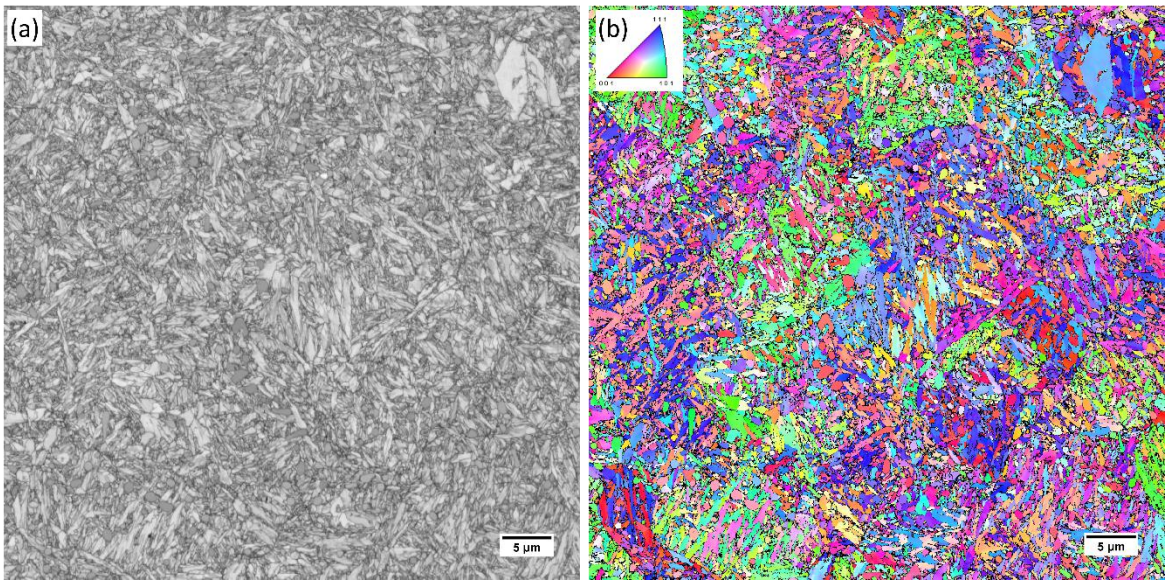

Figure 4.3: Orientation imaging maps of virgin material obtained by the SEM/EBSD method: (a) IQ map; (b) IPF colour map with respect to rolling normal direction.

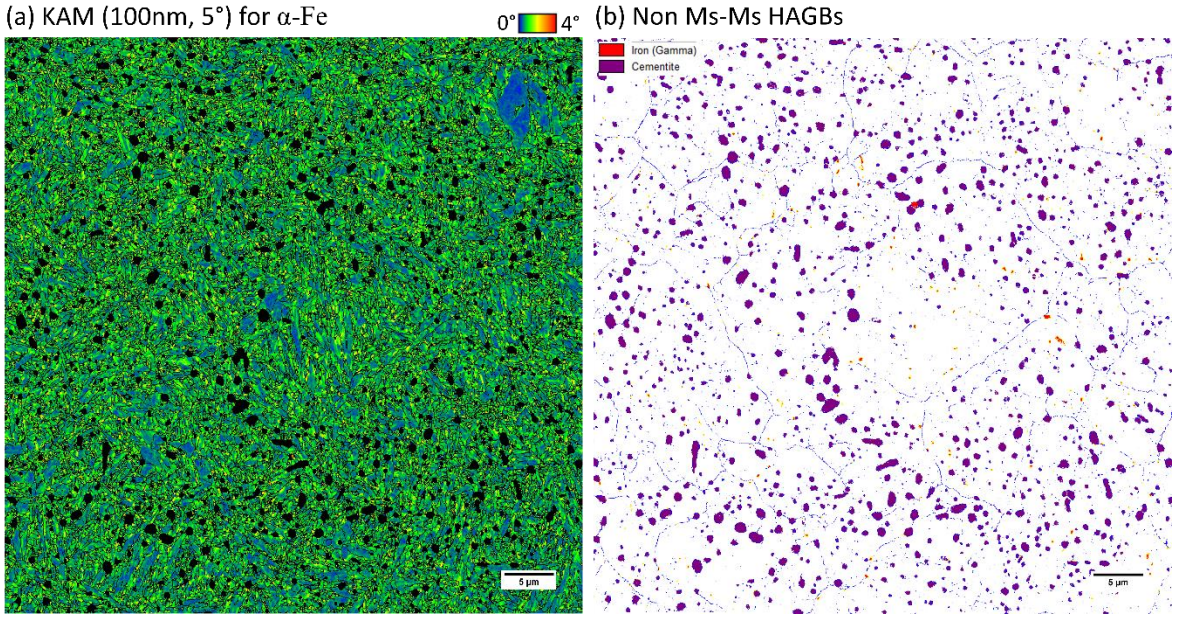

Figure 4.4: Maps of virgin material obtained by the SEM/EBSD method: (a) KAM(100nm, 5°) for α-Fe only; (b) non martensite/martensite HAGBs.

Lastly, the carbon and chromium distribution maps, which were measured by EDX during the EBSD scan as x-ray intensities in the energy ranges of C-Kα and Cr-Kα, and EBSD phase map of the virgin material are shown in Figure 4.5. Primary spheroidised $(Fe, Cr)_3C$ carbides are clearly shown as higher X-ray intensities in both Cr-Kα and C-Kα energy ranges, as well as easily indexed as cementite in the EBSD phase map. Such carbides typically appeared to be homogeneously

distributed, although locations with almost no primary carbides are also observed. Carbon seems to be distributed homogeneously around the spheroidised carbides as shown in Figure 4.5(a), whereas chromium depletes around the spheroidised carbides as shown in Figure 4.5(b). The EDX maps appear to be noisy due to the comparatively short dwell times of 20 ms during the EBSD measurement and the poor detection limits for the light elements like carbon, oxygen and others. However, these maps have been found to be useful in giving indications of chemical alterations when comparison is made between samples at different testing stages and with expected chemical distribution in the virgin material. In addition to α-Fe and cementite, γ-Fe has also been indexed in the EBDS phase map. However, γ-Fe is hardly visible in the virgin martensitic material as shown in Figure 4.5(c). This is typical in through-hardened martensitic AISI 52100 bearing steel as retained austenite has a high risk to be transformed into martensite during preparation stage.

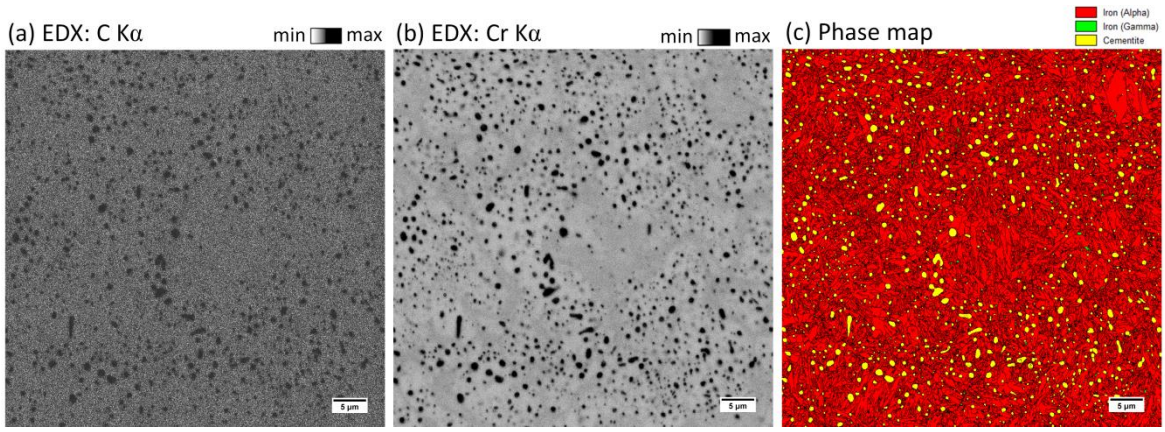

Figure 4.5: EDX maps of: (a) carbon; (b) chromium; and (c) EBSD phase map.

To observe more details, BSE and SE SEM images have been taken at 10 000 magnification from location 1 in Figure 4.1 & Figure 4.2 and are presented in Figure 4.6. From the SE and BSE images it is easy to identify primary spheroidised carbides that appear to be dark spherical areas in BSE SEM, but smooth and flat protrusions in SE SEM. Further observation under SEM shows that the primary spheroidised carbides are not necessarily in an ideal spherical shape, but appear in various shapes frequently as shown in Figure 4.6. The size of primary spheroidised carbides found to vary between approx. 0.2-1 µm in the virgin martensitic steel analysed in this study. The appearance of the carbides in different shades of grey or black in the BSE imaging is due to the differences in their orientation rather than variation in the composition, which is confirmed by the IPF

map shown in Figure 4.3(b). Twins and cementite lamellae have been identified in the BSE and SE SEM images respectively with a few examples marked in Figure 4.6.

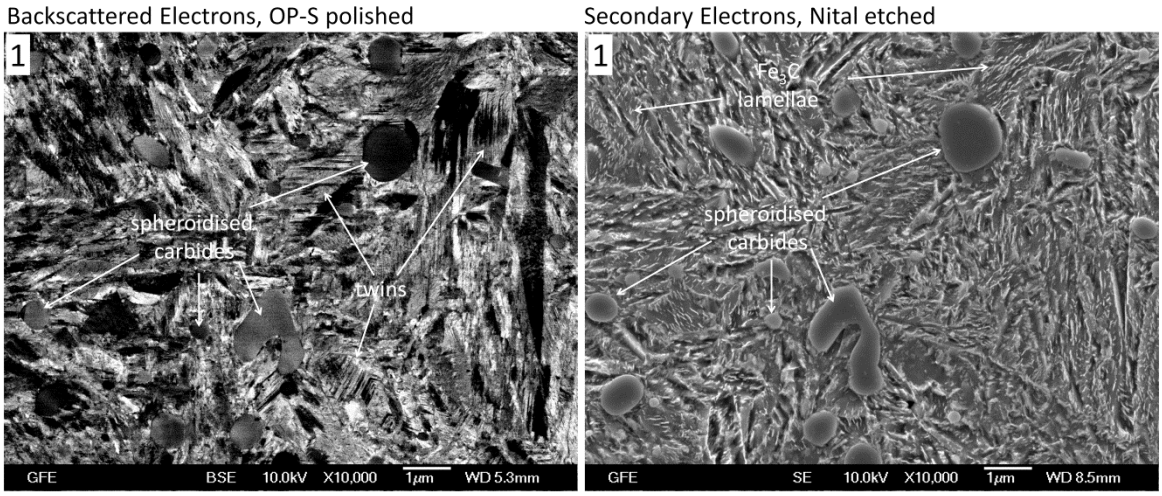

Figure 4.6: BSE and SE SEM images of virgin tempered martensite microstructure at location 1 marked in Figure 4.1 & Figure 4.2.

Figure 4.7 shows BSE and SE SEM images taken from locations 2, 3, and 4 shown in Figure 4.1 & Figure 4.2. It is clearly shown that the variations in intensity in the BSE SEM images are due to the variations in the orientation of the plate martensite. For example, location 2 shows darker patches in BSE image that could be interpreted as dark regions. However, after etching and SE imaging of the same area, it is clear that inhomogeneity in microstructure do not exist and that only the orientation of the martensite plates has resulted in the darker appearance. Similar orientation contrast but with appearance in white is shown at location 4. Location 3 shows a typical tempered martensite microstructure.

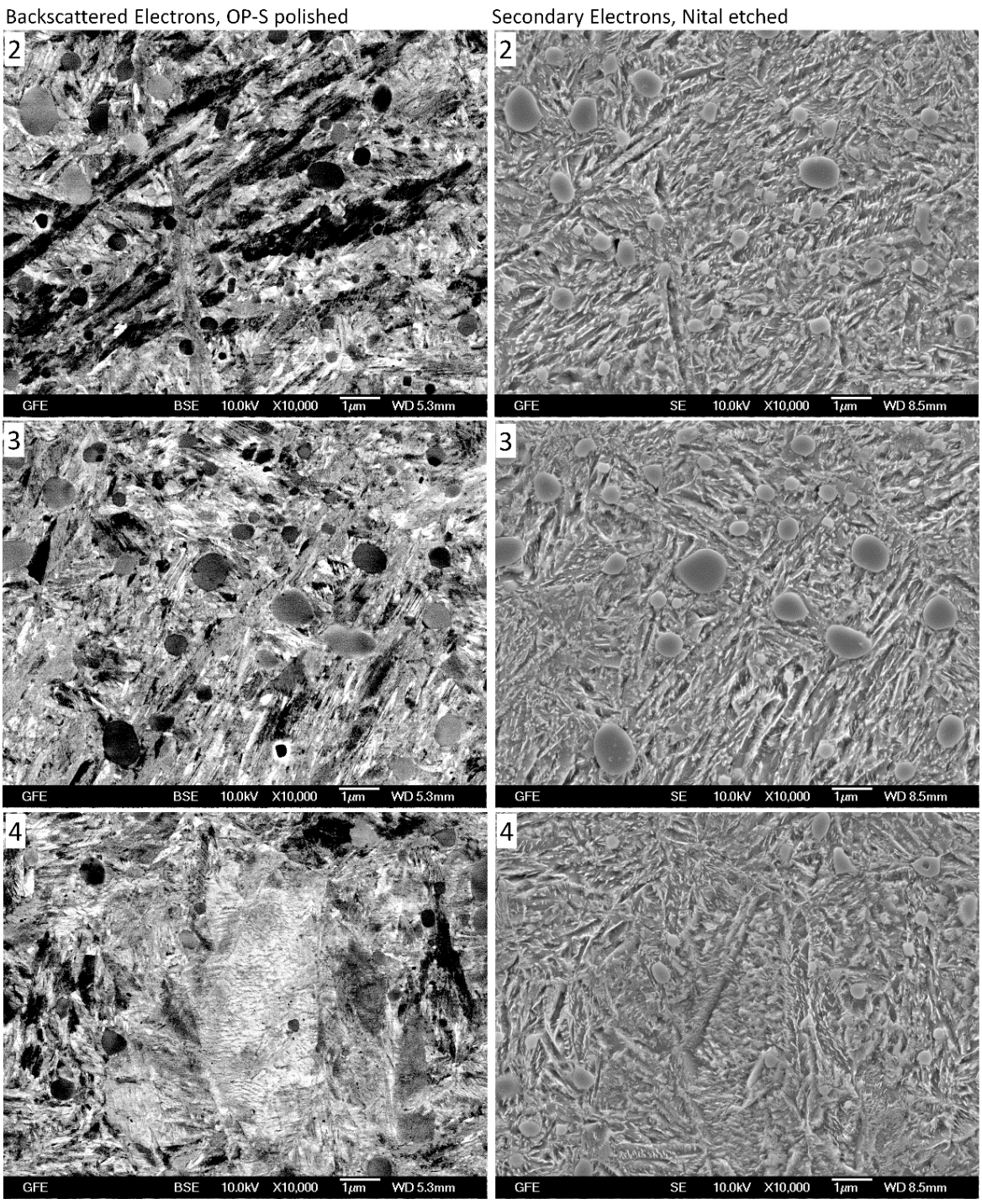

Figure 4.7: BSE and SE SEM images of virgin tempered martensite microstructure at locations 2, 3, 4 marked in Figure 4.1 & Figure 4.2.

4.2 Dark Etching Region, Low & High Angle Bands

4.2.1 Experimental Methods

The DER specimen was from a ball in a double row angular contact ball bearing exposed to RCF test on a Schaeffler L24-wheel bearing test rig. The bearing was grease lubricated. During the RCF test, the bearing rotating speed varied from 800 to 2000 rpm under a maximum contact pressure of 5287 MPa. The test was terminated at 244 hours of running when a ball failed with a surface spall. Each ball was exposed to the total of 169 million load cycles during the operation of the bearing (see Appendix B). The specimen examined here was cut from one of the balls without a spall.

The WEBs specimen was cut from the inner ring of an angular contact ball bearing of 7205B type. The bearing was exposed to RCF testing on Schaeffler L17 test rig, lubricated with ISO VG 68 oil under Elastohydrodynamic lubrication regime. The temperature of the lubricant was maintained at 80°C, the maximum applied pressure was 2900 MPa and the rotational speed was kept at 12000 rpm during the test. The test was terminated at 549 hours when the bearing failed with pitting resulting in approx. 3015 million load cycles faced by the inner ring (Appendix B).

The chemical composition of the specimens, measured by the Sheffield Assay Office using an inductively coupled plasma optical emission spectrometry, is given in Table 4.2. The elements carbon and sulphur were determined using combustion analysis.

Table 4.2: Chemical composition of the DER and LABs/HABs specimens, wt%.

	C	Cr	Si	Cu	Mn	Al	S	Ni	Co	Zn	P	Sn	Mo
DER	1.55	1.47	0.21	0.01	0.39	0.01	<0.003	<0.01			<0.01		
LABs/HABs	0.95	1.51	0.27	0.11	0.42	<0.01	0.005	0.03			<0.01		

4.2.2 Results

Both DER and LAB/HAB specimens have been firstly metallographically prepared and Nital etched to identify areas of interest, then re-polished with OP-S prior to BSE imaging in SEM. This has been followed by combined EBSD/EDX analyses. After which, the surface has been slightly re-polished to remove the contamination

layer then etched with 1% Nital solution for SE imaging on the same area imaged in the BSE SEM. TEM and indentation measurements have been conducted on slightly etched surface.

4.2.2.1 Dark Etching Region

The DER in the subsurface of the ball specimen is shown in the LOM image in Figure 4.8(a) (marked between the two white broken lines), extending from approximately 80 to 600 µm below the contact surface. In the zoomed in LOM image in Figure 4.8(b), it can be seen that the DER is a combination of small black patches intermixed with bright areas and small white primary spheroidised carbides. The dark patches observed in LOM are found to be correlated to clusters of elongated dark features appearing as deep grooves in the SE SEM (Figure 4.8(c); Nital etched), but as elongated grains in the BSE SEM (Figure 4.8(d); OP-S polished), where selected grains are marked with red arrows. Such elongated grains are similar to what has been presented in literature as parallel ferritic discs [52, 54, 57, 58]. In addition to the elongated grains, groups of small equiaxed grains were also detected in both images (some examples marked with yellow circles in Figure 4.8(c&d)). In order to eliminate confusion, a term 'DER' in this study represents a combination of microstructural alterations (i.e. elongated and equiaxed grains) with patches of residual martensite and primary spheroidised carbides. Hence, DER is a damage observed at a larger scale owing to the formation of the elongated and equiaxed grains that are etched away by Nital. A combination of stronger etching and the morphology of the grains have resulted in the dark appearance under LOM due to the scattering of the light rays in all directions and the shadowing of the surrounding walls.

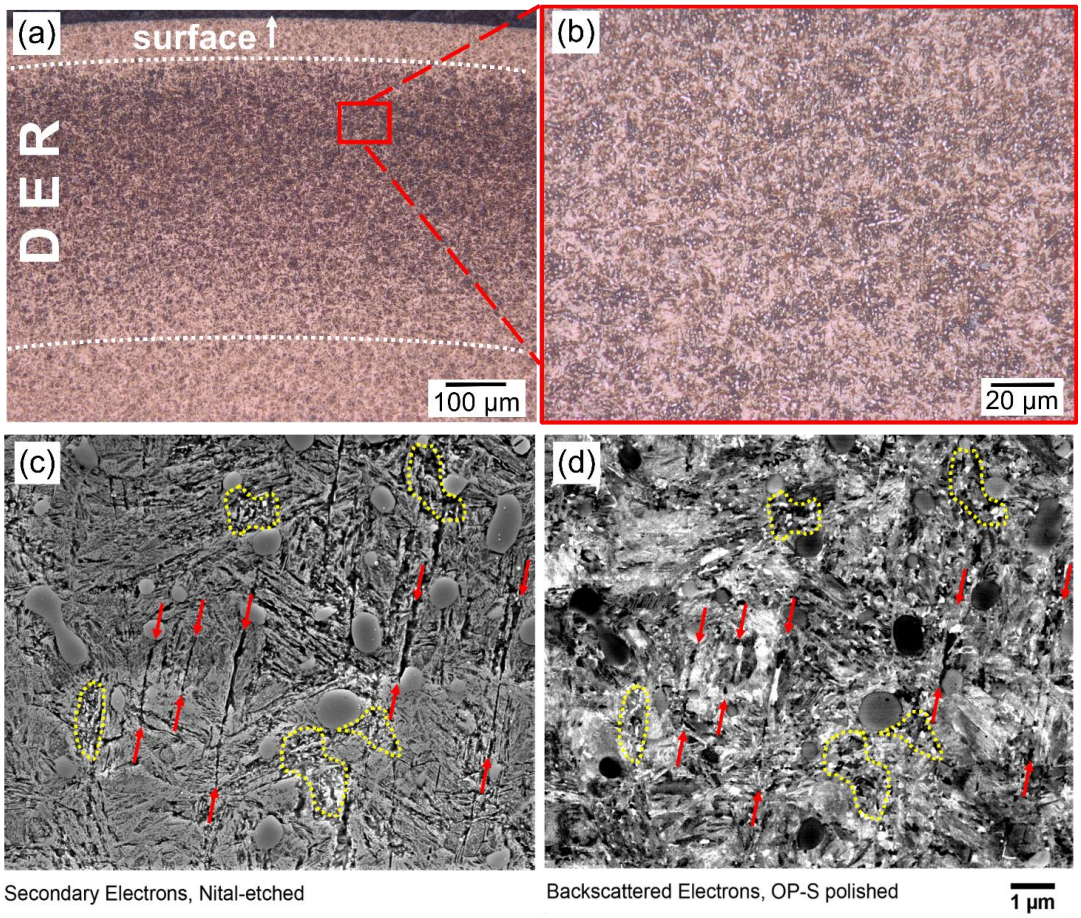

Figure 4.8: Images of DER: (a), (b) viewed with LOM (Nital etched), (c) viewed with SE SEM (Nital etched); (d) viewed with BSE SEM (OP-S polished). Elongated and equiaxed grains are marked with red and yellow, respectively.

Figure 4.9 shows the results of the combined EBSD/EDX measurement. Figure 4.9(a) shows an EBSD map of austenite and (Fe, $Cr)_3C$ carbides covering an area from the surface into depth of 200 µm below the surface. It can be seen that the amount of retained austenite is reduced considerably in the DER (from about 100 µm below the surface, corresponding to the depth at which DER starts as seen in Figure 4.8(a)) compared with that in the steel matrix. In contrast, the distribution of primary spheroidised carbides is seen to be homogeneous over the depth of the measured area.

The EDX analyses show a high concentration of carbon and chromium in the primary spheroidised carbides and a homogeneous distribution of carbon in the matrix surrounding the carbides, see Figure 4.9(b). A slightly inhomogeneous chromium distribution in the matrix of the DER is also observed, where chromium-

depleted regions appear around clusters of primary spheroidised carbides. However, both carbon and chromium distributions in DER are same as that in the typical AISI 52100 bearing steel microstructure, shown in Figure 4.5.

Both the martensitic matrix and the altered microstructure components in DER have been indexed as α-Fe (bcc), by EBSD. However, a KAM map shows slightly lower misorientation in the elongated and equiaxed grains, see Figure 4.9(c). Together with the fact that both elongated and equiaxed grains are seen to be attacked more by Nital, it is suggested that they are ferritic.

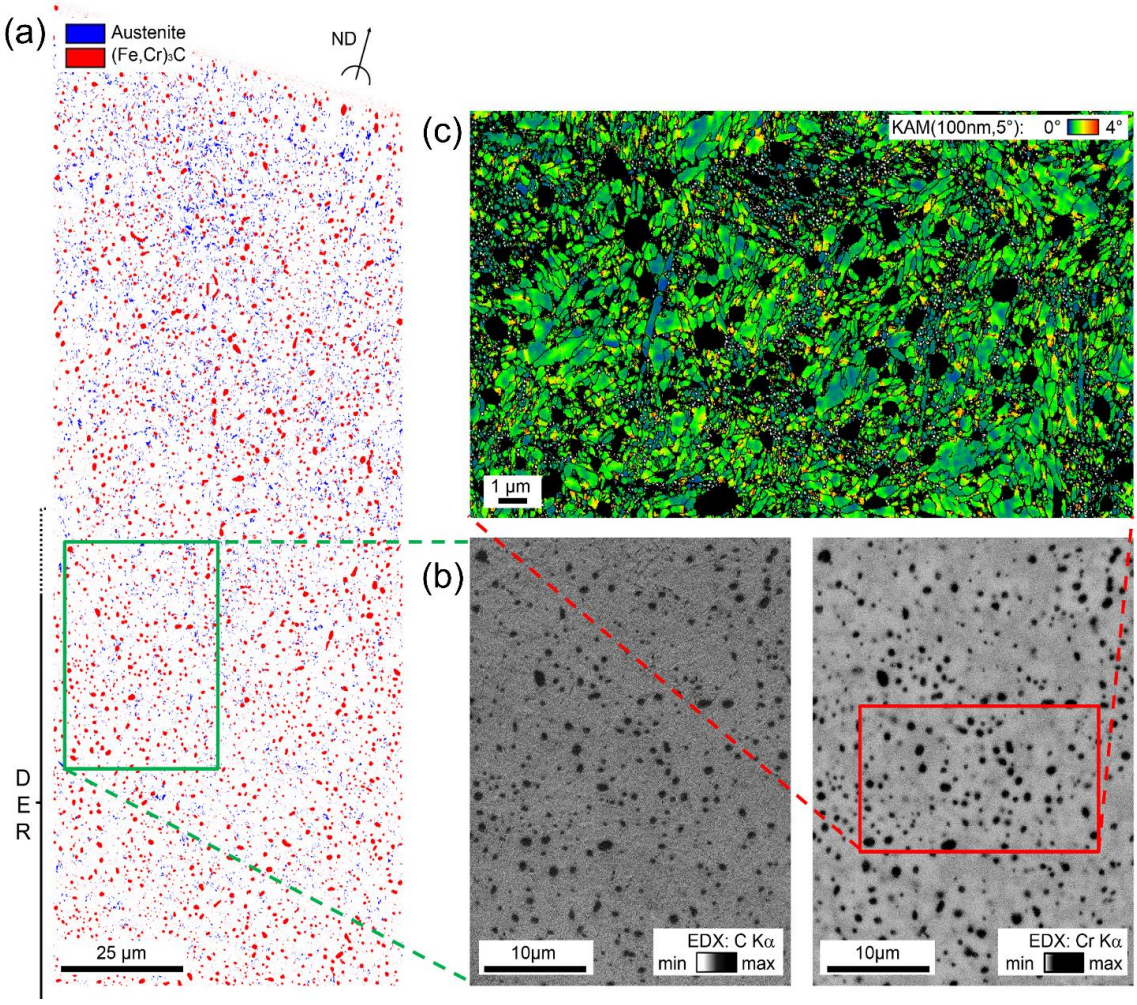

Figure 4.9: Maps of the DER: (a) An EBSD map of austenite and (Fe, Cr)$_3$C carbides covering an area from the surface into depth of 200 µm below the surface; (b) EDX maps of carbon (C-Kα) and chromium (Cr-Kα); (c) An EBSD KAM map of the points indexed as α-Fe.

SE SEM micrographs of the indents taken in an unaltered area between the surface and the DER as well as in areas with elongated and equiaxed grains within the

DER are shown in Figure 4.10. The unaltered area has an average hardness of 10 GPa (Nano Berkovich hardness) while the areas with elongated and equiaxed grains have approximately 7.5-7.9 GPa. Thus, the DER analysed in this study has a decreased hardness compared to the unaltered steel matrix. The extremely small features of the elongated and equiaxed grains have inevitably caused difficulties in performing indents at exact locations even in this study. Furthermore, it is not known how deep these grains extend and whether indents captured mostly altered microstructure or not cannot be confirmed.

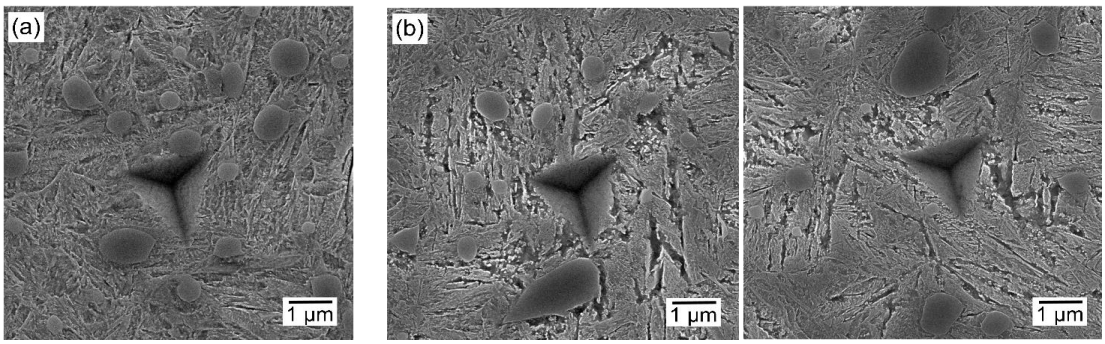

Figure 4.10: SE SEM micrographs of indents taken from specimen with DER: (a) unaltered area between surface and DER; (b) areas with presence of elongated and equiaxed grains.

4.2.2.2 Low & High Angle Bands

LABs and HABs appear orientated different depending on the cross-section viewed. They are observed as parallel bands in axial cross-section (perpendicular to the rolling direction; Figure 4.11(a)) or inclined bands in circumferential cross-sections (parallel to the rolling direction; Figure 4.11(b)) of a bearing race.

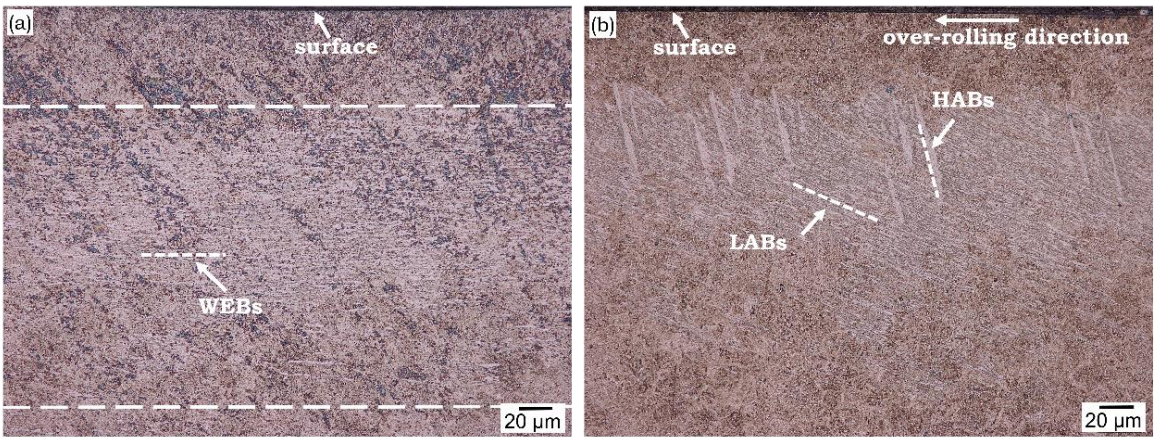

Figure 4.11: LOM micrographs of LABs and HABs in Nital etched condition: (a) in axial cross-section; (b) in circumferential cross-section.

Figure 4.12 shows the altered microstructures comprising both LABs and HABs viewed with SE SEM (Nital etched) in comparison with the EBSD IQ map and EDX maps (OP-S polished) of the same region. It can be seen that the primary spheroidised carbides have been completely disintegrated in the altered regions. Chromium from the primary spheroidised carbides was homogenised in the 30° and 80° bands region, see Figure 4.12(d). Carbon appears to be homogeneously depleted in the HABs giving lower X-ray intensities than in the martensitic parts of the unaltered matrix, see Figure 4.12(c). Similar carbon-depleted regions are seen intermixed with the carbon-rich areas among the LABs showing two different forms of etching behaviour, long grooved structures and a conchoidal surface structure mainly for the larger areas, see Figure 4.12 and Figure 4.14. The carbon-rich components show a stronger resistance to Nital etching and appear similarly unaffected by etchant as the primary spheroidised carbides in the SE SEM image. However, a closer comparison between chromium and carbon EDX maps shows that, in contrast to the primary spheroidised carbides, the carbon-rich areas are not chromium enriched. Carbon-rich areas were also detected by other researches and reported as 'rung-like carbides' [52], 'disc-shaped carbides' [54, 58], and also 'lenticular carbides' [55, 56, 69, 73, 74].

A KAM map of the features is shown in Figure 4.13. It can be seen that large parts of the altered regions appear as equiaxed grains showing considerably lower misorientations than the original matrix. Elongated grains with partly higher misorientations are also seen to be correlated with the elongated grooved structures in Figure 4.12. Together with the comparatively high IQ in the diffraction patterns, shown in Figure 4.12(b), and their etching behaviour, both components (equiaxed and elongated grains) are considered to be ferritic. These features are commonly named as cell ferrite and needle-like structures in the earlier literature.

Distinct regions marked in Figure 4.13 are shown in a high magnification SE SEM image in Figure 4.14(a), showing three different constituents in the 30° and 80° bands, i.e. equiaxed ferritic grains, elongated ferritic grains and carbon-rich areas (aka cell ferrite, needle-like structures and carbide discs in the earlier literature). A breaking-up or dissolution of the primary spheroidised carbides can be seen next to the carbon-rich areas, shown in Figure 4.14(b) with red arrows. Furthermore, intact primary spheroidised carbides are also observed in the residual area of the 30° bands, shown in Figure 4.14(b) with yellow arrows.

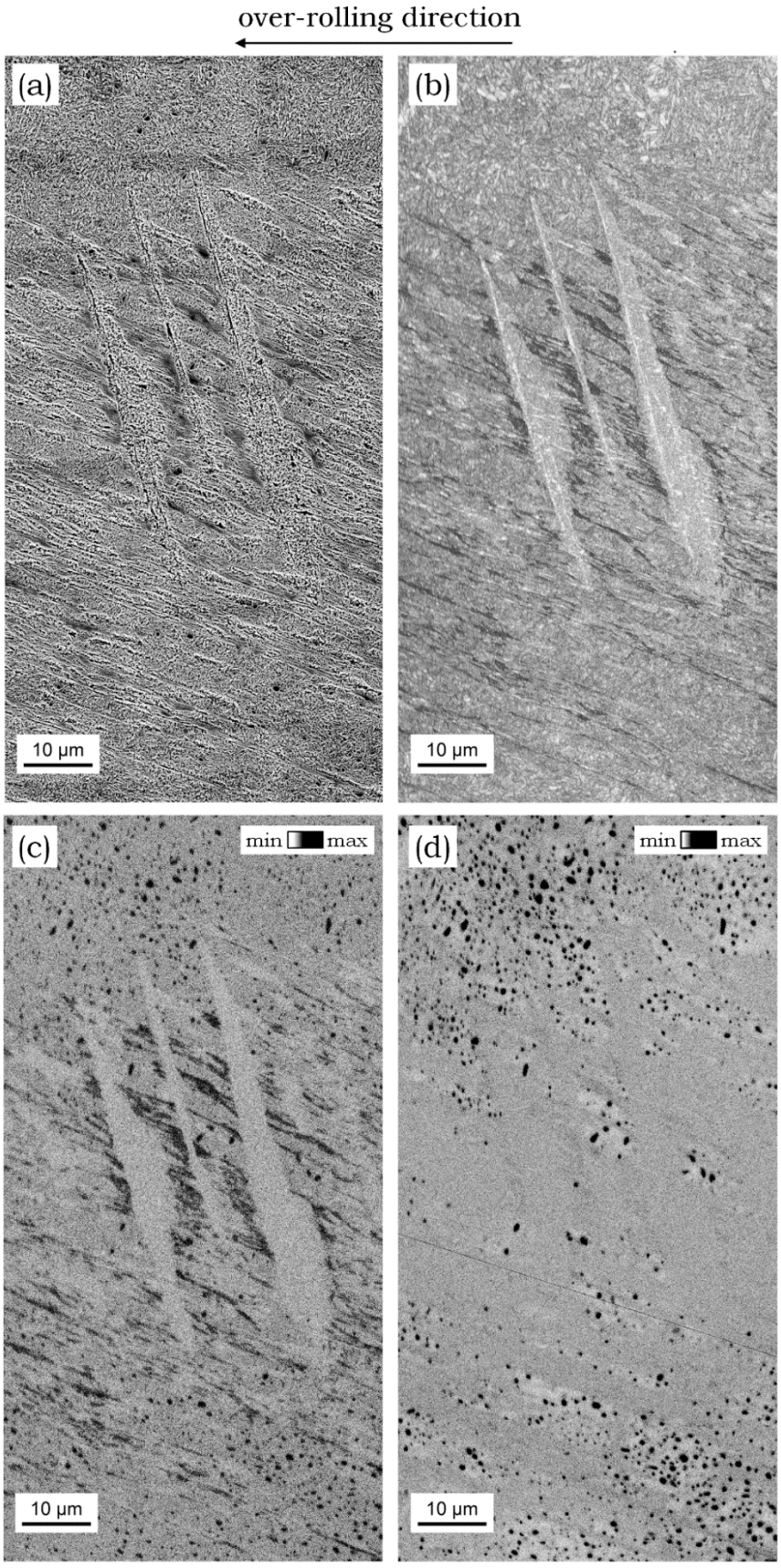

Figure 4.12: A region showing 30° and 80° bands: (a) SE SEM image (Nital etched); (b) IQ map; (c) EDX Carbon map; (d) EDX Chromium map.

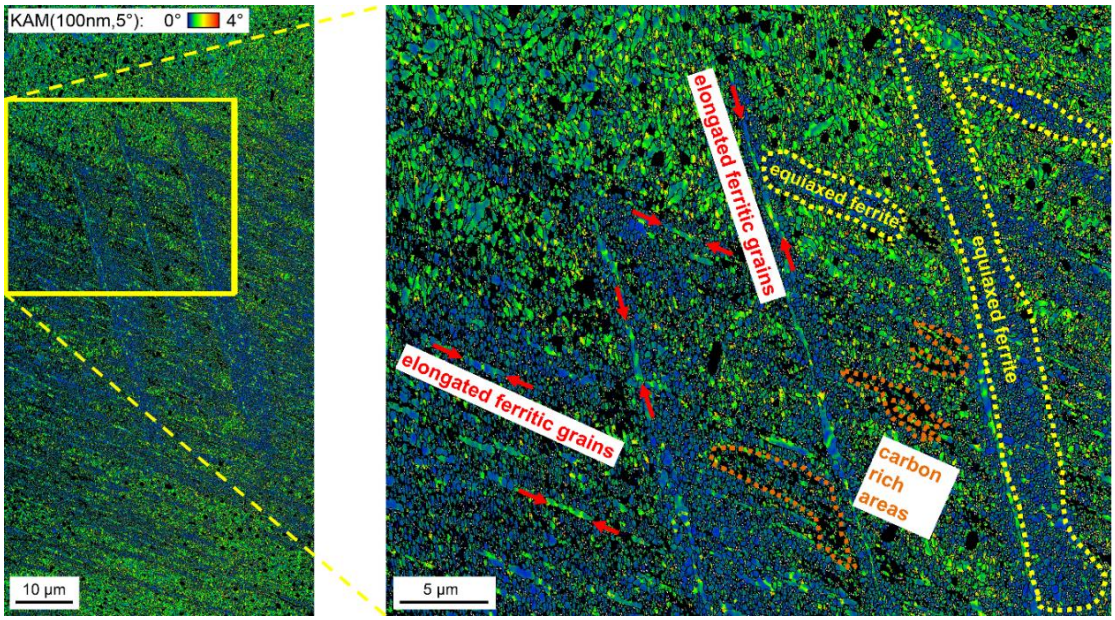

Figure 4.13: A KAM map of the area in Figure 4.12 for the points indexed as α-Fe.

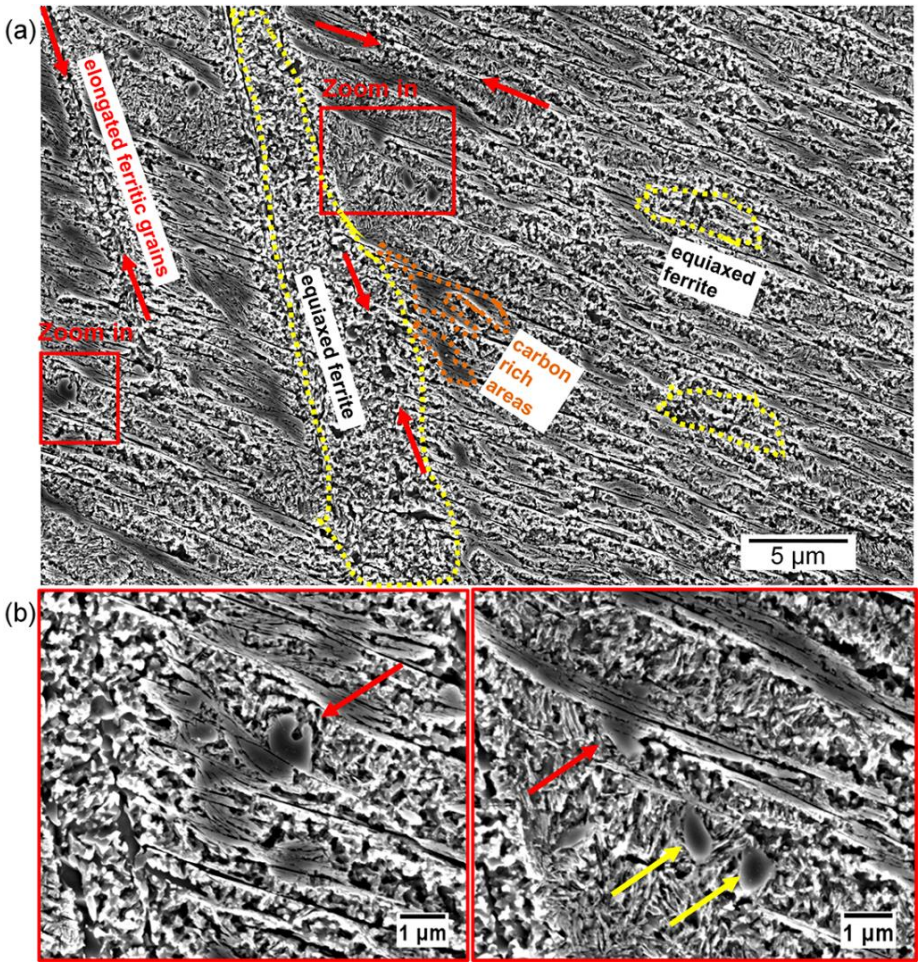

Figure 4.14: High magnification SE SEM (Nital etched) micrographs of 30° and 80° features showing: (a) main constituents; (b) zoom in examples of the dissolving carbides (red arrows) and intact carbides (yellow arrows).

In order to further investigate the carbon-rich component in the altered region, TEM analysis has been performed on a FIB lamella that was cut across 30° bands, see Figure 4.15. The equiaxed grains intermixed with disc-like structures are clearly seen in the dark field micrograph in Figure 4.15(a). Figure 4.15(b) shows morphology of one of the disc-like carbon-rich structure that appeared to consist of regular rectangular blocks of different widths, similar to what has been reported earlier in the literature [37, 58]. A high carbon content is observed in the disc-like structure (shown in Figure 4.15(c)) that is in accordance with earlier observations by SEM/EBSD/EDX (Figure 4.12). However, the diffraction pattern of carbon-rich disc-like structure (Figure 4.15(d)) shows that it is too complex to be unambiguously indexed, nevertheless it is clearly observed that features are not nanocrystalline.

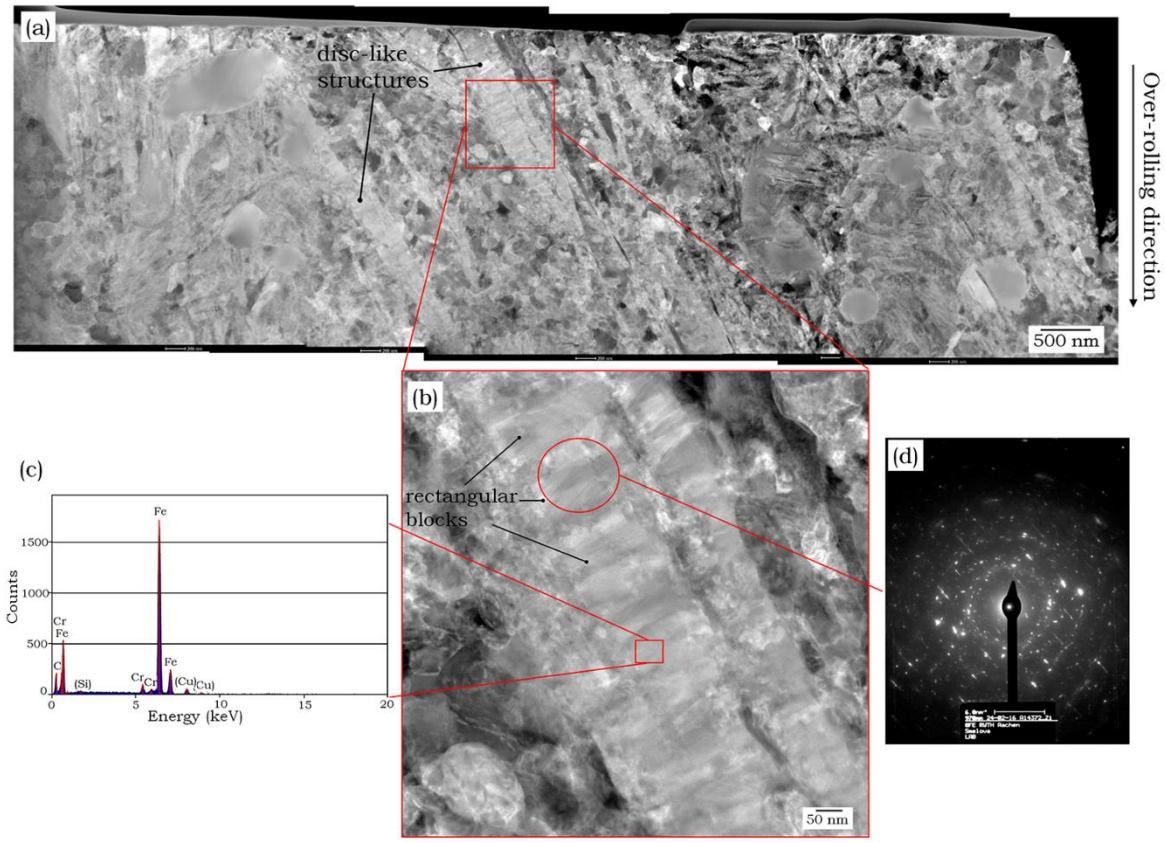

Figure 4.15: TEM analysis of 30° bands: (a) panorama of DF images covering the entire FIB lamella showing carbon-discs and equiaxed grains; (b) higher magnification carbon-disc with rectangular block morphology; (c) EDX spectrum on disc-like structures; (d) SAED pattern on disc-like structure. The raceway is parallel to the right side of the image with rolling approximately in vertical direction.

Figure 4.16 presents an SE SEM image of the microindents performed on the features of the 30° and 80° bands. Hardness measurements were also performed on an unaltered region between the surface and the start of the altered region. The average hardness of the unaltered region is 7.76 GPa (Nano Berkovich hardness) and the equiaxed ferritic grains (marked as A in Figure 4.16) and carbon-rich areas (marked as B in Figure 4.16) have an average hardness of 4.2-6 GPa and 9-11 GPa, respectively. Hence, the hardness is found to be decreased in regions with equiaxed ferritic grains but increased in regions with carbon-rich areas. These changes are thought to be a result of the grain size variation, crystallography and chemical composition.

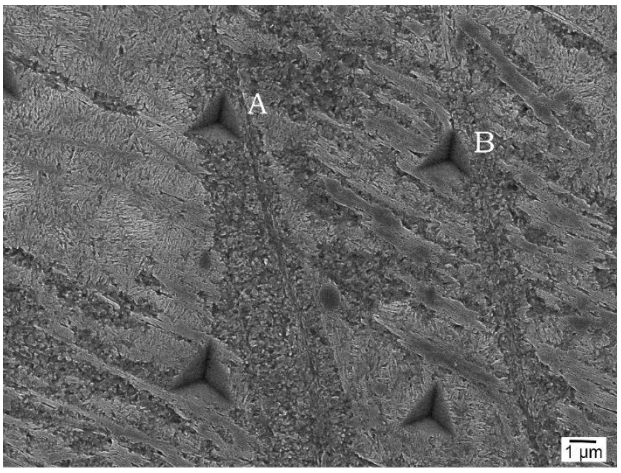

Figure 4.16: An SE SEM image of the microindents performed on the features of the 30° and 80° bands. A: equiaxed ferritic grains; B: carbon-rich areas.

Figure 4.17 shows IPF maps with respect to the local normal direction (ND) during bearing rolling for the DER and 30° and 80° bands. For easier observation, only newly formed grains in DER (i.e. α-Fe grains with CI>0.1 and grain orientation spread less than 0.3°) have been plotted on IPF map shown in Figure 4.17(a). It is clearly visible that the density of newly formed grains increases with the depth of the DER, which correlates with the earlier observations by SEM and EBSD. The blue/purple colour appearance indicates that the newly formed grains have a strong orientation with <111> axis parallel to the normal direction.

Distinct texture of an altered region of 30° and 80° bands is clearly observable in comparison to the initial base material as seen at the top of the image in Figure 4.17(b). The uniformed blue colour appearance also indicates that the elongated and equiaxed grains have very homogeneous crystal orientations. As it can be seen,

for a high number of grains a <111> axis is aligned with the normal direction of the bearing rolling.

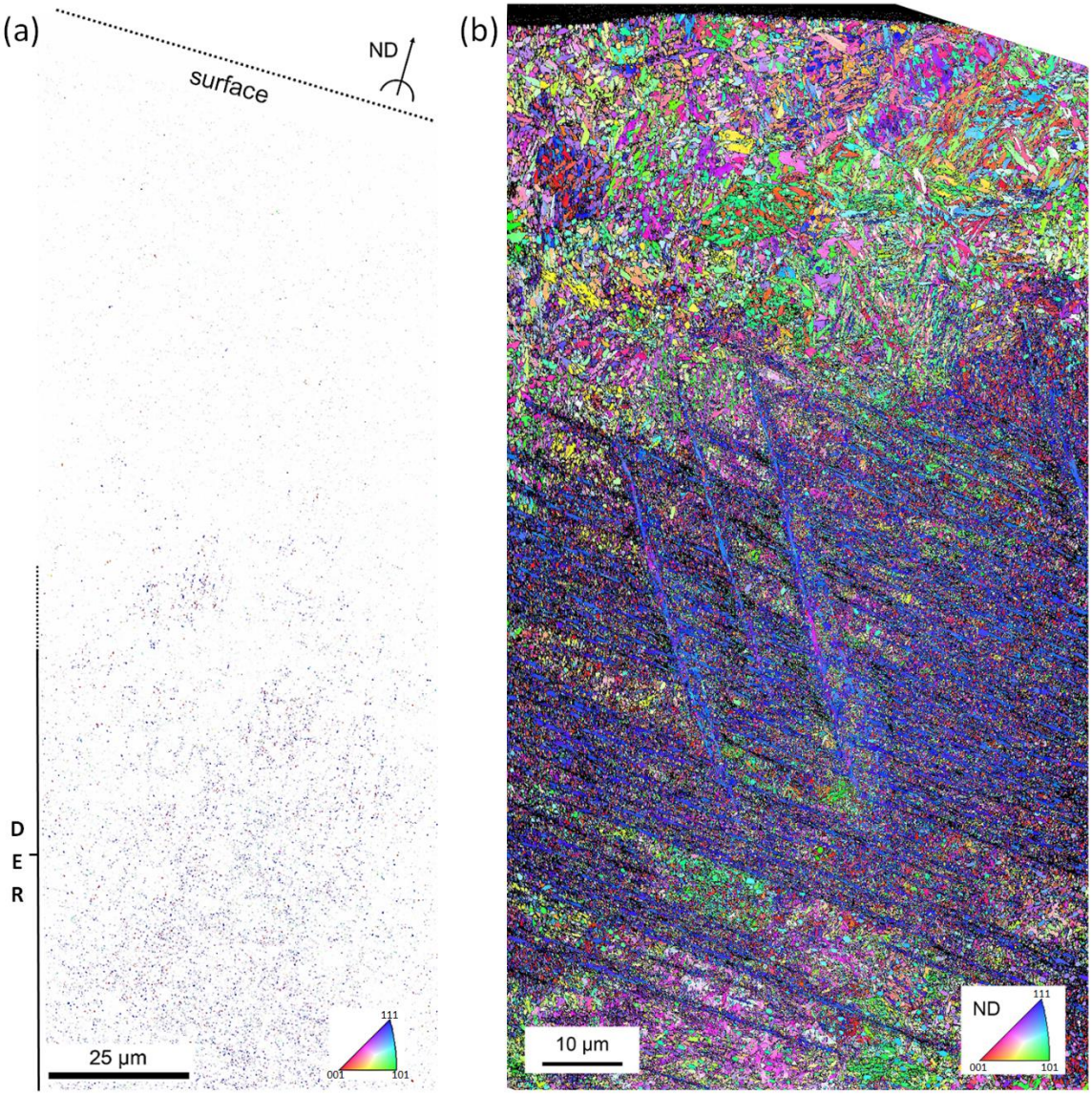

Figure 4.17: IPF maps with respect to the normal direction during bearing rolling: (a) for newly formed grains during DER formation; (b) for the all indexed points in LABs/HABs sample.

4.2.3 Discussions

Fully formed DER and WEBs in through-hardened martensitic AISI 52100 from failed bearings have been analysed using a range of characterisation and analysis methods. Comparing with the virgin material, newly formed equiaxed and elongated ferritic grains have been observed in the DER, which is however different from that reported in literature, e.g. only groups of parallel ferritic discs of 0.05-0.1 µm thickness and 1 µm width intermixed with residual martensite have

been observed in [52, 54, 57, 58]. The low misorientation, the occurrence of HAGBs between the grains, and the pronounced texture of these components suggest that newly formed grains in DER are products of recrystallisation processes, possibly by dynamic recrystallisation, in the material. The stress state, at which these alterations occur can be narrowed down by the distribution of primary spheroidised carbides and retained austenite. The primary spheroidised carbides are found chemically as well as crystallographically unaltered, whereas the retained austenite has been destroyed and transformed into martensite in the altered region. However, how far the austenite decomposition and how this relates to the subsequent alterations are unclear since the amount of retained austenite detected in the sample of the typical AISI 52100 bearing steel after metallographic preparation was rather unusually high.

In the EBSD/EDX measurements of the DER, carbon or chromium redistribution has not been observed. However, due to the very small recrystallised structures observed at this stage, it is suspected that redistribution may have happened but at scales below the spatial resolution of EDX under the given conditions. This recrystallisation could be the starting point of a chain of microstructure alterations during RCF but unfortunately, it was not possible to confirm due to the limitations of the specimens being analysed. It is possible that some martensite decay has happened before the observed recrystallisation as has been suggested repeatedly by others [52, 57, 63, 67, 77], however, was not captured.

In the later stages of RCF after 30° and 80° bands have formed, the primary spheroidised carbides are shown to have been destroyed. Equiaxed and elongated ferritic grains similar to those in the DER stage have been observed but with considerably larger grain sizes, indicating a continuous growth of the microstructure alterations and formation of ferrite crystals from the DER to WEBs stages.

The EDX maps of the 30° and 80° bands have shown a clear redistribution of the carbon and chromium elements. The chromium released by the destroyed primary spheroidised carbides is compatible with the bcc lattice of the growing ferrite and has been incorporated into the newly formed crystal structures, leading to a chromium homogenisation in the altered regions, independent of the 30° or 80° orientation. The carbon released by the carbides, however, is incompatible with the bcc lattice and is pushed out of the regions in which recrystallised ferrite grains

grow. It is, however, not clear whether or how much elevated temperature plays a role in the recrystallisation that has affected the carbon migration. It has also been suggested that a transformation that is thermodynamically improbable could still take place after more than 10 million cycles of high cyclic stresses, hence stress-induced carbon diffusion, though negligible during each cycle, can be of importance over millions of rolling contact cycles [52, 57, 73]. Carbon finally accumulates between the equiaxed regions of the 30° features and close to the corners where 30° and 80° bands intersect, forming carbon-rich areas, possibly in carbidic structures as being repeatedly suggested in literature [52, 54-56, 58, 69, 73, 74]. The size of the high carbon intensity areas is larger than the size of typical primary spheroidised $(Fe, Cr)_3C$ carbides, together with it block-like appearance and the fact that such carbon-rich areas are not chromium enriched, suggest that disc-like carbon-rich areas are not formed due to flattening of primary spheroidised carbides as suggested by [69]. Furthermore, homogeneous chromium distribution suggests that the primary spheroidised $(Fe, Cr)_3C$ carbides must have been disintegrated completely at this stage and sufficient time has been available for the chromium to diffuse and homogenise in the altered microstructure of LABs and HABs.

For elongated grains, in both of the 30° and 80° orientations, a <111> axis is found to lie close to the normal direction during the bearing rolling, which is similar to that have been found among the recrystallised equiaxed ferritic grains. Additionally, for the elongated grains in both 30° and 80° bands, a <111> axis lying in a {112} plane was reported to be aligned with the long shape-axis of the grains [159]. This suggests that the elongated grains are equiaxed grains in a suitable orientation, which glide on a {112} <111> slip system and become elongated [159].

All the microstructure alterations discussed here were created under controlled rolling conditions that have led to the formation of geometrically well-arranged features. It is noteworthy to mention that, in the fully developed 30° and 80° features, nanocrystalline components, similar to those found in the non-classical bearing failure due to WECs, have not been observed. More detailed comparison between DER, LAB/HABs and WECs are given in subchapter 4.4 after the results on WECs are presented.

4.3 White Etching Cracks

4.3.1 Experimental Methods

A cylindrical roller bearing of N216 type removed from the service screw compressor due to inner race surface spalling has been used in this study to investigate microstructural alterations in the bearing steel. The bearing had run for 18 000 hours at a rotating speed of 4285 rpm and was lubricated with PAO 68 oil (ISO VG 68, kinematic viscosity 60-70 mm^2/s). This resulted in approx. 48642 million load cycles on the inner ring (see Appendix B for calculations).

The chemical composition of the steel is shown in Table 4.3, analysed by Sheffield Assay Office using an inductively coupled plasma optical emission spectrometry. The elements carbon and sulphur were determined using combustion analysis.

Table 4.3: Chemical composition of the WECs specimen, wt%.

C	Cr	Si	Cu	Mn	Al	Sn	Ni	Mo	S	P	Co	Zn
0.944	1.65	0.20	0.20	0.37	0.03	0.01	0.16	0.03	0.005		<0.01	

4.3.2 Results

Figure 4.18 shows a LOM image of a WECs network found in the subsurface of the bearing raceway that has been examined in this study. The section of the WECs shown in this image appears to have no connection to the surface in this section and it extends from approximately 50 to 600 μm below the contact surface. No 3D serial sectioning has been performed to confirm whether the WECs network is entirely subsurface or if the surface has been reached in the other section.

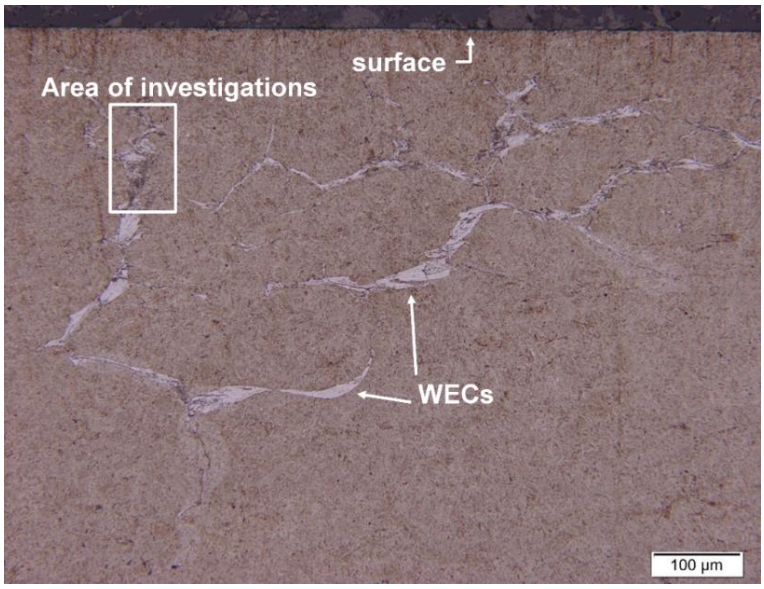

Figure 4.18: an LOM micrograph of WECs in circumferential cross-section (Nital-etched). The area for further investigations is marked with a rectangle.

An area (marked by the rectangle in Figure 4.18) of the WECs network has been chosen to be examined under SEM with SE and BSE imaging to reveal microstructural changes in the WECs and the results are shown in Figure 4.19. Extensive microstructure alterations are seen with only relatively small microcracks detected by the BSE SEM imaging on the OP-S polished specimen, shown in Figure 4.19 with white arrows pointing to the cracks observed. It is also evident that the WEA consists of four other constituents (which do not necessarily appear white in LOM after Nital etching), including coarse, fine, nanocrystalline and elongated grains marked in both the SE and BSE SEM images. The elongated dark features, appeared as deep grooves in the SE SEM (Nital etched), are clearly shown as elongated grains in BSE SEM (OP-S polished) shown in Figure 4.19, where selected areas of elongated grains are marked with red arrows. The elongated grains appear to be in the middle or close to the edge of the WEA as opposed to the findings presented by [100], where similar grains have been found next to cracks. While groups of parallel-elongated grains are seen in WEA, a uniform direction of grain growth comparable to the directional growth in WEBs during RCF, has not been observed. Different size grains in the WEA appear to be randomly distributed and do not have any correlation with the crack or any other features in the WEC. Primary spheroidised carbides are not observed in the WEC area.

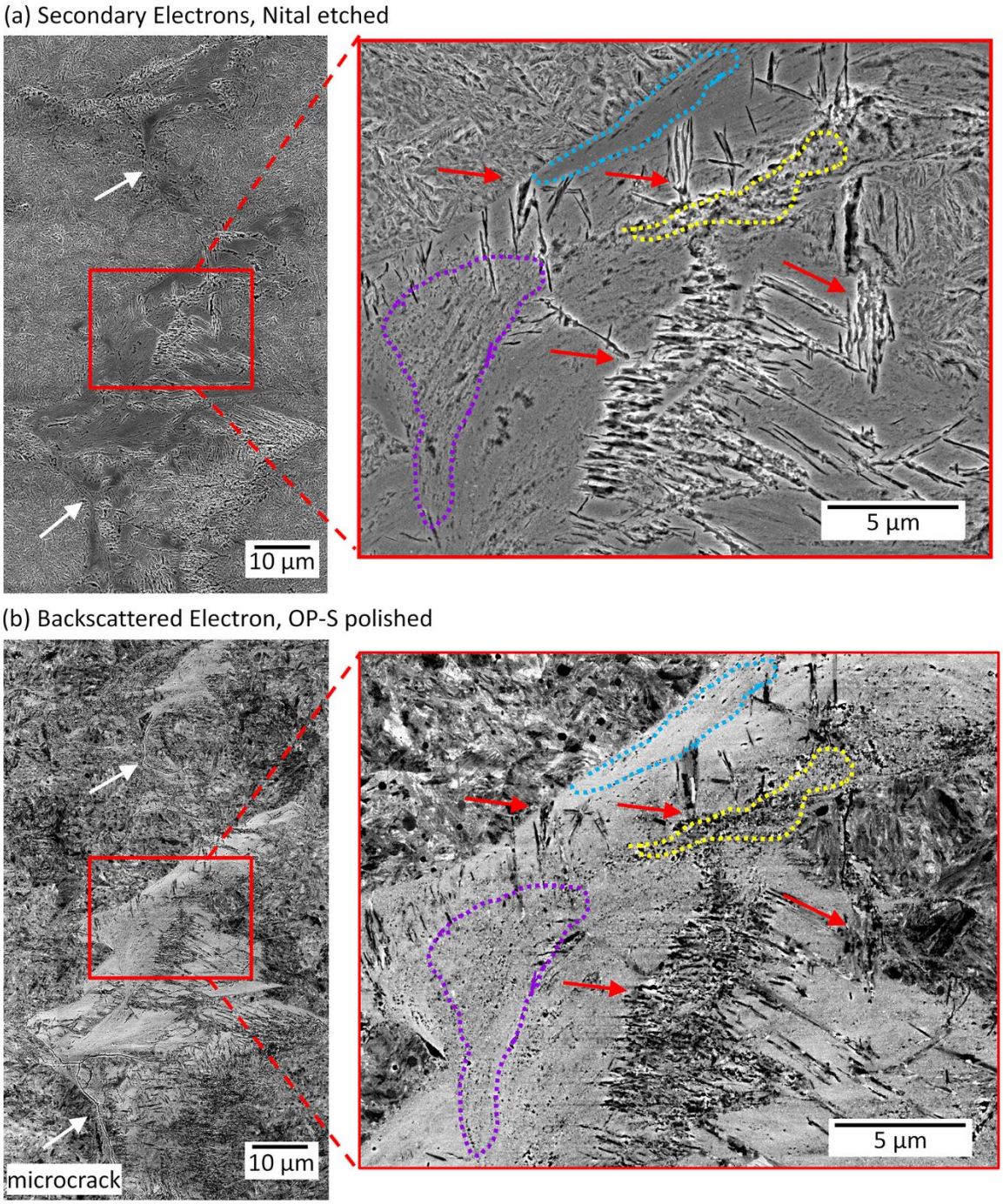

Figure 4.19: SEM images of the same area in the WEA attained by: (a) SE imaging in Nital-etched condition; (b) BSE imaging in OP-S polished condition. Examples of coarse, fine, nanocrystalline and elongated grains are marked with yellow, purple, blue dash line and red arrow respectively. Microcracks are marked with white arrow.

Figure 4.20 shows EBSD and EDX maps of the region shown in Figure 4.19, including an IQ map (Figure 4.20(a)), a map displaying the non martensite-martensite HAGBs (Figure 4.20(b)), a chromium EDX map (Figure 4.20(c)) and

carbon EDX map (Figure 4.20(d)). The nanocrystalline regions of the WEA are usually too fine to produce a good EBSD pattern, therefore they appear black/dark in the IQ map shown in Figure 4.20(a) or blue in the non martensite-martensite HAGBs shown in Figure 4.20(b). However, the large regions of coarser equiaxed and elongated grains embedded within these nanocrystalline areas show comparatively high IQ values. Figure 4.20(b) shows the non martensite-martensite HAGBs that correspond only to the boundaries of the prior-austenite grains in the unaltered steel matrix. However, around the WEC, a large amount of newly formed HAGBs, which do not have their origin in a martensitic transformation, are found. The overall extension of these HAGBs clearly coincides with the size of the microstructurally altered region.

For comparison, the chromium and carbon distributions measured by EDX during the EBSD scan in the energy ranges of Cr-Kα and C-Kα are shown in Figure 4.20(c) and Figure 4.20(d). In the unaltered matrix, primary carbides are clearly shown as higher x-ray intensities in both Cr-Kα and C-Kα energy ranges. In comparison, in the microstructurally altered region, no similar high intensity spots are seen. In the chromium map, the altered area shows more or less homogeneous intensities. In the carbon map some high-intensity areas within the altered region are detected and the average intensity in the altered area is slightly lower than that in the unaltered matrix. Since the detection of low energy X-rays is challenging at the scanning speed of an EBSD scan, the maps appear to be noisy and the count rates can only be evaluated statistically. A 13% drop for carbon and a 3% drop for chromium have been found by comparing the accumulated X-ray intensities over areas of 10 μm by 10 μm around positions 1 and 2 marked in Figure 4.20(d). In order to understand the causes of the inhomogeneous carbon intensities within the altered region, TEM analysis has been conducted on lamellae cut along the red lines shown in Figure 4.20(d).

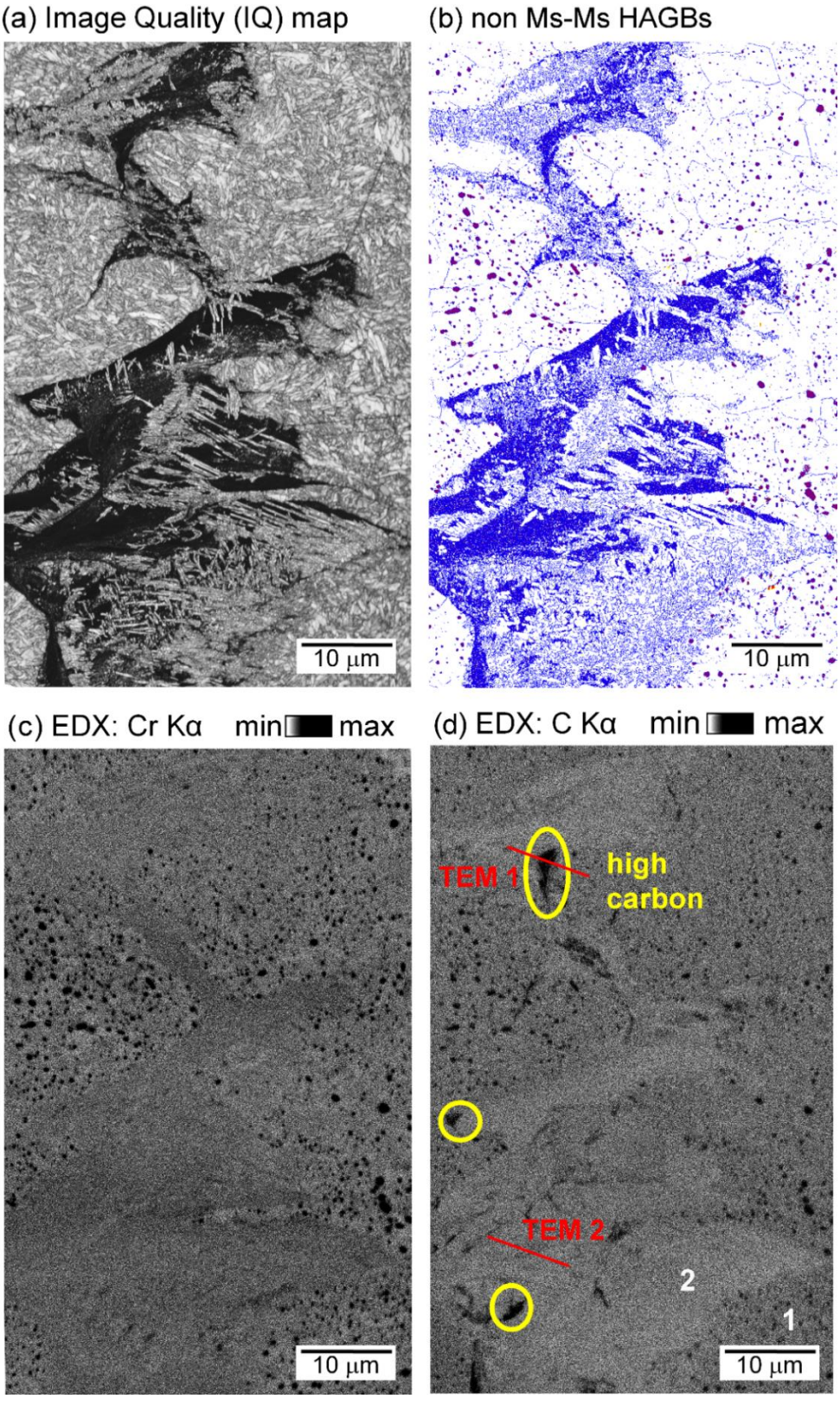

Figure 4.20: EBSD/EDX maps of the WEC: (a) IQ map; (b) non martensite-martensite HAGBs map; (c) chromium map; (d) carbon map with marked carbon-rich areas, positions of the TEM lamellae, and positions '1' and '2' discussed in the text.

From the EBSD scan, a KAM map has been obtained to get more details about the misorientations in the indexed part of the WEA, shown in Figure 4.21. It can be seen that the equiaxed grains and elongated grains have slightly lower misorientations than those in the initial matrix. Together with the HAGBs shown in Figure 4.20(b), it is suggested that recrystallisation has taken place in the WEA. The dark/black regions appeared in Figure 4.21 are areas of the unindexed WEA, where the grains are too small to give unambiguously indexable EBSD patterns.

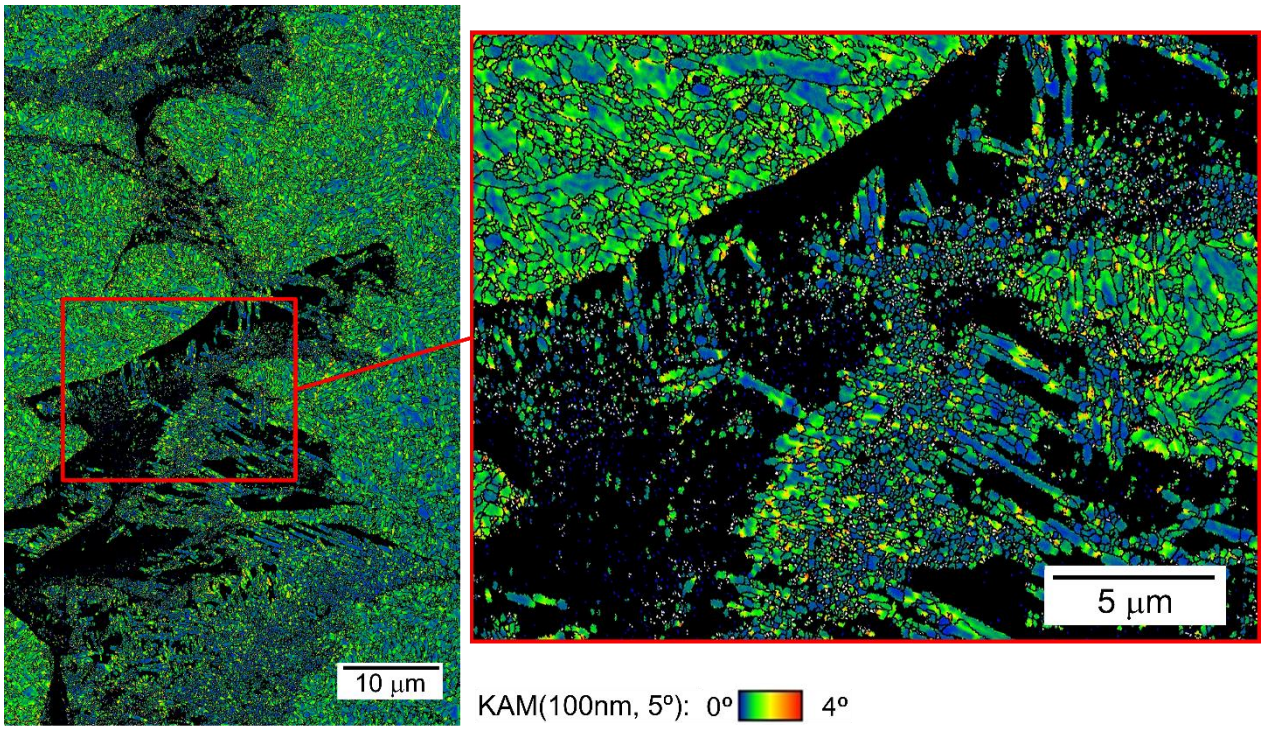

Figure 4.21: An EBSD KAM map of WEA for the points indexed as α-Fe, γ-Fe and $(Fe, Cr)_3C$ carbides.

IPF maps of the WEC area with respect to the rolling normal direction are plotted in Figure 4.22. Figure 4.22(a) shows an IPF map for all points indexed with CI>0.1; Figure 4.22(b) shows IPF map for bcc grains in altered region with grain size less than 250 nm; and Figure 4.22(c) shows IPF map for bcc grains in altered region with grain size more than 300 nm and aspect ratio less than 0.5. The grain parameters provide a clear separation between the equiaxed and elongated grains based on observations of the two types of grains. The indexable crystallites within the altered region appear to be present in clusters of preferred orientations, which, do not show any correlation with the prior-austenite grains of the martensitic matrix, see Figure 4.22(a). The altered microstructure components show

similarities in the preferred crystal orientation within each cluster but their crystal and shape orientation change from one cluster to another, see Figure 4.22(b&c).

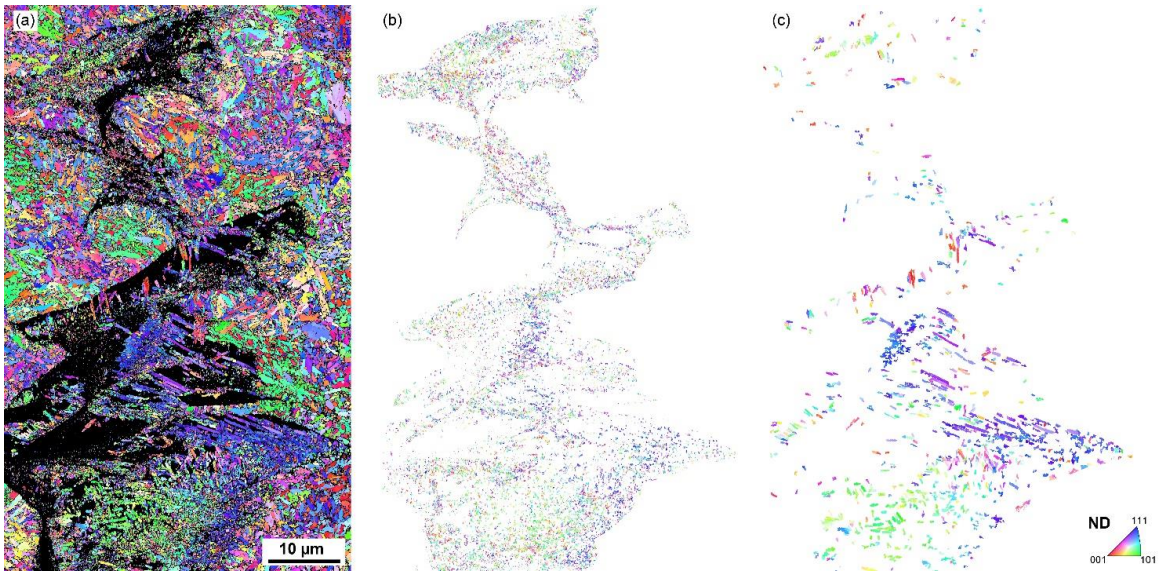

Figure 4.22: IPF maps with respect to the rolling normal direction: (a) all points indexed with CI>0.1; (b) bcc grains in altered region with grain size <250 nm; (c) bcc grains in altered region with grain size >300 nm and aspect ratio <0.5.

Figure 4.23 shows DF TEM images and corresponding SAED patterns for the two TEM lamella cuts at the positions shown in Figure 4.20(d). D-values and lattice constant for the TEM lamella 2, corresponding to low C-Kα intensity area, was calculated and was found to be compatible with a pure iron bcc crystal structure. Similar ring patterns have been reported in literature [17, 114, 115] for typical nanocrystalline WEA. This also agrees with recent APT results in [45, 46], which found a carbon segregation with carbon present at grain boundaries rather than in ferrite grains, hence lattice constant is the same as for pure ferrite [118, 124].

The SAED pattern of the TEM lamella 1, corresponding to the high C-Kα intensity area, clearly shows additional rings, suggesting a more complex phase or a mixture of phases in this region. Two different phases have been identified from SAED pattern, corresponding to bcc and hexagonal crystal structures. D-values and intensities of the reflexes corresponding to hexagonal crystal structure match with the space group $P6_3/mmc$ and M_2C (M stands for metal) crystal structure. This suggests that a mixture of typical WEA and newly formed carbidic structures is present in this area. In contrast to the primary spheroidised carbides in the unaltered matrix, the areas with high C-Kα intensities do not show an elevated

chromium content, which also indicates that they are not just ground primary spheroidised $(Fe, Cr)_3C$ carbides, but rather newly formed carbidic structures.

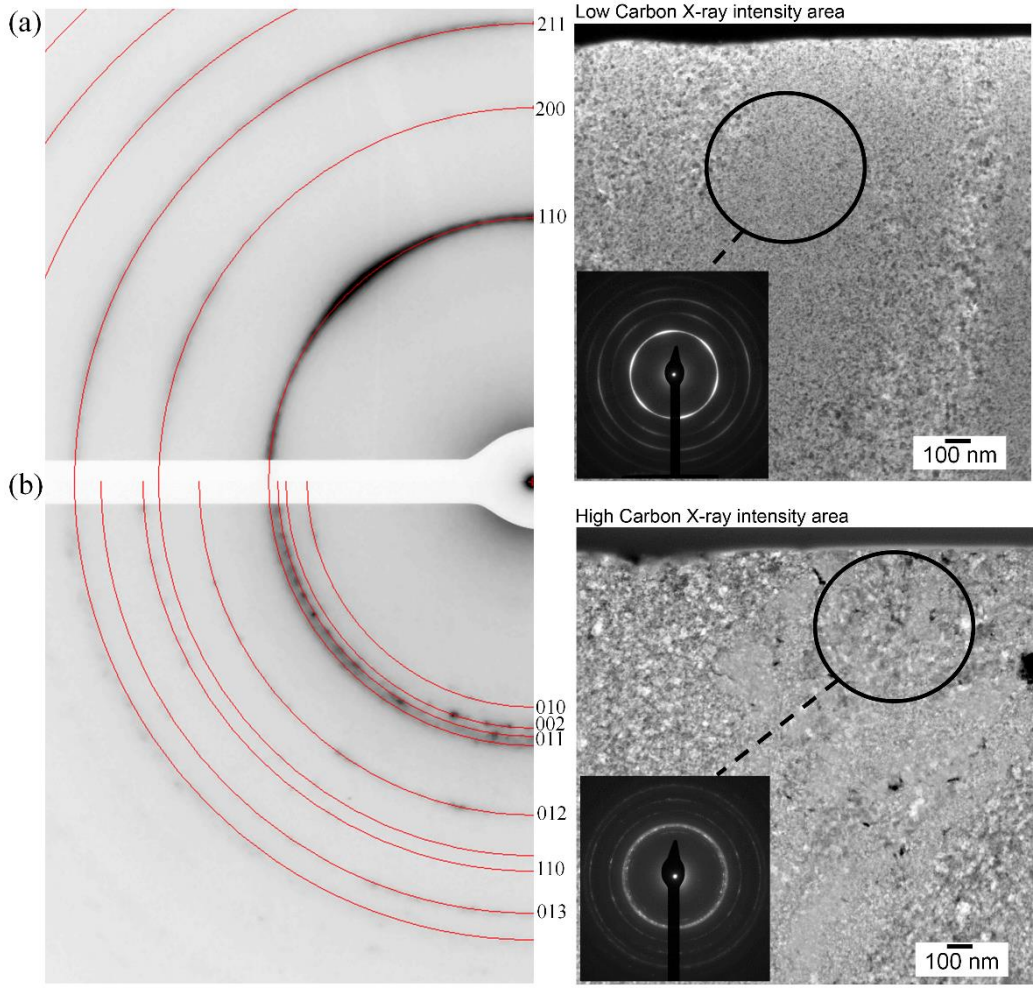

Figure 4.23: DF TEM images and corresponding SAED patterns of: (a) low carbon X-ray intensity area in the WEA (TEM 2) with typical bcc ring pattern; (b) high carbon X-ray intensity area in the WEA (TEM 1) with ring pattern showing mixture of bcc and hexagonal crystal structures.

Exemplary SEM images of nanoindents in four different regions are shown in Figure 4.24. Analysis of multi nanoindents in unaltered matrix has shown an average hardness of 900 HV0.001 with a standard deviation, σ, of 36 HV0.001. For the altered microstructures, however, each indented position is different due to slightly varied nanostructures and the difficulties in capturing exact the same features in two indents, thus individual local hardness values are presented. In the regions with coarse equiaxed and elongated grains (Figure 4.24(b)) the material is softer than the unaltered steel matrix (Figure 4.24(a)), while in the regions with finer grain (Figure 4.24(c)) and especially with the nanocrystalline structures

(Figure 4.24(d)) the materials are considerably harder than the unaltered martensitic matrix. All three reported values differ more than 3σ from the average matrix hardness and have to be considered as significant. It should be noted that different hardness measurement methods have been used for WEC altered microstructure compared to RCF features, which result in unreliable hardness unit conversion due to the ISE [157]. However, absolute hardness values of the individual altered features observed in WEC and RCF are not intended to be compared in this study.

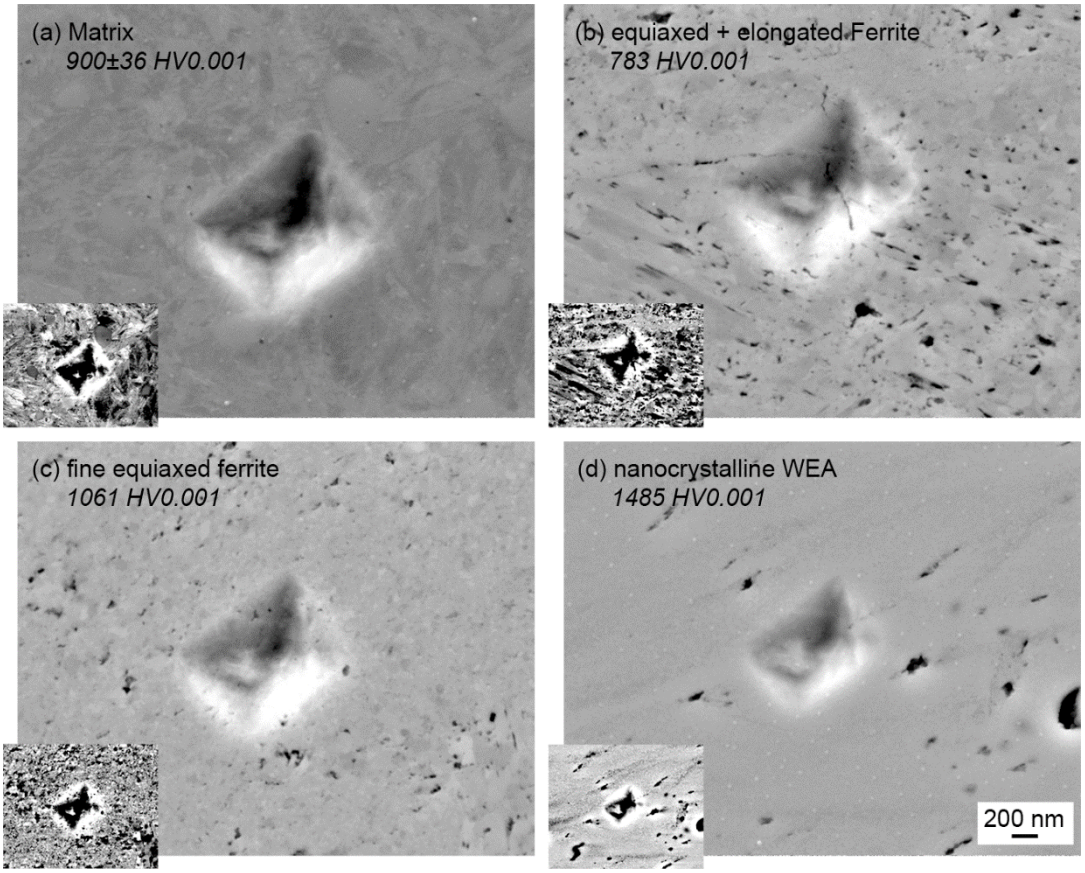

Figure 4.24: Nano-hardness indents with an applied force of 10 mN into the different microstructural components. Large images: SE images, small images: BSE images of the same region.

4.3.3 Discussions

In addition to the features reported in literature, this study has revealed that the analysed part of the WEC contains relatively small microcracks with extensive microstructural alterations known as WEA, but in fact consisting of elongated and varied size grains, which are typically located on one side of the microcrack (Figure

4.19). The relatively big altered area with small microcracks and the fact that the microstructure alteration only appears on one side of the crack suggest that the microstructural transformation does not occur due to rubbing of the crack faces [92, 95, 122]. Although it could be possible that microcracks formed initially, led to microstructure alteration due to face rubbing then closed under pressure, it has not been possible to confirm if or at which point what happened, since the analysis has been conducted on fully developed WECs. A time-resolved analysis on WEC formation has been conducted to further investigate these issues and the results are presented in Chapter 5.

This study has shown that the WEA microstructure consists of multiple constituents including equiaxed grains of various sizes and elongated grains (Figure 4.19). Irregular zones of coarser grains and elongated grains in WEAs from vacuum pump bearings have also been reported previously [100], where elongated grains were found to grow preferentially from the crack into the altered region. It was proposed that elongated grains grow as a result of a higher temperature due to internal friction and plastic deformation at the vicinity of cracks [100]. In this study, however, elongated grains have been seen in the altered regions: in the middle and close to boundaries of the material matrix. This suggests that different causes for the growth of elongated grains may exist. The findings on the low misorientation of the equiaxed and elongated grains in combination with the occurrence of new non-martensitic HAGBs from this study suggest that recrystallisation processes have occurred at some point during the microstructural alteration process. It is however difficult to explain the formation of the elongated grains, but it can be seen that the clustered crystal orientations differ from the appearance of the martensitic microstructure. For example, comparing the size of the blue/green clusters of elongated grains in the lower part of the altered region in Figure 4.22(a) with the typical size of the prior-austenite grains (indicated in the unaltered matrix regions of Figure 4.20(b)) clearly show that the elongated grains are not just isolated martensite plates remaining from the dissolving initial microstructure. Such elongated grains have also been misinterpreted as defects or microcracks under SEM of Nital-etched samples in many of previous studies [11, 88, 101, 105, 113, 114, 121].

4.4 WECs vs. DER, LABs/HABs

In this section, the WEC features found in field failed bearing are compared with those found in DER, LABs and HABs due to high-stress RCF tests to understand the differences and correlations between microstructural features in WECs, DER, LABs and HABs in rolling bearings, providing links in the microstructure transformation and derive drivers for the currently unpredictable WECs failure.

Similar equiaxed and elongated ferritic grains seen in the WECs have also been observed in DER, LABs and HABs specimens. However, different from the DER, LABs and HABs, where the newly formed grains have a defined growth direction, the elongated grains in the WECs network do not show any uniform local orientation that can be directly related to the external rolling conditions. The prevailing texture of the newly formed ferritic grains in the WECs varies from cluster to cluster in the WEC network. The elongated grains in the WECs show a similar crystal orientation (Figure 4.22(c)) as those of the smaller equiaxed grains (Figure 4.22(b)), suggesting that they have similar formation mechanism.

Primary spheroidised carbides have been found to be absent in both WECs [17, 29, 63, 73, 97, 106, 110, 117, 118, 123] and LABs/HABs [52, 54, 57, 73, 159]. This has been considered to be caused by carbide dissolution or breaking-up due to severe plastic deformation, increased dislocation interaction, or grain refinement. Through the EDX analysis, redistribution of chemical elements especially the homogenisation of chromium has been observed in both WECs and LABs/HABs. Also, Diederichs et al. [100] have previously shown a chromium redistribution in WECs, however in their results higher chromium concentration has been seen close to the location of former primary spheroidised carbides. This has led to believe that the chromium may have had sufficient time to diffuse and incorporate into the bcc lattice of the newly formed grains in the WECs studied here to show a homogeneous chromium distribution.

As for the carbon redistribution, even though the measurement of carbon is generally challenging using EDX, the corresponding X-ray map shows an inhomogeneous carbon redistribution within the microstructurally altered regions in both the WECs and LABs/HABs. The high carbon intensities found for the primary spherical $(Fe, Cr)_3C$ carbides in the unaffected matrix of the WECs and LABs/HABs specimens are not seen within the altered region, suggesting that not

only the decomposition of the crystal structure has occurred but also a movement of the elements enriched in the former primary spheroidised carbides. It is interesting that elevated carbon intensity is only seen at particular locations of the altered region in the WECs specimen, often at the boundaries of the altered region. Similar high carbon intensity areas, that are strongly resistant to etchant and result in EBSD unidexable regions, have also been observed in the LABs/HABs specimen where carbon appeared to have moved from ferritic microstructure of the 80° bands and accumulated between the equiaxed regions of the 30° bands and close to the corners where 30° and 80° bands intersect. Furthermore, the comparison of the WECs accumulated carbon intensities in larger areas of 1 and 2 marked in Figure 4.20(d) shows slightly lower intensities for the altered region (marked as 2) compared to the unaltered steel matrix (marked as 1). This is contrary to the results from an APT analysis, where total carbon in a WEA is similar or higher than that in an unaffected matrix [117]. However, the area analysed using APT was extremely small and the position of APT samples was chosen based on the appearance of the area in the etched condition, in which high and low carbon x-ray intensity areas could hardly be distinguished [117]. Further analysis, for example using Electron Probe Microanalysis (EPMA) or performing several APT measurements for a better average, is thus required to clarify the carbon concentration and movement during WEA formation.

The unique feature that has been seen in WECs but not in LABs/HABs is the nanocrystalline material with grains at about 10 nm sizes observed in the TEM [30]. Whereas the TEM analysis of the low carbon intensity position yielded the typical nanocrystalline bcc structure, the corresponding analysis of the elevated carbon intensity area in the WEC shows a mixture of the nanocrystalline bcc and newly formed also nanocrystalline M_2C (M stands for metal) structures, therefore, reconfirms the differences observed in the EDX carbon map. This mixture of two nanocrystalline phases in WEC is different to the crystal structure of high carbon intensity areas seen in the LABs/HABs that is a complex but not nanocrystalline structure.

Hardness heterogenisation has been observed in the WECs specimens for the first time in this study through the nanohardness analyses, shown in Figure 4.24. The hardness in regions of fine equiaxed grains and nanocrystalline areas is found to be considerably higher than that in the steel matrix (i.e. 18% and 65% increase, respectively). However, in regions with coarser equiaxed and elongated grains, the

material is found to be softer than the initial matrix (i.e. 13% decrease). Similar hardness variations were observed in LABs/HABs, where areas with high carbon X-ray intensities appear to have higher hardness, whereas equiaxed and elongated grains have lower hardness than the original steel matrix. The hardness variations observed seem to be related to phase, grain size variation and carbon concentration in the relevant microstructural features.

Furthermore, the loading conditions for WEC are found to be very different from those for DER and LABs/HABs formations especially in laboratory recreation testing. In addition to the normal loading conditions for DER and LABs/HABs creation, additional loading such as electrical [142], chemical [111, 116] or others as well as environmental conditions have been used to initiate WECs in laboratories. With pure and excessive mechanical loading, the AISI 52100 through-hardened martensitic bearing steel typically fails with the formation of the DER and LABs/HABs. The additional loading and/or environmental conditions must have caused the nanocrystalline material and crack formation in WECs resulting in bearings fail at much earlier stage of their life.

Non-metallic inclusions and other stress raisers (e.g. voids, large carbides etc.) in the maximum shear stress region under bearing surfaces have been proposed to be a driver for WECs formation [13, 63, 96, 101, 130]. This, however, contradicts the fact that DER and LABs/HABs form without cracks under much higher stress conditions than that for WECs in the same AISI 52100 through-hardened martensitic bearing steel with similar cleanliness or contents of stress raisers.

4.5 Conclusions

Using a combination of SEM, EBSD, EDX, TEM and indentation techniques, this study has provided a detailed analysis on the microstructure alterations in AISI 52100 through-hardened martensitic steel including WECs, DER, 30° and 80° bands. This investigation focuses not only on the detailed analysis of the complex microstructural transformations, but also provides a comparison between the microstructure alterations in WECs and those in DER and LABs/HABs due to RCF. The main conclusions from this study are:

- Elongated and equiaxed grains of various sizes have been observed in WECs. The elongated grains appeared within the altered region of the WECs as well as at the boundary between material matrix and the altered regions.

Similar elongated and equiaxed grains have also been observed in DER and LABs/HABs. In contrast, the elongated grains in LABs/HABs have a defined growth direction related to the rolling direction, whereas those in WECs are locally defined in clusters without a global direction that can be related to the rolling conditions. Additionally, transformed grains in the LABs/HABs specimen are much larger than those observed in the DER specimen.

- The primary spheroidised iron-chromium carbides $(Fe, Cr)_3C$ are found to be unaltered within the DER, whereas no primary spheroidised carbides have been observed in WECs or LABs/HABs, suggesting that they are likely to have experienced similar stages of the microstructure alteration processes. Dissolution of primary spheroidised carbides is shown in the redistributions of carbon and chromium in the altered areas.
- Inhomogeneous carbon redistribution within the WECs network is observed in the EDX carbon map where randomly distributed localised high carbon intensity areas are also shown. While similar carbon-rich areas were observed in LABs/HABs, these areas appeared to be crystallographically different from those in WECs under TEM investigations.
- A hardness heterogenisation within the WEC has been detected using nanoindentation measurements. It was found that the hardness in regions with fine equiaxed grains and nanocrystalline structures are higher than the unaltered steel matrix, whereas the regions with coarser equiaxed and elongated grains have nanohardness lower than the unaltered steel matrix. Similar hardness heterogenisation was observed in DER and LABs/HABs, where the regions with equiaxed and elongated ferritic grains have lower nanohardness and the regions with high carbon intensity have higher nanohardness compared with the unaltered steel matrix.

Although the studies have clearly shown that the microstructure transformation in WECs has many similarities with those in DER and LABs/HABs under the identical examination procedure, the causes of the distinguish nanocrystalline structure in the WECs that subsequently leads to the much earlier WSF bearing failures as compared to the high-stress cycle RCF are still unclear. It also remains unclear how microstructural transformation evolve and what the definitive mechanisms for the LABs and HABs growth are. Further investigations have been conducted on bearings tested at varied durations to study evolution of the

microstructure alterations in WECs, DER and LABs/HABs and are presented in the next chapter.

Chapter 5

Results: Initiation and Development Study

Following the initial study on fully developed RCF and WECs in failed bearings retrieved from service or laboratory rigs, laboratory tests and bearings microstructure examinations have been conducted to investigate the initiation and development of these features. Most of the studies conducted so far, similar to the results presented in Chapter 4, have focused on the analysis of well-developed WECs and those due to RCF that have been created in the laboratory environment or in failed specimens retrieved from service. Little investigations have been performed on time series specimens enabling the capture of the initiation of the microstructural changes and to discover their development mechanisms due to the difficulties in both testing and identifying them under microscopes in their very early stages.

This chapter presents experimental methods and results of the study on initiation and development of the microstructural alterations associated with RCF and WECs. All features formed in through-hardened martensitic inner rings of deep groove ball bearings from early to fully developed stages have been experimentally created and fully examined using the microstructure characterisation techniques outlined in Chapter 3.

5.1 Experimental Methods

A series of bearing tests have been conducted on an industrial bearing test rig called FAG L11 at Schaeffler (the industrial sponsor of this study) to create both RCF features and WECs under defined test conditions. Figure 5.1 shows schematics of the L11 test rig for the RCF tests and its modified version for the WECs tests where a direct electric current is applied to the test bearing. All tests

in this study have used standard DGBBs 6206 type with through-hardened martensitic AISI 52100 bearing steel. Virgin material characterisation of this steel has been performed on the sample cut from the unused DGBB 6206 type and presented in Chapter 4.

For the RCF testing two test bearings were mounted on the shaft at a time and were radially loaded at 8.5 kN per test bearing with a Hertzian stress of 3378 MPa on the inner ring, see Figure 5.1(a). This resulted in the maximum shear stresses of 1060 MPa at the depth of 175 µm below the surface (calculations were performed using Schaeffler developed software taking into account all test conditions). To trigger the formation of the WECs using the L11 test rig, a current flow as additional accelerator was applied. Therefore, for WECs testing a single test bearing was used so it can be isolated from the slave bearings, see Figure 5.1(b). In WECs configuration the DGBBs were radially loaded at 4 kN per test bearing with a Hertzian stress of 2634 MPa and 25 µA current load(DC) on the inner ring. This resulted in the maximum shear stresses of 820 MPa at the depth of 130 µm below the surface. A relatively high load/contact pressure has been used in the RCF tests since the DER and WEBs microstructural alterations are typically created under moderate to high contact stresses over a high number of rolling cycles [29, 52, 54, 58, 61-68]. All tests were running at a rotating speed of 9000 rpm with Total Transmission Ti75W80 lubricant, and a testing temperature was 80°C, which was determined by measuring the outer ring temperature. This lubricant has frequently been referred to as a 'bad lubricant', 'low-reference oil' or 'WEC critical oil' in the literature especially in WEC investigations [111, 116, 127, 129]. Details of the test conditions are given in Table 5.1.

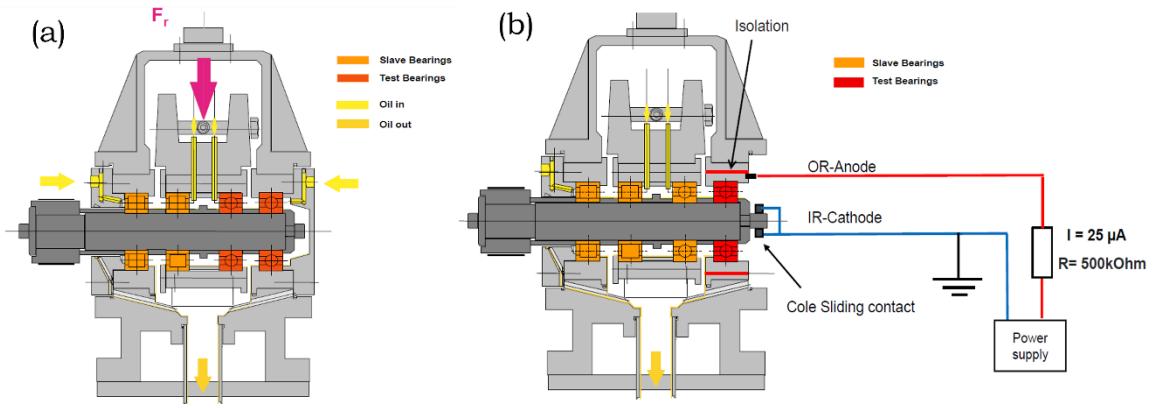

Figure 5.1: Schematics of the L11 test rig for: (a) DER, WEBs creation; (b) WECs formation. IR-inner ring; OR-outer ring.

The tests were terminated and bearings were disassembled after different runtimes in order to investigate the development of microstructure change during WEC and RCF failures. The RCF tests were suspended after 100, 200, 300, 400 and 670 hours, resulting in approx. 243, 486, 729, 972, and 1628 million load cycles on inner ring respectively (note there are 4.5 cycles within 1 revolution for 6206 type bearing; see details of the calculations for the number of the load cycles on inner ring in Appendix B). The WEC tests were suspended or failed at a range of runtimes between 10 and 50 hours with some (i.e. 10, 12.5, 15, 17.5, 20 hours) being repeated twice to check repeatability. A summary of all the RCF and WECs tests is given in Table 5.2.

Table 5.1: Test parameters for the production of DER, WEBs and WECs specimens.

Test parameters	**RCF**	**WECs**
Bearing type	Deep Groove Ball Bearing (DGBB) 6206 type	
Bearing material	AISI 52100 through-hardened martensite	
Lubrication	Total Transmission Ti75W80	
Temperature (OR)	80˚C	
Shaft rotation speed	9000 rpm	
Radial load per bearing	8.5 kN	4 kN
Hertzian stress (IR)	3378 MPa	2634 MPa
Direct electric current	-	25 μA

Table 5.2: A summary of the RCF and WECs tests.

	runtime [h]		cycles [x10^6]	damaged part	Failure mode
RCF	100		243	None	N/A
	200		486	None	N/A
	300		729	None	N/A
	400		972	None	N/A
	670		1628	None	N/A
WEC	**10**	repeated 2 times	24.3	None	N/A
	12.5		30.4	None	N/A
	15		36.5	None	N/A
	17.5		42.5	None	N/A
	20		48.6	None	N/A
	22.5		54.7	None	N/A
	30		72.9	None	N/A
	40		97.2	IR	Pitting
	47		114.2	IR	Pitting
	50		121.5	IR	Pitting

5.2 Examination of Dark Etching Region (DER) and White Etching Bands (WEBs)

All the bearings have been analysed following the procedures defined in the methodology chapter to investigate the initiation and development mechanisms of DER and WEBs progressing from the findings discussed in Chapter 4. Subsurface DER has been observed in inner rings of all RCF tested bearings between 100 and 670 hours (see examples shown in Figure 5.2 where DER is marked between two white dashed lines). DER appears to be a band parallel to the surface at a uniform depth below the surface in circumferential (parallel to the rolling direction) cross-section similar to observations in Chapter 4. As it can be seen, the density and region of DER appears to increase with the over-rolling cycles. However, the depth does not follow any obvious trend. This was later found to be influenced by the position of the circumference cross-section being cut.

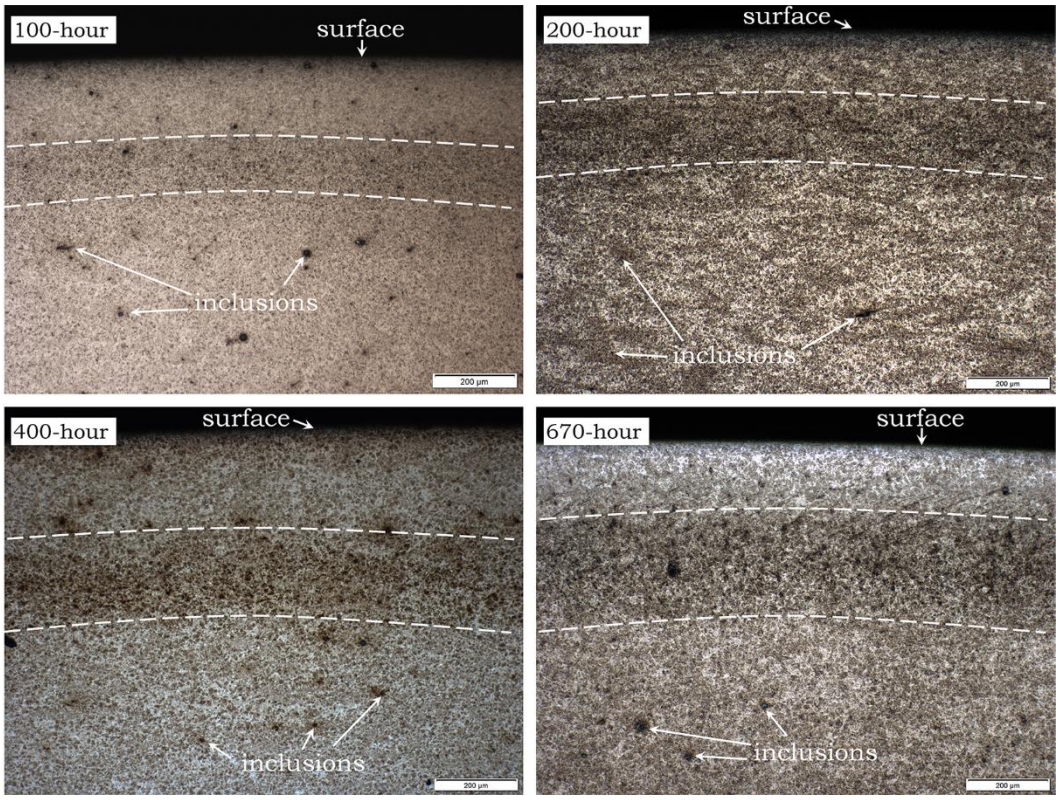

Figure 5.2: LOM images of DER in circumferential cross-section of bearing inner rings tested for 100, 200, 400, and 670 hours. (Nital Etched)

Figure 5.3 shows LOM images taken from axial (perpendicular to the rolling direction) cross-sections of the Nital etched sample tested for 400, where DER is observed to appear as a sickle-like shape, as shown in Figure 5.3(a), with a varying

depth along it shape. The deepest location of DER top boundary observed at the middle of the raceway, which corresponds to approx. 300 µm below the surface, and the tips of the sickle directly at the surface. Such sickle-like shape, therefore, lead to variation of the depth of the observed microstructure features in the circumferential cross-section. For example, if the cut is made precisely through the middle of the raceway, the top boundary of the DER should appear at approx. 300 µm below the surface, which corresponds to the depth shown in axial cross-section in Figure 5.3(a). In Chapter 4, the DER observed in the failed bearing sample appears to be groups of small black patches intermixed with bright areas and small white primary spheroidised carbide under LOM. However, groups of black lines instead of the previously observed small black patches are seen in the 400-hour samples, as shown in Figure 5.3(b). This is assumed to be due to the lower density of the altered microstructure components in DER in the 400-hour sample compared to the sample analysed in Chapter 4, which resulted in well distinguishable features even at the magnification of the LOM.

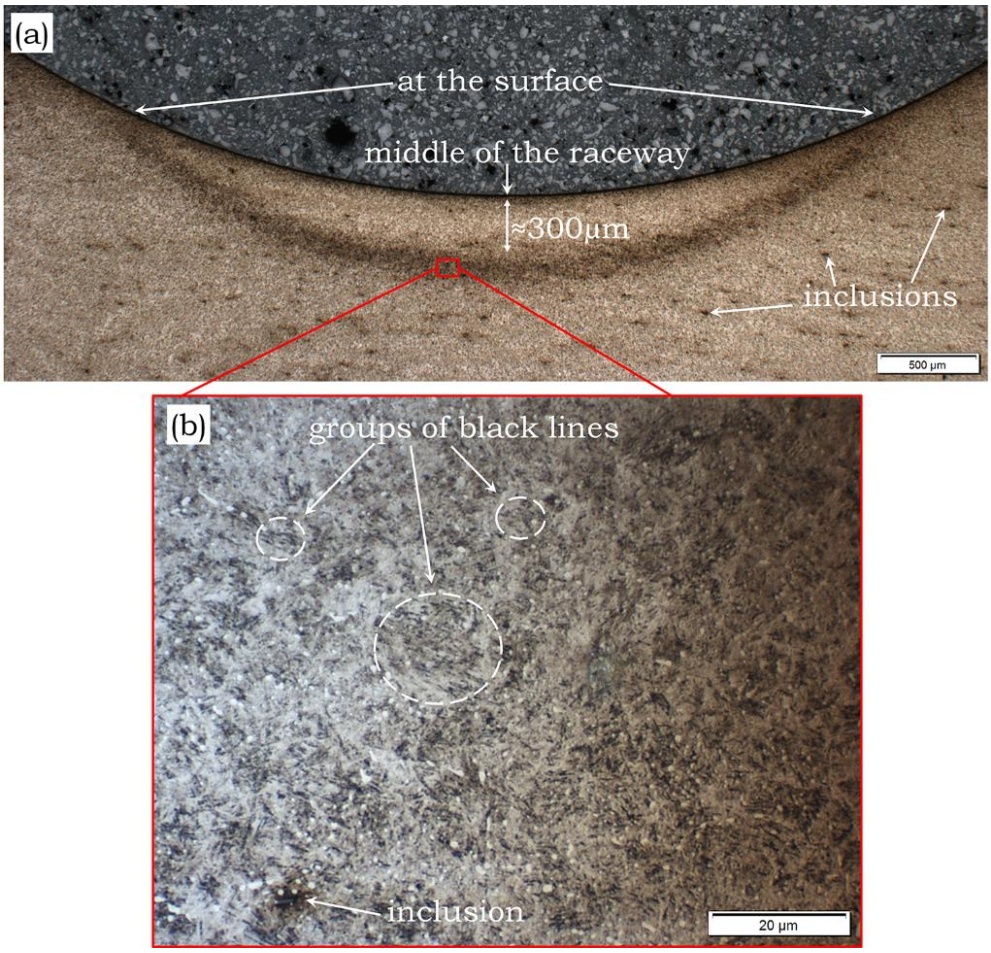

Figure 5.3: LOM images (Nital etched) of the axial cross-sections showing the DER in sample tested for 400 hours at two different scales.

It was also interesting to find that, LABs have been observed in all RCF tested samples from 100 to 670 hours although only a few randomly located LABs are seen in the 100 to 300-hour samples, which have only been detected using high magnification SEM. However, no HABs are observed in any of these samples, possibly due to insufficient rolling cycles under the test conditions. LOM images of the LABs in the 670-hour sample is shown in Figure 5.4. Similar to observations in Chapter 4, LABs are found to be parallel to the surface in axial cross-sections (see in Figure 5.4(a)) or inclined at a low angle to the contact surface in circumferential cross-sections (see in Figure 5.4(b)). Different to the observation in Chapter 4, the top boundary of LABs is found to be closer to the over-rolling surface compared to the DER formation, however lower boundary of the LABs is still found to be intermixed with DER, see Figure 5.4. Enlarged area in Figure 5.4(b) shows well-developed LABs inclined between 22° and 24° to the surface and unaltered primary spheroidised carbides between the bands in the 670-hour sample. LABs appear as white bands with thin dark lines next to the bands, which later were confirmed by SEM to be elongated grains. The direction of the bands inclination was always determined by the over-rolling direction as indicated in enlarged area in Figure 5.4(b).

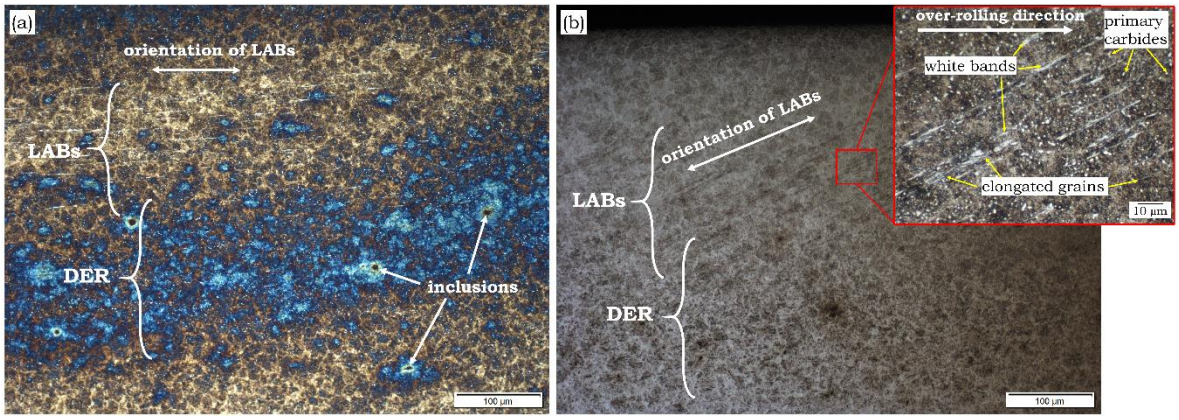

Figure 5.4: LOM images of LABs and DER observed in the 670-hour sample (Nital etched condition): (a) axial cross-section (blue tint is due to the over-etching of the sample); (b) circumferential cross-section in two magnifications; over-rolling direction is shown and examples of light bands, thin dark lines next to the light bands and primary carbides are marked.

Detailed analyses on the features using BSE and SE imaging in SEM and EBSD/EDX method are presented in the sections below to explore the initiation

and development processes. The results from the later stages of microstructure alterations formed in inner rings tested between 200 and 670 hours are presented first to compare them with the results presented in Chapter 4. Then the results from earlier stages in the 100-hour and 200-hour samples are presented to discuss the initiation of DER and LABs.

5.2.1 Late stages of DER and LABs

Similar features of LABs have been found in the 670-hour samples as those presented in Chapter 4, except that in the 670-hour samples lower concentration of the LABs are present. This has, however, provided an opportunity to examine individual bands more easily. Figure 5.5 shows BSE and SE SEM images of a LAB in the 670-hour sample, showing clearly the three LAB components discussed in Chapter 4: carbon-rich area, equiaxed and elongated grains. These features have also been reported as carbide discs, cell ferrite and needle-like ferrite respectively in literature [34, 52, 54-56, 58, 63, 69, 73, 74]. The carbon-rich areas associated with the LABs are clearly seen as a dark band with block-like morphology in BSE SEM and as an un-etched feature in the SE SEM. The block-like morphology of the carbon-rich areas has also been observed earlier in Chapter 4 in the TEM image of the LAB. The elongated grains (observed in BSE SEM in Figure 5.5) are shown to be deep grooves in the SE SEM and thin dark lines in the LOM (shown in Figure 5.4(b)). Equiaxed grains form in groups and are seen as etched away holes in SE SEM. The etching behaviour of equiaxed and elongated grains is due to their ferritic nature, as discussed in Chapter 4.

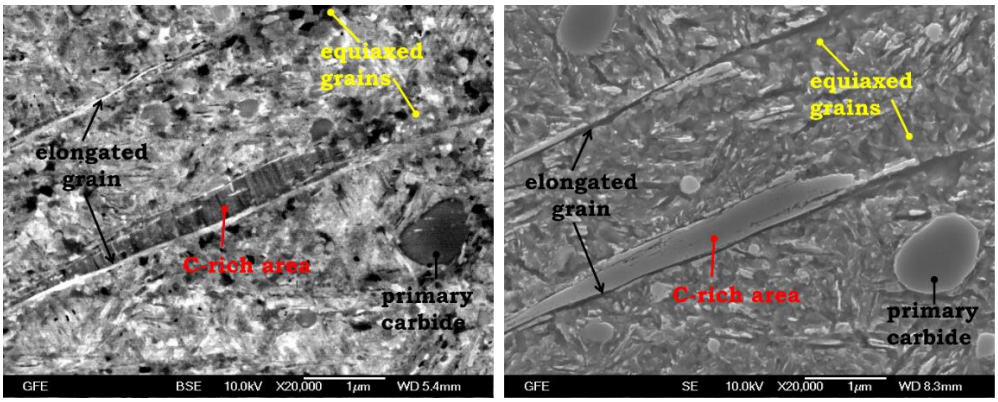

Figure 5.5: High magnification BSE (left) and SE (right) SEM images of LABs in a circumferential cross-section of the 670-hour sample. Examples of primary carbides, carbon-rich area, equiaxed and elongated grains are marked on the images.

Within the 670-hour samples, larger LABs span between 20 and 40 μm in length have also been observed (see an example shown in Figure 5.6) and it has become difficult to identify an individual LAB. These LABs consist of a mixture of elongated and equiaxed ferritic grains and elongated carbon-rich areas similar to those being shown earlier. It is also interesting to observe DER features as groups of short elongated grains (approx. 2 μm length) and fine equiaxed grains, shown in Figure 5.6(b). The short elongated grains in DER are shorter than those observed in Chapter 4 (up to ~7 μm), which may indicate an earlier RCF stage of the 670-hour sample than that of the bearing's ball analysed in Chapter 4. Residual martensitic matrix with intact primary spheroidised carbides still exists around and in-between the altered microstructure.

The 670-hour sample was further analysed using EBSD, the results are presented in Figure 5.7, where Figure 5.7(a) shows an IQ map and Figure 5.7(b) shows a KAM map of the same location shown in Figure 5.6 but slightly smaller area of the analysis. The IQ map depicts that equiaxed and elongated grains within LABs have comparatively high IQ that is typical for an unstrained ferrite structure, whereas carbon-rich areas appear as a dark areas with low IQ suggesting that such areas have a complex diffraction pattern and possibly much higher lattice imperfections (dislocation and/or defect density) [147]. As shown in the KAM map in Figure 5.7(b), equiaxed ferritic grains have lower misorientation compared to the martensitic matrix around, however elongated ferritic grains in the LABs appeared to have partly higher misorientation values than equiaxed grains. Elongated grains as a part of the DER appeared to have similar IQ and KAM values to the ones in LABs.

The results of the EDX analysis of the same area are presented in Figure 5.8(a&b), showing the distributions of carbon and chromium. Primary spheroidised carbides are seen to remain unchanged in the regions of unaltered microstructure between the LABs, however within the regions of LABs both carbon and chromium are seen to be redistributed, suggesting dissolution of primary spheroidised carbides at this stage. Chromium, presumably from existing primary spheroidised carbides, shows homogenous distribution, whereas carbon is seen heterogeneously distributed in the regions of microstructure alterations, showing lower carbon intensity in the areas of equiaxed grains and higher carbon intensities in carbon-rich areas. Under close inspection, using BSE and SE SEM imaging, primary spheroidised carbides

are frequently detected to be cut by elongated grains, equiaxed ferritic grains, or both, see examples shown in Figure 5.9.

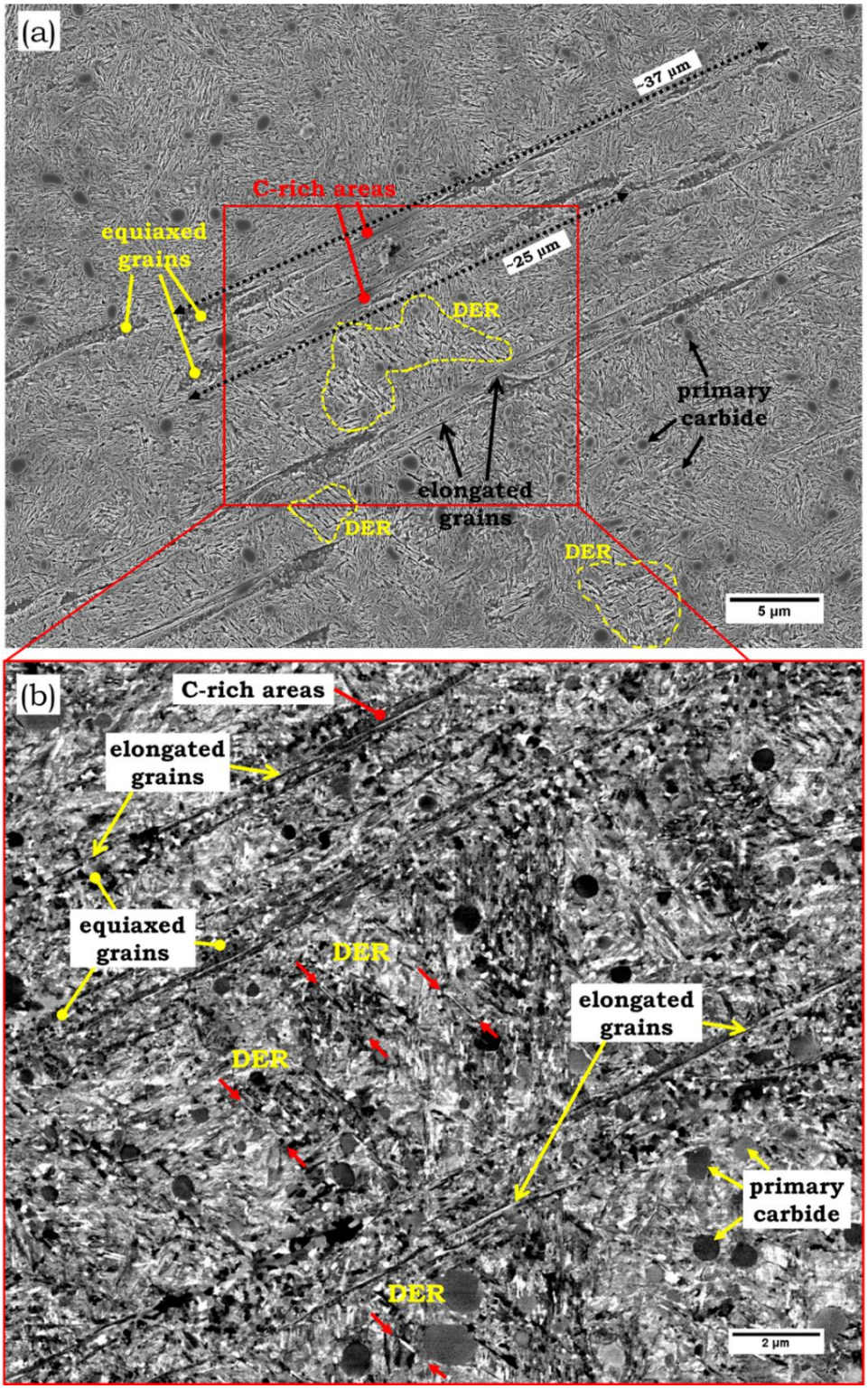

Figure 5.6: Well-developed LABs observed in circumferential cross-section of the 670-hour sample: (a) SE SEM; (b) BSE SEM. Examples of DER (with elongated grains between red arrows), primary carbides, C-rich areas, elongated and equiaxed grains are marked.

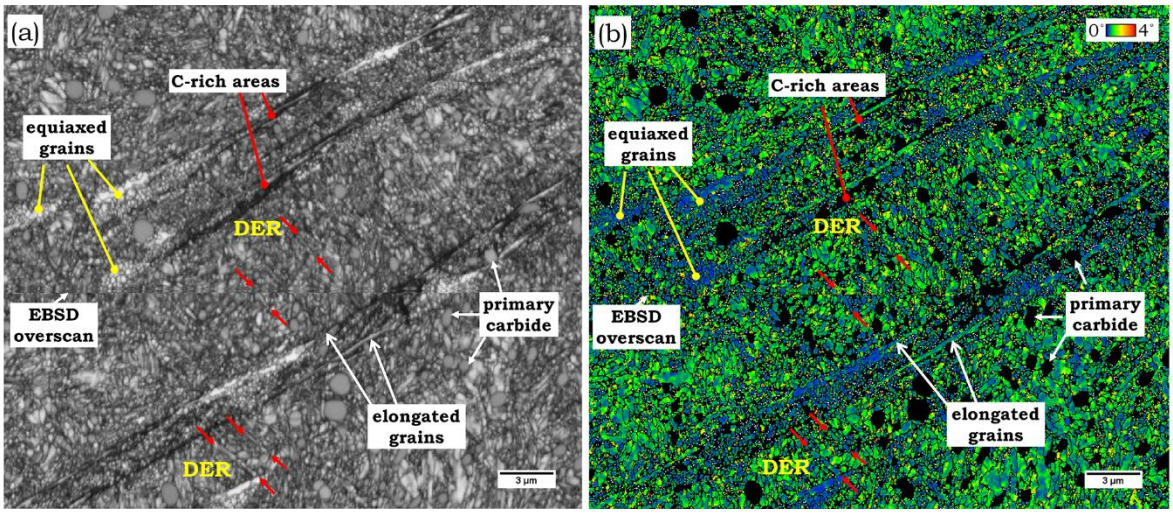

Figure 5.7: Slightly smaller part of well-developed LABs observed in circumferential cross-section of the 670-hour sample in Figure 5.6: (a) EBSD IQ map; (b) KAM (100, 5˚) map for α-Fe only.

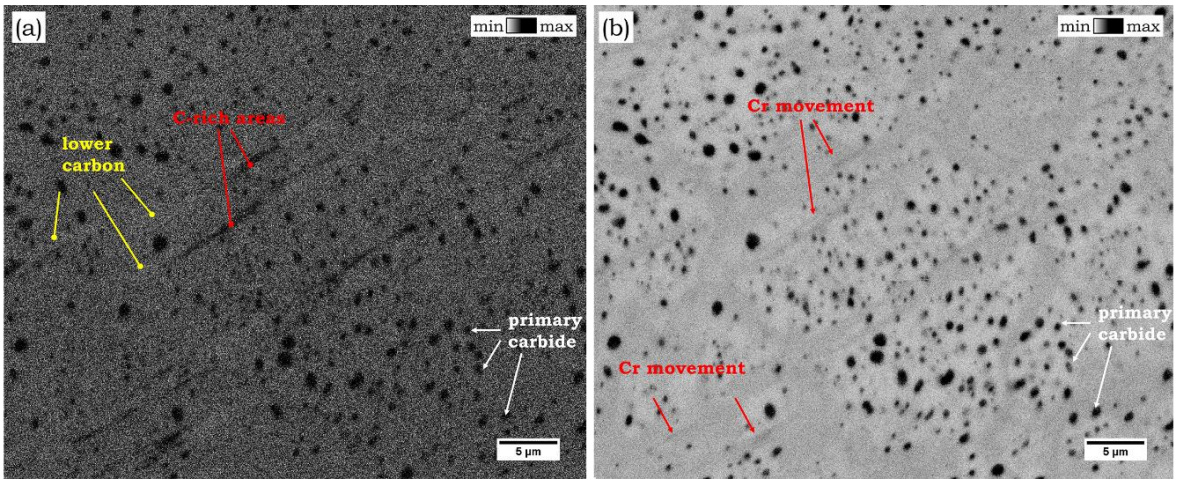

Figure 5.8: EDX maps of well-developed LABs observed in circumferential cross-section of the 670-hour sample in Figure 5.6: (a) C-Kα; (b) Cr-Kα.

In the 200-hour samples, another characteristic of the LABs is seen, i.e. LABs appear as 'cotton bud'-like shape with carbon-rich area at the 'stem' and equiaxed ferritic grains at the two ends, see examples given in Figure 5.10. Individual LABs are generally found to be no more than 15 µm in length at this stage, which is much shorter than those observed in samples tested for longer hours (see Figure 5.6). It has in general been observed that the length of LABs increases with the rolling cycles. Elongated grains appear to grow along one side or through the middle of the carbon-rich bands as shown in Figure 5.10(a), with the former case being more frequently observed. Areas of equiaxed grains typically have one side

bordered by an elongated grain resulting in a clean straight appearance, while the opposite side appears to be more in an undefined shape.

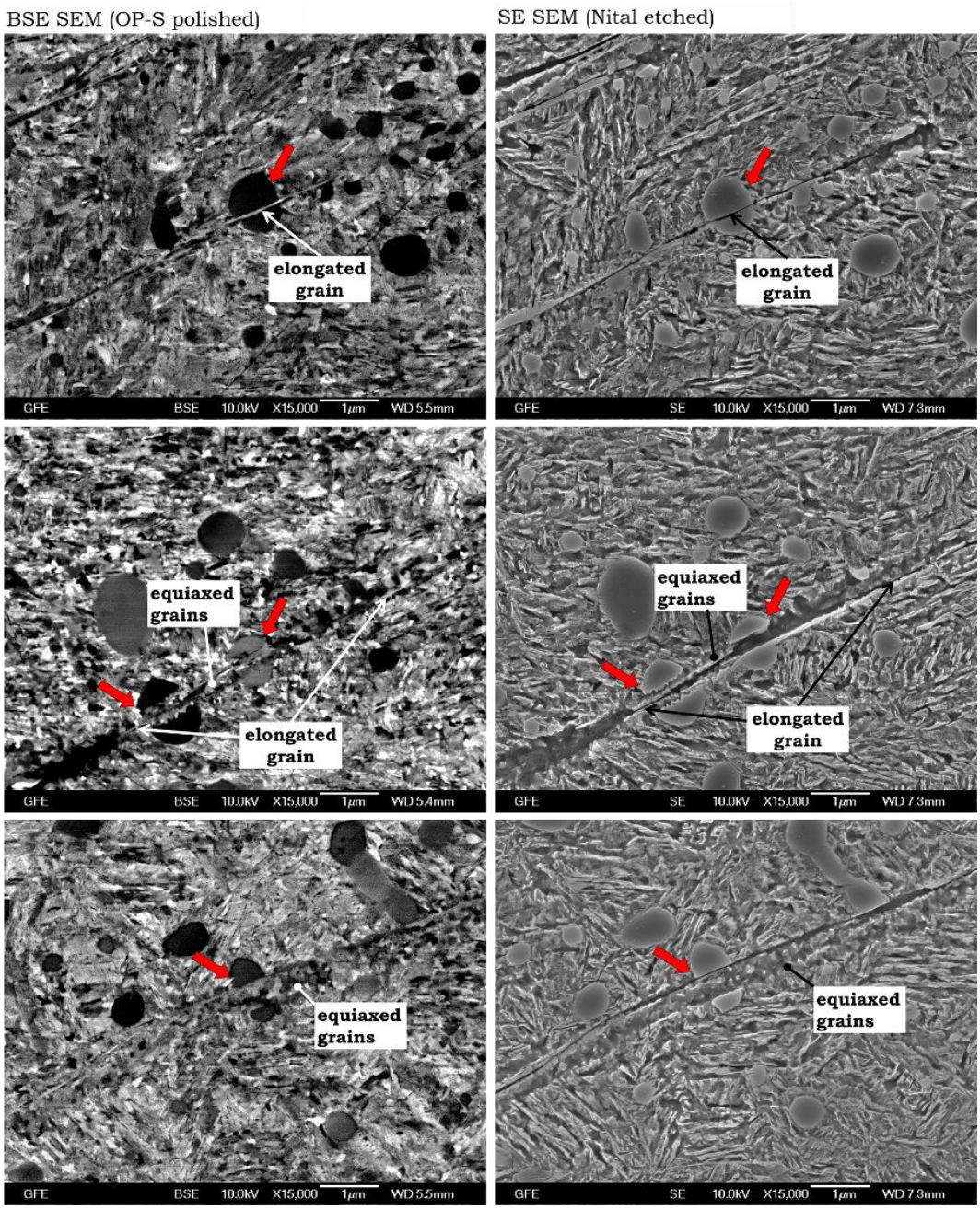

Figure 5.9: BSE (left) and SE (right) SEM images of primary spheroidised carbides cut through by LABs observed in the samples tested for 300 hours and above. Red arrows point to the primary carbides that are being cut.

EBSD analysis of the 200-hour sample depicts the same observations as in the 670-hour sample, where equiaxed grains show low misorientation and elongated grains slightly higher misorientation values, see in Figure 5.10(b). As before, both types of grains have high IQ values, whereas carbon-rich areas show low IQ, see

Figure 5.10(c). In EDX scan, carbon redistribution, similar to that observed in the 670-hour sample, is clearly seen in Figure 5.10(d) with carbon-rich areas being accompanied by the appearance of carbon-depleted areas at the location of equiaxed ferritic grains. However, no chromium redistribution is observed in Figure 5.10(e), which may correspond to the fact that no primary spheriodised carbides have been dissolved on the path of growing LABs. This suggests that movement of carbon atoms from parent martensite and tempered carbides during transformation into new ferritic grains is sufficient for the formation of the carbon-rich areas.

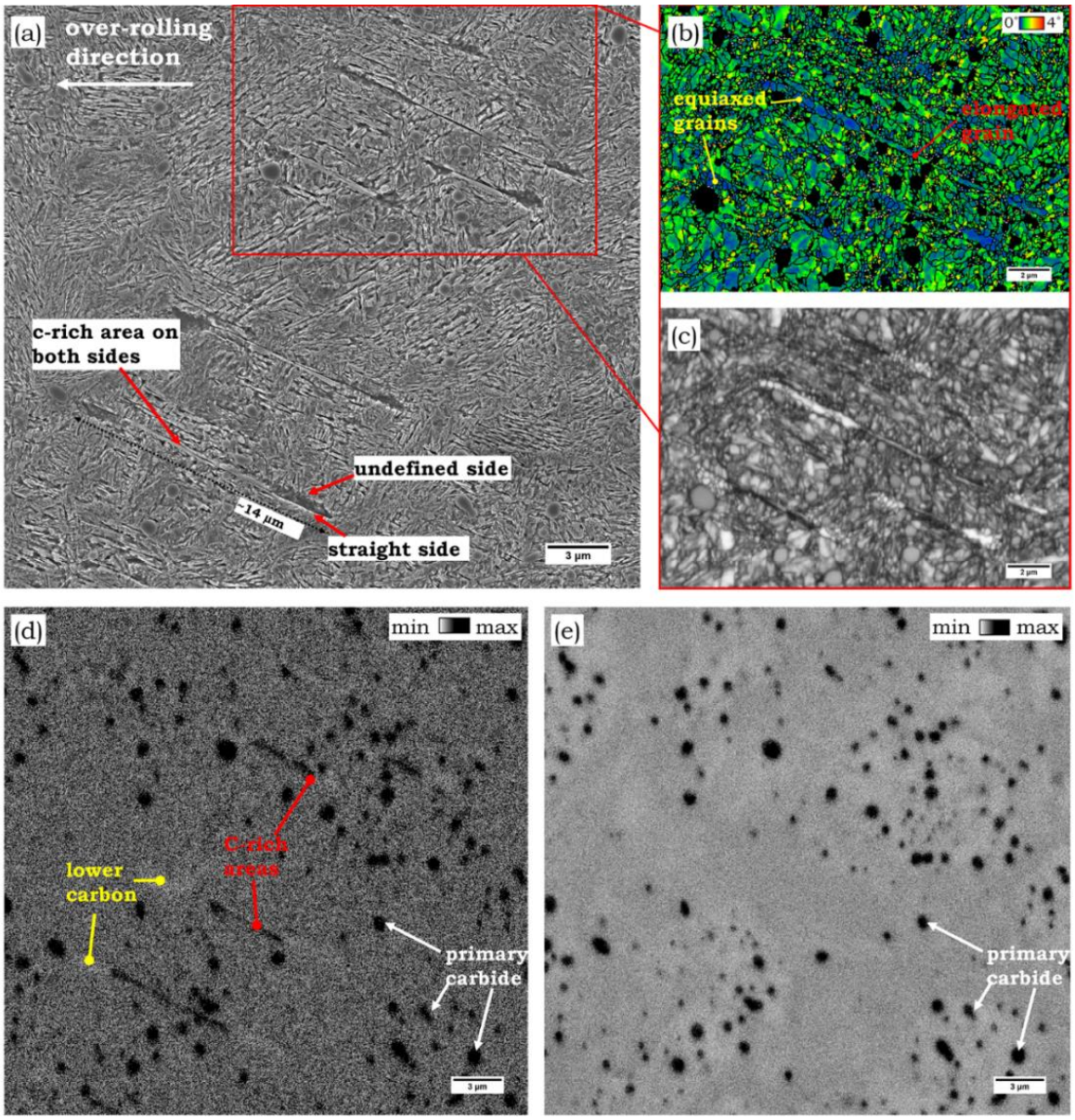

Figure 5.10: LABs observed in a circumferential cross-section of the 200-hour sample: (a) SE SEM (Nital etched); (b) KAM(100nm,5°) for the points indexed as α-Fe only; (c) IQ; (d) EDX C-Kα; (e) EDX Cr-Kα.

5.2.2 Early stages of DER and LABs

Also in the 200-hour sample, LABs at their much earlier stages have been seen, which was very challenging to detect, see examples given in Figure 5.11, especially in the BSE SEM image shown in Figure 5.11(a). After Nital etching, the etched away areas, similar to the equiaxed grains observed in the later stages, were identified in the SE SEM shown in Figure 5.11(b). Formation of new equiaxed grains with misorientation lower than that of the martensitic matrix, similar to those observed in well-developed LABs, has been confirmed by the KAM map (Figure 5.11(c)). The ferritic nature of the newly formed equiaxed grains is proven by the non martensite-martensite HAGBs, shown in Figure 5.11(d). As can be seen, no elongated grains or carbon-rich areas are visible at this stage. The corresponding EDX measurements of the same area have shown no changes in carbon or chromium intensities at this stage. This does not, however, exclude the possibility that localised chemical changes have started to take place but have not been detected due to the detection limitations of EDX.

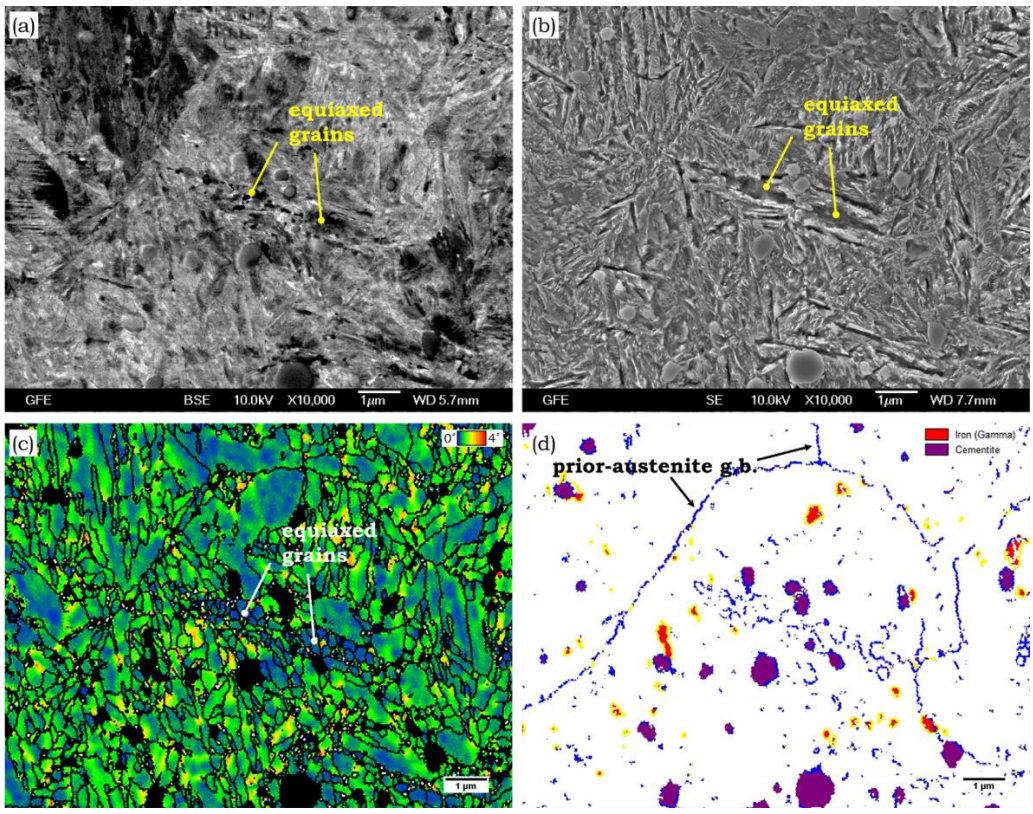

Figure 5.11: The earliest state of LAB formation observed in the 200-hour sample: (a) BSE SEM (OP-S polished); (b) SE SEM (Nital etched); (c) KAM(100nm,5°) for the points indexed as α-Fe; (d) non martensite-martensite HAGBs.

Similar features have also been observed in the 100-hour samples, see example shown in Figure 5.12. Although, the LAB appears to be slightly more developed than the one presented in Figure 5.11, however not as grown (maximum length of about 10 μm) as those shown in Figure 5.10 (also from the 200-hour sample). Equiaxed ferritic grains, similar to those observed in Figure 5.11 and those at late stages, are clearly depicted in the SEM images and EBSD maps shown in Figure 5.12. In addition, very small carbon-rich areas of approx. 2 μm length and elongated grains are identified by the SE SEM and IQ map shown in Figure 5.12(a&d). Carbon-rich areas have lower IQ, whereas equiaxed and elongated grains have higher IQ compared with the surrounding residual martensitic matrix. At this stage, both equiaxed and elongated grains have low KAM as seen in Figure 5.12(c), which is different from those in more developed LABs. Again, EDX analysis in this area shows no carbon or chromium movement at this stage of the, LABs likely due to detection limitations of EDX.

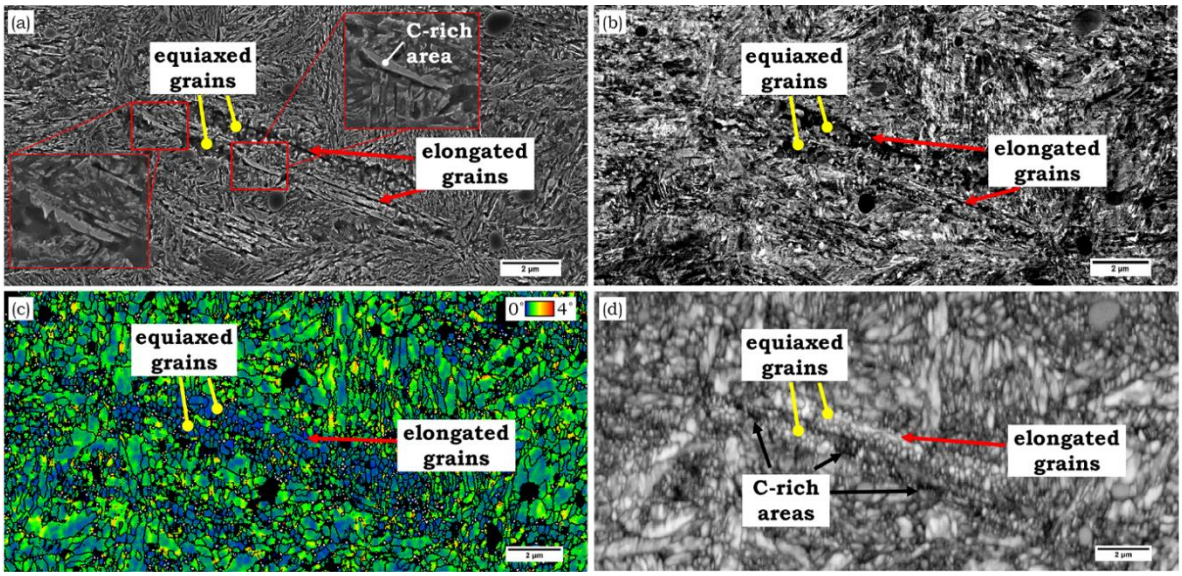

Figure 5.12: One of an early stages of LAB formation observed in circumferential cross-section of the 100-hour sample: (a) SE SEM (Nital etched); (b) BSE SEM (OP-S polished); (c) KAM(100nm,5°) for the points indexed as α-Fe; (d) IQ map.

Further analysis of the 100-hour sample has revealed various combinations of altered microstructure groups scattering in the area of the DER, see examples shown in Figure 5.13 and Figure 5.15. The groups have been found to be elongated grains corresponding to the groups of dark lines observed in LOM, see examples shown in Figure 5.3(b). However, the elongated grains, although parallel within

each group, appear to have grown in random orientations and scattered randomly in the DER (see examples pointed with red arrows in Figure 5.13). The 1-2 μm long elongated grains observed in the 100-hour sample are very similar to those in the 670-hour sample shown in Figure 5.6. It is also seen that these thin elongated grains are growing into primary spheroidised carbides (see Figure 5.14), which is comparable to similar observations reported in literature using TEM [52, 57, 68]. Similar to the findings reported in Chapter 4, groups of small equiaxed grains have also been detected in the 100-hour sample, see examples marked with pink dashed lines in Figure 5.13. In addition to the equiaxed and elongated grains, small features approx. 1 μm long next to elongated grains have been identified in the SE SEM due to its un-etched appearance (see examples marked with yellow arrows in Figure 5.13). Morphology of such un-etched features appeared to be similar to the carbon-rich areas found in the early stages of LABs shown in Figure 5.12.

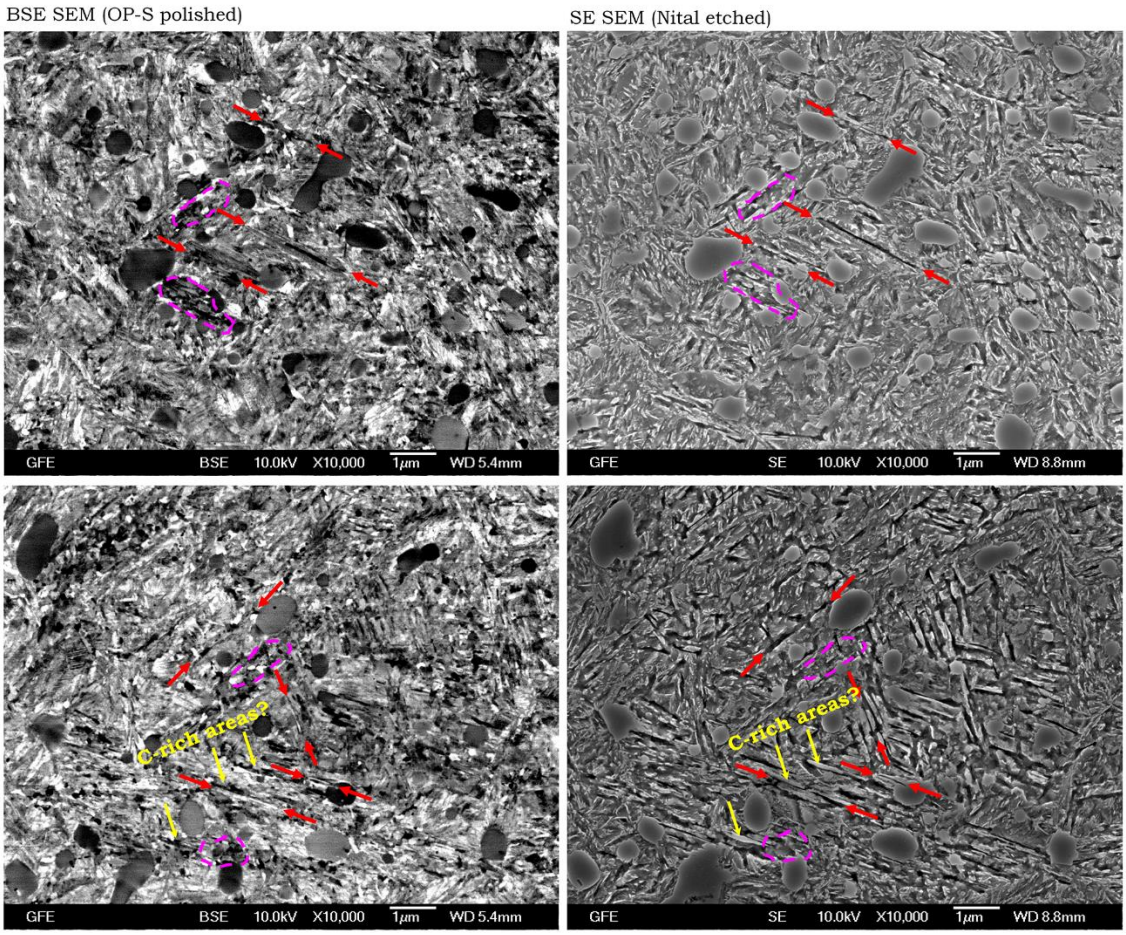

Figure 5.13: DER in the 100-hour sample viewed with BSE (left, OP-S polished) and SE (right, Nital etched) SEM. Examples of elongated grains shown with red arrows; equiaxed grains marked with pink dashed line; carbon-rich areas marked with yellow arrows.

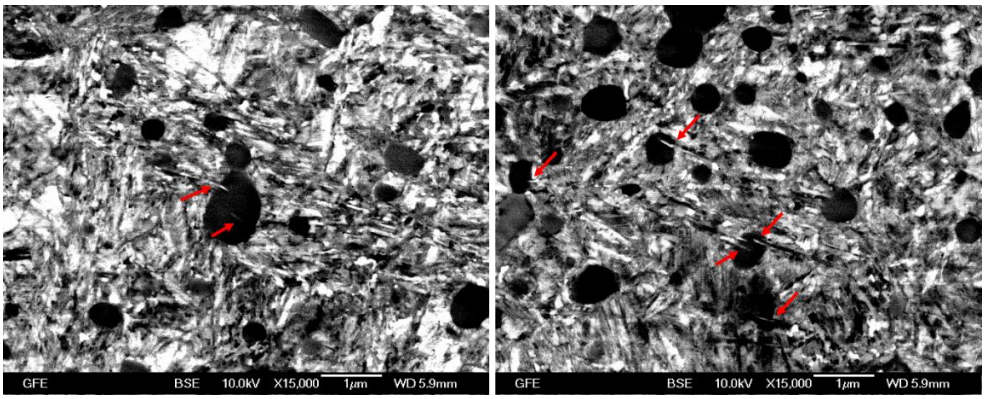

Figure 5.14: BSE SEM images of elongated grains growing into primary spheroidised carbides in the 100-hour sample.

Within the DER in the 100-hour sample, mixtures of equiaxed and elongated grains grouped in rounded areas (top images in Figure 5.15), as well as those with preferential orientation at approx. 20-25° to contact surface (bottom images in Figure 5.15) have been observed. It was also interesting to find the area, similar to the carbon-rich areas shown in Figure 5.13, next to the primary spheroidised carbide (see zoom-in areas shown in Figure 5.15).

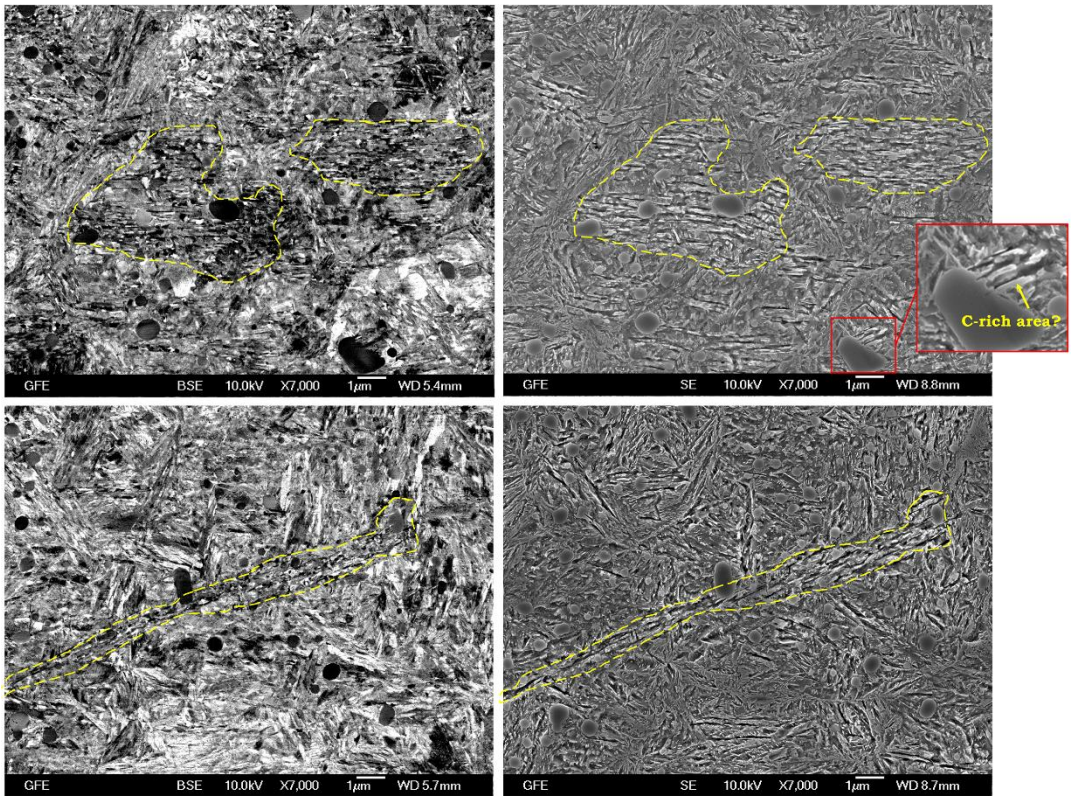

Figure 5.15: Groups of mixed equiaxed and elongated grains as part of the DER in the 100-hour sample viewed with BSE (left, OP-S polished) and SE (right, Nital etched) SEM: (top) more rounded groups; (bottom) a group aligned at approx. 20-25° to the contact surface.

To further understand the DER, the 100-hour sample has been analysed using EBSD and the results are presented in Figure 5.16, where Figure 5.16(a) shows a KAM map and Figure 5.16(b) shows non martensite-martensite HAGBs map of a chosen DER. Microstructure alterations are clearly seen showing groups of very small grains with slightly lower misorientation compared to the residual matrix around it (see KAM map in Figure 5.16(a)), as well as formation of non martensite-martensite HAGBs as shown in Figure 5.16(b). Together with the fact that these patches being etched stronger by Nital, the grains are suggested to be ferritic, which in agreement with the observations made in Chapter 4. Different to observations made in Chapter 4, the KAM map depicts that the newly formed areas consist of mostly equiaxed grains instead of elongated ones. This is most likely due to the thickness of the elongated grains being below the EBSD lateral resolution. EDX analysis of the same area has shown that the chemical distribution in the DER, in particular carbon and chromium, has remained the same as that in the virgin microstructure presented in Chapter 4 (thus not presented here).

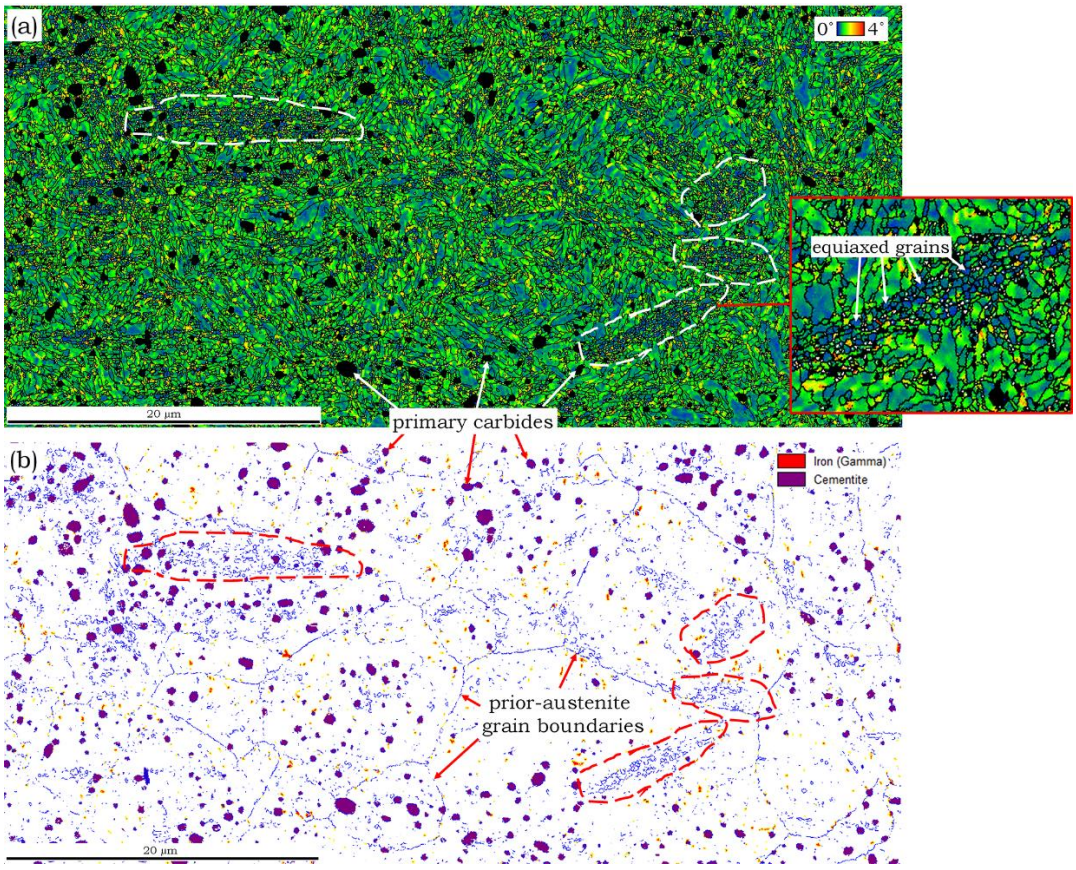

Figure 5.16: EBSD maps of the DER in 100-hour sample: (a) a KAM(100nm, 5˚) map of the points indexed as α-Fe; (b) a non martensite-martensite HAGBs map. Examples of groups of altered microstructure are marked with white/red dashed line.

5.2.3 Discussion

Initiation and further development of the microstructure alterations taking place in the through-hardened martensitic AISI 52100 has been observed through the analysis of DGBB inner rings after being tested for a series of durations between 100 and 670 hours. Acquiring both SE and BSE SEM images in combination with EBSD/EDX analysis help to capture and reveal all details of microstructural alterations, especially in the initiation stages.

DER has been found to form in all the bearings under the high contact loading similar to the observations reported in the literature [29, 52, 54, 58, 61-68]. It has also been observed that the DER density and the width of the DER band increases with running time that have also been discussed by others [34, 51, 52, 61, 63, 69]. Some studies have shown a sickle-like shape DER appearing at uniform depths from the surface [35], however, for the first time, tips of the DER sickle-like shape appeared to reach the surface in an axial-cross section of bearing inner rings. Unfortunately, the sickle-like appearance of DER symmetrically located from the middle of the raceway in the axial-cross section and the tips of the sickle appear to reach the bearing surface cannot be explained by well-established bearing subsurface stress models. Although sliding may move the subsurface maximum shear stresses towards the surface and that formation of DER is a result of shear stresses [29, 52, 54, 58, 61-68], it would not have resulted the shear stress moving to the surface in this study since the bearings have been run under full film lubrication. Further investigation is required to understand this phenomenon.

The SEM analyses have shown that DER contains randomly distributed groups of parallel short elongated grains and small equiaxed grains within residual martensitic microstructure. Two types of the groups are observed, one in rounded areas and the other with grains in a preferential orientation at approx. 20-25° to the contact surface. The latter type of groups with preferential orientation have not been observed in the DER in the failed bearing discussed in Chapter 4, possibly due to the very late DER stage of the failed bearing. Furthermore, short elongated grains (approx. 1-2 μm length) in DER have been observed in all the bearings tested on L11, indicating that these grains remain unchanged at this length even under extended over-rolling cycles of up to 670 hours. This is different from the much longer elongated grains observed in the DER in the failed bearing. However, the elongated grains in the DER of the failed bearing appear to be more comparable

with the elongated grains observed in the LABs in the 670-hour sample from L11, suggesting that possibly, a mixture of DER and LABs has been analysed in failed bearing. Random orientation of the LABs in failed bearing could be due to the fact that bearing's ball has been used for the Chapter 4 where rotational axis was free to vary.

It is established that the newly formed elongated and equiaxed grains in DER are ferritic through the SEM and EBSD/EDX analyses. Ferrite is known to have lower carbon solubility, hence lead to being heavily attacked by etchant. To where the excess carbon moves during martensite to ferrite transformation is still undetermined. However, the 1 μm long features that are similar to the carbon-rich areas in the early stages of LABs (see Figure 5.12) were identified by SE SEM due to their un-etched appearance in the DER (shown in Figure 5.13 & Figure 5.15). This may answer the question as to the locations of the excess carbon during the formation of equiaxed and short elongated ferritic grains. Further analysis will be required to confirm whether they are carbon-rich areas as being suggested in this study.

Although no carbon or chromium movements are shown in the early stages of DER around the newly formed grains, spheroidised carbides have been observed to be cut by newly formed thin elongated ferrite grains at this stage. This, as well as the fact that martensite has been transformed into ferritic grains, suggests that a chemical redistribution must have started but at the level that cannot be detected by the EDX. This could be further confirmed if the 1 μm features in the DER are confirmed to be carbon-rich areas, which also were not detected up by EDX measurements. Recently, a study of DER using an APT has shown that DER has lower carbon saturation than original matrix, although transition carbides were observed in the areas next to it, which were proposed to be carbon absorbers [72]. Hence, the 1 μm long un-etched features observed in this study could be the so called 'carbon absorbers', which could possibly become the carbon-rich areas as part of LABs at later stages of over-rolling. Further analysis using APT or other high-resolution techniques should be conducted to confirm this.

It was interesting to observe LABs in a region above the DER below the contact surface, which is different from that has been widely reported, i.e. WEBs form within the DER [34, 52, 54, 58, 67, 68, 74, 75]. This suggests that LABs could potentially form independently from the formation of DER in bearings, as

suggested by a few previous studies [34, 55, 76]. This, however, challenges the assumption made based on the investigation of the failed bearing samples in Chapter 4, i.e. elongated and equiaxed grains in DER grow further to form LABs. The reason why LABs form closer to the surface than DER is unclear. Similar to that reported in literature, the density of LABs was found to increase with the rolling cycles and LABs incline to the surface at an angle between 22° and 24° in the DGBBs [52, 55, 68, 73, 74, 77].

The earliest stage of LAB formation is found to be the formation of equiaxed ferritic grains of low misorientation without carbon-rich areas or elongated grains in the 200-hour sample. Similar to the discussions above about the DER, carbon atoms must have started to move accompanying the formation of ferrite structures at this stage although it was not detected by EDX. As the over-rolling cycles increase carbon atoms would have sufficient time to move and localise at areas such as between clusters of newly formed equiaxed ferritic grains, forming carbon-rich areas, also known as carbides discs [34, 52, 54-56, 58, 63, 69, 73, 74]. Very small carbon-rich areas have already been detected in the 100-hour sample based on its etching behaviour and comparatively low IQ (see Figure 5.12).

The 'cotton bud'-like shape LABs with carbon-rich area as a 'stem' and equiaxed grains at it two ends occur in most samples and they are found to be independent of the size of altered microstructure area. It is unclear why carbon moves between two groups of equiaxed grains and forms as a 'stem' between the two 'buds' rather than moving along the equiaxed grains clusters as being recently modelled by [37]. The rectangular block-like morphology of carbon-rich areas observed in high magnification SEM images in this chapter and under TEM discussed in Chapter 4 are similar to those reported by Lindahl et al. [58]. These results further confirm that carbon-rich areas do not originate from deformation or flattening of pre-existing primary spheroidised carbides [69]. It has also shown that the size of the carbon-rich areas depends on the LABs formation stage, for example, short 2 μm carbon-rich areas have only been found in LABs at their early stages, whereas up to 35 μm long carbon-rich areas have been observed in LABs at much later stages. Carbon-rich areas are found to form without evident dissolution of primary spheroidised carbides, however LABs have been observed to cut through primary carbides in many cases. It is thus suggested that primary spheroidised carbides are not required for the LABs formation process, however it is clear that primary carbides located on the path of growing LABs will be dissolved and contribute to

the LABs growth. Dissolution of primary spherical carbides has only been observed at the very late stages of LABs formation (over 300 hours), where not only carbon redistribution, but also chromium homogenisation has occurred. Further investigations on carbon-rich areas are required to identify their crystal structure and understand their growth mechanism.

Similar to carbon-rich areas, elongated grains in LABs also continuously grow in length with the increase of over-rolling. At the earliest stage of LABs formation, equiaxed grains are found to form without the formation of elongated grains. This is in agreement with the results presented in Chapter 4 of this thesis, where elongated ferritic grains have been suggested to form due to the elongation of equiaxed grains subjected to slip processes. The KAM maps have shown that elongated grains have low misorientation in the early stages of LABs formation, which has been found to increase slightly in the later stages of LABs formation. This suggests that dislocations may have formed within elongated grains during continuous over-rolling.

Based on the observation of low missorientation and formation of non martensite-martensite HAGBs between the newly formed grains, it is assumed that ferritic grains do not form in DER or LABs due to recovery of an existing lattice, but a result of the rearrangement of iron atoms possibly due to stress-induced dislocation movement [37, 52, 57, 72, 73]. It has been proposed that under high over-rolling stresses of over millions of cycles, constant dislocation movement leads to localised high dislocation density regions where new grains form. Dislocation movement triggers a dislocation assisted carbon migration, which might be too low to be detected by EDX. Carbon subsequently precipitates either at existing transition carbides (in DER) or at locations that later appear as carbon-rich areas (in LABs) [37, 72]. It is, however, unclear why carbon could precipitate in two different ways. Similar equiaxed grains were observed in shear localisation as a result of the severe dynamic plastic deformation [160-163]. A microstructural evolution was suggested to start from a homogeneously distributed dislocations then rearranging themselves into elongated dislocation cells further followed by dislocation accumulation in subgrain boundaries due to an increase of misorientation under continuous deformation and finally breaking up of elongated subgrains into equiaxed grains. However, different to the above proposed mechanism, low misorientation has been observed in the groups of elongated and equiaxed grains in DER in this study, which suggests that either different

mechanism of microstructure evolution has taken place or these elongated and equiaxed grains have already reached the most advanced stage of transformation.

5.2.4 Conclusions

This chapter has presented the results from a detailed study of altered microstructure initiation and development in DER and LABs using a combination of microstructure characterisation techniques. A detailed microstructure observations occurred in the inner rings of DGBB subjected to RCF testing over a range of test durations has revealed the following:

- Mixtures of equiaxed and small-elongated grains grouped in various combinations, for example rounded areas or with preferential orientation at approx. 20-25° to contact surface, have been observed randomly scattered in the areas of the DER as early as in the 100-hour sample. It was not possible to identify whether equiaxed or small-elongated grains formed first or whether it is a cooperative growth of both grain types. The small-elongated grains although parallel within each group, appear to have grown in random orientations.
- The density and region of DER appears to increase with the over-rolling cycles. However, 1-2 μm length elongated grains were observed in all tested bearings, suggesting that these grains remain unchanged at this length even under extended over-rolling cycles of up to 670 hours. It is, thus, the increase of the amount of altered microstructure groups that contribute to the observed growth of DER under LOM.
- No changes in carbon or chromium distribution are observed in the DER through the EDX analysis. However, small features approx. 1 μm long with similar morphology as carbon-rich areas in the early stages of LABs, have been identified next to short-elongated grains in the DER. This, therefore, suggested that localised chemical changes have started to take place but have not been detected due to the detection limitations of EDX.
- Sickle-like shaped DER with depth at the middle of the raceway approx. 300 μm below the surface and the tips directly at the surface has been detected for the first time. However, the stresses resulting in such shape are still undetermined.

- It was also interesting to find that, LABs have been observed in all RCF tested samples from 100 to 670 hours although only a few randomly located LABs are seen in the 100 to 300-hour samples. However, no HABs are observed in any of these samples, possibly due to unsufficient rolling cycles under the test conditions. The top boundary of LABs at late stages is found to be closer to the over-rolling surface compared to the DER formation, however lower boundary of the LABs is still found to be intermixed with DER. In DGBBs inner rings, LABs observed to be inclined between 22° and 24° to the surface with direction of the bands inclination determined by the over-rolling direction.
- Formation of new ferritic equiaxed grains with low misorientation and stronger attacked by etching has been suggested to be the earliest stage of LAB formation found in 200-hour sample. At this stage no elongated grains or carbon-rich area were detected. Neither changes in carbon or chromium intensities were observed, which is assumed to be due to the detection limitations of EDX.
- Slightly more developed LABs with maximum length of about 10 μm were detected in the 100-hour sample. At this stage, in addition to equiaxed ferritic grains, very small carbon-rich areas of approx. 2 μm length were identified that are assumed to form as result of carbon diffusion from the newly formed ferritic grains due to their incompatibility with bcc lattice in the early stage of LABs. Elongated ferritic grains were also found to have formed in this stage, making it difficult to confirm whether elongated ferritic grains form independently or simultaneously with carbon-rich areas around them.
- LABs growth up to 15 μm is observed in 200-hour samples, where individual LABs can still be distinguishable and appear as the 'cotton bud'-like shape with carbon-rich area at the 'stem' and equiaxed ferritic grains at the two ends. Elongated grains appear to grow along one side or through the middle of the carbon-rich bands, with the former case being more frequently observed. At this stage, carbon redistribution is observed, but no chromium redistribution is detected in EDX, which may correspond to the fact that no primary spheriodised carbides have been dissolved on the path of growing LABs. This further suggests that movement of carbon atoms from residual

martensite and tempered carbides during transformation into new ferritic grains is sufficient for the formation of the carbon-rich areas.

- Continuous grain growth, predominantly in length-wise subjected to more over-rolling cycles is observed, where LABs extending to 40 μm length in the 670-hour samples have been observed and it has become difficult to identify individual LABs. At the late stages, both carbon and chromium are seen to be redistributed in the regions of LABs, suggesting that not only tempered carbides, but also primary spheroidised carbides dissolution is taking place at this stage.

5.3 White Etching Cracks (WECs)

Investigations on the evolution of WEC formation started with the samples of the highest amount of rolling cycles, i.e. the 50-hour bearing, to confirm and locate the subsurface damages in the bearing inner ring. The analysis was initially performed on a few cuts close to the surface damage (spalling) and focused on the subsurface WEC features. As expected a high quantity of well-developed WEC networks were observed and analysed using both LOM and SEM. The second bearing analysed was the 30-hour sample, which had no surface damage. Two sections at different locations of the 30-hour inner ring were cut, amounting to approx. 1/4 of the whole ring. WECs have been observed in both sections, however the WEC networks are much smaller than those in the 50-hour samples. In both the 30 and 50-hour bearings, the depth of most WECs has been observed to be about 100 μm below the surface, which is above calculated maximum shear stresses (maximum shear stresses approx. 130 μm below the surface). However, the influence of shear stresses on microcracks formation are not excluded since it is know that sliding may move the subsurface maximum shear stresses towards the surface [44, 164]. Subsequently samples from the bearings tested for 10 to 20 hours were analysed to study the evolution of WECs. The results presented below are in two sections, starting with the early stages followed by the later stages of WECs formation.

All SEM images presented here have been done on OP-S polished circumferential cross-sections and the bearing contacting surface has always been placed horizontally above the images.

5.3.1 Early stages of WEC/WEA formation (10 - 20 hours)

Although the analysis of the bearings has been conducted from the 20-hour samples to 10-hour samples, the results are presented from short to long test durations to discuss the initiation and growth of WECs.

In the 10-hour samples, very short microcracks have been observed without microstructural alterations found around the cracks, see examples given in Figure 5.17. The microcracks are found to be approx. 2-4 µm in length scattering randomly below the surface at approx. 100 µm depth. They orientate either vertically or horizontally with a slight inclination to the surface and have no connection to inclusions or primary spheroidised carbides. The microstructure around the microcracks are identical to that of the virgin steel matrix presented in Chapter 4.1.

The analysis of the 12.5-hour samples revealed similar microcracks (thus not presented).

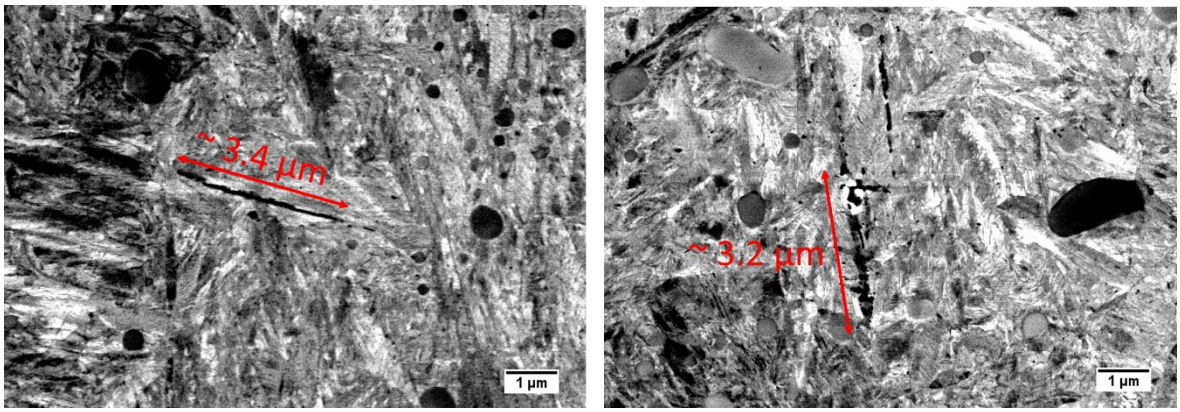

Figure 5.17: BSE SEM images of the 10-hour DGBB inner ring subsurface, showing very short microcracks (2-4µm).

Slightly longer microcracks have been observed in the 15-hour bearing samples, see examples shown in Figure 5.18. As can be seen, the length of the cracks has grown to over 6 µm. No cracks longer than 10µm have been observed in the samples analysed. However, the EBSD analysis of the equivalent areas (see examples of IQ maps in Figure 5.18(b); green arrows in the images pointing to primary carbides to help identify the locations) cannot identify the microcracks, possibly due to their shallowness. It is also clearly shown that no microstructure changes have occurred at this stage.

Similar characteristics have been observed in the 17.5-hour samples, hence have not been presented here.

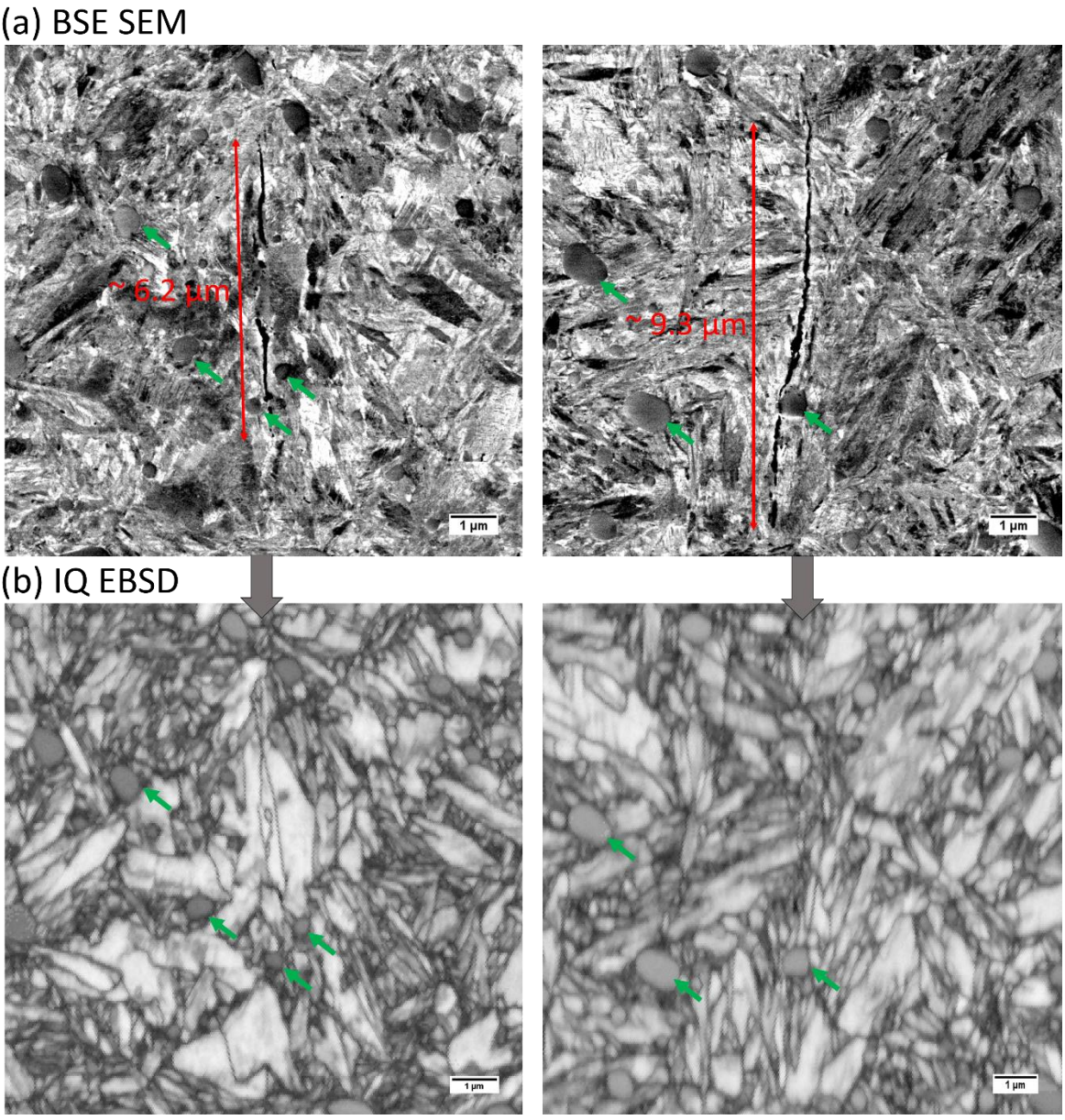

Figure 5.18: Images of the 15-hour DGBB inner ring subsurface showing microcracks of 6-10µm lengths: (a) BSE SEM imaging; (b) EBSD IQ map. Green arrows point to few primary carbides for easier identification of the location.

Apart from the short microcracks observed in the 10-hour and 12.5-hour samples, microcracks with multiple closely located parts orientated horizontally or vertically to the surface have been observed in the 15-hour and 17.5-hour samples, see examples shown in Figure 5.19.

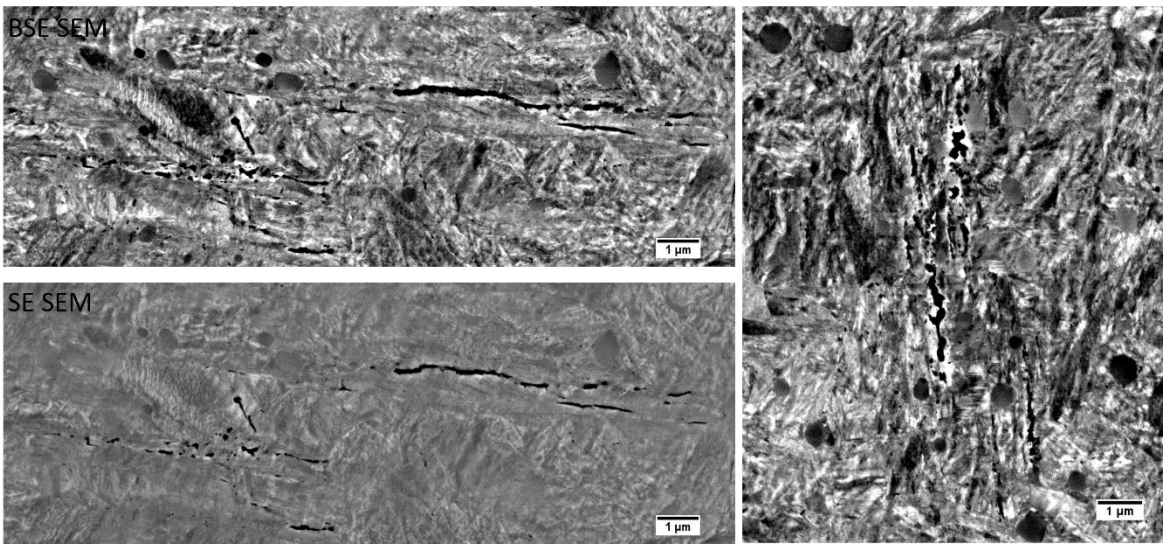

Figure 5.19: BSE and SE SEM images of multiple part microcracks in the DGBB inner rings tested for 15 and 17.5 hours.

Different from the singular or multiple microcracks shown above, joining together microcracks are seen for the first time in the 15-hour samples, see a close-up image shown in Figure 5.20.

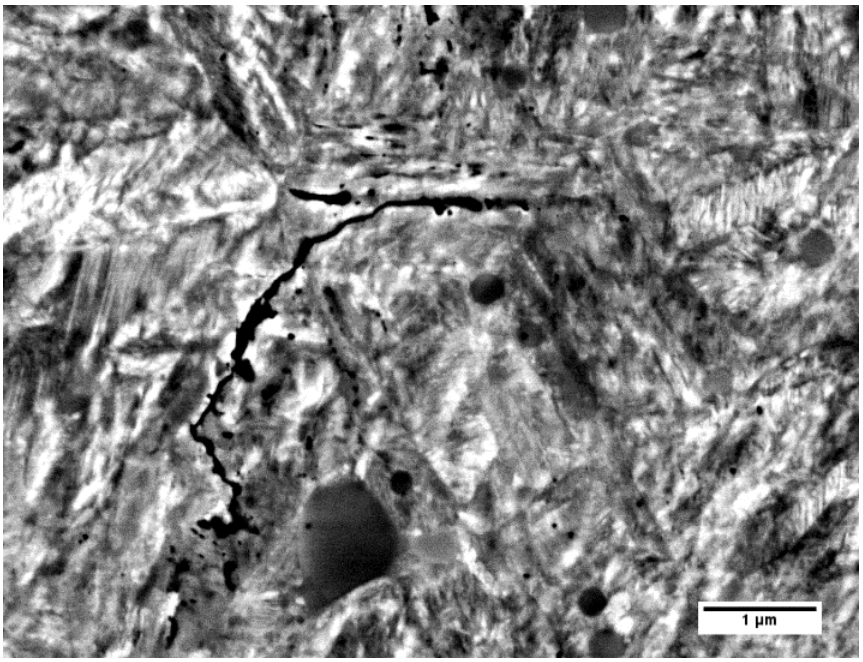

Figure 5.20: A BSE SEM image of vertically and horizontally joined microcracks in the 15-hour DGBB inner ring sample.

Furthermore, microcracks as small as 1 µm have been observed to interact with primary spheroidised carbides in the samples tested between 10 and 17.5 hours, see examples given in Figure 5.21. A variety of sizes and shapes of primary carbides

have been observed to interact with microcracks in these samples, however bigger primary spheroidised carbides (≥ 1 μm) have been seen to interact with microcracks more frequently than smaller ones (< 1 μm).

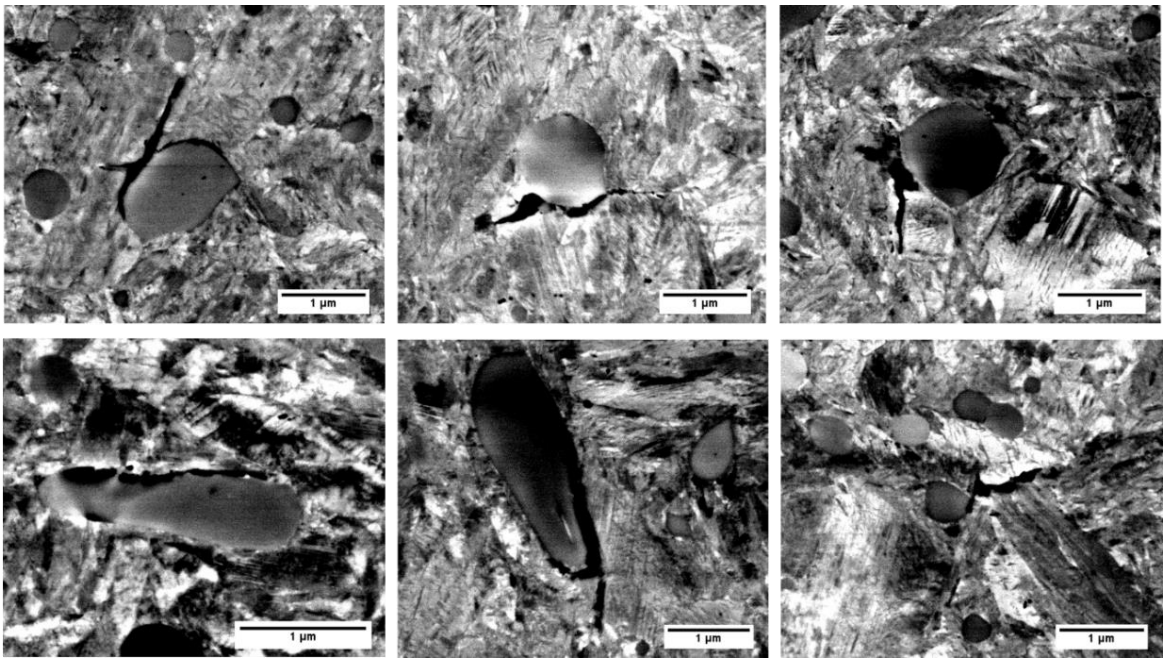

Figure 5.21: BSE SEM images of ~1 μm microcracks interacting with primary spheroidised carbides in the DGBB inner rings tested between 10 and 17.5 hours.

Similar microcrack-carbide interactions have been observed in 20-hour samples, however, the cracks are much bigger in size, as showed in Figure 5.22. In some cases, microcracks have cut through the primary spheroidised carbides. It is not clear whether the longer microcracks observed in the 20-hour samples have been extensions of the short (~1 μm) microcracks in the 10 to 17.5-hour or microcracks coincidentally passed next/through to the primary spheroidised carbides during their growth.

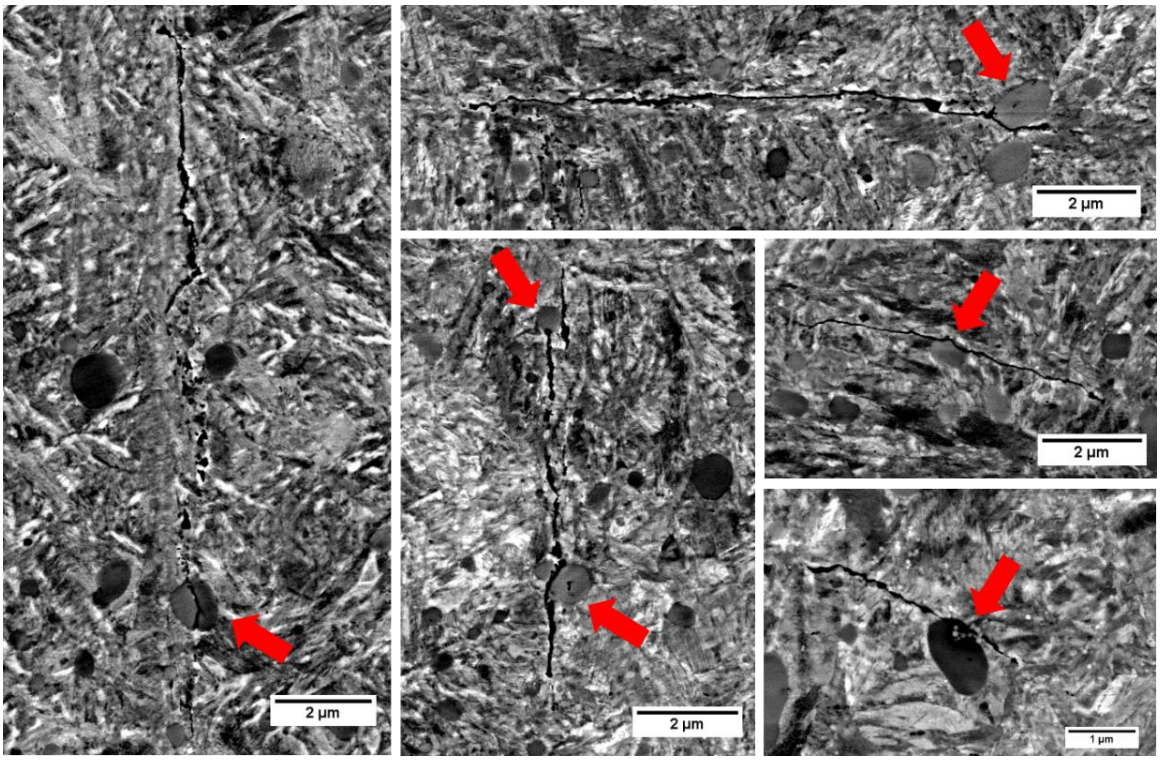

Figure 5.22: BSE SEM images of microcrack-carbides interaction in the 20-hour DGBB inner ring samples. Red arrows point to the primary spheroidised carbides.

In the 20-hour samples, a large amount of microcracks similar to those in the samples tested between 10 and 17.5 hours have been observed. Initial attempts in analysing the microcracks using the EBSD/EDX method showed to be similar to those found in the earlier hours samples, i.e. no cracks shown in the EBSD map. After persistent and careful examinations of a large amount of microcracks, some slightly deeper microcracks were identified in EBSD/EDX images as shown in Figure 5.23. The microcracks circled with red dash lines have appeared to be deeper than the one circled with pink dash lines, which are distinguishable due to their strong white contour in the BSE SEM image in Figure 5.23(a) and clear appearance in an SE SEM image and an IQ map in Figure 5.23(b)&(c). From the KAM map shown in Figure 5.23(e), no change in misorientation is observable around the deep microcracks. An increase in carbon intensities in the areas of the microcracks has been detected through EDX mapping showed in Figure 5.23(f). However, this is related to the microcracks topography effect, which is typically stronger for the low energy x-rays, although contamination due to the BSE imaging of the area beforehand cannot be excluded. For the microcrack adjacent to the primary carbides (circled by pink dash lines), significant changes have not been

observed in the EBSD and EDX imaging except for formation of a few new non martensite-martensite HAGBs, which indicate formation of equiaxed grains. In addition, more newly formed equiaxed grains have been observed within the analysed area (marked with red arrows) as shown in Figure 5.23(a-e). The equiaxed grains have been detected through the EBSD analysis, based on their comparatively higher IQ values (see Figure 5.23(c)), the new non martensite-martensite HAGBs (see Figure 5.23(d)), and low KAM values (see Figure 5.23(e)). The combination of these factors suggests that newly formed equiaxed grains are ferritic.

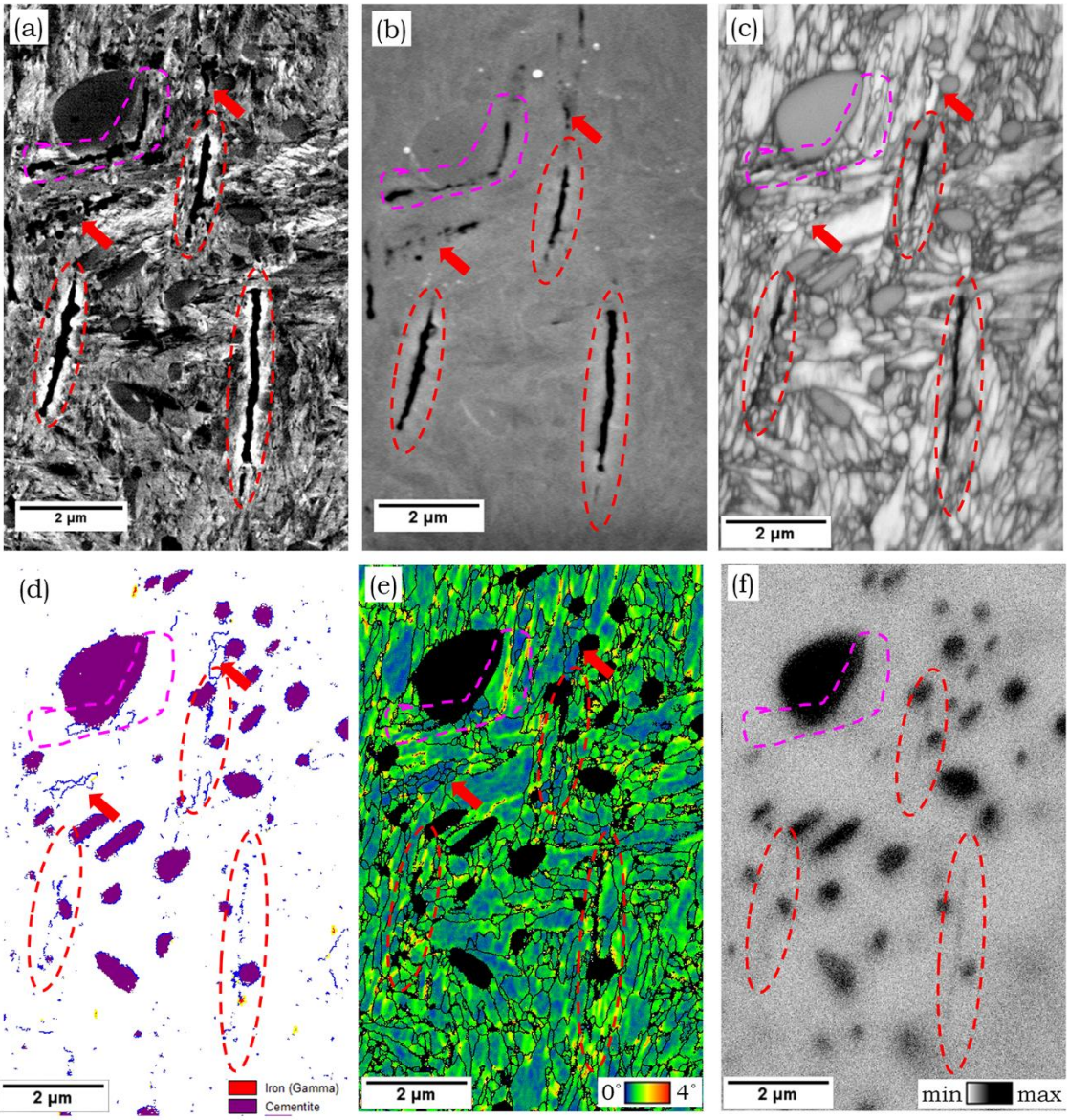

Figure 5.23: Results on microcracks in the 20-hour DBGG inner ring sample: (a) BSE SEM imaging; (b) SE SEM imaging in OP-S condition; (c) IQ map; (d) non martensite-martensite HAGBs map; (e) KAM(50nm,5˚); (f) EDX map of carbon (C-Kα).

In addition to the high quantity, much bigger and branched microcracks have been observed regularly in the 20-hour samples. Thin nanocrystalline WEA (<0.5µm width) at some crack surfaces has also been observed, see an example shown in Figure 5.24. Three enlarged areas in Figure 5.24 (areas marked as 1, 2, 3) show primary spheroidised carbides that have been cut through by microcracks and progressively transformed into WEA. In area 1, very small WEA is seen in one half of the carbide while the WEA has grown bigger in area 2. In area 3, half of carbide has been fully transformed into WEA.

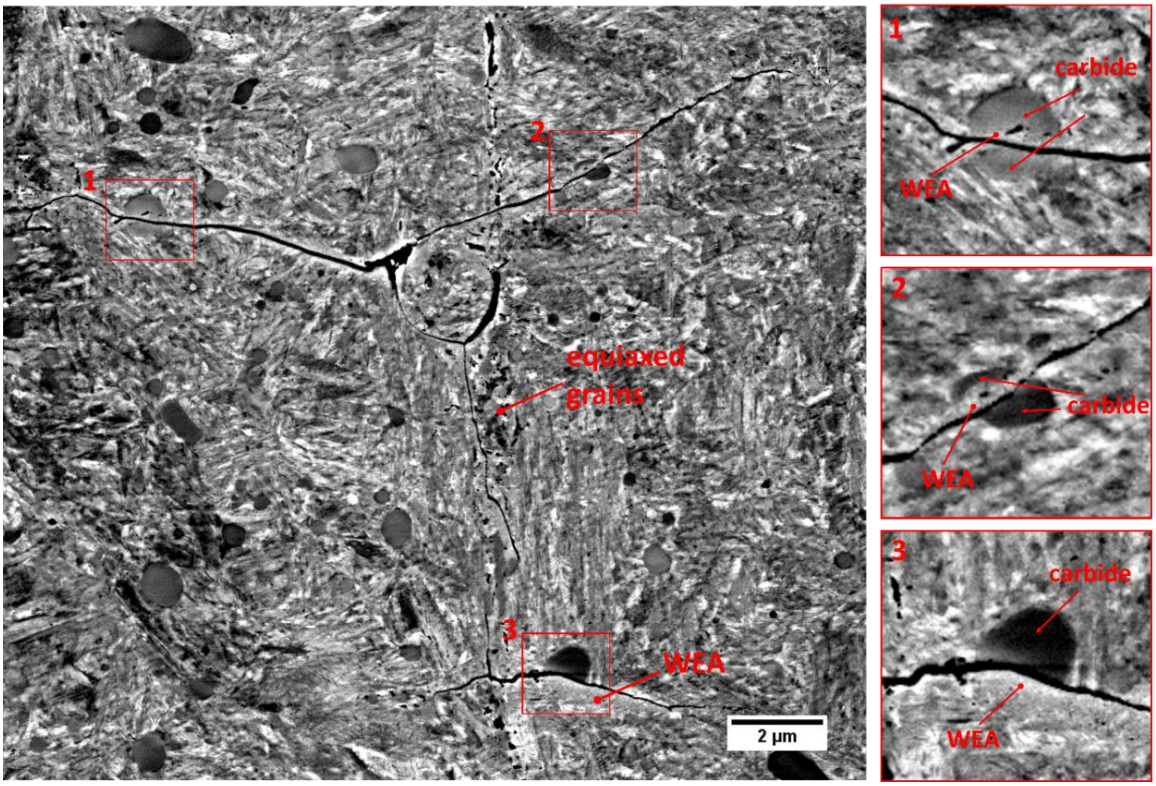

Figure 5.24: BSE SEM images of branched microcracks and evidences of carbide transforming to WEA in the 20-hour DGBB inner ring samples.

WEA has also been found to initiate at microcrack tips as shown in Figure 5.25, where two small areas of nanocrystalline WEA are marked in the BSE SEM image in Figure 5.25(a). It is observed that the nanocrystalline regions have formed asymmetrically relative to the microcrack (above or below the microcrack in the upper right or lower left part of the microcrack, respectively). These WEAs appear to be black spaces in the corresponding EBSD maps shown in Figure 5.25(b&c) due to the limitations in the EBSD resolution that is not sufficient to resolve the nanocrystalline grains in WEA and left them unindexed. It is also evident that the microcrack propagation direction appeared to change around the regions

decorated by nanocrystalline WEA. From the KAM map in Figure 5.25(b), it can be seen that low misorientation fine equiaxed grains have formed next to the WEAs, as a transition zone between the nanocrystalline WEA and the martensitic matrix. The EBSD map in Figure 5.25(c) shows that the WEC has grown through the martensitic matrix without following the grain boundaries, i.e. WECs are transgranular cracks, which is in agreement with the findings reported in [17].

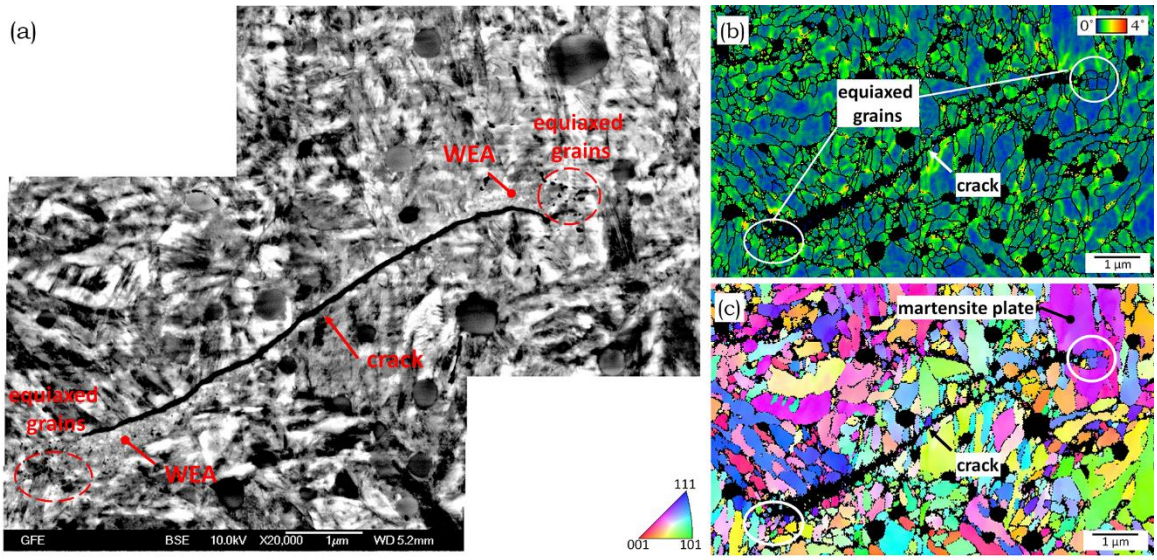

Figure 5.25: Images of a microcrack with WEA at the crack tips in a 20-hour sample: (a) a BSE SEM image; and the corresponding (b) KAM(50nm;5˚); (c) IPF with respect to the normal of the rolling direction.

Figure 5.26 presents examples of cracks in the 20-hour sample that appear to be 'rough' with less smooth curves as opposed to those shown earlier. Figure 5.26(a) shows one of the early stages of 'rough' crack formation that is followed by further growth, branching and appearance of microstructural alterations, but no nanocrystalline WEA around it as shown in Figure 5.26(b). Lastly, such cracks extend into bigger cracks with smoother curves and nanocrystalline WEA, which is formed around some parts of the cracks and only on one side of the crack, as seen in Figure 5.26(c). Microstructural alterations have been observed around the 'rough' microcracks as seen in Figure 5.26(a&b) and at the top of the WEC in Figure 5.26(c) and have been confirmed to be equiaxed grains through EBSD analysis of the similar area (see maps shown in Figure 5.27). The equiaxed grains have shown a comparatively high IQ value (Figure 5.27(b)), a low KAM value (Figure 5.27(c)) and formation of new non martensite-martensite HAGBs (Figure 5.27(d)), which suggests that newly formed equiaxed grains are of ferritic structure. For

comparison, the carbon and chromium distributions in this area, measured by EDX during the EBSD scan in the energy ranges of C-Ka and Cr-Ka, are presented in Figure 5.27(e&f). It is observed that a carbon homogenisation with slightly lower average intensity is observed in the region of equiaxed grains compared to that in the unaltered microstructure (Figure 5.27(e)). This is similar to that observed during the typical nanocrystalline WEA formation. However, no similar phenomenon is observed in the chromium distribution (Figure 5.27(f)). This has led to suggest that the carbon redistribution in the equiaxed grain region is due to the carbon migration from martensite and tempered carbides instead of primary spheroidised carbides during equiaxed ferritic grain formation.

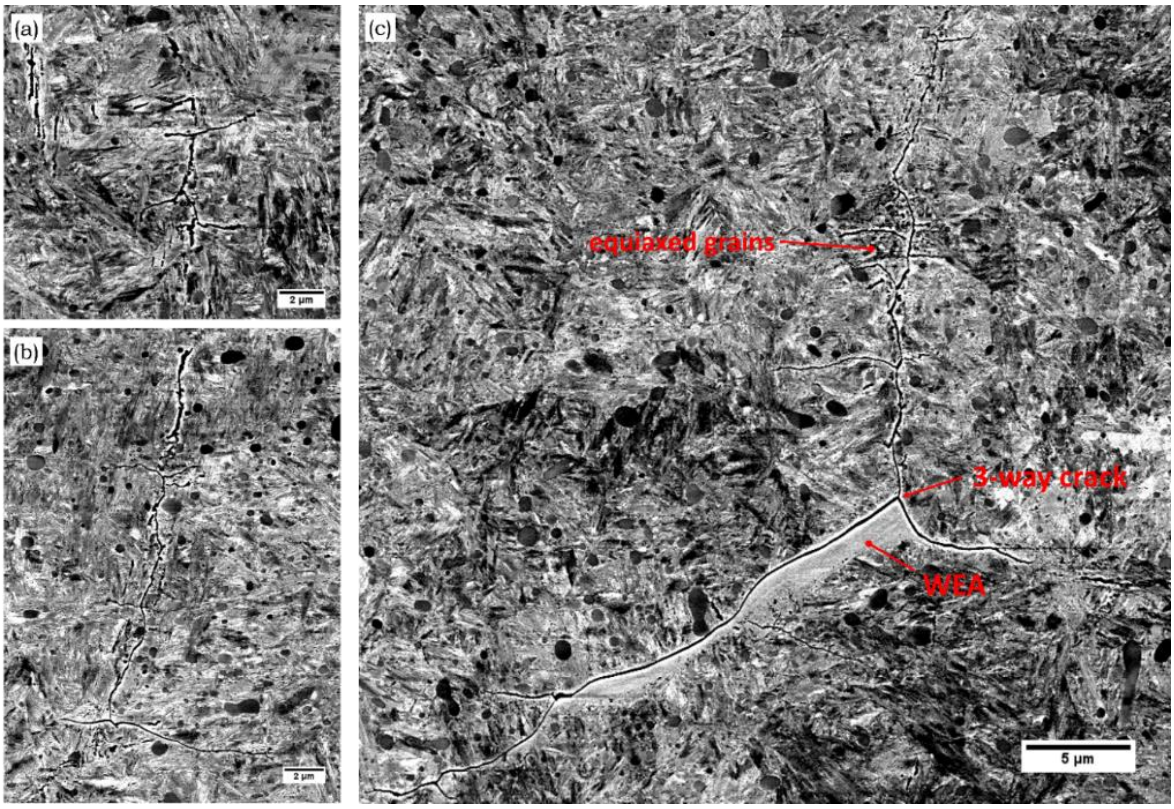

Figure 5.26: BSE SEM images of branched microcracks with rougher crack faces in a 20-hour DGBB inner ring sample: (a&b) without nanocrystalline WEA; (c) grown crack with nanocrystalline WEA.

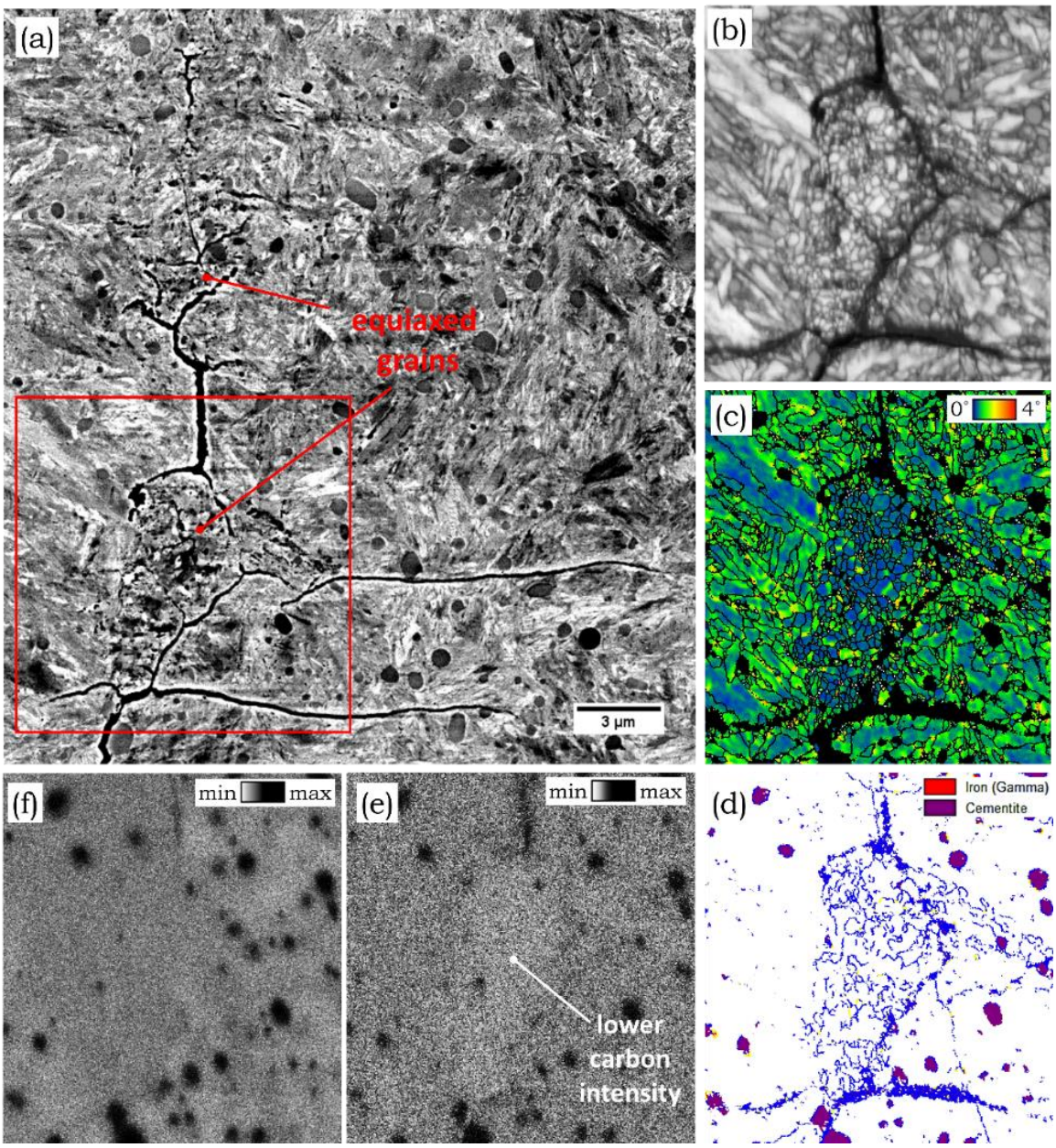

Figure 5.27: Maps of microcracks surrounded by equiaxed grains in the 20-hour sample: (a) BSE SEM imaging. EBSD/EDX maps of an area marked in a red rectangle: (b) IQ map; (c) non martensite-martensite HAGBs map; (d) KAM(50nm,5˚); (e) EDX map of carbon; (f) EDX map of chromium.

Larger WEAs are found to consist new microstructural features as shown in Figure 5.28. The microstructural features observed under BSE SEM (see in Figure 5.13(a)) have been confirmed to be newly formed elongated grains through the EBSD analysis shown in Figure 5.28(b, c, d). The elongated grains are relatively small of approx. 1-2 μm in length in the 20-hour sample compared to that in well-developed WECs shown in Chapter 4 (of approx. 5 μm length). The microstructure of area around the WEA/altered microstructure have the same appearance of the virgin

material (presented in Chapter 4) without any changes or preferred grain orientations, which indicates that no significant deformations or strains distributions is present in the surrounding matrix. The orientation of the elongated grains, marked with red lines in Figure 5.28(a), appears to be almost perpendicular to the striations (i.e. the deformation flow lines in WEA, marked with green lines in the same image), suggesting that the elongated grains have formed after the formation of WEA (i.e. nanocrystalline material). Furthermore, the appearance of the equiaxed grains with low KAM values (shown in Figure 5.28(b)), which do not normally exist in the initial martensitic microstructure, also suggests that the elongated grains are later stage of the microstructure changes instead of being residual fragments of martensite plates. In Figure 5.28(d), it can be seen that the orientation of the elongated grains does not match the martensite orientations within the prior-austenite grain (in the lower left corner). It is clearly seen that the WEC has traversed the prior-austenite and martensite grain boundaries.

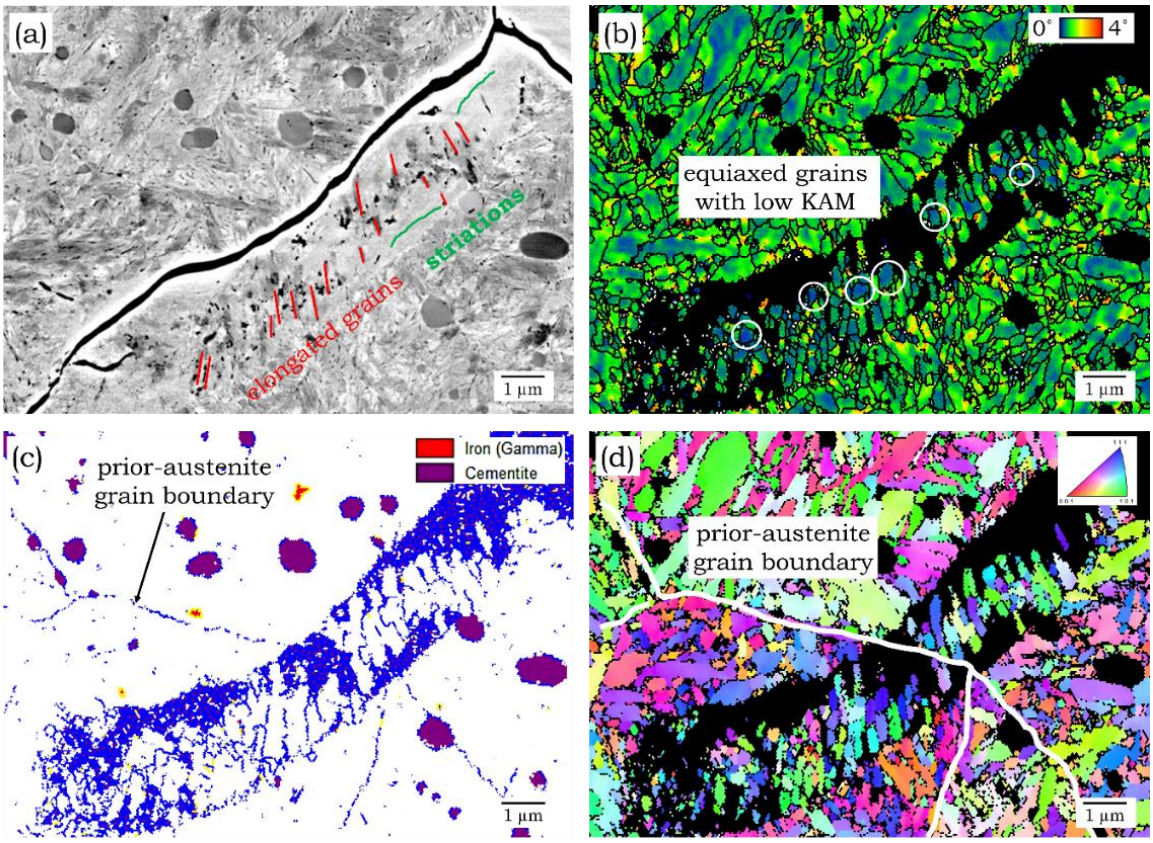

Figure 5.28: Elongated grains within WEA in the 20-hour sample: (a) BSE SEM imaging; (b) KAM(100nm,5˚) map; (c) non martensite-martensite HAGBs map; (d) IPF with respect to the normal direction during rolling.

5.3.2 Later stages of WEC/WEA formation (30 – 50 hours)

A number of occasions have been observed where WECs have reached the bearing surface in a 30-hour sample without any surface damage (based on the visual examination), as shown in Figure 5.29. However large subsurface WEC networks together with surface spalls have been frequently observed in a 40-hour and a 50-hour samples. This suggests that WECs initiate, form and develop in the subsurface of the bearings prior to reaching the surface and leading to final bearing failure.

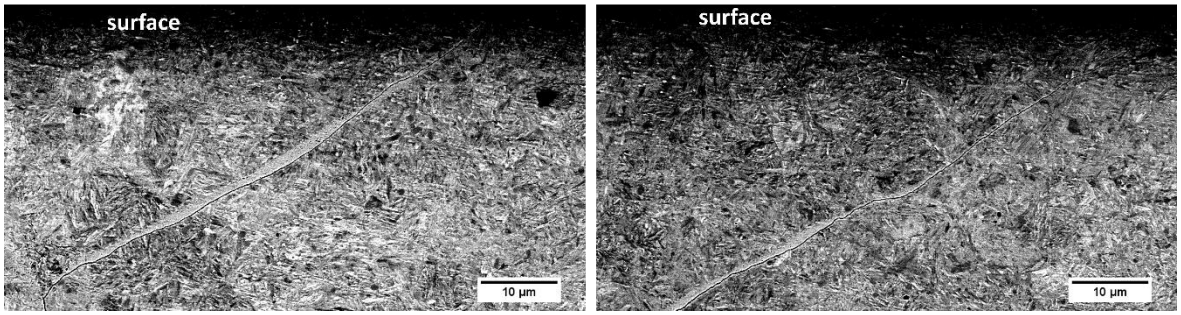

Figure 5.29: BSE SEM images of WECs reaching to the surface in the 30-hour sample.

Detailed investigations have been conducted on the 50-hour samples to study the characteristics of the fully developed WECs under the defined test conditions in addition to that of the sample from service presented in Chapter 4.

Figure 5.30 shows a BSE SEM image of a Y-shaped WEC (or 3-way crack branching) in the 50-hour sample, indicating features including nanocrystalline WEA, equiaxed grains, primary spheroidised carbides, microcracks and main cracks in the area. It is interesting to see that, the WEA appears mostly on one side of the crack at the end of the Y-crack (on the left side of the image), however, changes to border both sides of the crack when moving towards the Y junction then reduces to one side again. In the middle of the Y-shaped crack, altered microstructure similar to the area in the 20-hour sample shown in Figure 5.27 is observed. However, different to the 20-hour sample, intact primary spheroidised carbides with some being cut through or bordered by microcracks are also present. This, therefore, assumed to be undeveloped-WEA where altered microstructure in form of equiaxed ferritic grains, microcracks and intact primary spheroidised carbides are observed.

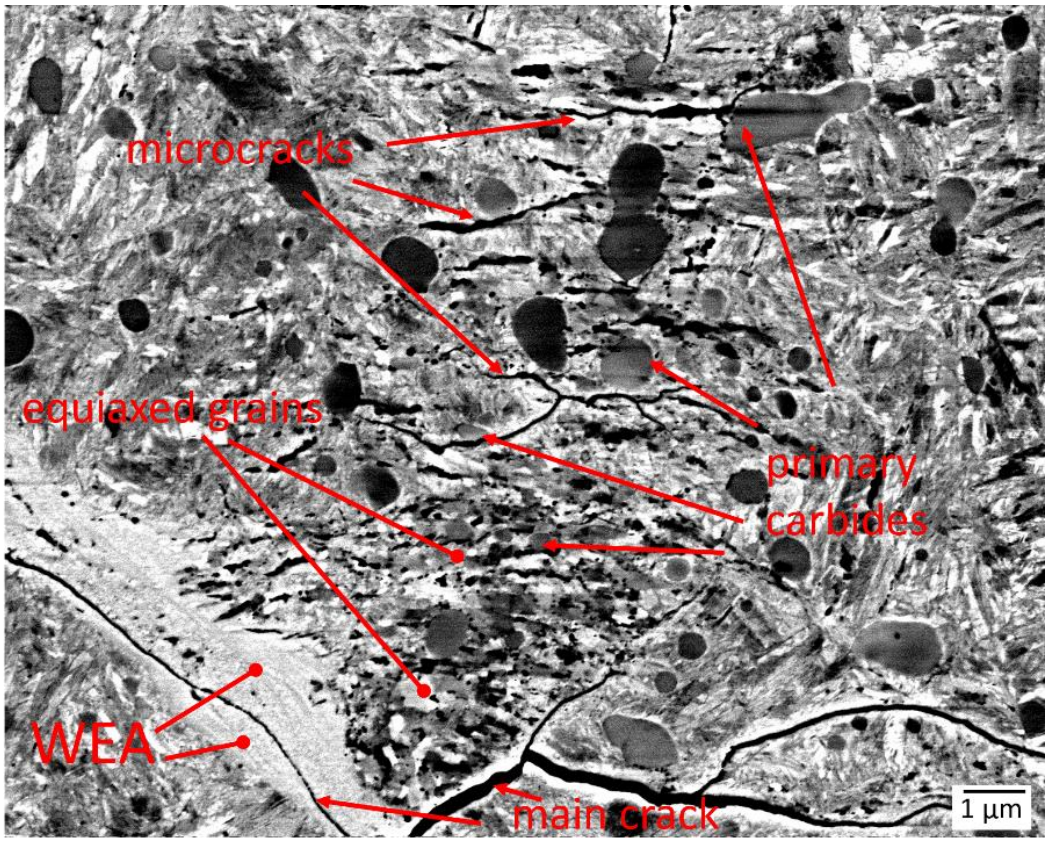

Figure 5.30: A BSE SEM image of the Y-shaped WEC showing microstructure changes and surrounding features in the 50-hour sample.

Figure 5.31 shows a collage of BSE SEM images taken at a magnification of 5000 in the 50-hour sample of a large area with multiple cracks and microstructure altered regions. As shown in the collage, two types of cracks, i.e. Y-shape and S-shape branching cracks, as well as WECs branched in random directions, are frequently observed. The S-shaped crack marked in the figure is seen to associate with a well-developed WEA observed in the middle of the BSE SEM collage. Below the WEA of the S-shaped WEC, Y-shaped WEC is seen with undeveloped-WEAs (similar to that observed in Figure 5.30). Above the WEA of the S-shaped WEC, microstructure alterations containing multiple parallel elongated grains are seen. Many intact primary spheroidised carbides are observed in the altered regions, indicating that the microstructure alterations in these regions are less advanced compared to the often observed nanocrystalline WEAs, e.g. those very close to the S-shaped cracks. Striations (deformation flow lines) in the WEA being mostly parallel/along the cracks, are however shown to vary, possibly due to the changing directions of stress distributions around the microcracks.

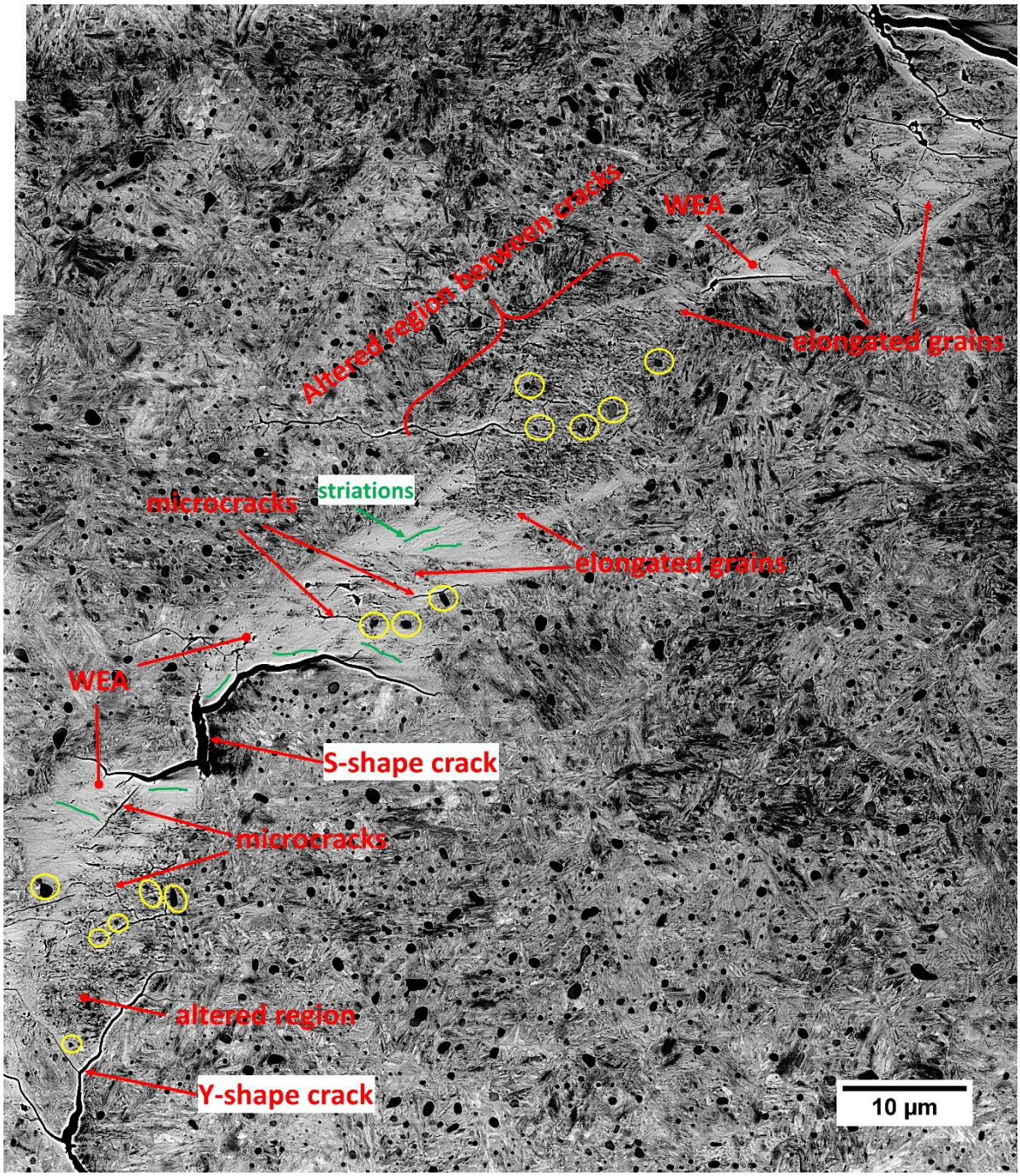

Figure 5.31: A BSE SEM collage showing microstructural features of WECs in the 50-hour sample. Green lines indicate the direction of striations (deformation flow lines) in the WEA; yellow circles highlight examples of intact primary spheroidised carbides in the microstructure altered regions.

Furthermore, WECs with WEA on both sides of the cracks have been often observed in the study, see examples given in Figure 5.32. However, no deformed or sheared carbide-like structures have been observed in WEAs throughout this study.

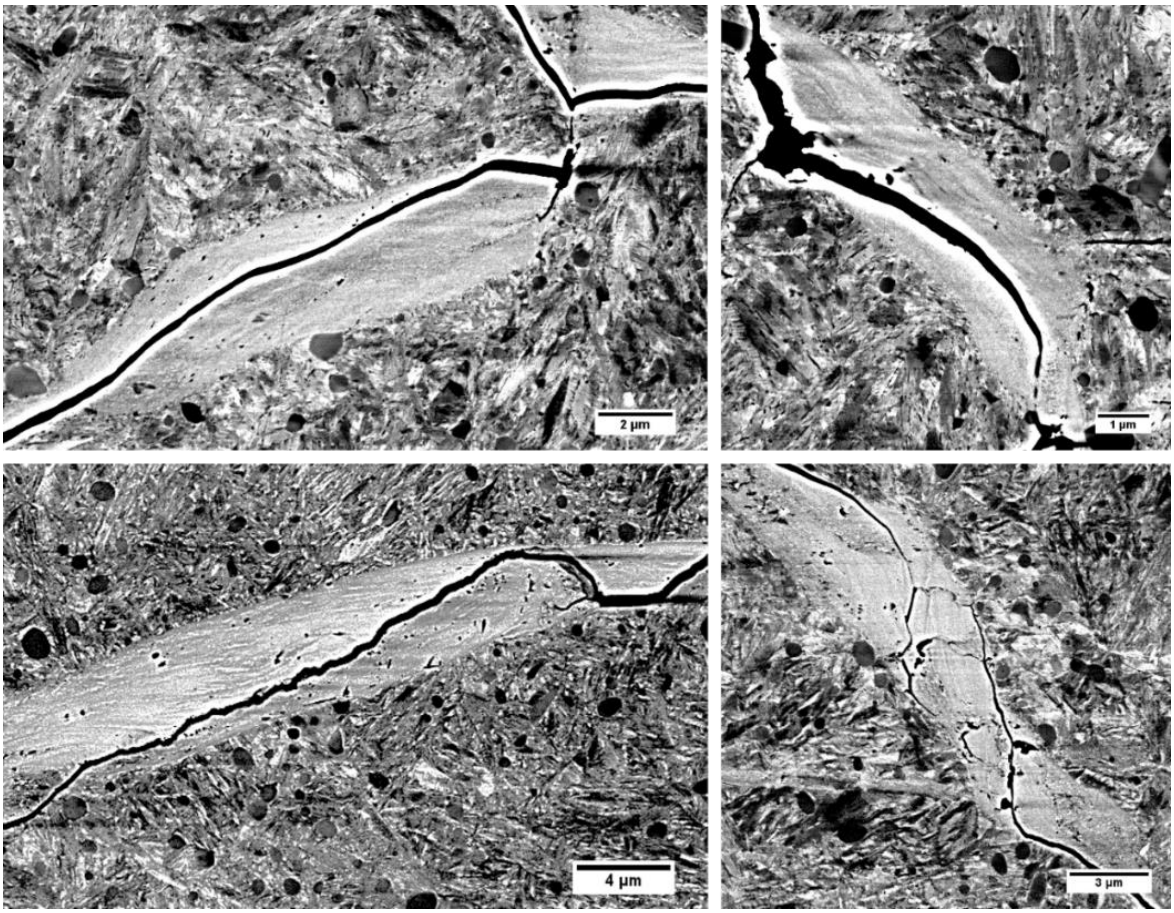

Figure 5.32: BSE SEM imaging of WEA on the both sides of the crack.

5.3.2.1 WECs under heat treatment

To investigate the influence of heat on WECs, especially to observe if elongated grains grow with increase of the temperature, a 50-hour sample with WEC networks has been heated up to different temperatures with the microstructure being examined under an SEM. The experiments have been performed in a large chamber SEM (Mira VP), where a special heating platform has been installed as a sample holder and the sample was pressed down by a needle, see a picture of the set-up inside of large chamber SEM in Figure 5.33. The samples must be prepared as thin as possible (approx. 2 mm) to ensure it being heated evenly across the whole sample. Such setup enables an in-situ imaging during heating experiment in vacuum conditions. However, due to the sensitivity of the BSE detector to heat and set-up of the experiment, which resulted in working distance to be restricted to no less than 16 mm, led to poor BSE images resolution during in-situ imaging. Therefore, instead of imaging the WEA in-situ, the sample was firstly heated to 300˚C, held at that temperature for 1 hour then cooled down to room temperature inside the large chamber SEM under the vacuum to avoid oxidation. The sample

was then transferred to a JEOL JSM-7000F SEM for inspection. The same procedure has been repeated at 400˚C.

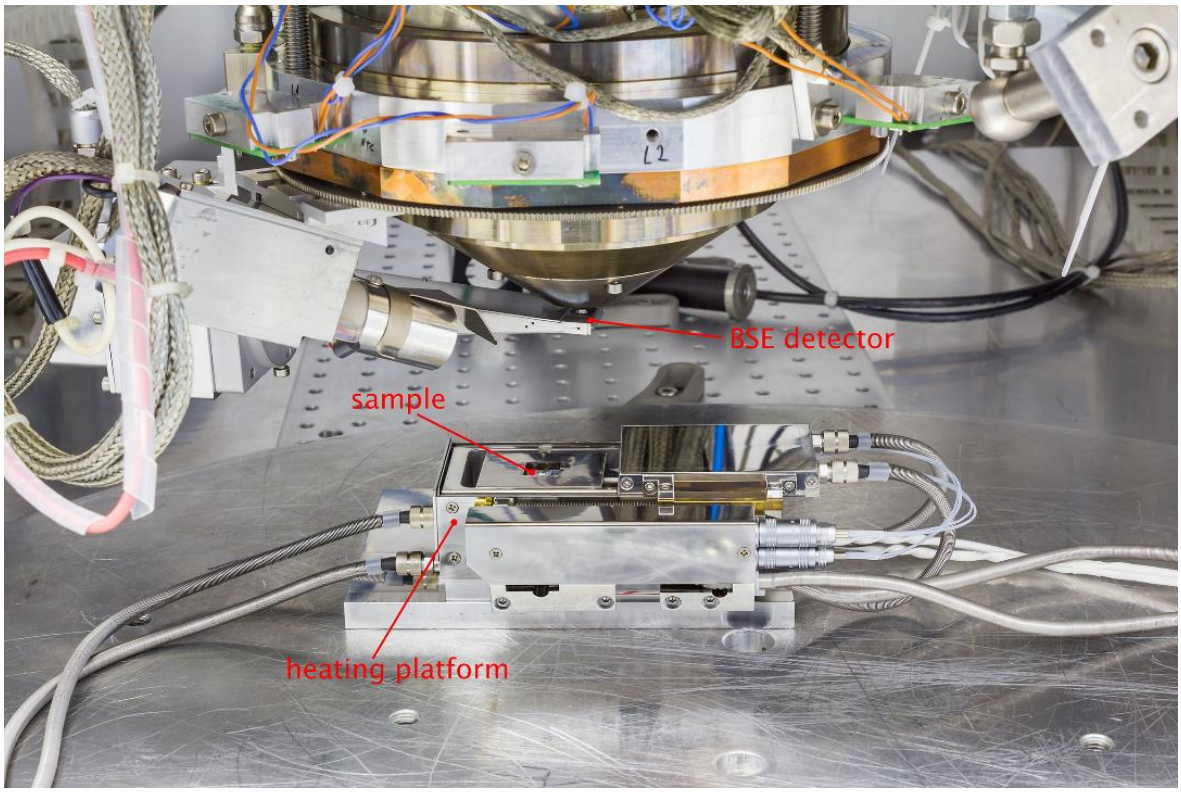

Figure 5.33: A picture of the inside of large chamber SEM (Mira VP) showing the heating platform and sample location.

The BSE SEM images of the original 50-hour WECs sample and the same sample after 300˚C and 400˚C heat treatments are shown in Figure 5.34. The WEA and elongated grains observed in the original 50-hour sample do not show any obvious changes after being heated at 300˚C for 1 hour. The same sample was then returned to the large chamber SEM and heated to 400˚C for another hour. After which, microstructural changes in the WEAs are clearly detectable using BSE SEM imaging: the elongated grains become harder to be identified and grain coarsening is observed in areas of the original nanocrystalline zones.

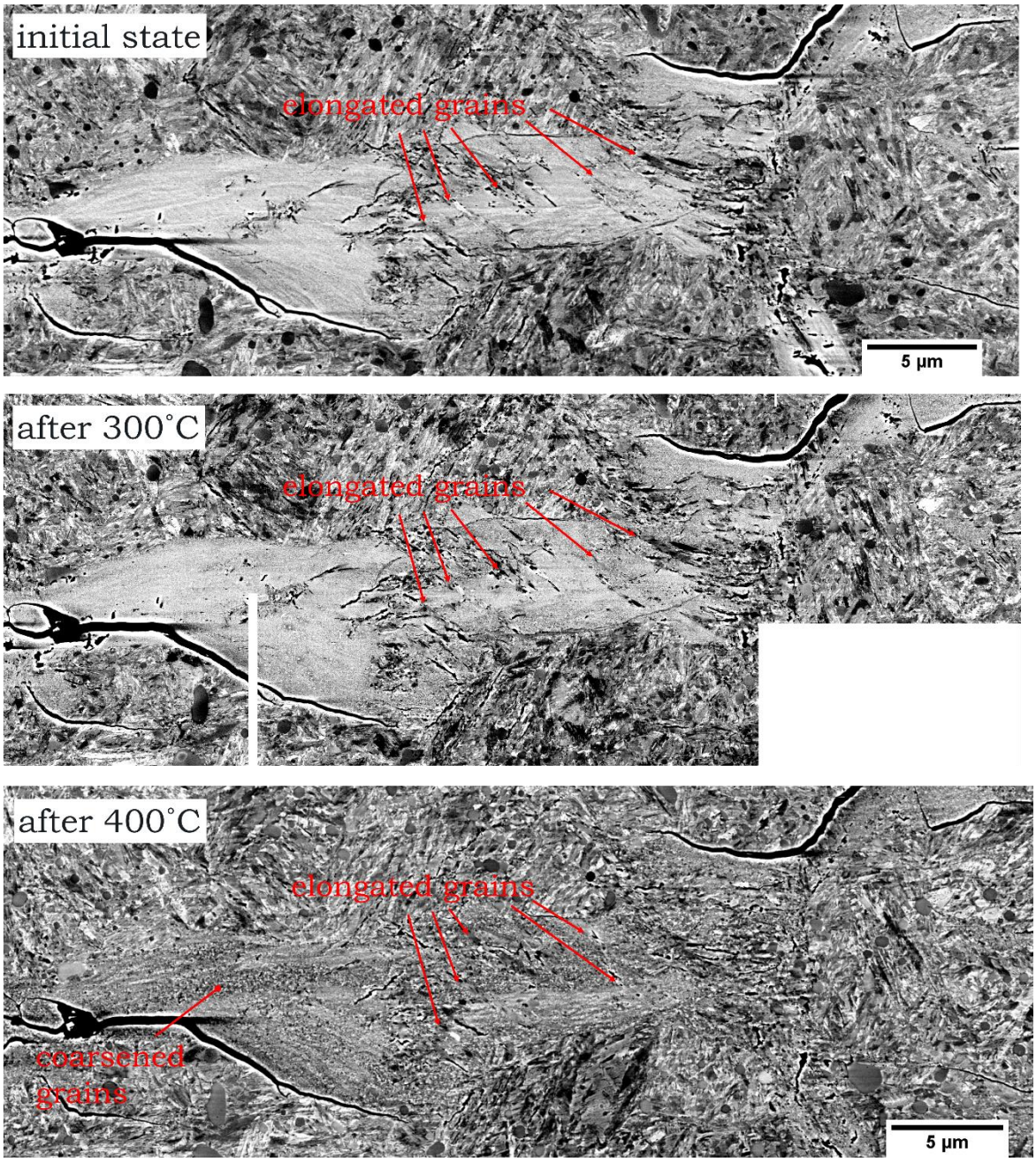

Figure 5.34: BSE SEM images of the original 50-hour WEC sample and the same area after being heat treated at 300˚C for 1 hour then at 400˚C for another hour.

EBSD/EDX analysis has been performed on the sample after the 400˚C heat treatment and compared with the original 50-hour sample to further understand the changes in the elongated grains and WEAs. Before the EBSD analysis the heat treated sample was slightly re-polished with OP-S to remove contamination from previous imaging that resulted in slight change in analysed surface layer, hence some differences between initial state and after 400˚C are expected. Figure 5.35

shows the EBSD IQ and EDX carbon maps of the WECs in its initial state and after the 400˚C heat treatment. The heat treatment has resulted in grain coarsening (i.e. Ostwald ripening) of the nanocrystalline WEA. The fact that grain coarsening has occurred at temperature as low as 400˚C suggests that the nanocrystalline material is unstable. A higher concentration of coarsened grains has been detected in the areas with slightly higher carbon intensity as shown in the EDX carbon map (Figure 5.35(d)). Due to the fact that the sample surface has been slightly re-polished after 400˚C heat treatment, it is difficult to confirm the influence of heat treatment on elongated grains. However, no significant growth of the elongated grains is observed, which suggests that their growth is not driven just by increase of the temperature.

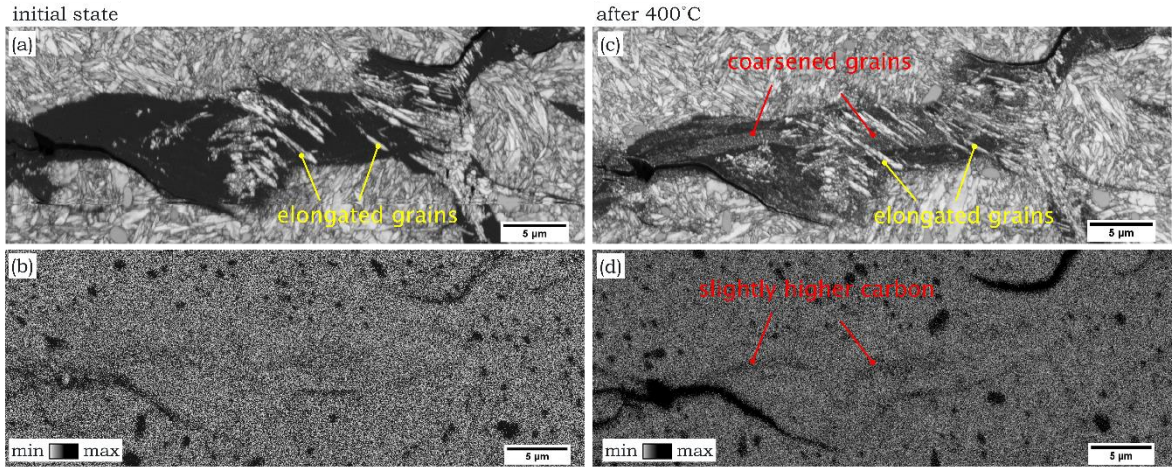

Figure 5.35: EBSD IQ and EDX carbon maps (C-Kα) for WECs in a 50-hour sample (a&b) and the corresponding area in the same sample after being heated at 300˚C for an hour and at 400˚C for an hour (c&d).

5.3.3 Discussion

Many studies have been conducted over decades to understand WEC/WEA and the drivers for its formation. However, the initiation, development and the relationship of WECs with related material microstructural changes are still not well understood. This study, for the first time investigated the temporal evolution of WEC through detailed analysis of WECs formed at different stages of its life reproduced in DGBBs under electrical current influence in laboratory.

- Initiation of microcrack and WEA (less than 20 hours)

The results show that randomly scattered shallow horizontal and vertical microcracks of a few microns in length without any microstructural changes have been found to form in the subsurface of the DGBB inner rings (i.e. approx. 100 μm below the surface), which is close to the depth of the calculated maximum shear stresses (i.e. approx. 130 μm below the surface) in the early hours of the over-rolling (less than 20 hours). However, formation of these microcracks cannot be related to pure stress induced cracking in the maximum shear stresses zone, since when the electrical current flow is absent the bearing survives hundreds of millions of rolling cycles and only result in formation of DER/LABs without microcracks in the subsurface. Interaction of electrical current with tribofilm has been reported to result in lubricant decomposition leading to formation of atomic hydrogen, which know to accelerate subsurface cracking (i.e. hydrogen embrittlement) [165]. Therefore, this may be a result of the electrical current applied to the bearing during the tests, although cannot be confirmed at this stage.

Microcracks formed next to or cutting through primary spheroidised carbides observed at this stage could be a result of electro-thermal effects due to the differences in electrical and thermal properties of primary carbides and martensitic matrix [142]. However, microcracks are also frequently seen without primary spheroidised carbides or inclusions in vicinity, suggesting that there is more than one mechanism for microcrack initiation. The exact microcracks initiation processes require further confirmation in future studies.

Microcracks growth and branching have been observed with further cyclic loading that could be associated with an increased stress level around initial shallow vertical or horizontal microcracks that act as stress raisers in the material matrix. As crack branching occurs, thin areas of nanocrystalline WEA is observed adjacent to the microcracks as early as 20 hours of testing. As shown in Figure 5.24, primary spheroidised carbide dissolution processes have also been observed during early stage of WEA formation adjacent to microcracks. At this stage, it is difficult to confirm whether formation of the nanocrystalline WEA next to a crack is attributed to severe plastic deformation [107, 118] or rubbing at the microcrack faces [30, 98, 119] leading to grain refinement under cyclic loading. Severe plastic deformation [107, 118], where local areas are plastically deformed resulting in high dislocation density, can develop dislocation cell structures. Under further cyclic

loading the dislocation cell structures can evolve into newly formed ferritic nanograins with carbon segregation at the grain boundaries such as nanocrystalline WEA as a result of a dynamic recrystallisation processes [91, 107, 117]. Whereas, according to the crack face rubbing hypothesis, WEA forms due to high adhesion and friction between the faces of subsurface cracks due vacuum conditions and absence of lubricant in the subsurface [166]. On a number of occasions throughout this study WEA has been observed to form on both sides of cracks, hence the possibility of crack faces rubbing cannot be excluded. However, the fact that the majority of the microstructure alteration only appears on one side of cracks suggest that the microstructural transformation can occur not only due to rubbing of the crack faces.

Small nanocrystalline WEAs have also been observed to form asymmetrically along a microcrack, where the microcrack appears to curve around the WEAs. This may suggest that the concentrated stress at the crack tip has triggered the formation of nanocrystalline WEA rather than rubbing at the microcrack faces [30, 98, 119]. Once nanocrystalline WEA is formed it acts as a barrier for crack propagation, resulting in a slight change in the propagation direction of microcracks. The transition zone of fine equiaxed ferritic grains between the nanocrystalline WEA and the martensitic matrix, similar to the transition from WEA to material matrix in the butterfly wings [113], may explain the stress concentration in front of the crack tip.

About which forms first: cracks or WEAs? As shown in the very early life of the bearings (<20 testing hours), WEA has not been observed without microcracks, whereas very short microcracks (2-4 μm) without WEA have been observed in as early as 10-hour samples. However, these microcracks are extremely small (and difficult to identify), and WEA has been found to initiate very soon after these microcracks have formed (in 20-hour samples), suggesting although microcracks form before WEAs but possibly develop cooperatively afterwards. Even though other researchers have also reported ‘crack first’ [2, 92, 106], this study has presented detailed evidence in chronologically tested bearings. Another observation is that, after WEA started to form, microcracks and WEA growth is found to be rapid, e.g. longer cracks and increasing size of WEAs, as shown in the 20-hour samples.

- Growth of WECs (>20 hours)

As microcracks grow and branch out, cracks with 'rough' crack surfaces and groups of equiaxed grains intermixed with intact primary spheroidised carbides start to emerge in the vicinity of the so-called 3-way or Y-shape cracks bordered by WEA. The groups of ferritic equiaxed grains are thought to be undeveloped WEA since primary spheroidised carbides were found to remain intact resulting in insufficient carbon [119]. Therefore, the motion of the dislocation was not inhibited due to carbon segregation at the grain boundaries, and the equiaxed grains continued to grow. However, it is not clear why in some areas primary carbides are destroyed, leading to carbon pinning to grain boundaries and stabilisation; and in other regions primary carbides remain intact while undeveloped nanocrystalline WEAs (equiaxed grain groups intermixed with intact primary carbides) form. This suggests that primary spheroidised carbides play an essential role in the WEA stabilisation process by carbon segregation at grain boundaries, thus formation of hard WEA [92, 119].

Elongated grains within nanocrystalline WEA, as well as in undeveloped WEAs, are observed in the samples tested for as short as 20 hours at lengths between 1 and 2 μm. These grains grow up to 7 μm in samples tested for 50 hours, hence it is suggested that elongated grains form after WEA and grow in length under increased over-rolling cycles [91]. Similar to the elongated grains found in this study, engineering bands within WEA and slip bands outside WEA have been reported to form due to severe plastic deformation by Ooi et al. [91]. It is also possible that elongated grains form due to adiabatic shearing in localised areas of deformed WEA [91, 167], where high strain rate leads to the generation of heat that cannot be dissipated fast enough into the surrounding, resulting in localised areas that are softened and consequently promoting the growth of the grains (similar to what has been observed in heat treatment). Growth of the grains under stresses available in the area may have resulted in the elongation of the grains. Microstructure changes in the form of grain coarsening have occurred between 300-400˚C in the heat treatment experiment without induced stresses, which suggests that the temperature sufficient for grain growth during cyclic loading should be below 400˚C. It is also possible that with further over-rolling, areas with elongated grains become deformed resulting in nucleation of new dislocations that arrange in subgrains, and later lead to another cycle of equiaxed grain formation [160].

At the latest stage, different branching WECs (S-shaped and Y-shaped cracks) with highly inhomogeneous microstructure containing defects and grains of varying sizes in WEA have been observed. The morphology of WECs and microstructure alterations at this stage are similar to those reported in [91], where a hydrogen pre-charged DGBB inner ring was used in the study under test conditions near identical to those in this study. Instead of hydrogen pre-charging, constant electrical direct current has been applied to pass through the DGBB in this study. Electrical loading has been suggested to accelerate dislocation movement and enhance nucleation rate of ferrite during recrystallisation to form ultrafine-grained ferrite [145]. However, it is not clear whether the comparable low current used in this study has led to the microstructure transformation similar to that observed by [145]. Others [165] have suggested that testing with electrical current and 'bad lubricant' may have resulted in hydrogen diffusion due to electrochemical reaction leading to WECs formation in bearings. Hydrogen is also known to reduce the energy required for the crack formation and increase dislocation density via mechanisms such as hydrogen-enhanced local plasticity (HELP), hydrogen-induced cracking (HIC), hydrogen-enhanced decohesion (HEDE), hydrogen-enhanced strain induced vacancy (HESIV) or others [14, 30, 168, 169]. Hence, it can accelerate crack development and also facilitate nucleation of cell-dislocation structures that transform into equiaxed ferritic grains. Since the hydrogen concentration has not been quantified in this study, its influence on the microstructure changes is not completely disregarded. Even though, hydrogen has been commonly accepted as an accelerator for the WECs formation, it should also be commonly accepted that the hydrogen is not the only possible driver for WECs initiation. It was demonstrated that WECs formed in bearings of vacuum pumps that were tested with a fully fluorinated lubricant to exclude the influence of hydrogen on the WECs formation [100].

5.3.4 Conclusions

A detailed microstructure investigation on the temporal evolution of WECs in radially loaded DGBB inner rings under electrical current influence has revealed the following:

- Very small microcracks of <4 μm length are found to form randomly scattered vertically and horizontally in the 10-hour bearing samples and are

suggested to be the earliest stage or initiation of WECs; at this stage, no microstructure alteration has been observed. No microcracks and non-metallic inclusion interaction is found, however microcrack-carbide interaction is observed at this stage. The driver of the microcracking is thought to be the electrical load applied to the bearing in this study, however requires further investigation to confirm.

- The microcracks are found to grow slowly to up to 7 μm in the bearings tested for 12.5, 15 and 17.5 hours and no microstructural alterations occurred until it increased to 20 hours. Several new features have been observed to be created in the 20-hour samples, including branched microcracks, early states of nanocrystalline WEA, transition zones in the form of equiaxed grains at crack tips as well as small-elongated grains within WEA. Although WECs observed in the 20-hour samples are small, it is believed to be the first stage of nanocrystalline WEA formation.
- After 20 hours, WECs are found to grow rapidly and to reach the surface after 30 hours of testing when no visible surface damages have been observed. Following which, large WEC networks are formed in the 40 and 50-hour samples similar to those observed in the failed bearing samples in Chapter 4.
- Primary spheroidised carbide dissolution has been observed to transform to WEA at very early stages when microcracks cut through the carbides. Primary spheroidised carbides although might be not critical for initiation of the microcracks, but however are possibly the essential part for WEA stabilisation by carbon segregation at the grain boundaries, thus hard WEA formation.
- WEAs are found to form mostly on one side of the crack faces, hence it is suggested that WEA formation mechanism is unlikely to be crack rubbing.
- Elongated grains are found to form at the later stages of WECs formation and appeared to grow in localised areas of nanocrystalline WEAs or undeveloped WEAs as the over-rolling cycle increases.
- The WEC heat treatment experiment has shown that temperature of approx. 400˚C is sufficient to cause microstructure change in nanocrystalline WEA.

Chapter 6

Results: Root Cause Investigations with Other Parameters

To further investigate and confirm the WEC initiation/formation mechanism proposed in Chapter 5, especially whether the electrical current is the driver of the very short microcracks in the early stages of WECs, a few additional experiments have been conducted on DGBBs under different test conditions. The main aim was to understand the influence of the current, lubrication and its interaction. Two types of tests have been performed to investigate the influence of:

- Direct current loading, and whether it is responsible for the development and the formation of WEA once microcracks were formed. The test was conducted on the L11 test rig under same testing conditions as those tests described in Chapter 5 except that the electrical current applied to the bearing was turned off after 15 hours and the test continued to run for additional 50 hours;
- Lubricant, and whether interaction of the electrical current loading with lubricant is responsible for the development of WECs. The test was also conducted on the L11 test rig under same testing conditions as those described in Chapter 5, except that a 'high reference' oil (PAO 8 base oil) was used instead of the 'low reference' oil (Total Transmission Ti75W80).

Due to the time available to this study, only limited number of tests have been conducted hence serve as points of check rather than full detailed investigations.

6.1 15 hours with electrical current + 50 hours without it

From the investigations presented in Chapter 5, it becomes clear that microcracks form in a subsurface of the inner ring as early as after 10 hours of testing under the defined test conditions where electrical current is applied and a 'low reference

lubricant' is used. This experiment aims to understand whether the electrical current loading is essential for microcracks to develop into WEC networks. Details of the test conditions are listed in Table 6.1 under Test 1. According to the results obtained in Chapter 5, microcracks should have formed in the bearing inner ring at the point that the electrical current was switched off at 15 hours. No bearing surface damage was observed after the test was stopped after a total of 65 hours. Same metallographic analysis and microscopy analysis procedures as described in Chapter 3 have been used to analyse the inner ring from this test. The results are presented in the next section.

Table 6.1: Test conditions for the tests on L11 test rig; Test 1 presented in subchapter 6.1, Test 2 in subchapter 6.2.

	TEST 1	**TEST 2**
Test bearing:	deep grove ball bearing (DGBB) 6206 type	
Bearing material:	AISI 52100 through-hardened martensite	
Oil Temperature (OR):	80˚C (self-regulating)	
Speed:	9000 rpm	
Radial load:	4 kN per test bearing	
Hertzian stress (IR):	2634 MPa	
Direct Current:	25 μA	
Lubrication:	Total Transmission Ti75W80	PAO 8 base oil
Duration:	15 hours with current + 50 without it	20 and 50 hours with current

6.1.1 Results and Discussion

Two sections/samples from the 15 hours with direct current and additional 50 hours without current tested DGBB inner ring (see TEST 1 in Table 6.1) were cut in randomly selected locations and metallographically prepared as described in Chapter 3. Initially, the samples were checked for WECs using a LOM, however no microstructural changes were observed at a maximum possible magnification of the microscope. BSE SEM observations were then performed focusing on depths of approx. 100 μm below the surface, where most of the cracks were found in the study presented in Chapter 5.

Vertically and horizontally orientated microcracks of up to 5 μm length have been detected in the subsurface of the samples with few examples showed in Figure 6.1. The microcracks found here appeared to be similar to the microcracks observed in the samples tested for 10, 12.5, 15, and 17.5 hours presented in Chapter 5. An interaction between primary spheroidised carbides and microcracks, similar to those presented in Chapter 5, has also been observed in the sample and examples are shown in Figure 6.2. These features are very similar to those observed in samples in bearings tested for up to 15 hours as described in Chapter 5, although, an additional 50 hours have been run in this test.

Further analysis with BSE SEM has confirmed that branching of the microcracks or WEC formation had not occurred in this test after an extensive examination of the samples has been conducted. Therefore, it is suggested that continuous current loading may be essential for the microcrack growth, branching and evolving into WEC. It also suggests that rubbing of the crack surfaces is unlikely the mechanism for the WEA formation [9, 13, 59, 88, 92, 95, 98, 119, 122]. Since microcracks were formed in the first 15 hours of the test conducted with the continuous current loading, but microstructural alterations next to the microcracks could not be detected even though the sample was RCF tested for additional 50 hours. It is worth pointing out that only limited number of cross-sections of a ¼ of the DGBB inner ring has been examined, thus it cannot be 100% confirmed that no WECs formed in other parts of the inner ring. Nevertheless, based on the comparatively large number of samples being analysed in this study, the probability of WECs being not discovered in the inner ring is very low, especially for the extended duration of 65 hours of RCF in this test, if WECs existed, it should not have been very difficult to be observed. For example, the WECs formed in the 30-hour bearing had been extensive and had led to surface spalls after 40 and 50 hours of testing in those described in Chapter 5 when electrical current was applied throughout the tests.

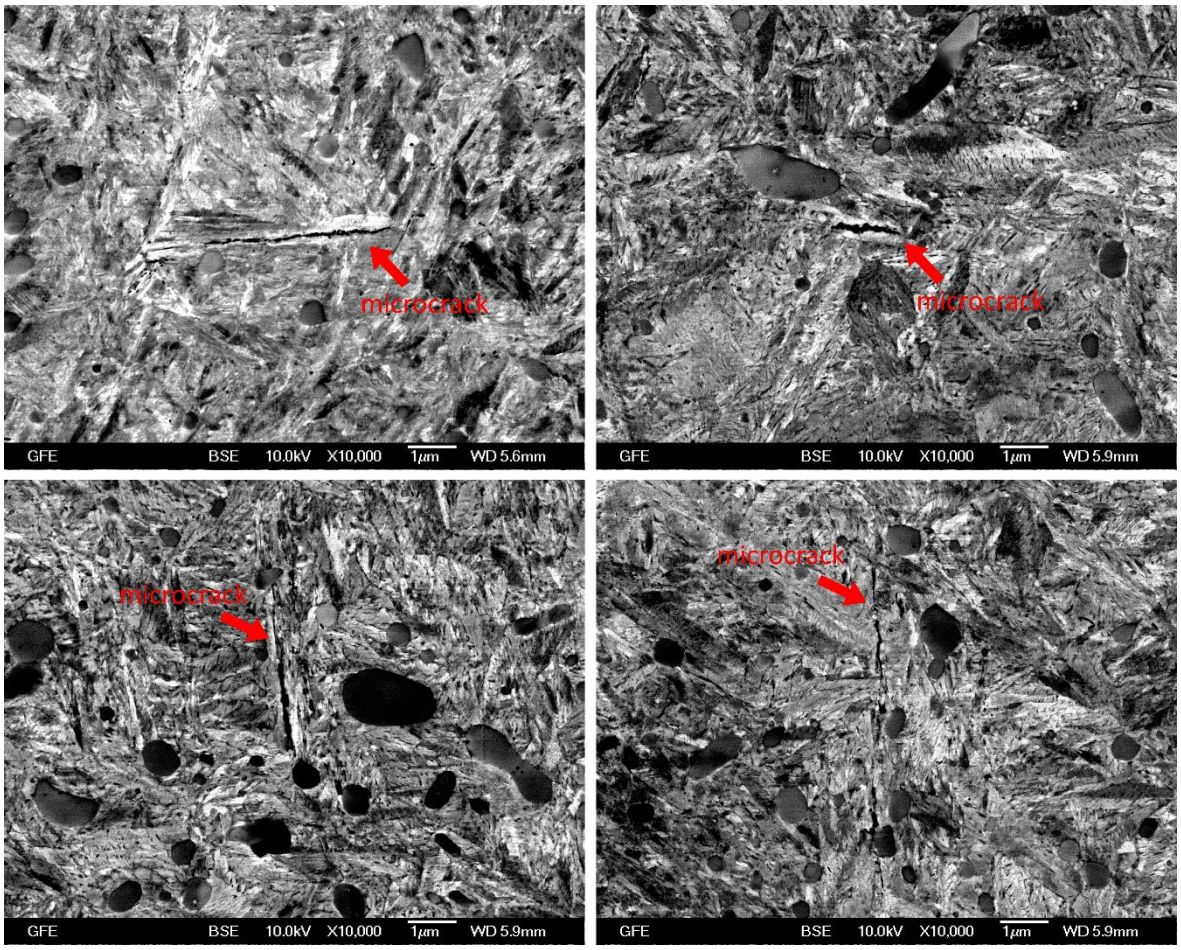

Figure 6.1: BSE SEM images of microcracks found in the sample tested for 15 hours with current plus additional 50 hours without current.

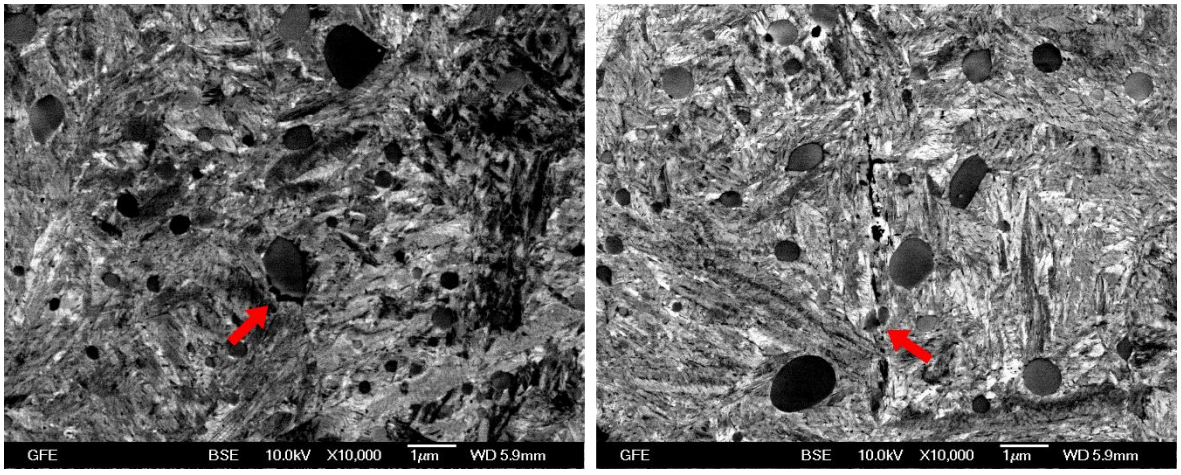

Figure 6.2: BSE SEM images of interaction between primary spheroidised carbide and microcrack found in the sample tested for 15 hours with current plus additional 50 hours without current. Red arrows point to the location of the primary carbide.

6.2 Tests on L11 Test Rig with high ref. oil + current

From the results presented in subchapter 6.1, it has been shown that microcracks formation, growth, branching and development of WEC in subsurface of the bearing inner rings are influenced by the continuous current loading. This experiment aims to understand whether WECs form purely due to interaction of material with current loading or due to a combination of current loading and lubricant. The tests were performed on the same L11 test rig under current flow. The test conditions for this study were almost identical to those described in Chapter 5 (summarised above as Test 2 in Table 6.1) except that the 'low reference' lubricant Total Transmission Ti75W80 used in Chapter 5 has been replaced by a 'high reference' lubricant Total PAO 8 in the new tests. Two tests of 20 and 50 hours were conducted. As shown in Chapter 5, similar tests at these test durations have created extensive amount of microcracks (in the 20-hour samples) and widespread WEC networks and surface spalls (in the 50-hour samples). Both tests in this study were deliberately aborted without any surface damage generated (no spalls or cracks).

6.2.1 Results and Discussion

Two sections/samples in randomly selected locations from both 20 and 50 hours tested DGBB inner rings were cut and metallographically prepared following the procedure described in Chapter 3. Initially samples were checked for WECs using LOM, however no microstructural changes were observed at a maximum possible magnification of the microscope. BSE SEM examinations were then performed focusing on depths of approx. 100 µm below the surface, where most of the cracks were found in the study presented in Chapter 5.

A comprehensive subsurface BSE SEM analysis has been performed on all four sections of the tested DGBB inner rings, however microstructural changes of any form have not been observed. Figure 6.3 shows examples of BSE SEM images of the samples tested for 20 and 50 hours, where microstructure has not shown any alterations compared with that of the virgin material matrix presented in Chapter 4. This suggested that the combination of 'low reference' oil and electrical current is critical to the formation of WECs as presented in Chapter 5. The 'low reference' lubricant (i.e. 'bad lubricant' or 'WEC critical oil') used in the tests discussed in Chapter 5 has frequently been suggested to be responsible for WECs failures [111,

116, 127, 129]. One of the hypothesis is that this lubricant causes WECs due to its decomposition into hydrogen which subsequently diffuses into the bearing steel. However, no sufficient evidence has been provided to confirm the proposed hypothesis, although some correlations between number of formed WECs and diffusible hydrogen in post-test samples tested with 'bad lubricant' have been shown [144]. Hydrogen measurements were not performed in this study, thus hydrogen influence cannot be excluded. Similar to that discussed above, the fact that only one ¼ of each bearing inner ring was examined and it is not possible to completely exclude that other parts of the bearings may contain WECs, but the probability of this to happen is extremely low.

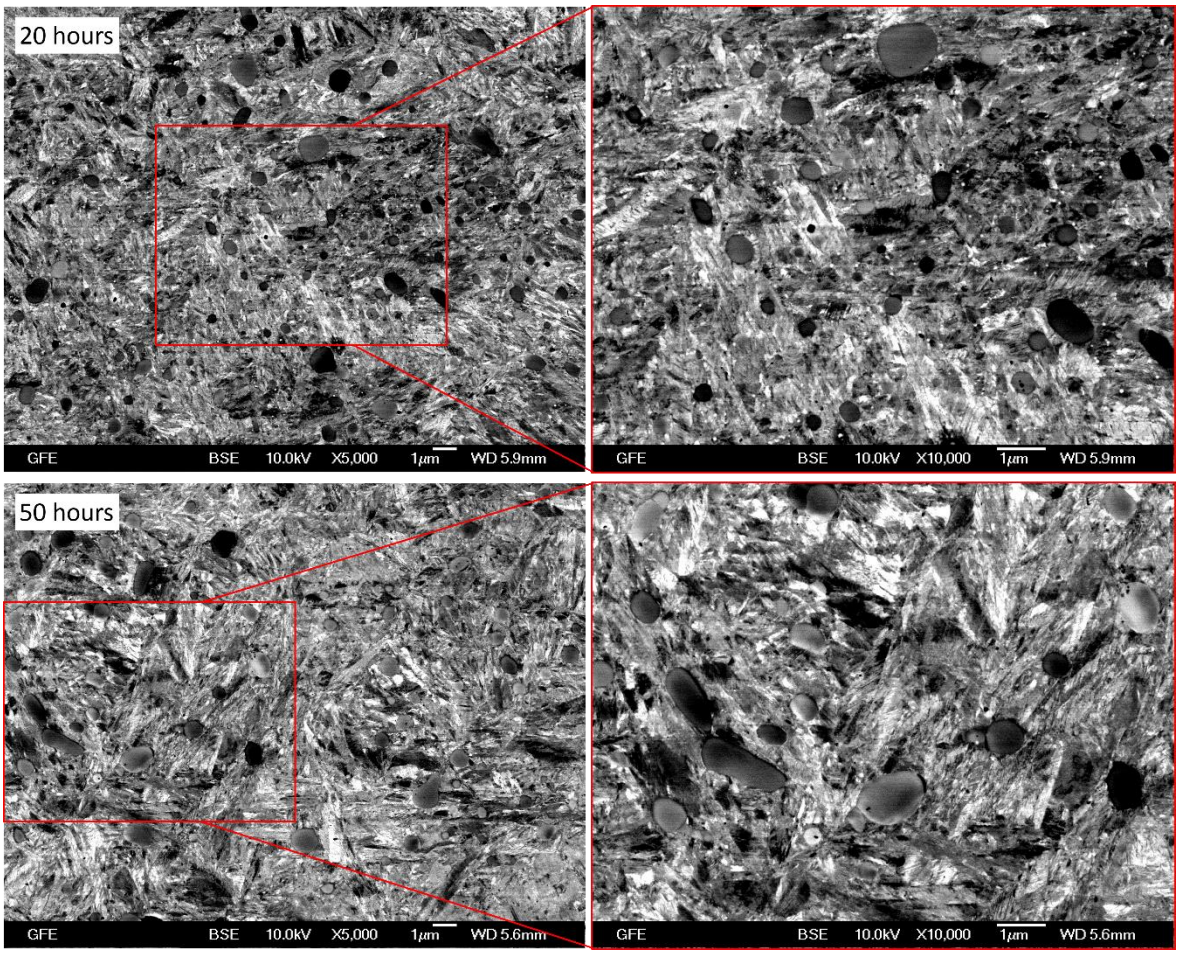

Figure 6.3: BSE SEM images of microstructure found in samples tested for 20 and 50 hours with continuous current loading and 'high reference' lubricant

6.3 Conclusions

This chapter has presented the results from two types of experiments that were performed to investigate the influence of electrical current loading and lubricant

by conducting two types of purposely designed tests on the L11 test rig. Based on the observations made during the microstructure investigations the following conclusions are drawn:

- Combination of continuous electrical current loading and 'low reference' oil is found to be one of the drivers for the WECs formation (microcrack initiation and WEA development). No microcracks or WECs have been observed in subsurface of the samples tested with continuous current loading and 'high reference' lubricant. Whereas, microcracks were found to form in subsurface of the samples tested with continuous current loading and 'low reference' lubricant, although no further development into WECs was observed after the electric current was switched off.
- Rubbing of the crack surfaces is unlikely the mechanism for WEA formation associated with subsurface microcracks, since no WEA has been observed to form on the sides of microcracks during 50 hours of RCF testing with 'low reference' lubricant, but without electrical current loading.

Chapter 7

Conclusions and Further Work

This chapter provides an overview of the main findings and conclusions of this study, followed by recommendations for future work to advance the relevant research fields.

7.1 Overview

WECs have been investigated by industry and at research institutions around the world over the past few decades. Many studies have been conducted to understand the drivers of WECs formation, however the initiation and formation mechanisms of the WECs were under immense debate between different researchers at the beginning of this study. The complex microstructure of WECs containing various shape and size grains have only been reported in recent studies, and the understanding on the material microstructural changes and it influence on WEC formation remained limited. Relations between crack and WEA, roles of the inclusions and primary spheroidised carbides were not clear. A comprehensive literature review at the beginning of this study has revealed several failure hypotheses proposed by the research community accompanied with numerous unanswered questions related to WEC and WEA. It also came to attention that, similar microstructure transformation, such as DER and WEBs observed in bearings due to prolonged RCF loading may have connections with WEA and WECs. DER and WEBs were frequently reported in literature between the 1940s and 1990s, however despite the amount of efforts made, it was not very clear about the detailed microstructure transformation mechanisms possibly due to limitations in the characterisation techniques available at the time. No studies had been conducted or reported comparing WECs with DER and WEBs in the literature prior to the investigations in this study.

In this thesis, a combination of microscopy techniques has been used to characterise microstructure changes in details to find initiation, formation and

growth of WEA and cracks in through-hardened martensitic AISI 52100 bearing steel in order to identify the root cause of the WSF failure in bearings. For comparison, the behaviour of the typical AISI 52100 through-hardened martensitic steel under prolonged cyclic loading has also been investigated in details to understand the microstructure transformation in RCF and whether it has any connections with the formation of the unpredictable WEC failure.

Initially the virgin material microstructure of AISI 52100 through-hardened martensitic steel from untested DGBB similar to the ones used in Chapter 5 & 6, has been analysed. Typical martensitic microstructure with variously orientated martensite plates with some containing twins has been observed. Randomly distributed primary spheroidised carbides in various shapes and sizes, as well as cementite lamellae have been detected. Material defects, for example microcracks in martensite plates, pores or voids, have not been observed in the virgin microstructure. EBSD IQ analysis shows that virgin martensitic material has homogenised strain distribution without any localised strain points. Higher KAM values have not been observed around primary spheroidised carbides suggesting they are well integrated into the material and do not act as stress raisers in the virgin steel material.

Following virgin material microstructure analysis, fully developed WECs, DER and WEBs in failed bearings have been analysed to understand the morphology and characteristics of the microstructural alterations in detail. The results have shown that the RCF microstructural alterations have many similarities to those in WECs. For example, elongated and equiaxed grains have been found to form in altered areas of the WECs, as well as DER and WEBs due to the RCF; dissolution of primary spheroidised carbide and hardness heterogenisation have been found in both WEAs and WEBs regions.

To further investigate the initiation mechanisms of the altered microstructural features, evolution studies on WECs and RCF have been performed on a laboratory bearing test rig L11 under two sets of conditions (known to be critical for WEC and RCF damages). All tests used AISI 52100 though-hardened martensitic bearings and detailed post-test analysis has been conducted to reveal microstructure changes from very early to late stages. Firstly, a number of RCF tests were conducted and terminated at runtime between 100 and 670 hours, where DER and early stages of LABs have been observed. Secondly, WECs testing was

performed with continues current loading and 'low reference' lubricant as drivers for the WEC formation. The results from the analyses have provided considerable insight in the formation mechanisms of RCF and WECs development, formation of the globular and elongated grains, the role of the carbides and influence of carbon and chromium movement on formation of the microstructure alterations.

Lastly, a few additional experiments have been conducted on DGBBs under different test conditions to further investigate the influence of electrical current loading and lubricant on the initiation and formation of WECs initiation. The combination of electrical current loading and 'low reference' lubricant has been found to be one of the drivers for the WECs formation.

7.2 Conclusions

This section provides the conclusions from this study related to WECs, followed by the conclusions on microstructural features formed due to the prolonged RCF, and finally conclude the links between the two phenomena.

7.2.1 Altered microstructure in WECs

During the detailed study on the WECs both from failed bearing samples and from bearings tested under electrical influence over a range of running time, not only a wide range of microstructural features have been observed at different stages of WEC formation, but also links between stages are speculated. The main findings are summarised below.

- In very early hours of the testing, randomly scattered shallow horizontal and vertical microcracks in the size of few microns *without* microstructure alterations have been observed in the bearing inner race, which is thus suggested to be the earliest stage or initiation of WECs during the over-rolling testing with current loading and 'low reference' lubricant. These microcracks are found to grow to up to 7 µm length *without* microstructural alterations adjacent to the crack till approx. 48 million load cycles (20 hours of testing).
- Once branching of the microcracks has started at around 48 million load cycles (20-hour sample), areas of nanocrystalline WEA is found to have formed adjacent to the microcracks. Stress concentration in front of the

crack tip is suggested as one of the mechanisms that triggered the formation of small nanocrystalline WEAs asymmetrically along the microcrack, where the microcrack appeared to curve around the WEAs subsequently leading to WEA on only one-side of the crack. However, thin nanocrystalline WEAs adjacent to microcracks cutting through primary spheroidised carbides accompanied by carbide dissolution have also been observed, suggesting it is a different formation mechanism of WEA from the one described above, although it is difficult to confirm at this stage. The WECs formed at this stage are very small and it is believed to be the first stage of nanocrystalline WEA formation.

- Following the initiation of WEA and WECs, it is found that WECs grow rapidly between 20 and 50 hours of testing, accompanied by the formation of elongated grains within WEA and large WEC networks eventually reach bearing surface leading to spall failures. The elongated ferritic grains form at later stages of WECs appear to grow with the over-rolling cycles.

- For the first time, cracks with rough crack faces together with microstructural alterations in the form of equiaxed grains as well as horizontal microcracks with intact primary spheroidised carbides in the surrounding area have been observed at around 48 million load cycles (20-hour sample). These are considered to be undeveloped WEA, where primary carbides remaining intact resulting in insufficient amount of carbon to stabilise the newly nucleated equiaxed grains. However, it is still unclear why in some areas primary carbides get destroyed, leading to carbon pining to grain boundaries and resulting in hard nanocrystalline WEA, while in other regions the primary carbides remain intact, resulting in the formation of undeveloped WEAs.
- WEAs have been observed to have predominantly lower carbon intensity compared to the residual matrix, although small randomly located high carbon intensity areas have also been found in WEA of the failed bearing retrieved from service (Chapter 4). These areas are a mixture of typical ferritic nanocrystalline WEA and newly formed nanocrystalline carbidic structures.
- Hardness heterogenisation has been observed in the WEC specimens for the first time in this study through nanohardness analyses. The hardness in regions of fine equiaxed grains and nanocrystalline areas is found to be

considerably higher than that in the steel matrix (i.e. increase between 18 and 65%). However, in regions with coarser equiaxed and elongated grains, the material is found to be softer than the initial matrix (i.e. decrease of approx. 13%).

- Heat treatment of a sample containing WECs at 400˚C for 1 hour has been shown to lead to grain coarsening of nanocrystalline grains in WEA, suggesting that during cyclic loading temperature below 400˚C is sufficient for microstructure change within nanocrystalline WEA.

- Primary spheroidised carbides might not be critical for the initiation of microcracks, although they might be an essential part for WEA stabilisation by carbon segregation at the grain boundaries and formation of hard WEA.
- Microcracks are likely to precede WEA based on the findings from the evolution test and analysis. However, WEAs with less clearer connections to cracks have been observed in the failed bearing from service as presented in Chapter 4, suggesting a possibility of WEA being formed without necessarily a connection to cracks.
- Relatively big WEA with a small microcrack observed in fully formed WECs in the failed bearing from service (Chapter 4) and majority of WECs involve WEAs on only one side of a crack, suggest that WEA formation by rubbing of crack faces is unlikely to be the dominant mechanism. Moreover, no WEA has been found to form on the pre-formed microcracks (during the first 15 hours of test with electrical current loading) after a prolonged cyclic loading period (an additional 50 hours of RCF testing without electrical current loading) as shown in Chapter 6.
- The combination of 'low reference' lubricant and electrical current loading is thus proposed to be one of the drivers for WECs formation.

7.2.2 Altered microstructure in RCF samples

While WEC has been a research topic attracted much attention from the community, it was considered to be not related to the conventional RCF features such as DER and WEBs albeit having similar distinct appearances in steel rolling bearings. The main findings from the investigation on RCF samples are:

- DER is found to contain randomly scattered small equiaxed ferritic grains and thin elongated ferritic grains oriented in random directions. The small equiaxed and thin elongated grains appear to group either in rounded areas or in a preferential orientation at approx. 20-25° to contact surface. It has also been found that the length of thin elongated grains at approx. 1-2 μm has not changed throughout the evolution stages (between 100 and 670 hours of RCF testing), suggesting that such grains are distinctive features of DER.
- Although it has been reported in the literature that DER forms a sickle-like shape with top boundary located parallel to the bearing contacting surface, it is found in this study, for the first time that the two tips of the sickle-like shape DER reach to the contact surface when viewed in the axial cross-section plane. The reasons why DER appears to reach the surface symmetrically from the centre of the raceway is yet to be investigated.
- LABs have been observed to form at a shallower depth than the DER, although some parts of LABs intermixed with DER have been detected in the later stages. All LABs in the DGBBs have been observed to have an inclination angle between 22° and 24° to the surface in the circumferential cuts. The direction of the bands inclination is defined in relation to the over-rolling direction (or shaft rotating direction).
- During the early stages of LABs formation (in the 200-hour samples), equiaxed ferritic grains with low misorientation form without elongated grains or carbon-rich areas. EDX measurements have shown no changes in carbon or chromium intensities at this stage. However, it is possible that localised chemical changes have started to take place but have not been detected due to the detection limitations of EDX.
- As the rolling cycle increases, very small carbon-rich areas (approx. 2 μm long) and elongated grains start to form in addition to equiaxed grains. During this stage LABs are found to have grown to up to 15 μm long and appear as 'cotton bud'-like shape features with carbon-rich area at the 'stem' and equiaxed ferritic grains at the two ends. It is, however, difficult to confirm whether elongated ferritic grains form separately or simultaneously with carbon-rich areas around them. Within the LABs, while carbon redistribution has been found, no chromium redistribution was observed at this stage, which corresponds to that primary spheriodised carbides are seen

to be intact around the newly formed features. Hence, the carbon-rich areas are thought to have formed as a result of the carbon movement from the newly formed ferritic grains due to the incompatibility with its bcc lattice.

- LABs continuously grow in size and density with the increase of over-rolling cycles. Once most of residual martensitic matrix is altered and primary spheroidised carbides dissolved, which is detected by carbon and chromium redistributions in the EDX maps, HABs are formed. HABs consist of slightly coarser equiaxed ferritic grains that are depleted in carbon.
- Hardness heterogenization has been observed in LABs/HABs, where carbon-rich areas appear to have higher hardness, whereas equiaxed and elongated grains have lower hardness than the original steel matrix.

7.2.3 Comparison of the altered microstructures in WECs and DER/WEBs

- Elongated and equiaxed grains have been found to form in altered areas of the WECs, as well as DER and WEBs due to the RCF. However, different from those in the RCF samples, where newly formed elongated grains have a defined growth direction, elongated grains in WEC networks do not show any overall preferential orientation.
- Primary spheroidised carbides are shown not to be the initiation points for either WECs or RCF features. However, they might be an essential part for the stabilisation of hard nanocrystalline WEA by carbon segregation at the grain boundaries, whereas in RCF, carbon-rich areas of possibly carbidic structure are found to form due to sufficient time available for carbon atom migration.
- Hardness heterogenization has been observed in the altered areas of both WECs and RCF. Hardness variations observed seem to be related to the phase, grain size variation and carbon concentration in the relevant microstructural features.
- DER and LABs/HABs typically form in AISI 52100 through-hardened martensitic bearing steel under pure and excessive mechanical loading. While microcracks and nanocrystalline hard WEA, which result in bearings failure at much earlier stage of their life due to WSF, form when an additional loading is applied (e.g. electrical loading in this study).

- Non-metallic inclusions or other stress raisers in the bearing steel have not been observed to interact with any of the microstructural alterations in WECs, suggesting that they are unlikely to be the initiation point for WECs formation under the test conditions in this study. Moreover, the fact that DER and LABs/HABs form without microcrack formation under much higher stress conditions in the same AISI 52100 through-hardened martensitic bearing steel of similar cleanliness or content of stress raisers, contradicts with the 'WEC initiation at non-metallic inclusions' hypothesis.

7.3 Future work

Based on the studies performed in this thesis, the following work is suggested to be conducted in the future to further the research in this field:

1. It would be beneficial to further analyse the areas of equiaxed grains, such as DER, parts of LABs and WECs, with high resolutions techniques such as TEM and/or APT to compare their structures and chemical distribution, especially carbon, in order to clarify their formation mechanisms.
2. Carbon-rich areas in LABs have been successfully identified throughout all stages of its formation by using SEM in this study. Although attempted, the TEM analysis in this study was not successful. Hence, further analysis on such carbon-rich areas in LABs using TEM or other higher resolution techniques would be useful to identify their structure, chemical composition and possible formation mechanisms.
3. Through the evolution study of WECs it has been proposed that spheroidised carbides might play an essential role in nanocrystalline WEA development, therefore it would be beneficial to performed WECs testing on modified materials containing less or no carbides.
4. During the study of early stage RCF and WECs, microstructural alterations were searched arbitrarily by initially cutting the sample on randomly chosen locations following by metallographic sample preparation and after examination of cross-sections were done by use of 2D imaging techniques. It would be highly informative if a non-destructive technique can be used to detect and map the microstructural alterations. This would be more efficient and could have saved a large amount of time in searching the features blindly. A high energy X-ray method available at synchrotron facilities may

provide the necessary penetration power and resolution required to detect and map the microstructural alterations.

5. Additionally, only 2D imagining techniques has been used in this study, which although a powerful method for microstructure characterisations, it would be highly beneficial to map more sections containing early stages of microstructural alterations in 3 dimensions using techniques, such as serial sectioning in FIB/SEM, to gain more understanding whether starting points are somehow dependent on spheroidised carbides, grain boundaries or any other parts of microstructure.
6. The preliminary experiments under conditions different from those described in Chapter 5 have provided an initial understanding of the influences of the electrical current loading and 'low reference' lubricant. More detailed investigations should be conducted to study the interactions between electrical current loading and 'low reference' lubricant to understand the mechanisms further. Additionally, hydrogen measurements should be performed to confirm whether hydrogen has influenced the formation of WECs.
7. Currently different test rigs, such as FE8, micro-pitting rig (MPR) and others, have been used to successfully create WEC networks, under completely different conditions, thus may have different WEC drivers. Evolution studies, similar to the one performed in this work, by use of different test rigs could be beneficial to understand whether initiation and development of WECs are the same or different depending on drivers used for WECs production.

Tests on a FAG FE8 rig had already been conducted towards the end of this study, where axial cylindrical roller bearings (F-562831 type) made of AISI 52100 through-hardened martensitic steel were tested under axial loading with the 'low reference' lubricant without electrical current applied to the bearings. Details of the FE8 test rig can be found elsewhere in the literature [116, 170] and DIN 51 819 specifications [171]. In this study, an axial load of 60 kN was applied (~ 1.9 GPa of contact pressure), the drive shaft was rotated at a speed of 750 rpm, and the temperature of the bearings was set at 100°C. Total transmission Ti75W80 lubricant (i.e. 'low reference' lubricant), the same as in the studies presented in Chapters 5 & 6, was used for this experiment. These test conditions are proven to produce WECs repeatedly due to the negative SRR that is generated toward the

inner radius of the raceway because the velocity of the rollers' surface is higher than that of the raceway's surface. The tests were run for 5, 10, 15, 20, and 25 hours. Ultrasound examination on all samples were performed, however no WEC were identified. However, this is likely due to the detection limits, as typically only cracks that are longer than 100 μm will produce the signal. Preliminary SEM analysis has been conducted on a small section of one of the washers from each of the bearings, but no WEC has been identified so far.

A new study following from this project has already begun in the same research group and more detailed analysis will be conducted on the FE8 and new bearing samples to further this study in the near future.

Appendices

Appendix A : Non Martensite-Martensite HAGBs mapping

List of the directions and angles of the martensite-martensite boundaries that are predicted by the usual orientation relation models of the martensitic transformation developed by Kurdyumov-Sachs [150], Nishiyama-Wassermann [151], Greninger-Troiano [152] and Pitsch [153] shown in the list below with label 'martensite-martensite'. Grain boundaries between γ-Fe and α-Fe also listed and marked with yellow label 'γ-α'. Tolerance for each angle is ±5˚.

	Greninger-Troiano		**Kurdyumov-Sachs**		**Pitsch**		**Nishiyama-Wassermann**	
	direction	angle	direction	angle	direction	angle	direction	angle
γ-α	15 3 2	44.23˚	27 5 5	42.85˚	2 5 25	45.98˚	24 2 5	45.98˚
martensite- martensite	6 5 5	60.1744˚	1 1 1	60˚	-17 17 -7	62.8˚	0 -1 -1	60˚
	1 0 1	60˚	1 1 0	60˚	1 -1 1	60˚	0 1 1	60˚
	1 1 0	60˚	10 -20 17	57.2˚	21 16 12	53.68˚	-1 -3 -3	53.691˚
	20 5 18	57.5155˚	-7 -18 -21	57.2˚	16 -12 21	53.68˚	-1 3 3	53.691˚
	18 5 20	57.5155˚	-10 -17 -20	57.2˚	-21 12 16	53.68˚	-3 -1 3	53.691˚
	12 11 4	55.5675˚	-21 -7 18	57.2˚	-16 21 -12	53.68˚	-3 1 -3	53.691˚
	11 4 12	55.5675˚	-11 6 -11	51.7˚	-11 3 11	50.04˚	-4 3 -4	50.046˚
	1 1 0	54.2786˚	-5 20 16	50.5˚	11 11 3	50.04˚	-4 -3 4	50.046˚
	15 5 17	51.9146˚	-14 -13 21	50.5˚	0 -1 -1	19.48˚	1 0 0	19.471˚
	15 17 5	51.9146˚	21 13 -14	50.5˚	-1 -17 0	13.76˚	12 -12 -1	13.76˚
	11 7 11	50.8283˚	-16 5 -20	50.5˚	1 0 -17	13.76˚	12 12 1	13.76˚
	13 11 16	50.1833˚	0 -1 -1	49.5˚				
	16 13 11	50.1833˚	-1 -1 1	49.5˚				
	16 15 6	50.0306˚	-7 -15 -17	47.1˚				
	16 15 6	50.0306˚	-17 7 -15	47.1˚				
	8 8 7	49.5916˚	20 -9 0	21.1˚				
	4 0 1	19.9529˚	11 11 6	20.6˚				
	0 6 1	19.813˚	16 0 -5	20.6˚				
	8 8 3	17.2555˚	10 -27 -2	14.9˚				
	13 8 1	14.0999˚	27 10 2	14.9˚				
	1 8 13	14.0999˚	0 1 1	10.5˚				
	8 8 3	11.2792˚	1 -1 1	10.5˚				
	1 0 1	5.72141˚						

Appendix B : Load Cycles Calculations

In rating life analysis one load cycle is defined as a small patch of the raceway being over-rolled by one rolling element. The number of load cycles occurring on inner ring per bearing revolution is:

$$n_i = \frac{z}{2} \times \left(1 + \frac{D_w \times \cos\alpha}{D_{pw}}\right) \quad (1)$$

where: z is a number of rolling elements, D_w is a rolling element diameter, α is a nominal contact angle (which is derived from the line through the theoretical centres of both contact ellipses), D_{pw} is a pitch diameter (length between the middle of the opposite rolling elements).

A DGBB 6206 type has 9 balls (z = 9) and under pure radial load α = 0, hence equation (1) becomes:

$$n_i = \frac{z}{2} \quad (2)$$

Therefore to calculate the total number of load cycles occurring on inner ring, n_t, per specific test is:

$$n_t = n_i \times 60 \times speed \times test\ hours \quad (3)$$

Exact testing conditions and bearing parameters are confidential for the bearings used in Chapter 4. However, number of load cycles per revolution, n_i, has been provided by Schaeffler, as:

- DER (a double row angular contact ball bearing): *8.43*
- LABs/HABs (an angular contact ball bearing 7205B type): *7.628*
- WECs (a cylindrical roller bearing of N216 type): *10.511*

Hence, total number of load cycles was possible to obtain.

Appendix C : Publications and Awards

C.1 Journal Papers

- V. Šmeļova, A. Schwedt, L. Wang, W. Holweger, and J. Mayer, *"Electron Microscopy Investigations of Microstructural Alterations Due to Classical Rolling Contact Fatigue (RCF) in Martensitic AISI 52100 Bearing Steel,"* International Journal of Fatigue, vol. 98, pp. 142-154, 2017.

- V. Šmeļova, A. Schwedt, L. Wang, W. Holweger, and J. Mayer, *"Microstructural Changes in White Etching Cracks (WECs) and Their Relationship with Those in Dark Etching Region (DER) and White Etching Bands (WEBs) Due to Rolling Contact Fatigue (RCF),"* International Journal of Fatigue, vol. 100, Part 1, pp. 148-158, 2017.

C.2 Conference proceedings

- "Evolution of Rolling Contact Fatigue Microstructure Alterations In 100Cr6 Martensitic Bearings"
  V. Šmeļova, A. Schwedt, L. Wang, W. Holweger, J. Mayer
  6th World Tribology Congress (WTC) 2017. Beijing, China. 17-22 September 2017
  Contribution: Oral & Poster
- "A Study on the Evolution of Microstructure Alterations in White Etching Cracks"
  V. Šmeļova, A. Schwedt, L. Wang, W. Holweger, J. Mayer
  72nd STLE Annual Meeting & Exhibition. Atlanta, GA, USA. 21-25 May 2017
  Contribution: Oral & Poster
- "A Study on White Etching Crack Root Causes and its Relation to Material Microstructures"
  V. Šmeļova, A. Schwedt, L. Wang, W. Holweger, J. Mayer
  TriboUK 2017. Imperial College London, UK. 27-28th April 2017
  Contribution: Oral
- "A microstructural study of White Etching Cracks in AISI 52100 bearings"
  V. Šmeļova, A. Schwedt, L. Wang, W. Holweger, J. Mayer
  5th PGR Engineering Faculty Conference 2016. Southampton, UK. 2nd November 2016
  Contribution: Poster

- "A study of microstructure alteration in AISI 52100 bearings due to classic rolling contact fatigue and white etching crack"
  V. Šmeļova, A. Schwedt, A. M. Diederichs, J. Mayer, L. Wang, W. Holweger
  71st STLE Annual Meeting & Exhibition. Las Vegas, NV, USA. 15-19 May 2016
  Contribution: Oral & Poster
- "Aspects of microstructure heterogenization in rolling contact fatigue of 100cr6 bearings"
  V. Šmeļova, A. Schwedt, A. M. Diederichs, J. Mayer, L. Wang, W. Holweger
  37. Meeting of DGM-Fachausschuss "Texturen" and DGM-Arbeitskreis "EBSD"; Joint French-German meeting. Dresden, Germany. 31 March - 1April 2016
  Contribution: Oral
- "Influence of tempering on white etching area in wind turbine gearbox bearings"
  V. Šmeļova, L. Wang, T.J. Harvey, W. Holweger
  PGR Engineering Faculty Conference 2015. Southampton, UK. 4th November 2015
  Contribution: Oral

C.3 Awards

2016 Travel Funding from **the Armourers and Brasiers Gauntlet Trust** in sum of £900

2017 Travel Bursary from **Royal Microscopy Society (RMS)** in sum of £300

2017 Conference Grant from **Institution of Mechanical Engineers (IMechE)** in sum of £1250

List of References

[1] T. A. Harris, *Rolling Bearing Analysis*, 3rd ed. New York: Wiley, 1991.

[2] J. Kang, "Mechanisms of Microstructural Damage During Rolling Contact Fatigue of Bearing Steels," PhD Thesis, University of Cambridge, 2014.

[3] E. V. Zaretsky, "Rolling Bearing Steels - a Technical and Historical Perspective," *Materials Science and Technology,* vol. 28, pp. 58-69, 2012.

[4] M. Cerullo and D. Mekanik, *Computational Stress and Damage Modelling for Rolling Contact Fatigue*: DTU Mechanical Engineering, 2014.

[5] Koyo. Ball & Roller Bearings: Failures, Causes and Countermeasures. Accessed 05 December 2017 [Online]. Available: http://www.midpointbearing.com/wp-content/uploads/2017/01/Koyo-Failures-Causes-and-Countermeasuress.pdf

[6] H. K. D. H. Bhadeshia, "Steels for Bearings," *Progress in Materials Science,* vol. 57, pp. 268-435, 2012.

[7] A. Grabulov, "Fundamentals of Rolling Contact Fatigue," Faculty of Applied Sciences; Department of Nanoscience, Delft University of Technology, 2010.

[8] Y. Murakami, H. Takemura, A. Fujii, and K. Furumura, "Rolling Contact Fatigue Life under Contaminated Lubrication with Several Foreign Particles," *NSK Tech J,* vol. 655, pp. 17-24, 1993.

[9] K. Stadler and A. Studenrauch, "Premature Bearing Failures in Wind Gearboxes and White Etching Cracks (WEC)," *Evolution - business and technology magazine from SKF,* 2013.

[10] K. Stadler, "Premature Wind Gearbox Bearing Failure '&' (Not 'by') White Etching Cracks (WEC)," in *NREL GRC meeting*, 2014.

[11] A. Greco, S. Sheng, J. Keller, and A. Erdemir, "Material Wear and Fatigue in Wind Turbine Systems," *Wear,* vol. 302, pp. 1583-1591, Apr-May 2013.

[12] A. V. Olver, "The Mechanism of Rolling Contact Fatigue: An Update," *Proceedings of the Institution of Mechanical Engineers, Part J: Journal of Engineering Tribology,* vol. 219, pp. 313-330, 2005.

[13] W. J. Davies and K. L. Day, "Surface Life Bearings for Automotive Alternator Applications," *Institution of Mechanical Engineers,* pp. 23-40, 1963.

[14] M. H. Evans, "White Structure Flaking (WSF) in Wind Turbine Gearbox Bearings: Effects of 'Butterflies' and White Etching Cracks (WECs)," *Materials Science and Technology,* vol. 28, pp. 3-22, Jan 2012.

[15] W. Holweger, "White Etching Cracks," in *NREL Wind Turbine Tribology Seminar*, Argonne, IL, USA, 2014.

[16] R. Errichello, R. Budny, and R. Eckert, "Investigations of Bearing Failures Associated with White Etching Areas (WEAs) in Wind Turbine Gearboxes," *Tribology & Lubrication Technology,* vol. 70, pp. 1069-1076, Oct 2014.

[17] O. H. E. West, A. M. Diederichs, H. Alimadadi, K. V. Dahl, and M. A. J. Somers, "Application of Complementary Techniques for Advanced Characterization of White Etching Cracks," *Praktische Metallographie-Practical Metallography,* vol. 50, pp. 410-431, 2013.

[18] J. Luyckx, "WEC Failure Mode on Roller Bearings from Observations Via Analysis to Understanding and a Solution," *VDI-Berichte,* vol. Nr. 2147, 2011.

[19] M.-H. Evans, "White Structure Flaking Failure in Bearings under Rolling Contact Fatigue," PhD Thesis, University of Southampton, 2013.

[20] National Renewable Energy Laboratory (NREL), Gearbox Reliability Collaborative; Accessed: June/2015. Available: http://www.nrel.gov/wind/grc/publications.html

[21] J. Ribrant and L. Bertling, "Survey of Failures in Wind Power Systems with Focus on Swedish Wind Power Plants During 1997-2005," *IEEE Transactions on Energy Conversion,* vol. 22, pp. 167-173, 2007.

[22] M. N. Kotzalas and G. L. Doll, "Tribological Advancements for Reliable Wind Turbine Performance," *Philosophical Transactions of the Royal Society a-Mathematical Physical and Engineering Sciences,* vol. 368, pp. 4829-4850, Oct 2010.

[23] R. McKenna, P. Ostman v.d. Leye, and W. Fichtner, "Key Challenges and Prospects for Large Wind Turbines," *Renewable and Sustainable Energy Reviews,* vol. 53, pp. 1212-1221, 2016.

[24] S. Sheng, "Investigation of Various Wind Turbine Drivetrain Condition Monitoring Techniques," in *NREL Wind turbine Reliability Workshop*, Albuquerque, NM, USA, 2011.

[25] S. Knight. (2011) The Gearbox Repair Market Continues to Grow, Accessed: Feb/2016 *Wind Power Monthly*. Available: http://www.windpowermonthly.com/article/1086978/gearbox-repair-market-continues-grow

[26] S. Hyde, "Improving Gearbox Reliability by Analyzing Axial Cracking on Bearings and Recommending a Solution," 2012.

[27] D. McVittie, "Wind Turbine Gearbox Reliability: The Nature of the Problem," *Gear Engineers,* 2006.

[28] P. J. Tavner, J. Xiang, and F. Spinato, "Reliability Analysis for Wind Turbines," *Wind Energy,* vol. 10, pp. 1-18, 2007.

[29] D. Scott, B. Loy, and G. H. Mills, "Paper 10: Metallurgical Aspects of Rolling Contact Fatigue," *Proceedings of the Institution of Mechanical Engineers, Conference Proceedings,* vol. 181, pp. 94-103, 1966.

[30] M. H. Evans, "An Updated Review: White Etching Cracks (WECs) and Axial Cracks in Wind Turbine Gearbox Bearings," *Materials Science and Technology,* vol. 32, pp. 1133-1169, 2016.

[31] B. J. Hamrock and W. J. Anderson, "Rolling-Element Bearings," 1983.

[32] "Heat-Treated Steels, Alloy Steels and Free-Cutting Steels - Part 17: Ball and Roller Bearing Steels," in *International Standard ISO 683-17*, ed. Geneva, Switzerland, 2014.

[33] J. Beswick, "The Effects of Alloying Elements in High Carbon Bearing Steels," *Ball Bear J,* vol. 231, pp. 2-11, 1988.

[34] J. Beswick, "Measurement of Carbon Levels in Structurally Transformed SAE 52100 Ball Bearing Steel by Microprobe Analysis," *Praktische Metallographie,* vol. 12, pp. 200-206, 1975.

[35] H. J. Böhmer, T. Hirsch, and E. Streit, "Rolling Contact Fatigue Behaviour of Heat Resistant Bearing Steels at High Operational Temperatures," *Materialwissenschaft und Werkstofftechnik,* vol. 30, pp. 533-541, 1999.

[36] W. Song, P. P. Choi, G. Inden, U. Prahl, D. Raabe, and W. Bleck, "On the Spheroidized Carbide Dissolution and Elemental Partitioning in High Carbon Bearing Steel 100Cr6," *Metallurgical and Materials Transactions A,* vol. 45, pp. 595-606, 2014.

[37] H. Fu, E. I. Galindo-Nava, and P. E. J. Rivera-Díaz-del-Castillo, "Modelling and Characterisation of Stress-Induced Carbide Precipitation in Bearing Steels under Rolling Contact Fatigue," *Acta Materialia,* vol. 128, pp. 176-187, Apr 2017.

[38] J. H. Kang and P. E. J. Rivera-Diaz-del-Castillo, "Carbide Dissolution in Bearing Steels," *Computational Materials Science,* vol. 67, pp. 364-372, Feb 2013.

[39] A. M. Diederichs, "Electron Microscopy Investigations on the Formation Mechanisms of White Etching Areas in Wind Turbines," Bachelor Thesis, Faculty of Georesources and Materials Engineering, RWTH Aachen University, 2012.

[40] A. M. Diederichs, "Einfluss Der Karbid-Degradation Auf Die Versagensmechanismen in Wälzlagerstählen," Masters Thesis, Faculty of Georesources and Materials Engineering, RWTH Aachen University, 2015.

[41] H. R. Hertz, "Miscellaneous Papers," ed: Jones and Schott. Macmillan, London, UK, 1896.

[42] A. P. Voskamp, "Microstructural Changes During Rolling Contract Fatigue: Metal Fatigue in the Subsurface Region of Deep Groove Ball Bearing Inner Rings," PhD thesis, Technical University of Delft, 1997.

[43] W. Solano Alvarez, "Microstructural Degradation of Bearing Steels," Phd Thesis, University of Cambridge, 2015.

[44] K. L. Johnson, *Contact Mechanics*: Cambridge university press, 1985.

[45] J. Halme and P. Andersson, "Rolling Contact Fatigue and Wear Fundamentals for Rolling Bearing Diagnostics-State of the Art," *Proceedings of the Institution of Mechanical Engineers, Part J: Journal of Engineering Tribology,* vol. 224, pp. 377-393, 2010.

[46] G. W. Stachowiak and A. W. Batchelor, "Engineering Tribology," vol. 24, ed. Amsterdam, the Netherlands: Elsevier Science Publishers B.V., 1993.

[47] E. V. Zaretsky, "Rolling Bearing Life Prediction, Theory, and Application," *Recent Developments in Wear Prevention, Friction and Lubrication,* vol. 37, 2010.

[48] R. L. Norton, *Machine Design: An Integrated Approach*. New York, USA: Pearson Education, 2011.

[49] FAG. Rolling Bearing Failure Analusis. Accessed 05 December 2017 [Online]. Available: https://www.farrellbearings.co.nz/site/farrellbearings/files//Rolling%20Bearing%20Failure%20V2.pdf

[50] W. Musial, S. Butterfield, and B. McNiff, "Improving Wind Turbine Gearbox Reliability," in *European Wind Energy Conference, Milan, Italy*, 2007, pp. 7-10.

[51] A. B. Jones, "Metallographic Observations of Ball Bearing Fatigue Phenomena," in *Proc. 49th Annual Meeting on 'Testing of bearings'*, Buffalo, NY, USA, 1946, pp. 35-52.

[52] H. Swahn, P. C. Becker, and O. Vingsbo, "Martensite Decay During Rolling-Contact Fatigue in Ball-Bearings," *Metallurgical Transactions a-Physical Metallurgy and Materials Science,* vol. 7, pp. 1099-1110, 1976.

[53] D. Scott and D. Scott, *The Application of Electron Microscopy to the Study of Pitting Failure of Rolling Bearings*, 1960.

[54] R. Osterlund and O. Vingsbo, "Phase-Changes in Fatigued Ball-Bearings," *Metallurgical Transactions a-Physical Metallurgy and Materials Science,* vol. 11, pp. 701-707, 1980.

[55] J. Martin, S. Borgese, and A. Eberhardt, "Microstructural Alterations of Rolling—Bearing Steel Undergoing Cyclic Stressing," *Journal of Fluids Engineering,* vol. 88, pp. 555-565, 1966.

[56] S. Borgese, "A Study of the Growth Mechanism of Lenticular Carbides in Cyclically Stressed 52100 Steel," *Journal of Tribology,* vol. 92, pp. 54-58, 1970.

[57] H. Swahn, P. Becker, and O. Vingsbo, "Electron-Microscope Studies of Carbide Decay During Contact Fatigue in Ball Bearings," *Metal Science,* vol. 10, pp. 35-39, 1976.

[58] E. Lindahl and R. Österlund, "212 Transmission Electron Microscopy Applied to Phase Transformations in Ball Bearings," *Ultramicroscopy,* vol. 9, pp. 355-364, Jan 1982.

[59] H. Muro and N. Tsushima, "Microstructural, Microhardness and Residual Stress Changes Due to Rolling Contact," *Wear,* vol. 15, pp. 309-330, 1970.

[60] Y. Imai, T. Endo, D. Dong, and Y. Yamamoto, "Study on Rolling Contact Fatigue in Hydrogen Environment at a Contact Pressure Below Basic Static Load Capacity," *Tribology Transactions,* vol. 53, pp. 764-770, 2010.

[61] N. Mitamura, H. Hidaka, and S. Takaki, "Microstructural Development in Bearing Steel During Rolling Contact Fatigue," in *Materials science forum*, 2007, pp. 4255-4260.

[62] L. Rosado, N. H. Forster, K. L. Thompson, and J. W. Cooke, "Rolling Contact Fatigue Life and Spall Propagation of AISI M50, M50NiL, and AISI 52100, Part I: Experimental Results," *Tribology Transactions,* vol. 53, pp. 29-41, 2009.

[63] K. Sugino, K. Miyamoto, M. Nagumo, and K. Aoki, "Structural Alterations of Bearing Steels under Rolling Contact Fatigue'," *Transactions of the Iron and Steel Institute of Japan,* vol. 10, pp. 98-111, 1970.

[64] A. Warhadpande, F. Sadeghi, and R. D. Evans, "Microstructural Alterations in Bearing Steels under Rolling Contact Fatigue Part 1-Historical Overview," *Tribology Transactions,* vol. 56, pp. 349-358, May 2013.

[65] J. L. O'Brien and A. H. King, "Electron Microscopy of Stress-Induced Structural Alterations near Inclusions in Bearing Steels," *Journal of Fluids Engineering,* vol. 88, pp. 568-571, 1966.

[66] G. Vasilca and V. Raszillier, "A Study of Dark Etching Area (D.E.A.) Type Structure Modification of Material and Hertzian Contact Area Induced by Ball Bearing Type Motion," *Wear,* vol. 19, pp. 1-15, 1972.

[67] A. Voskamp, "Material Response to Rolling Contact Loading," *Journal of tribology,* vol. 107, pp. 359-364, 1985.

[68] A. Voskamp, R. Österlund, P. Becker, and O. Vingsbo, "Gradual Changes in Residual Stress and Microstructure During Contact Fatigue in Ball Bearings," *Metals Technology,* vol. 7, pp. 14-21, 1980.

[69] J. Bush, W. Grube, and G. Robinson, "Microstructural and Residual Stress Changes in Hardened Steel Due to Rolling Contact," *ASM Transactions,* vol. 54, pp. 390-412, 1961.

[70] A. P. Voskamp and E. J. Mittemeijer, "Crystallographic Preferred Orientation Induced by Cyclic Rolling Contact Loading," *Metallurgical and Materials Transactions A,* vol. 27, pp. 3445-3465, Nov 1996.

[71] N. H. Forster, L. Rosado, W. P. Ogden, and H. K. Trivedi, "Rolling Contact Fatigue Life and Spall Propagation Characteristics of AISI M50, M50 Nil, and AISI 52100, Part III: Metallurgical Examination," *Tribology Transactions,* vol. 53, pp. 52-59, 2009.

[72] H. Fu, W. Song, E. I. Galindo-Nava, and P. E. J. Rivera-Díaz-del-Castillo, "Strain-Induced Martensite Decay in Bearing Steels under Rolling Contact Fatigue: Modelling and Atomic-Scale Characterisation," *Acta Materialia,* vol. 139, pp. 163-173, Oct 2017.

[73] J. Buchwald and R. W. Heckel, "An Analysis of Microstructural Changes in 52100 Steel Bearings During Cyclic Stressing," *Transactions of the ASM,* vol. 61, pp. 750-756, 1968.

[74] R. Tricot, J. Monnot, and M. Lluansi, "How Microstructural Alterations Affect Fatigue Properties of 52100 Steel," *Met Eng Q,* vol. 12, pp. 39-47, 1972.

[75] O. Zwirlein, "Rolling Contact Fatigue Mechanisms—Accelerated Testing Versus Field Performance," in *Rolling element bearings*, London, 1983, pp. 23-27.

[76] N. Maharjan, W. Zhou, and Y. Zhou, "Micro-Structural Study of Bearing Material Failure Due to Rolling Contact Fatigue in Wind Turbine Gearbox," in *Proceedings of the international symposium on current research in hydraulic turbines*, 2016.

[77] J. A. Martin, S. F. Borgese, and A. D. Eberhardt, "Structural Studies of Bearing Steel Undergoing Cyclic Stressing," Defense Technical Information Center (DTIC)1967.

[78] H. Schlicht, E. Schreiber, and O. Zwirlein, "Effects of Material Properties on Bearing Steel Fatigue Strength," *Effect of steel manufacturing processes on the quality of bearing steels,* pp. 81-101, 1986.

[79] I. A. Polonsky and L. M. Keer, "On White Etching Band Formation in Rolling Bearings," *Journal of the Mechanics and Physics of Solids,* vol. 43, pp. 637-669, 1995.

[80] V. Bhargava, G. T. Hahn, and C. A. Rubin, "Rolling Contact Deformation, Etching Effects, and Failure of High-Strength Bearing Steel," *Metallurgical Transactions A,* vol. 21, pp. 1921-1931, July 1990.

[81] A. Muroga and H. Saka, "Analysis of Rolling Contact Fatigued Microstructure Using Focused Ion Beam Sputtering and Transmission Electron Microscopy Observation," *Scripta Metallurgica et Materialia,* vol. 33, pp. 151-156, 1995.

[82] R. Osterlund, M. Aucouturier, and O. Vingsbo, "High-Resolution Autoradiography Determination of Carbon Diffusion During Rolling-Contact Fatigue in Ball-Bearings," *Scandinavian Journal of Metallurgy,* vol. 10, pp. 67-72, 1981.

[83] H. Swahn, L. Hellner, C. Andersson, B. Zetterlund, and O. Vingsbo, "Phase Transformations and Residual Stress Changes in Steel Rolls During Contact Fatigue," *Scandinavian Journal of Metallurgy,* vol. 4, pp. 263-266, 1975.

[84] J. Beswick, A. Voskamp, J. v.d. Sanden, M. Verburgh, and S. Horton, "Bearing Material/Treatment Developments at the SKF Engineering and Research Centre," in *Creative Use of Bearing Steels*, ed: ASTM International, 1993.

[85] T. Lund, "Structural Alterations in Fatigue-Tested Ball- Bearing Steel," *Jernkontorets Ann,* vol. 153, pp. 337-343, 1969.

[86] A. Gentile and A. Martin, "The Effects of Prior Metallurgically Induced Compressive Residual Stress on the Metallurgical and Endurance Properties of Overload Tested Ball Bearings," in *American Society of Mechanical Engineers*, Chicago, ILL, USA, 1965.

[87] N. Kino and K. Otani, "The Influence of Hydrogen on Rolling Contact Fatigue Life and Its Improvement," *JSAE Review 24,* pp. 289-294, 2003.

[88] J. Gegner, *Tribological Aspects of Rolling Bearing Failures*: INTECH Open Access Publisher, 2011.

[89] K. Tamada and H. Tanaka, "Occurrence of Brittle Flaking on Bearings Used for Automotive Electrical Instruments and Auxiliary Devices," *Wear,* vol. 199, pp. 245-252, Nov 1996.

[90] T. B. Lund, "Sub-Surface Initiated Rolling Contact Fatigue-Influence of Non-Metallic Inclusions, Processing History, and Operating Conditions," *Journal of ASTM International,* vol. 7, pp. 1-12, May 2010.

[91] S. W. Ooi, A. Gola, R. H. Vegter, P. Yan, and K. Stadler, "Evolution of White-Etching Cracks and Associated Microstructural Alterations During Bearing Tests," *Materials Science and Technology,* vol. 33, pp. 1657-1666, 2017.

[92] H. Bhadeshia and W. Solano-Alvarez, "Critical Assessment 13: Elimination of White Etching Matter in Bearing Steels," *Materials Science and Technology,* vol. 31, pp. 1011-1015, May 2015.

[93] J. Luyckx, "Hammering Wear Impact Fatigue Hypothesis WEC/irWEA Failure Mode on Roller Bearings," in *NREL Wind Turbine Tribology Seminar*, Broomfield, CO, USA, 2011.

[94] G. L. Doll, "Tribological Challenges in Wind Turbine Technology," in *NREL wind turbine tribology seminar*, Broomfiled, CO, 2011.

[95] R. H. Vegter and J. T. Slycke, "The Role of Hydrogen on Rolling Contact Fatigue Response of Rolling Element Bearings," *Journal of ASTM International,* vol. 7, 2010.

[96] M. H. Evans, A. D. Richardson, L. Wang, and R. J. K. Wood, "Serial Sectioning Investigation of Butterfly and White Etching Crack (WEC) Formation in Wind Turbine Gearbox Bearings," *Wear,* vol. 302, pp. 1573-1582, Apr-May 2013.

[97] M. H. Evans, L. Wang, H. Jones, and R. J. K. Wood, "White Etching Crack (WEC) Investigation by Serial Sectioning, Focused Ion Beam and 3-D Crack Modelling," *Tribology International,* vol. 65, pp. 146-160, Sep 2013.

[98] A. Ruellan, F. Ville, X. Kleber, A. Arnaudon, and D. Girodin, "Understanding White Etching Cracks in Rolling Element Bearings: The Effect of Hydrogen Charging on the Formation Mechanisms," *Proceedings of the Institution of Mechanical Engineers Part J-Journal of Engineering Tribology,* vol. 228, pp. 1252-1265, Nov 2014.

[99] F. Gutiérrez Guzmán, M. O. Oezel, G. Jacobs, G. Burghardt, C. Broeckmann, and T. Janitzky, "Influence of Slip and Lubrication Regime on the Formation of White Etching Cracks on a Two-Disc Test Rig," *Lubricants,* vol. 6, p. 8, 2018.

[100] A. M. Diederichs, A. Schwedt, J. Mayer, and T. Dreifert, "Electron Microscopy Analysis of Structural Changes within White Etching Areas," *Materials Science and Technology,* vol. 32, pp. 1683-1693, 2016.

[101] M. H. Evans, A. D. Richardson, L. Wang, and R. J. K. Wood, "Effect of Hydrogen on Butterfly and White Etching Crack (WEC) Formation under Rolling Contact Fatigue (RCF)," *Wear,* vol. 306, pp. 226-241, 2013.

[102] B. Gould, A. Greco, K. Stadler, and X. Xiao, "An Analysis of Premature Cracking Associated with Microstructural Alterations in an AISI 52100 Failed Wind Turbine Bearing Using X-Ray Tomography," *Materials & Design,* vol. 117, pp. 417-429, 2017.

[103] B. Gould, A. Greco, K. Stadler, E. Vegter, and X. Xiao, "Using Advanced Tomography Techniques to Investigate the Development of White Etching Cracks in a Prematurely Failed Field Bearing," *Tribology International,* vol. 116, pp. 362-370, July 2017.

[104] R. Osterlund, O. Vingsbo, L. Vincent, and P. Guiraldenq, "Butterflies in Fatigued Ball-Bearings - Formation Mechanisms and Structure," *Scandinavian Journal of Metallurgy,* vol. 11, pp. 23-32, 1982.

[105] H. Harada, T. Mikami, M. Shibata, D. Sokai, A. Yamamoto, and H. Tsubakino, "Microstructural Changes and Crack Initiation with White Etching Area Formation under Rolling/Sliding Contact in Bearing Steel," *ISIJ International,* vol. 45, pp. 1897-1902, 2005.

[106] K. Hiraoka, M. Nagao, and T. Isomoto, "Study on Flaking Process in Bearings by White Etching Area Generation," in *Bearing Steel Technology-Advances and State of the Art in Bearing Steel Quality Assurance: 7th Volume*. vol. 1465, J. M. Beswick, Ed., ed W Conshohocken: American Society Testing and Materials, 2007, pp. 234-240.

[107] J. H. Kang, B. Hosseinkhani, C. A. Williams, M. P. Moody, P. A. J. Bagot, and P. E. J. Rivera-Diaz-del-Castillo, "Solute Redistribution in the Nanocrystalline Structure Formed in Bearing Steels," *Scripta Materialia,* vol. 69, pp. 630-633, Oct 2013.

[108] H. Yamada and H. Uyama, "The Effects of Alloy Elements an Heat Treatments on White Structure Flaking in Rolling Bearings," in *STLE Annual Meeting & Exhibition*, Dalas, TX, USA, 2015.

[109] W. Liu, "The Failure Analysis of the Repeat Geartooth Breakage in a 40 MW Steam Turbine Load Gearbox and the Butterfly in the Carburized Case," *Engineering Failure Analysis,* vol. 46, pp. 9-17, Nov 2014.

[110] M. H. Evans, A. D. Richardson, L. Wang, R. K. Wood, and W. B. Anderson, "Confirming Subsurface Initiation at Non-Metallic Inclusions as One Mechanism for White Etching Crack (WEC) Formation," *Tribology International,* vol. 75, pp. 87-97, Jul 2014.

[111] M. H. Evans, L. Wang, and R. J. K. Wood, "Formation Mechanisms of White Etching Cracks and White Etching Area under Rolling Contact Fatigue," *Proceedings of the Institution of Mechanical Engineers Part J-Journal of Engineering Tribology,* vol. 228, pp. 1047-1062, Oct 2014.

[112] P. C. Becker, "Microstructural Changes around Non-Metallic Inclusions Caused by Rolling-Contact Fatigue of Ball-Bearing Steels," *Metals Technology,* vol. 8, pp. 234-243, 1981.

[113] A. Grabulov, U. Ziese, and H. W. Zandbergen, "TEM/SEM Investigation of Microstructural Changes within the White Etching Area under Rolling Contact Fatigue and 3-D Crack Reconstruction by Focused Ion Beam," *Scripta Materialia,* vol. 57, pp. 635-638, Oct 2007.

[114] A. Grabulov, R. Petrov, and H. W. Zandbergen, "EBSD Investigation of the Crack Initiation and TEM/FIB Analyses of the Microstructural Changes around the Cracks Formed under Rolling Contact Fatigue (RCF)," *International Journal of Fatigue,* vol. 32, pp. 576-583, Mar 2010.

[115] M. H. Evans, J. C. Walker, C. Ma, L. Wang, and R. J. K. Wood, "A FIB/TEM Study of Butterfly Crack Formation and White Etching Area (WEA) Microstructural Changes under Rolling Contact Fatigue in 100Cr6 Bearing Steel," *Materials Science and Engineering a-Structural Materials Properties Microstructure and Processing,* vol. 570, pp. 127-134, May 15 2013.

[116] W. Holweger, M. Wolf, D. Merk, T. Blass, M. Goss, J. Loos*, et al.*, "White Etching Crack Root Cause Investigations," *Tribology Transactions,* vol. 58, pp. 59-69, Jan-Feb 2015.

[117] Y. J. Li, M. Herbig, S. Goto, and D. Raabe, "Atomic Scale Characterization of White Etching Area and Its Adjacent Matrix in a Martensitic 100Cr6 Bearing Steel," *Materials Characterization,* vol. 123, pp. 349-353, 2017.

[118] H. K. Danielsen, F. G. Guzmán, K. V. Dahl, Y. J. Li, J. Wu, G. Jacobs*, et al.*, "Multiscale Characterization of White Etching Cracks (WEC) in a 100Cr6 Bearing from a Thrust Bearing Test Rig," *Wear,* vol. 370–371, pp. 73-82, 2017.

[119] W. Solano-Alvarez and H. K. D. H. Bhadeshia, "White-Etching Matter in Bearing Steel. Part Ii: Distinguishing Cause and Effect in Bearing Steel Failure," *Metallurgical and Materials Transactions a-Physical Metallurgy and Materials Science,* vol. 45A, pp. 4916-4931, Oct 2014.

[120] S.-X. Li, Y.-S. Su, X.-D. Shu, and J.-J. Chen, "Microstructural Evolution in Bearing Steel under Rolling Contact Fatigue," *Wear,* vol. 380–381, pp. 146-153, 2017.

[121] H. Uyama, H. Yamada, H. Hidaka, and N. Mitamura, "The Effects of Hydrogen on Microstructural Change and Surface Originated Flaking in Rolling Contact Fatigue," *Tribology Online,* vol. 6, pp. 123-132, 2011.

[122] B. Gould and A. Greco, "The Influence of Sliding and Contact Severity on the Generation of White Etching Cracks," *Tribology Letters,* vol. 60, p. 13, Nov 2015.

[123] W. Holweger, F. Walther, J. Loos, M. Wolf, J. Schreiber, W. Dreher*, et al.*, "Non-Destructive Subsurface Damage Monitoring in Bearings Failure Mode Using Fractal Dimension Analysis," *Industrial Lubrication and Tribology,* vol. 64, pp. 132-137, 2012.

[124] Y. J. Li, M. Herbig, S. Goto, and D. Raabe, "Formation of Nanosized Grain Structure in Martensitic 100Cr6 Bearing Steels Upon Rolling Contact Loading Studied by Atom Probe Tomography," *Materials Science and Technology,* pp. 1-6, 2016.

[125] W. Solano-Alvarez, E. J. Pickering, and H. Bhadeshia, "Degradation of Nanostructured Bainitic Steel under Rolling Contact Fatigue," *Materials Science and Engineering a-Structural Materials Properties Microstructure and Processing,* vol. 617, pp. 156-164, Nov 2014.

[126] W. Solano-Alvarez, E. J. Pickering, M. J. Peet, K. L. Moore, J. Jaiswal, A. Bevan*, et al.*, "Soft Novel Form of White-Etching Matter and Ductile Failure of Carbide-Free Bainitic Steels under Rolling Contact Stresses," *Acta Materialia,* vol. 121, pp. 215-226, Sep 2016.

[127] A. Ruellan, X. Kleber, F. Ville, J. Cavoret, and B. Liatard, "Understanding White Etching Cracks in Rolling Element Bearings: Formation Mechanisms and Influent Tribochemical Drivers," *Proceedings of the Institution of Mechanical Engineers Part J-Journal of Engineering Tribology,* vol. 229, pp. 886-901, Aug 2015.

[128] J. Gegner and W. Nierlich, "The Bearing Axial Cracks Root Cause Hypothesis of Frictional Surface Crack Initiation and Corrosion Fatigue Driven Crack Growth," in *NREL wind turbine tribology seminar*, Broomfiled, CO, USA, 2011.

[129] M. Paladugu, D. R. Lucas, and R. Scott Hyde, "Effect of Lubricants on Bearing Damage in Rolling-Sliding Conditions: Evolution of White Etching Cracks," *Wear,* vol. 398-399, pp. 165-177, 2018.

[130] A. M. Diederichs, S. Barteldes, A. Schwedt, J. Mayer, and W. Holweger, "Study of Subsurface Initiation Mechanism for White Etching Crack Formation," *Materials Science and Technology,* pp. 1-9, 2016.

[131] T. Bruce, H. Long, T. Slatter, and R. Dwyer-Joyce, "Formation of White Etching Cracks at Manganese Sulfide (MnS) Inclusions in Bearing Steel Due to Hammering Impact Loading," *Wind Energy,* 2016.

[132] A. Greco, "White Etching Crack Failure Overview, Tomography Analysis, and Test Development," in *NREL Wind Turbine Tribology Seminar*, Argonne National Laboratory, 2014.

[133] K. Tamada, H. Tanaka, and N. Tsushima, "A New Type of Flaking Failure in Bearings for Electrical Instruments of Automotive Engines," in *Bearing Steels: Into the 21st Century*, ed: ASTM International, 1998.

[134] H. W. Walton, "The Influence of Residual Stresses on the Susceptibility to Hydrogen Embrittlement in Hardened Steel Components Subjected to Rolling Contact Conditions," SAE Technical Paper, 2002.

[135] K. Iso, A. Yokouchi, and H. Takemura, "Research Work for Clarifying the Mechanism of White Structure Flaking and Extending the Life of Bearings," SAE Technical Paper, 2005.

[136] M. Kohara, T. Kawamura, and M. Egami, "Study on Mechanism of Hydrogen Generation from Lubricants," *Tribology Transactions,* vol. 49, pp. 53-60, Jan-Mar 2006.

[137] H. Uyama, "The Mechanism of White Structure Flaking in Rolling Bearings," in *NREL Wind Turbine Tribology Seminar*, Broomfield, CO, USA, 2011.

[138] B. A. Szost and P. E. J. Rivera-Díaz-del-Castillo, "Unveiling the Nature of Hydrogen Embrittlement in Bearing Steels Employing a New Technique," *Scripta Materialia,* vol. 68, pp. 467-470, 2013.

[139] Y. Kadin, "Modeling of Hydrogen Transport in Static and Rolling Contact," *Tribology Transactions,* vol. 58, pp. 260-273, 2015.

[140] T. Imran, B. Jacobson, and A. Shariff, "Quantifying Diffused Hydrogen in AISI-52100 Bearing Steel and in Silver Steel under Tribo-Mechanical Action: Pure Rotating Bending, Sliding–Rotating Bending, Rolling–Rotating Bending and Uni-Axial Tensile Loading," *Wear,* vol. 261, pp. 86-95, 2006.

[141] M. Grujicic, S. Ramaswami, R. Yavari, R. Galgalikar, V. Chenna, and J. S. Snipes, "Multiphysics Computational Analysis of White-Etch Cracking Failure Mode in Wind Turbine Gearbox Bearings," *Proceedings of the Institution of Mechanical Engineers Part L-Journal of Materials-Design and Applications,* vol. 230, pp. 43-63, Feb 2016.

[142] M. Ščepanskis, A. Jakovičs, I. Kaldre, W. Holweger, B. Nacke, and A. Diederichs, "The Numerical Model of Electrothermal Deformations of Carbides in Bearing Steel as the Possible Cause of White Etching Cracks Initiation," *Tribology Letters,* vol. 59, pp. 1-10, 2015.

[143] B. Gould and A. Greco, "Investigating the Process of White Etching Crack Initiation in Bearing Steel," *Tribology Letters,* vol. 62, pp. 1-14, 2016.

[144] A. D. Richardson, M.-H. Evans, L. Wang, R. J. K. Wood, and M. Ingram, "Thermal Desorption Analysis of Hydrogen in Non-Hydrogen-Charged Rolling Contact Fatigue-Tested 100Cr6 Steel," *Tribology Letters,* vol. 66, p. 4, Nov 2017.

[145] W. J. Lu and R. S. Qin, "Stability of Martensite with Pulsed Electric Current in Dual-Phase Steels," *Materials Science and Engineering: A,* 2016.

[146] S. Zaefferer, P. Romano, and F. Friedel, "EBSD as a Tool to Identify and Quantify Bainite and Ferrite in Low-Alloyed Al-TRIP Steels," *Journal of microscopy,* vol. 230, pp. 499-508, 2008.

[147] J. Wu, P. J. Wray, C. I. Garcia, M. Hua, and A. J. Deardo, "Image Quality Analysis: A New Method of Characterizing Microstructures," *ISIJ International,* vol. 45, pp. 254-262, 2005.

[148] L. Ryde, "Application of EBSD to Analysis of Microstructures in Commercial Steels," *Materials Science and Technology,* vol. 22, pp. 1297-1306, 2006.

[149] S. I. Wright and M. M. Nowell, "EBSD Image Quality Mapping," *Microscopy and Microanalysis,* vol. 12, pp. 72-84, 2005.

[150] T. Furuhara, H. Kawata, S. Morito, and T. Maki, "Crystallography of Upper Bainite in Fe–Ni–C Alloys," *Materials Science and Engineering: A,* vol. 431, pp. 228-236, June 2006.

[151] H. Kitahara, R. Ueji, M. Ueda, N. Tsuji, and Y. Minamino, "Crystallographic Analysis of Plate Martensite in Fe–28.5 at.% Ni by Fe-SEM/EBSD," *Materials Characterization,* vol. 54, pp. 378-386, 2005.

[152] A. B. Greninger and A. R. Troiano, "Orientation Habit of Martensite," *Nature,* vol. 141, p. 38, 1938.

[153] Y. He, "Grain-Scale Characterization of Fcc/Bcc Correspondence Relations and Variant Selection," Department of Mining, Metals and Material Engineering, McGill University, Montreal, Canada, 2005.

[154] Oxford Instruments Analytical - Technical Briefing. "Electron Backscattered Diffraction - Explained" Accessed: Feb/2016. Available: http://www.material.ntnu.no/ebsd/EBSD/EBSD_Explained.pdf

[155] C. J. Smithells, "Smithells Metals Reference Book, Edited by E. A. Brandes and G. B. Brook," seventh edition ed: Butterworth-Heinemann, London, 1992.

[156] "ISO/DIS 14577-1.2 Metallic Materials - Instrumented Indentation Test for Hardness and Materials Parameters," in *International Organization for Standardization*, ed, 2001.

[157] G. Z. Voyiadjis and R. Peters, "Size Effects in Nanoindentation: An Experimental and Analytical Study," *Acta Mechanica,* vol. 211, pp. 131-153, April 2010.

[158] V. Šmeļova, A. Schwedt, L. Wang, W. Holweger, and J. Mayer, "Microstructural Changes in White Etching Cracks (WECs) and Their Relationship with Those in Dark Etching Region (DER) and White Etching Bands (WEBs) Due to Rolling Contact Fatigue (RCF)," *International Journal of Fatigue,* vol. 100, Part 1, pp. 148-158, 2017.

[159] V. Šmeļova, A. Schwedt, L. Wang, W. Holweger, and J. Mayer, "Electron Microscopy Investigations of Microstructural Alterations Due to Classical Rolling Contact Fatigue (RCF) in Martensitic AISI 52100 Bearing Steel," *International Journal of Fatigue,* vol. 98, pp. 142-154, 2017.

[160] Y. Xu, J. Zhang, Y. Bai, and M. A. Meyers, "Shear Localization in Dynamic Deformation: Microstructural Evolution," *Metallurgical and materials transactions A,* vol. 39, p. 811, 2008.

[161] U. Andrade, M. A. Meyers, K. S. Vecchio, and A. H. Chokshi, "Dynamic Recrystallization in High-Strain, High-Strain-Rate Plastic Deformation of Copper," *Acta Metallurgica et Materialia,* vol. 42, pp. 3183-3195, Sep 1994.

[162] M. A. Meyers, Y. B. Xu, Q. Xue, M. T. Pérez-Prado, and T. R. McNelley, "Microstructural Evolution in Adiabatic Shear Localization in Stainless Steel," *Acta Materialia,* vol. 51, pp. 1307-1325, 2003.

[163] M. A. Meyers, V. F. Nesterenko, J. C. LaSalvia, and Q. Xue, "Shear Localization in Dynamic Deformation of Materials: Microstructural Evolution and Self-Organization," *Materials Science and Engineering: A,* vol. 317, pp. 204-225, 2001.

[164] G. W. Stachowiak and A. W. Batchelor, *Engineering Tribology*, Third Edition ed. Burlington: Butterworth-Heinemann, 2006.

[165] J. Loos, I. Bergmann, and M. Goss, "Influence of Currents from Electrostatic Charges on WEC Formation in Rolling Bearings," *Tribology Transactions,* vol. 59, pp. 865-875, June 2016.

[166] Y. Kadin and M. Y. Sherif, "Energy Dissipation at Rubbing Crack Faces in Rolling Contact Fatigue as the Mechanism of White Etching Area Formation," *International Journal of Fatigue,* vol. 96, pp. 114-126, 2017.

[167] W. Solano-Alvarez, J. Duff, M. C. Smith, and H. K. D. H. Bhadeshia, "Elucidating White-Etching Matter through High-Strain Rate Tensile Testing," *Materials Science and Technology,* 2016.

[168] G. Juilfs, "Das Diffusionsverhalten Von Wasserstoff in Einem Niedriglegierten Stahl Unter Berücksichtigung Des Verformungsgrades," 2000.

[169] J. Song and W. Curtin, "Atomic Mechanism and Prediction of Hydrogen Embrittlement in Iron," *Nature materials,* vol. 12, p. 145, 2013.

[170] W. Kruhöffer and J. Loos, "WEC Formation in Rolling Bearings under Mixed Friction: Influences and “Friction Energy Accumulation” as Indicator," *Tribology Transactions,* pp. 1-14, 2016.

[171] D. 819-1:1999-12, "Testing of Lubricants - Mechanical - Dynamic Testing in the Roller Bearing Test Apparatus FE8 - Part-1:General Working Principles," ed. Beuth Verlag GmbH: Berlin, 1999.